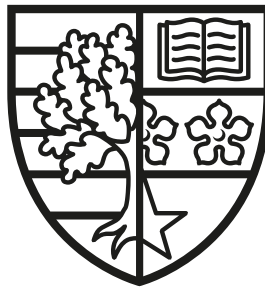


Tailored quantum light for photonic quantum technologies

Francesco Graffitti

SUBMITTED FOR THE DEGREE OF
DOCTOR OF PHILOSOPHY

HERIOT-WATT UNIVERSITY



DEPARTMENT OF PHYSICS,
SCHOOL OF ENGINEERING AND PHYSICAL SCIENCES.

28th January 2021

The copyright in this thesis is owned by the author. Any quotation from the thesis or use of any of the information contained in it must acknowledge this thesis as the source of the quotation or information.

Abstract

Photonic quantum technologies rely on the deterministic preparation of qubits encoded in quantum states of light: advances in this field are therefore contingent with the development of reliable photon sources. In this Thesis, I address this challenge presenting a novel and versatile approach to single-photon generation based on nonlinearity engineering in parametric down-conversion. By tailoring the effective nonlinearity of a crystal, this scheme enables access to the spectral degree of freedom of photonic qubits with unprecedented precision, and translates into a number of different applications based on the manipulation of the biphoton spectral/temporal properties. A thorough theoretical and numerical description of such approach is provided and paired with experimental benchmarks conducted in three main experiments. The first experiment tackles the single-photon spectral purity problem in down-conversion sources: pure photons are in fact required for achieving perfect two-photon interference, a keystone of most quantum protocols. The second experiment demonstrates the feasibility of nonlinearity engineering to produce tailored entanglement encoded in the spectrum of biphoton states. Finally, the third experiment certifies the compatibility of this technique with different degrees of freedom, demonstrating hyperentanglement of spatially and spectrally structured quantum light. In conclusion, this Thesis stands as a cookbook for designing simple yet flexible and highly-efficient single-photon sources based on tailored parametric down-conversion processes.

Acknowledgements

All the results and achievements reported in this manuscript would not have been possible without all the people I had the luck of meeting and interacting with in the last four years. Surely, it wouldn't have been possible without the guidance and support of my Ph.D. supervisor, Alessandro Fedrizzi. I'm extremely grateful for your trust and support, for all the time spent chatting about interesting physics and new crazy ideas, about politics in academia, and many other topics. Your door was always open for long, challenging discussions, even in the busiest periods: I think this made a huge difference making my Ph.D. experience incredibly stimulating, and I didn't take it for granted. You also taught us—on our own flesh—to always double-check the email recipients (*“And perhaps it was a mistake to “reply all”, including the █████ editor...”*) and we'll always be grateful for this gem you gifted us with!

Special thanks go to Agata Brańczyk for her patient collaboration, for the endless emails full of calculations and plots, and for sharing her theoretical insights with me. Whenever Sandro lacked in interest in the mathematical minutiae, I knew I could count on long and insightful discussions with you. It's a shame we never managed to meet in person, but I hope there will be a time for that as well.

I would like to acknowledge all the people in the Edinburgh Mostly Quantum Lab, that shared with me pain and joy of working in the lab. Dmytro Kundys, with whom at the beginning of this journey I shared an empty lab—with no table, no laser, not even walls or a finished ceiling—and a similarly empty group, before many others joined us. Massimiliano Proietti, for countless discussions and jokes.

We shared laughs and tears when something worked or (inevitably) broke, and it was great to have someone to share my Roman roots—and many blasphemies—that kept me company during these years. Peter Barrow, who introduced me to Python and shared with me his passion for coding: all those discussions motivated me to look into programming myself with a more critical approach. Alex Pickston, who was first a student and then a colleague, for all the good music he put on in the lab, from Johnny Cash to Buena Vista Social Club, making a memorable soundtrack of all these years. Martin, for many incredibly insightful discussions on foundations of quantum mechanics and quantum information in general, and for the bike rides and hikes we did together: they weren't even nearly enough, and I hope our paths will cross again soon. Chris Morrison and Markus Rambach, for sharing many beers alongside discussions on and beyond physics. Our after-work drinks have been a great distraction from long weeks of work, and I really hope we'll manage to re-group soon for some more laughs. Joseph Ho, for endless conversation on literally everything, from physics to coffee, from computers to food. Your critical eye and maniacal attention to the details equals (and often exceeds) mine, making our working together a real pleasure. Berke Ricketti, despite we didn't work on the same projects, for many discussions on food, baking, recipes and whatnot. For any place one wants to go, you always have a brilliant suggestions on where to find a great coffee or food. I'd also like to thank Vincenzo D'Ambrosio: you were a great supervisor back in the Rome times, where my passion for quantum information started, and after all these years I found a great collaborator on our new projects together.



Massimiliano and I seeking QIP-expert advise during one of the few Scottish summer days.

I thank all the people I met during my Ph.D., both in Heriot-Watt and in many conferences around the world, as well as my university colleagues I've been in touch with during these years: you are way too many to list one by one, but I surely enjoyed all your unexpected calls for discussing physics or just for a chat.

I thank my family and my parents for their never-ending support. You taught me the value of hard work, of never being tired of improving myself and what I do, and to always try to achieve more: I'm very thankful for those lessons that made me what I am today. I also thank my brother, for his humour and sarcasm, for many laughs and for the free physiotherapy sessions: all those years as your guinea pig are finally paying back!

Finally, I thank Alessia for her love and support. You have always been there for me, you made the hard times more bearable, and I'm extremely grateful for that. You always believed in me, but you also reminded me, from time to time, that there are a world of things to do outside work, dragging me away from the monitor and forcing me to take some rest. We shared so many experiences that is impossible to count them all, and these years would have been much harder without you.

Research Thesis Submission

Please note this form should be bound into the submitted thesis.

Name:	Francesco Graffitti		
School:	School of Engineering and Physical Sciences		
Version: <small>(i.e. First, Resubmission, Final)</small>	First	Degree Sought:	Doctor of Philosophy

Declaration

In accordance with the appropriate regulations I hereby submit my thesis and I declare that:

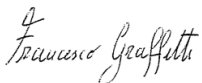
1. The thesis embodies the results of my own work and has been composed by myself
2. Where appropriate, I have made acknowledgement of the work of others
3. The thesis is the correct version for submission and is the same version as any electronic versions submitted*.
4. My thesis for the award referred to, deposited in the Heriot-Watt University Library, should be made available for loan or photocopying and be available via the Institutional Repository, subject to such conditions as the Librarian may require
5. I understand that as a student of the University I am required to abide by the Regulations of the University and to conform to its discipline.
6. I confirm that the thesis has been verified against plagiarism via an approved plagiarism detection application e.g. Turnitin.

ONLY for submissions including published works

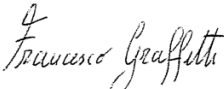
Please note you are only required to complete the Inclusion of Published Works Form (page 2) if your thesis contains published works)

7. Where the thesis contains published outputs under Regulation 6 (9.1.2) or Regulation 43 (9) these are accompanied by a critical review which accurately describes my contribution to the research and, for multi-author outputs, a signed declaration indicating the contribution of each author (complete)
8. Inclusion of published outputs under Regulation 6 (9.1.2) or Regulation 43 (9) shall not constitute plagiarism.

* Please note that it is the responsibility of the candidate to ensure that the correct version of the thesis is submitted.

Signature of Candidate:		Date:	
-------------------------	---	-------	--

Submission

Submitted By <small>(name in capitals)</small> :	Francesco Graffitti
Signature of Individual Submitting:	
Date Submitted:	25/08/2020

For Completion in the Student Service Centre (SSC)

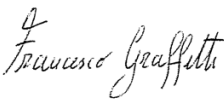
Limited Access	Requested	Yes		No		Approved	Yes		No	
<i>E-thesis Submitted (mandatory for final theses)</i>										
Received in the SSC by <small>(name in capitals)</small> :						Date:				


Inclusion of Published Works


Please note you are only required to complete the Inclusion of Published Works Form if your thesis contains published works under Regulation 6 (9.1.2)

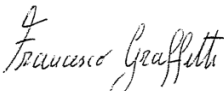
Declaration

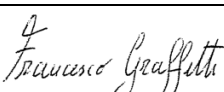
This thesis contains one or more multi-author published works. In accordance with Regulation 6 (9.1.2) I hereby declare that the contributions of each author to these publications is as follows:

Citation details	F. Graffitti , D. Kundys, D. T. Reid, A. M. Brańczyk and A. Fedrizzi, Pure down-conversion photons through sub-coherence-length domain, engineering, Quantum Science and Technology 2 , 035001 (2017)
Authors 1,3,4	Developed the algorithms and performed the simulations, wrote the manuscript
Author 2	Discussed the results and provided useful feedbacks, wrote the manuscript
Author 5	Conceived the project, wrote the manuscript
Signature:	
Date:	25/08/2020

Citation details	F. Graffitti , P. Barrow, M. Proietti, D. Kundys and A. Fedrizzi, Independent high-purity photons created in domain-engineered crystals, Optica 5 , 514-517 (2018)
Authors 1,2,3,4	Designed and performed the experiment, collected and analysed the data, wrote the manuscript
Author 5	Conceived the project, wrote the manuscript
Signature:	
Date:	25/08/2020

Citation details	F. Graffitti , J. Kelly-Massicotte, A. Fedrizzi and A. M. Brańczyk, Design considerations for high-purity heralded single-photon sources, Physical Review A 98 , 053811 (2018)
Authors 1,2	Performed the simulations, wrote the manuscript
Authors 1,3,4	Conceived the project, discussed the results and wrote the manuscript
Signature:	
Date:	25/08/2020

Citation details	F. Graffitti , P. Barrow, A. Pickston, A. M. Brańczyk and Alessandro Fedrizzi, Direct Generation of Tailored Pulse-Mode Entanglement, Physical Review Letters 124 , 053603 (2020)
Authors 1,2,3	Designed and performed the experiment, collected and analysed the data, wrote the manuscript
Author 4	Provided theoretical support, wrote the manuscript
Authors 1,5	Conceived the project, wrote the manuscript
Signature:	
Date:	25/08/2020

Citation details	F. Graffitti , V. D'Ambrosio, M. Proietti, J. Ho, B. Piccirillo, C. de Lisio, L. Marrucci and Alessandro Fedrizzi, Hyperentanglement in structured quantum light, arXiv:2006.01845 (2020)
Authors 1,2	Conceived and performed the experiment
Authors 1,3,4	Analysed the data
Author 5	Prepared the q-plates
All Authors	Discussed the results and the data interpretation, wrote the manuscript
Signature:	
Date:	25/08/2020

Contents

List of Abbreviations	iv
List of Publications	vi
1 Introduction	1
2 Parametric Down-Conversion	7
2.1 Generation of PDC photons	8
2.1.1 Three-wave mixing: a hint of classical and quantum descriptions	8
2.1.2 Photon number statistics	12
2.2 PDC spectral properties	15
2.2.1 Pump-envelope function	15
2.2.2 Phase-matching function	16
2.2.3 Joint spectral amplitude	21
2.2.4 Schmidt decomposition and JSA separability	23
3 Design Considerations for PDC Sources	27
3.1 Designing a down-conversion source	28
3.1.1 Spectral filtering	28
3.1.2 Group-velocity matching	29
3.1.3 Symmetric group-velocity matching	35
3.1.4 Chirped pump pulses and their effect on photon purity	37
3.2 Benchmarking a down-conversion source	40
3.2.1 JSA reconstruction	41

3.2.2	Two-photon interference	46
3.2.3	HOM: the general case	47
3.2.4	Signal-idler interference	48
3.2.5	Heralded-photon interference	51
3.3	Conclusion and discussion	53
4	Nonlinearity Engineering	55
4.1	Quasi-phase-matching and periodic poling	56
4.2	Tailoring the PMF: a brief overview	61
4.3	Novel nonlinearity engineering techniques	62
4.3.1	Theory behind the scenes	63
4.3.2	Choosing the width parameter	67
4.3.3	“Two-domain blocks” tracking	70
4.3.4	“One-domain blocks” tracking	72
4.3.5	Simulated annealing algorithm	73
4.3.6	Sub-coherence length domains	77
4.4	Engineering techniques comparison	81
4.5	(A)periodic poling in realistic crystals	83
4.5.1	Undesirable PDC generation far from central peak	84
4.5.2	Crystal Imperfections	86
4.6	Irregular momentum mismatch: an edge case	90
4.7	Down-conversion in KTP at telecom wavelength: a case study	90
4.8	Conclusion and discussion	93
5	Pure Single Photon Generation Enabled Via Nonlinearity Engineering	94
5.1	Heralded-photons interference for purity estimation	95
5.2	Experiment	99
5.2.1	Experimental setup	99
5.2.2	Signal-idler interference	104
5.2.3	Heralded-photons interference	104

5.3 Sneak peek at the latest results	107
5.4 Conclusion and discussion	109
6 Generation of Time-Frequency Mode Entanglement	111
6.1 TFM framework	112
6.2 Nonlinearity engineering for TFM encoding	115
6.3 Experimental TFM entanglement generation	118
6.3.1 Target TFM-entangled state	118
6.3.2 Experimental setup	120
6.3.3 Dispersive fibre spectroscopy	122
6.3.4 Two-photon interference	123
6.3.5 Effective JSA reconstruction	126
6.4 TFM entanglement swapping	129
6.5 Conclusion and future directions	132
7 Conclusion	134
Appendix A Poling errors effects at smaller spectral range	137
Appendix B Hyperentanglement in Structured Quantum Light	140
Bibliography	154

Glossary

BS beam-splitter

DFG difference frequency generation

DOF degree of freedom

FWHM full width at half maximum

GVM group-velocity matching

HG Hermite-Gauss

HOM Hong-Ou-Mandel

HWP half-wave plate

JSA joint spectral amplitude

JSI joint spectral intensity

KTP potassium titanyl phosphate

OAM orbital angular momentum

OR optical rectification

PBS polarising beam-splitter

PDC parametric down-conversion

PEF pump-envelope function

PMF phase-matching function

SD Schmidt decomposition

SFG sum frequency generation

SHG second harmonic generation

SNSPD superconducting nanowire single-photon detector

SVD singular value decomposition

TFM time-frequency modes

VVB vector vortex beam

List of Publications

Publications contained in this Thesis

Francesco Graffitti, Dmytro Kundys, Derryck T. Reid, Agata M. Brańczyk and Alessandro Fedrizzi, “*Pure down-conversion photons through sub-coherence-length domain engineering*”, Quantum Science and Technology, Vol. **2**, no 3 (2017)

Francesco Graffitti, Peter Barrow, Massimiliano Proietti, Dmytro Kundys, and Alessandro Fedrizzi, “*Independent high-purity photons created in domain-engineered crystals*”, Optica **5**, 514-517 (2018)

Francesco Graffitti, Jérémy Kelly-Massicotte, Alessandro Fedrizzi, and Agata M. Brańczyk, “*Design considerations for high-purity heralded single-photon sources*”, Physical Review A **98**, 053811 (2018)

Francesco Graffitti, Peter Barrow, Alexander Pickston, Agata M. Brańczyk, and Alessandro Fedrizzi, “*Direct Generation of Tailored Pulse-Mode Entanglement*” Physical Review Letters **124**, 053603 (2020)

Francesco Graffitti, Vincenzo D’Ambrosio, Massimiliano Proietti, Joseph Ho, Bruno Piccirillo, Corrado de Lisio, Lorenzo Marrucci and Alessandro Fedrizzi “*Hyperentanglement in structured quantum light*”, Physical Review Research **2**, 043350 (2020)

Additional publications

Richard A. McCracken, Francesco Graffitti, and Alessandro Fedrizzi, “*Numerical investigation of mid-infrared single-photon generation*”, Journal of the Optical Society of America B **35**, C38-C48 (2018)

Massimiliano Proietti, Martin Ringbauer, Francesco Graffitti, Peter Barrow, Alexander Pickston, Dmytro Kundys, Daniel Cavalcanti, Leandro Aolita, Rafael Chaves, and Alessandro Fedrizzi, “*Enhanced Multiqubit Phase Estimation in Noisy Environments by Local Encoding*”, Physical Review Letters **123**, 180503 (2019)

Massimiliano Proietti, Alexander Pickston, [Francesco Graffitti](#), Peter Barrow, Dmytro Kundys, Cyril Branciard, Martin Ringbauer, Alessandro Fedrizzi, “*Experimental test of local observer independence*”, Science Advances, Vol. **5**, no. 9, eaaw9832 (2019)

Farid Shahandeh, Martin Ringbauer, Massimiliano Proietti, Fabio Costa, Austin P. Lund, [Francesco Graffitti](#), Peter Barrow, Alexander Pickston, Dmytro Kundys, Timothy C. Ralph, and Alessandro Fedrizzi “*Assisted Macroscopic Quantumness*” arXiv:1711.10498v3 (2019)

[Francesco Graffitti](#), Alexander Pickston, Peter Barrow, Massimiliano Proietti, Dmytro Kundys, Denis Rosset, Martin Ringbauer, and Alessandro Fedrizzi, “*Measurement-Device-Independent Verification of Quantum Channels*”, Physical Review Letters **124**, 010503 (2020)

Dmytro Kundys, [Francesco Graffitti](#), Richard A. McCracken, Alessandro Fedrizzi and Bohdan Kundys, “*Numerical Study of Reconfigurable Mid-IR Single Photon Sources Based on Functional Ferroelectrics*”, Advanced Quantum Technology, 1900092 (2020)

Conference and workshop contributions

Pure single photon generation from nonlinear processes, Oral contribution, CLEO Europe, Munich (2017)

Pure downconversion photons through sub-coherence length domain engineering, Poster presentation, International Conference on Integrated Quantum Photonics: PICQUE, Rome (2017).

Towards medium-scale photonic quantum technology via pure single-photon generation, Oral contribution, QUISCO meeting, University of Strathclyde, Glasgow (2017).

Pure downconversion photons through sub-coherence length domain engineering, Poster presentation, Quantum Simulation & Computation: Advantage, Scalability and Verification, Bilbao (2018).

Enabling new quantum technologies via source-engineering techniques, Invited seminar, Naples (2018).

Enabling new quantum technologies via source-engineering techniques, Oral contribution, Workshop: “Quantum Christmas”, Rome (2018).

Time/frequency high-dimensional entanglement via engineered parametric down con-

version , Oral contribution, APS March Meeting, Boston (2019).

Time/frequency high-dimensional entanglement via engineered parametric downconversion , Poster presentation, Quantum Information and Measurement (QIM) V: Quantum Technologies, Rome (2019).

High efficiency pulsed spectral-mode entanglement generation , Oral contribution, 26th Central European Workshop on Quantum Optics, Paderborn (2019).

Time/frequency high-dimensional entanglement via engineered parametric downconversion, Oral contribution, CLEO Europe, Munich (2019).

Tailored quantum light for novel quantum photonics applications, Poster presentation, BQIT Workshop, Bristol (virtual workshop) (2020). Best experimental poster prize winner.

The trail narrows, Diane. I'm close, but the last few steps are always the darkest and most difficult.

Agent Cooper, *Twin Peaks*

CHAPTER 1

Introduction

Half-way through the 14th century, during the Black Death pandemic, Giovanni Boccaccio wrote the “Decameron”, gifting the world with one of the most irreverent and funny literature masterpieces ever written. In the second half of the 17th century, while forced to isolation due to the Great Plague pandemic, a very young Isaac Newton developed his theories on calculus, optics, and the laws of gravitation. In 2020, during the Covid-19 pandemic and the longest lock-down in a European country (we are on day 95 as I write this very sentence), I'm forced home, writing this manuscript. I certainly lack Boccaccio's creativity and talent for writing and, needless to say, I obviously don't possess Newton's brilliant mind: I, therefore, feel the moral obligation to warn the reader that this piece of work will be as boring (if not more) as countless other doctorate theses. However, I tried to write down, here and there, some considerations and analyses that—I believe—cannot be found in published literature. By doing so, I hoped to turn what at first looked like just a mere exercise of self-inflicted pain into something that might actually be of some use to someone. I'm not sure I achieved this goal, but a man can dream.

Half a century ago, in the late sixties, the generation of photon pairs mediated by a nonlinear crystal was observed in the lab [1–4], and the theory behind it was in the process of being developed [5]. It’s hard to believe that the deep impact of these results was already clear at that time: it was the beginning of a “*parametric down-conversion* (PDC) era”.

After two decades, PDC allowed researchers to observe for the first time non-classical two-photon interference on a beam-splitter, which is nowadays commonly known as [6, 7] *Hong-Ou-Mandel* (HOM) effect. Parametric down-conversion was at that point used for many fundamental tests of quantum mechanics, but it struggled to achieve high efficiencies in entanglement-based applications due to probabilistic schemes: type-I parametric down-conversion was often used due to higher nonlinearities, and entanglement generated in post-selection sending the two down-converted photons on a *polarising beam-splitter* (PBS)

It took a few more years for a second major breakthrough in down-conversion sources to come: in 1995 Kwiat et al. proposed and demonstrated the first efficient source of polarisation entanglement [8]. At last, a simple and efficient source of entangled photons was readily available, enabling countless experiments that so far had only been theorised, and many other yet to be proposed.

Since then, many techniques for entangled photon generation via parametric down-conversion have been developed. Double-pass schemes allowed type-I PDC to be used for efficient generation of polarisation entanglement [9] and polarisation-momentum hyperentanglement [10]. *Orbital angular momentum* (OAM) entangled states were also originally demonstrated with a PDC source [11]. Sandwich-type sources [12] were used to achieve 12-photon entanglement [13]. Moving away from the non-collinear emission typical of most “early days” sources, we find that collinear down-conversion can also generate entanglement in a highly efficient way. Sagnac interferometer sources [14] and Mach-Zehnder interferometer sources [15] are the main examples: both have been successfully used in very many experiments, amongst which are two loophole-free Bell tests [16, 17]. This list is far from being exhaustive—one could spend a whole Ph.D. digging the literature for PDC-related schemes—but it only aims to give the reader a flavour of how extensively

down-conversion has been investigated in the last 50 years, and how it happened to establish itself as the backbone of many quantum optics experiments

Being myself a huge fan of down-conversion processes, it hurts to admit that life for parametric down-conversion sources is not as idyllic as I presented it so far. Indeed, PDC suffers from intrinsic limitations, from its probabilistic nature and the multi photon-pair emissions to unwanted correlations within the biphoton state, that seems to have brought these sources to a major roadblock. Some of these problems can be overcome with none or small overheads—as I’ll discuss in this manuscript—while others are of a fundamental nature and appear to be hardly surmountable, jeopardising the scalability of PDC sources for large scale applications. Several possible solutions have been proposed, prototypes have been built, and might succeed in overcoming these problems: indeed, recent schemes have demonstrated that parametric sources can approximate a nearly deterministic photon source with high production rates and photon purity [18–24]. However, the future is still uncertain.

It must be mentioned that, in the five decades that separate the pioneering PDC experiments from our days, the competition for building the best single-photon source has become tougher. First of all, other parametric sources (based on four-wave-mixing in optical fibres [25] or in integrated silica-based chips [26]) are quickly catching on in the field, owing to the promise of being easily scalable from the manufacturing and miniaturisation point of view, paving the way to large-scale quantum applications. However, due to their probabilistic and nonlinear-optical nature, I think it is fair to group them together with PDC sources. Other platforms have been proposed and developed for efficient generation of quantum light, from solid-state devices, such as quantum dots [27] and colour centres [28], to trapped-ions [29], from single atoms [30] to molecules [31], etc. Such sources are now routinely used in many quantum optics lab, and recently stole down-conversion’s thunder in two major breakthrough experiments—a loophole-free Bell test [32] and boson sampling [33], fields that until then were monopolised by PDC-based experiments.

However, the simplicity of parametric down-conversion combined with its cost-effectiveness is still unparalleled, arguably making it the most widespread technique

to routinely generate single photons in hundreds of quantum optics lab around the world—as well as in space [34–37]!

In this Thesis, I build upon the knowledge of uncountable previous works by adding a small piece to the understanding of parametric down-conversion. I report and expand on the results I obtained during the last four years with the invaluable contributions of my supervisor and colleagues. In particular, I focus on understanding the spectral properties of biphoton states produced in down-conversion processes: this is of great importance for quantum technology applications, where the ability of producing single-photons in a well-defined spectral state is crucial for the success of most quantum protocols. Indeed, multi-photon schemes (such as recent proposals for loss-robust photonic cluster-state percolation [38] amongst many others) rely on a high number of successive two-photon interference events: any reduction in interference visibility leads to a drastic resource cost increase in the required number of photon sources, detectors and circuit complexity [39, 40]. Since perfect interference can only be achieved with spectrally-pure and indistinguishable photons [41], understanding how to manipulate the PDC biphoton spectrum to development of high performance single-photon sources is essential.

Here, I introduce theoretical, numerical, and experimental methods to understand, characterise, and tailor the joint spectral properties of down-converted pairs: part of the analysis described in the following pages is completely general and applies to almost any kind of parametric source; other parts are more specific, concerning PDC in periodically-poled nonlinear crystals. When either one or the other case occurs, I tried to specify it in the text: whenever I failed in doing so, I trust the reader to be able of understanding it from the context (and from the physics itself).

The discussion of the results presented in this Thesis is structured as follows:

In [Chapter 2](#) I briefly discuss the theory of PDC, introducing all the notions that will be needed to understand the results discussed in the following chapters. Well-known concepts as *pump-envelope function* (PEF), *phase-matching function* (PMF), *joint spectral amplitude* (JSA) etc. are presented to the reader, focusing on

the properties that will play a role in the rest of this manuscript.

In [Chapter 3](#) I discuss two practical issues that arise when we want to build an efficient PDC source: what are the optimal parameters for designing the best possible source, and how to faithfully characterise the source once it has been built. I address these questions considering realistic source parameters (several PEF and PMF shape combinations) and realistic outputs of the most common characterisation setups.

In [Chapter 4](#), I introduce domain engineering in poled crystals, a technique for shaping the phase-matching function of nonlinear processes to, amongst other applications, tailor the biphoton spectrum of down-converted photons. After a quick recap of pre-existing domain engineering methods, I introduce the nonlinearity engineering technique that we developed at the beginning of my Ph.D. This scheme not only outperforms previous schemes in generating pure heralded single-photons, but it also enables new possibilities in tailoring the single-photon spectra.

The first application of our novel nonlinearity engineering technique consists in certifying its capability of tailoring the PMF as a Gaussian shape, in order to maximise the separability of the JSA, hence the spectral purity of the heralded photons. I discuss this in [Chapter 5](#), introducing a method for estimating the spectral purity of heralded photons via two-photon interference, and experimentally proving the effectiveness of our engineering scheme for generating pure heralded photons.

While nonlinearity engineering techniques applied to PDC sources have only been used in the past for maximising the separability of the biphoton spectrum, the possibilities enabled by such techniques are not limited to this standard scenario. I expand this idea in [Chapter 6](#), introducing the *time-frequency modes* (TFM) framework for photonic quantum information processing, and discussing an experiment where generation and measurement of TFM-entanglement enabled by our domain engineering scheme.

One can move beyond homogeneous encoding, and exploit different degrees of freedom of light to encode quantum information, enlarging the accessible Hilbert space and enabling new quantum protocols. This is discussed in [Appendix B](#), where I report an experiment that combines TFM-encoding with polarisation- and

OAM-encoding, generating hyperentanglement between spectrally- and spatially-structured light. Unlike previous Chapters, here I don't have additional material to present or further comments to discuss with respect to what appeared on arXiv [42], hence I attach the pre-print version of this work. A careful reader would have noticed that this Chapter appears as an Appendix after the Conclusions, and not as Chapter 7, where it would more naturally stand. The reason is of bureaucratic nature: due to University policy, whenever a published article is attached to a thesis, it should appear as the last appendix before the List of References. I bend my knee to the red tape, and apologise to the reader for forcing them to jump back and forth in this manuscript.

Finally, in the [Conclusions](#) I take stock of what I presented in the Thesis, discussing open challenges, and outlining a number of possible research directions that can be explored to improve, complement and move beyond the results I presented in this manuscript.

I'm sciencing as fast as I can!

Prof. Farnsworth, *Futurama*

CHAPTER 2

Parametric Down-Conversion

A light beam passing through a nonlinear optical material can interact with the medium, decaying into two lower-energy photons (namely *signal* and *idler*) under conservation of energy and momentum. This process is a second order nonlinear effect known as (spontaneous) *parametric down-conversion* (PDC), and is a widespread technique for generating high quality single photons for optical quantum technologies. The basic theory of three-wave mixing and, in particular, of PDC has been discussed in many articles, books, and theses. Different derivations have been provided, some more rigorous and detailed than others, but at the end of the day they all converge to analogous results. For this reason, we will only give a very brief introduction to PDC as a three-wave mixing process, without going into the mathematical details of quantum nonlinear optics (interested readers are referred to, e.g., [43–45]). We will instead focus on those PDC properties that will be relevant for understanding the results discussed in the following chapters, introducing the concepts of *pump-envelope function* (PEF), *phase-matching function* (PMF), and how they relate to the *joint spectral amplitude* (JSA) and the heralded single-photon spectral purity.

		Contents
2.1	Generation of PDC photons	8
2.1.1	Three-wave mixing: a hint of classical and quantum descriptions	8
2.1.2	Photon number statistics	12
2.2	PDC spectral properties	15
2.2.1	Pump-envelope function	15
2.2.2	Phase-matching function	16
2.2.3	Joint spectral amplitude	21
2.2.4	Schmidt decomposition and JSA separability	23

2.1 Generation of PDC photons

2.1.1 Three-wave mixing: a hint of classical and quantum descriptions

When an electromagnetic wave passes through a nonlinear optical material, it will induce a polarisation (dipole moment) of the form:

$$P(t) = \epsilon_0 \left(\chi^{(1)} E(t) + \chi^{(2)} E^2(t) + \chi^{(3)} E^3(t) + \dots \right) = P^{(1)}(t) + P^{(2)}(t) + P^{(3)}(t) + \dots, \quad (2.1)$$

where ϵ_0 is the vacuum permittivity, $\chi^{(1)}$ is the linear optical susceptibility, and $\chi^{(n)}$ (with $n > 1$) are the n -th order nonlinear susceptibilities. In a more thorough picture, both P and E would have vectorial nature, while the susceptibilities $\chi^{(n)}$ would be tensors [46].

In the nonlinear interaction, electromagnetic fields with different energies can interact in what are, effectively, frequency conversion processes. In particular, second-order nonlinear effects are also known as three-wave mixing processes, as three waves interact in a non-centrosymmetric medium and, under conservation of total energy and momentum, they can exchange energy. Let's assume an incident electric field of the form:

$$E(t) = E_1 e^{-i\omega_1 t} + E_2 e^{-i\omega_2 t} + \text{h.c.} . \quad (2.2)$$

According to Eq. (2.1), the corresponding second-order polarisation reads:

$$P^{(2)}(t) = \left(P^{(2)}(2\omega_1) e^{-2i\omega_1 t} + P^{(2)}(2\omega_2) e^{-2i\omega_2 t} + P^{(2)}(\omega_1 + \omega_2) e^{-i\omega_1 + \omega_2 t} \right) \quad (2.3)$$

$$+ P^{(2)}(\omega_1 - \omega_2) e^{-i\omega_1 - \omega_2 t} + \text{h.c.}) + P^{(2)}(0), \quad (2.4)$$

where the addends in the right-hand side correspond to *second harmonic generation* (SHG), *sum frequency generation* (SFG), *difference frequency generation* (DFG),

and *optical rectification* (OR) respectively:

$$\begin{aligned}
 P^{(2)}(2\omega_1) &= \epsilon_0 \chi^{(2)} E_1^2 && (SHG) \\
 P^{(2)}(2\omega_2) &= \epsilon_0 \chi^{(2)} E_2^2 && (SHG) \\
 P^{(2)}(\omega_1 + \omega_2) &= 2\epsilon_0 \chi^{(2)} E_1 E_2 && (SFG) \\
 P^{(2)}(\omega_1 - \omega_2) &= 2\epsilon_0 \chi^{(2)} E_1 E_2^* && (DFG) \\
 P^{(2)}(0) &= 2\epsilon_0 \chi^{(2)} (E_1 E_1^* + E_2 E_2^*) && (OR). \tag{2.5}
 \end{aligned}$$

By considering a nonlinear polarisation in Maxwell's equations, one can easily derive the field's amplitude equations for these nonlinear processes under the slowly varying envelope approximation, as shown in many nonlinear optics books [46]. As an example, we show below the coupled-amplitudes equations for the SFG process—the other $\chi^{(2)}$ effects have analogous classical coupled equations:

$$\begin{cases}
 \frac{d^2 A_3}{dz^2} = \frac{2id\omega_3^2}{k_3 c^2} A_1 A_2 e^{i(k_1+k_2-k_3)z} \\
 \frac{d^2 A_1}{dz^2} = \frac{2id\omega_1^2}{k_1 c^2} A_3 A_2^* e^{-i(k_1+k_2-k_3)z} \\
 \frac{d^2 A_2}{dz^2} = \frac{2id\omega_2^2}{k_2 c^2} A_3 A_1^* e^{-i(k_1+k_2-k_3)z}
 \end{cases} . \tag{2.6}$$

All the $\chi^{(2)}$ processes described in Eq. (2.5) are characterised by two input fields producing a single output field. However, a $\chi^{(2)}$ process can also occur when a single input field is converted into two output fields. This is known as parametric down-conversion (or, nowadays less common, parametric fluorescence), and is in some sense the reverse process of SFG: a strong input field gets (partially) converted into two lower-energy fields.

A full description of PDC requires a quantum mechanical approach. The quantum Hamiltonian of the process can be written as [45]:

$$H = \underbrace{\frac{1}{2} \int d^3 r \left(\frac{1}{\mu_0} B_i B_i + \epsilon_0 (1 + \chi_{ii}^{(1)}) E_i E_i \right)}_{H_0} + \underbrace{\frac{2}{3} \epsilon_0 \int d^3 r \chi_{ijk}^{(2)} E_i E_j E_k}_{H_I}, \tag{2.7}$$

where H_0 is the linear part of the Hamiltonian and H_I is the interaction part: we will focus on the H_I term, that captures the dynamics of the nonlinear processes. We also need to consider quantised electromagnetic fields [47]:

$$\hat{E}_i(z, t) = i \int d\omega_i A \left(e^{i(\vec{k}_i(\omega_i) \cdot \vec{r} - \omega_i t)} \hat{a}_i(\omega_i) - e^{-i(\vec{k}_i(\omega_i) \cdot \vec{r} - \omega_i t)} \hat{a}_i^\dagger(\omega_i) \right) \quad (2.8)$$

where A includes all the constant factors, and $\hat{a}_i(\omega_i)$, $\hat{a}_i^\dagger(\omega_i)$ are the photon annihilation and creation operators, respectively, for frequency ω_i and momentum $k(\omega_i)$. Finally, the quantised fields (2.8) can be inserted in the interaction Hamiltonian H_I to obtain the quantum description of all the $\chi^{(2)}$ processes, including the ones already discussed in Eq. (2.5) from the classical point of view. However, here we are interested in the Hamiltonian part specific to parametric down-conversion, where the higher energy photon (namely the pump, “ p ”) gets *down-converted* into two lower energy photons (“signal”, ‘ s ’, and “idler”, ‘ i ’). This translates into a Hamiltonian of the form:

$$\hat{H}_{\text{PDC}} \propto \int d\omega_p d\omega_s d\omega_i d^3 r \chi^{(2)} \left(e^{i(\vec{k}_p \cdot \vec{r} - \vec{k}_s \cdot \vec{r} - \vec{k}_i \cdot \vec{r}) - i(\omega_p - \omega_s - \omega_i)t} \hat{a}(\omega_p) \hat{a}_s^\dagger(\omega_s) \hat{a}_i^\dagger(\omega_i) + \text{h.c.} \right), \quad (2.9)$$

where we can replace the pump annihilation operator $\hat{a}(\omega_p)$ with its classical counterpart $\alpha(\omega_p)$, assuming the pump field to be a strong laser field (more details on this in Section 2.2.1). More details on $\alpha(\omega_p)$ and the pump spectral properties are discussed in Section 2.2.1.

The PDC output state can hence be calculated in the interaction picture according to the Schrödinger equation [48]:

$$\begin{aligned} i\hbar \frac{d}{dt} |\psi(t)\rangle &= \hat{H}_I(t) |\psi(t)\rangle \\ |\psi\rangle_{\text{PDC}} &= \mathcal{T} \exp \left[-\frac{i}{\hbar} \int_0^t dt' \hat{H}_{\text{PDC}}(t') \right] |0\rangle, \end{aligned} \quad (2.10)$$

where \mathcal{T} is the time-ordering operator, that we will neglect from now on as it doesn’t play a role in relatively low pump-power regimes (the validity of this approximation is discussed extensively in [49–52]). The integral over time in Eq. (2.10) leads to the

energy conservation relation:

$$\int dt' e^{-i(\omega_p - \omega_s - \omega_i)t'} = \delta(\omega_p - \omega_s - \omega_i). \quad (2.11)$$

Following from Eqs. (2.9), (2.10) and (2.11), considering a collinear process where the signal and idler photons co-propagate with the pump field, and neglecting the variety of spatial modes that can be emitted in the process, the PDC biphoton state can be written as:

$$|\psi\rangle_{s,i} = \exp \left[BO \iint d\omega_s d\omega_i \underbrace{\int dz g(z) e^{i\Delta k(\omega_s, \omega_i)z}}_{\phi(\Delta k(\omega_s, \omega_i))} \alpha(\omega_s + \omega_i) \hat{a}_s^\dagger(\omega_s) \hat{a}_i^\dagger(\omega_i) + \text{h.c.} \right] |0\rangle_{s,i}, \quad (2.12)$$

where $g(z)$ is the normalised nonlinearity along the crystal, $\Delta k(\omega_s, \omega_i) = \omega_p - \omega_s - \omega_i$ is the phase mismatch, $\phi(\Delta k(\omega_s, \omega_i))$ is the PMF (see Section 2.2.2 for details), O is a constant related to the overlap of the transverse modes of the photons [45], and $B = \pi \chi_0^{(2)} \sqrt{\frac{\hbar \omega_p \omega_s \omega_i}{\epsilon_0 \pi^3 c^3 n_p n_s n_i}}$, with $\omega_{0,j}$ being the central frequencies of the fields and n_j the corresponding refractive indices. Eq. (2.12) assumes that the spectral part of the PDC biphoton is in a pure bipartite quantum state: this assumption neglects the correlations between the spatial and the spectral part of the state that might occur when particular focusing condition are considered [53].

In order to analyse the PDC biphoton state, we can perform a Magnus expansion (see Ref. [51] for details) of Eq. (2.12) and consider only the first order term, which reads (neglecting the constant pre-factors):

$$\boxed{|\psi\rangle_{s,i} = \iint d\omega_s d\omega_i \underbrace{\phi(\Delta k(\omega_s, \omega_i)) \alpha(\omega_s + \omega_i)}_{f(\omega_s, \omega_i)} \hat{a}_s^\dagger(\omega_s) \hat{a}_i^\dagger(\omega_i) |0\rangle_{s,i}} \quad (2.13)$$

Equation (2.13) captures the spectral properties of PDC biphoton state by means of the quantity $f(\omega_s, \omega_i)$, commonly referred to as joint spectral amplitude or joint spectrum: we note that, following from the assumptions in Eq. (2.12), the biphoton state in Eq. (2.13) is also a pure bipartite state. Most of the following discussions will be about understanding the JSA properties and how to manipulate and measure

them.

As a last remark of this introductory Section, let us point out that parametric down-conversion can occur in collinear (where the down-converted photons co-propagate with the pump) or non-collinear (where they are emitted with a non-zero angle with respect to the pump incident beam) configuration. Moreover, PDC is usually categorised in three different types:

type-0, where pump and PDC photons share the same polarisation;

type-I, where the pump has opposite polarisation respect to the PDC photons;

type-II, where the pump share same polarisation of either signal or idler, while the other photon has opposite polarisation.

In this Thesis, we will focus on collinear, type-II down-conversion: however, most of the discussion will be general and independent from what type of PDC one is interested in (indeed, most results will also hold for other nonlinear processes, such as difference frequency generation or spontaneous four-wave mixing).

2.1.2 Photon number statistics

Before digging into the spectral domain, let's briefly discuss photon number statistics in parametric down-conversion, as it will play a role in the “experimental chapters”.

As mentioned in the introduction, an ideal photon source is required to emit photons that are pure in all their degrees of freedom. Clearly, this is not the case for bare PDC: even if we neglect the spectral degree of freedom, the down-converted photons are not pure in the photon number space. Indeed, the expansion of Eq. (2.12) contains infinite terms, each one corresponding to the emission of n photon pairs—where n can vary from 0 to ∞ —degrading the photon-number purity of the state. While a thorough description of the PDC photon number statistics is a complex problem, and it has been extensively discussed in many works both in low- and high-gain regime (e.g. [54–58] amongst many others), here I'll keep it as basic as possible to stress the most relevant points for this Thesis.

Omitting the spectral part of the wavefunction and considering a single frequency component, the expansion of Eq. (2.12) can be written as:

$$|\psi\rangle_{s,i} = \sqrt{1 - |\lambda|^2} \sum_{n=0}^{\infty} \lambda^n |n\rangle_s |n\rangle_i, \quad (2.14)$$

where $|n\rangle$ is the photon number state defined as:

$$|n\rangle_j = \frac{(\hat{a}_j^\dagger)^n}{\sqrt{n!}} |0\rangle_j, \quad (2.15)$$

while the parameter λ relates to the source brightness [19, 59] and can be expressed as a function of the pump power P and a constant τ , determined by the overall efficiency of the nonlinear interaction: $\lambda = \sqrt{P\tau}$, that holds for $\lambda \ll 1$. From Eq. (2.14) we can calculate the normalised probability of emitting n photon pairs in a given pump pulse:

$$P(\lambda, n) = (1 - |\lambda|^2) |\lambda|^{2n} \sum_{n=0}^{\infty} P(\lambda, n) = 1. \quad (2.16)$$

While eq. (2.16) is just a rough approximation of the PDC process in the Fock space, it serves the purpose of showing why using down-conversion as a *single*-photon source might not look very promising. First of all, even from this somewhat naive approach (that neglects spectro-temporal properties, losses, time ordering effects, etc.) we can see how the photon pair emission maxes out at 25% when $\lambda = 1/\sqrt{2}$, meaning that increasing the power indefinitely doesn't lead to an ever increasing production of PDC photons, see red line in Figure 2.1. Secondly, and possibly more importantly, for any value of λ greater than 0, the production of a single photon pair always goes together with the production of none or higher order terms, which are detrimental in most photonic quantum protocols. In fact, we can define a simple metric for the signal to noise ratio as the ratio between a single pair emission and multiple pairs emissions, where we consider bucket detectors (i.e. not able to resolve

the number of detected photons within the same time bin):

$$\text{SNR} = \frac{P(\lambda, 1)}{\sum_{n=2}^{\infty} P(\lambda, n)} = \frac{(1 - |\lambda|^2) |\lambda|^2}{\underbrace{1 - (1 - |\lambda|^2)}_{P(\lambda, 0)} - \underbrace{(1 - |\lambda|^2) |\lambda|^2}_{P(\lambda, 1)}} = -1 + \frac{1}{|\lambda|^2}. \quad (2.17)$$

It's worth noting that this metric doesn't capture all the drawbacks of PDC probabilistic nature, as the probability of not emitting any pair (which is actually the dominant term) also compromises significantly the usefulness of such sources. More sophisticated (and setup-dependent) metrics are needed for a more accurate description of noise: for example, photon-number resolving detectors can mitigate the multi-photon noise contribution, however in the (inevitable) presence of losses some noise will always be present.

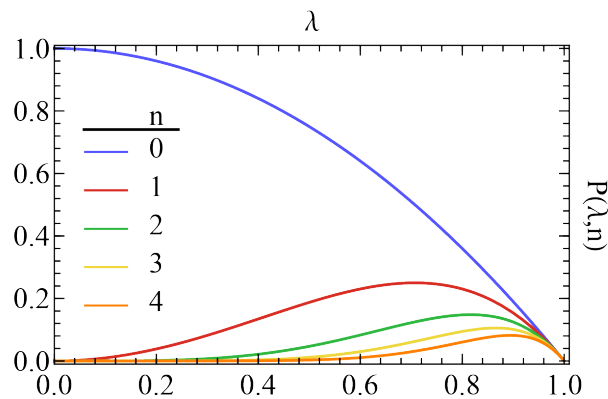


Figure 2.1: Photon pairs' emission probability. The emission of n photon pairs as a function of the parameter λ is reported in different colours. As λ increases (e.g. by increasing the pump power or the nonlinear interaction strength), the probability of not producing any photon pair decreases monotonically, while the probability of producing $n > 0$ pairs increases. However, the probability of emitting exactly n pairs doesn't increase indefinitely, while it reaches a maximum at $\lambda_n > \lambda_{n-1}$ and then decreases to 0 when $\lambda_n = 1$. Clearly, this approximation only holds for low values of λ , and a more thorough approach should be used when considering the high squeezing case, as discussed in the main text.

Luckily, possible solutions to the zero- and multi-photon emission problem have been proposed and significant progress has been made in this sense, spanning temporal multiplexing of the pump [19, 60] and of the down-converted photons [22, 23, 61], as well as spatial multiplexing of multiple sources [20, 62], keeping alive the

dream of a scalable PDC-based source for practical quantum photonics application. A thorough description of these schemes is beyond the scope of this Thesis, and we point the reader to the aforementioned references (and possibly many others that we failed to report) for more details.

2.2 PDC spectral properties

Let's now go back to the first-order term of the parametric down-conversion state, as described in Eq. (2.13), and focus on the spectral properties of the photon pair. The PDC joint spectrum is characterised by the pump-envelope function, $\alpha(\omega_s + \omega_i)$, and the material properties of the crystal (through its dispersion relations) that are captured by the phase-matching function, $\phi(\omega_s, \omega_i)$:

$$f(\omega_s, \omega_i) = \alpha(\omega_i + \omega_s)\phi(\omega_s, \omega_i). \quad (2.18)$$

Before analysing these quantities in detail, let's specify the convention adopted throughout this Thesis. When discussing the purely theoretical properties of the PEF, PMF and JSA, without loss in generality we'll consider the (ω_s, ω_i) plane to be centred at zero—we'll refer to these shifted axes as (Ω_s, Ω_i) , see Figure 2.2 for an example. However, when discussing numerical simulations of PDC for actual applications and experiments, we will represent the results as a function of the photon wavelengths in the (λ_s, λ_i) -plane for ease of reading.

2.2.1 Pump-envelope function

The so called pump-envelope function $\alpha(\omega_p) = \alpha(\omega_s + \omega_i)$ carries the spectral properties of the pump photon, and due to energy conservation depends on the sum of the signal and idler frequencies. For this reason, when represented in the (ω_s, ω_i) plane, the pump function always appears parallel to the top-left bottom-right diagonal, independently from the functional form of α . This can be visualised in Figure 2.2, where we show a standard Gaussian-shaped pump and a third-order Hermite-Gauss mode-shaped pump. While most theoretical works assumed a Gaussian pump spec-

trum, this is not always the case in realistic experiments. A detailed discussion on the possible PEF shapes in relation to the heralded-photon source performances is provided in the next chapter, [Section 3.1.2](#), while more exotic pump shapes are briefly considered in [Chapter 6](#) where we discuss time-frequency modes encoding.

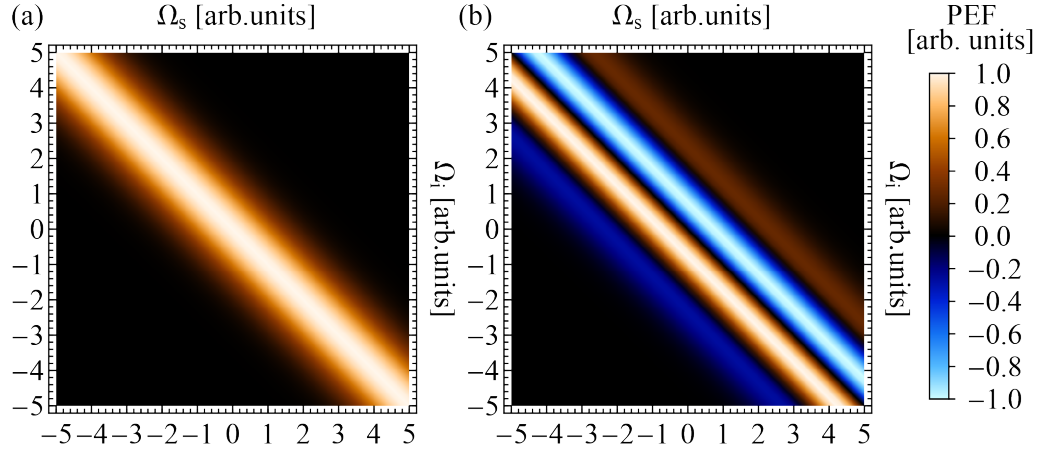


Figure 2.2: Pump-envelope function. Two examples of PEF, a “standard” Gaussian-shaped (a) and a third-order Hermite-Gauss mode (b). The PEF, $\alpha(\omega_p) = \alpha(\omega_s + \omega_i)$, always lies on the anti-diagonal of the (ω_s, ω_i) plane due to energy conservation, independently from the spectral shape of the pump.

2.2.2 Phase-matching function

The phase-matching function accounts for the material properties, in particular dispersion, as well as longitudinal variations in the crystal’s nonlinearity. There exist a number of related, but slightly different definitions of PMF in the literature. Here, we define it as:

$$\phi(\Delta k(\omega_s, \omega_i)) = \int_{-\infty}^{+\infty} g(z) e^{i\Delta k(\omega_s, \omega_i)z} dz \quad (2.19)$$

where $g(z) = \chi^{(2)}(z)/\chi_0^{(2)}$ is the normalised nonlinearity along the crystal (note that $g(z)$ is a real function), and:

$$\Delta k(\omega_s, \omega_i) = k_p(\omega_s + \omega_i) - k_s(\omega_s) - k_i(\omega_i), \quad (2.20)$$

is the phase (or momentum) mismatch, which depends on the material dispersion, with the wave vectors $k_j(\omega_j) = \omega_j n_j(\omega_j)/c$. It is worth noting that this definition has units of length, while in other popular definitions, the PMF is dimensionless.

When defined as above, the PMF for consecutive crystals is the sum of the PMFs for the individual crystals. Take for example a block composed of two crystals. If the normalised nonlinearity function for the i -th crystal ($i = 1, 2$) is $g_i(z)$, then the normalised nonlinearity function for both crystals is $g_{1,2}(z) = g_1(z) + g_2(z)$. According to Eq. (2.19), the PMF for both domains is then:

$$\begin{aligned} \phi_{12}(\Delta k) &= \int_{-\infty}^{+\infty} g_{12}(z) e^{i\Delta k z} dz = \\ &= \int_{-\infty}^{+\infty} g_1(z) e^{i\Delta k z} dz + \int_{-\infty}^{+\infty} g_2(z) e^{i\Delta k z} dz = \phi_1(\Delta k) + \phi_2(\Delta k) \end{aligned} \quad (2.21)$$

where $\phi_i(\Delta k)$ is the PMF for the i -th domain, and we dropped the dependency of Δk on the photons' frequencies for brevity. Take, on the other hand, another popular definition for the PMF:

$$\phi^{\text{other}}(\Delta k) = L^{-1} \int_{-\infty}^{+\infty} g(z) e^{i\Delta k z} dz. \quad (2.22)$$

The function $\phi^{\text{other}}(\Delta k)$ is dimensionless, but in this case

$$\begin{aligned} \phi_{12}^{\text{other}}(\Delta k) &= (L_1 + L_2)^{-1} \int_{-\infty}^{+\infty} g_{12}(z) e^{i\Delta k z} dz \\ &\neq \phi_1^{\text{other}}(\Delta k) + \phi_2^{\text{other}}(\Delta k) = L_1^{-1} \int_{-\infty}^{+\infty} g_1(z) e^{i\Delta k z} dz + L_2^{-1} \int_{-\infty}^{+\infty} g_2(z) e^{i\Delta k z} dz. \end{aligned} \quad (2.23)$$

While this might not seem particularly relevant, it actually plays a crucial role when considering poled crystals, as we will extensively do in [Chapter 4](#). In such case, each individual domain is by all means equivalent to an independent crystal, and the additivity of our PMF definition in Eq. (2.19) makes the calculation of the overall PMF mathematically simpler and more scalable.

Let's now consider, as an example, the simplest crystal possible, i.e. a bulk crystal. The nonlinearity of such crystal has the form of a rectangular function, equal zero before and after the crystal edges, and one in the crystal itself. This

translates into a phase-matching function of the form:

$$\phi(\Delta k(\omega_s, \omega_i)) = \int_0^L e^{i\Delta k(\omega_s, \omega_i)z} dz = L e^{i\frac{\Delta k(\omega_s, \omega_i)L}{2}} \operatorname{sinc}\left[\frac{\Delta k(\omega_s, \omega_i)L}{2}\right], \quad (2.24)$$

where L is the crystal length. As expected, the PMF grows linearly with the crystal length, hence the intensity of the nonlinear effect grows quadratically with it. Moreover, Eq. (2.24) recovers the well-known *sinc* shape of the PMF typical of standard optical nonlinear processes [46] and arising from what is, for all intents and purposes, the Fourier transform of a rectangular function. The phase term $e^{i\Delta k(\omega_s, \omega_i)z}$ is not particularly relevant in this general discussion, but we will get back to it for a more detailed discussion in Chapter 6. We plot Eq. (2.24) in Figure 2.3, highlighting its absolute value and its phase.

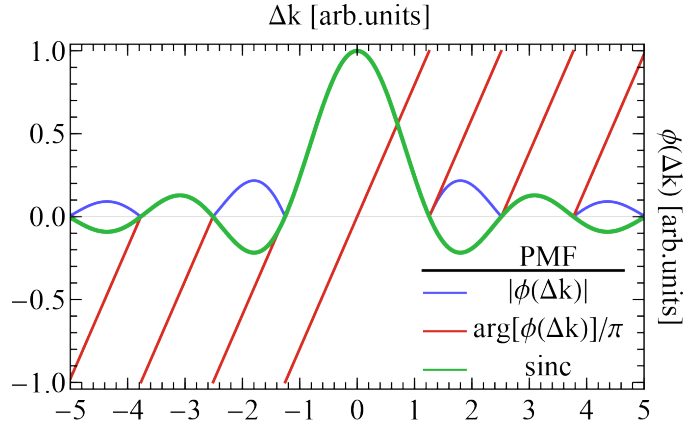


Figure 2.3: Phase-matching function. The PMF of a standard bulk crystal can be thought of as a sinc function (green), as shown by its absolute value (blue) and normalised phase (red), which is linear in Δk .

Equation. (2.24) and its representation in Figure 2.3 describe the PMF as a function of the momentum mismatch. However, we need to consider the PMF in the (ω_s, ω_i) space for relating it to the PDC-photons' spectral properties, as we did for the pump-envelope function in Figure 2.2. To do so, we can consider the dependence of Δk on the frequencies of the photons involved in the PDC process. Since the photon wave vector, $k(\omega) = \omega n(\omega)/c$, depends on the refractive index of the material, $n(\omega)$, we need frequency-dependent refractive index equations to properly describe the momentum mismatch. The natural choice falls on the Sellmeier

equations [63]: empirical equations that link refractive index and wavelength of the (nonlinear) material. Such equations are typically of the form:

$$n(\lambda) = \sqrt{1 + \sum_j \frac{A_j \lambda^2}{\lambda^2 - B_j}}, \quad (2.25)$$

where λ is the vacuum wavelength, the coefficients A_j and B_j are obtained experimentally, and the number of poles in the equation is empirically chosen on a case-by-case basis to reduce the sum of the residuals squared in the fitting procedure. Slightly different forms of Eq. (2.25) exist in literature, where additional terms can be introduced to, e.g., extend the validity of the equations to larger wavelength ranges, or include temperature effects.

Let's consider for example *potassium titanyl phosphate* (KTP), a common crystal that is routinely used in nonlinear and quantum optics labs, and that we use in the experiments discussed in the second half of this Thesis. Different Sellmeier equations for KTP crystals can be found in the literature: for the simulations discussed in this work, I'll refer to the values reported in Ref. [64–66].

Figure 2.4 helps us to visualise $\Delta k(\lambda_s, \lambda_i)$ as a function of the signal and idler wavelengths for a type-II down-conversion in KTP. The lines, representing the contours where Δk is constant, highlight two important features. Firstly, the contours are not necessarily linear in the photons' frequencies, especially when considering large spectral ranges: in fact, there are extreme cases where they might be so curved that lead to PDC generation at two very different wavelengths. Secondly, the slope of such contours is not fixed to a given value, but changes as we sweep the signal and idler frequencies. This slope can be approximately calculated in a simplified picture. We can expand the wave numbers to first order $k_j(\omega) = k_j(\bar{\omega}_j) + v_j^{-1} \Omega_j$, where $v_j = d\omega/dk_j(\omega)|_{\omega=\bar{\omega}_j}$ is the group velocity of photon j , $\Omega_j = \omega_j - \bar{\omega}_j$ —with $\bar{\omega}_j$ being the central frequency of photon j —are the frequencies shifted to 0, and the relation $\bar{\omega}_p = \bar{\omega}_s + \bar{\omega}_i$ holds. We can ignore quadratic and higher-order terms corresponding to group-velocity dispersion if the photons in each mode are not too spread out around the central frequencies, and if we are considering ordinary nonlinear materials. It's worth keeping in mind that “edge-cases” are not infrequent,

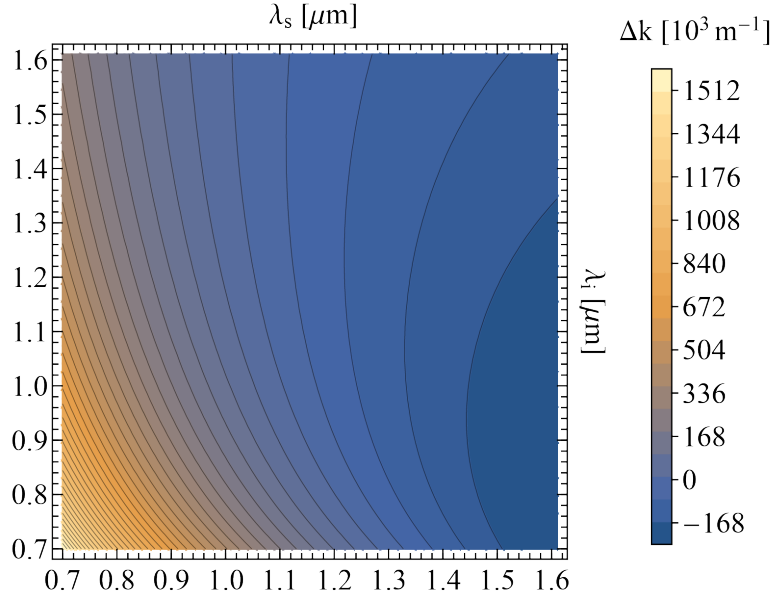


Figure 2.4: Momentum mismatch in type-II down-conversion in KTP. This contour plot shows the momentum mismatch $\Delta k = k_p - k_s - k_i$ in the signal-idler wavelengths space. While Eq. (2.24) suggests that the phase-matching condition is only satisfied when $\Delta k \simeq 0$, where the sinc-shaped PMF has non-zero values, we’ll see in Chapter 4 how quasi-phase-matching can be used to overcome this limitation, allowing the PMF to be shifted so that it is non-zero at $\Delta k \neq 0$.

and should be considered whenever ultra-short pulses are involved in the process, or when the nonlinear material has a strong wavelength dependence of its refractive index. If this is not the case, we can write:

$$\Delta k(\omega_s, \omega_i) = \Delta k_0 + (v_p^{-1} - v_i^{-1})\Omega_i + (v_p^{-1} - v_s^{-1})\Omega_s, \quad (2.26)$$

where $\Delta k_0 = k_p(\bar{\omega}_s + \bar{\omega}_i) - k_s(\bar{\omega}_s) - k_i(\bar{\omega}_i)$. When plotted as a function of Ω_i and Ω_s , the PMF lies along an axis defined by the angle θ , which depends on the group velocities according to:

$$\tan \theta = -\frac{v_p^{-1} - v_s^{-1}}{v_p^{-1} - v_i^{-1}}. \quad (2.27)$$

Picking group velocities appropriately for optimal PDC-pairs generation is a problem known as *group-velocity matching* (GVM), and we will discuss it in Chapter 3.

Now that we know how to calculate the momentum mismatch as a function of the PDC photons frequencies, the final step to compute the PMF is straightforward. We can in fact calculate $\phi(\Delta k(\omega_s, \omega_i))$ in the relevant frequency range of signal and idler, obtaining the phase-matching function in the (ω_s, ω_i) space. A visual representation of this procedure is provided in Figure 2.5, where we consider a 775 nm pump down-converted into 1550 nm photons in a type-II PDC process. A sinc-shaped PMF is considered, and calculated point-by-point in the (ω_s, ω_i) space according to the corresponding momentum mismatch value.

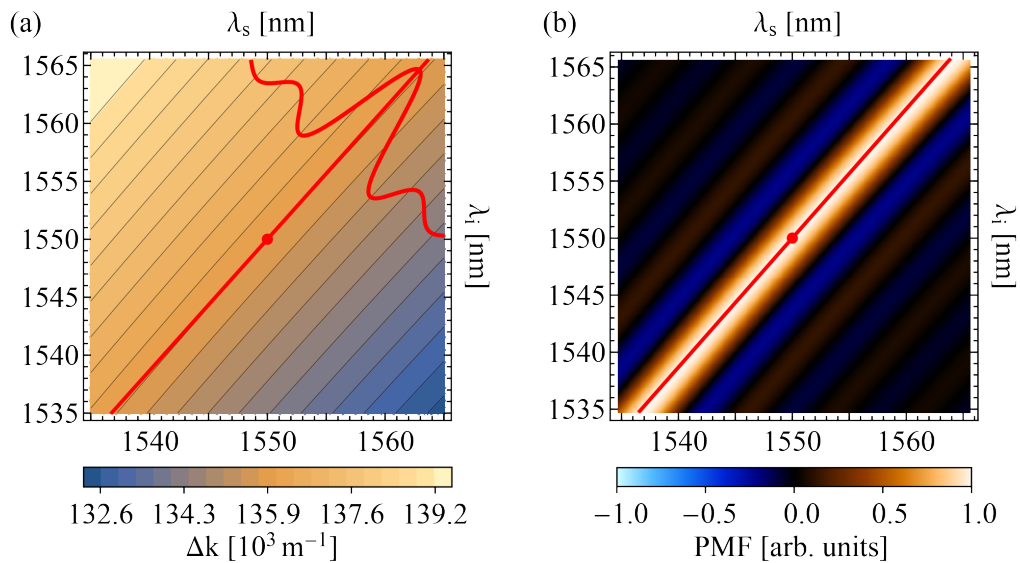


Figure 2.5: Phase-matching function in the signal-idler plane. (a) Momentum mismatch in the signal-idler frequencies space on a smaller spectral range with respect to Figure 2.4. Here the Δk contours are approximately linear, but some slight curvature is already evident despite the reduced range. This is highlighted by the red line, having a slope of approximately 48° calculated accordingly to Eq. (2.27) at 1550 nm for both signal and idler: indeed, the Δk contour starts to deviate from the red line when we move away from the central point, where the slope is calculated. The red sinc-shaped function corresponds to the PMF that will be calculated at each $\Delta k(\omega_s, \omega_i)$, resulting in the function shown in (b).

2.2.3 Joint spectral amplitude

So far, we have discussed what the pump-envelope function represents, and how the phase-matching function is related to the crystal properties via the dispersion relations and the nonlinearity of the crystal. The last—trivial—step consists in

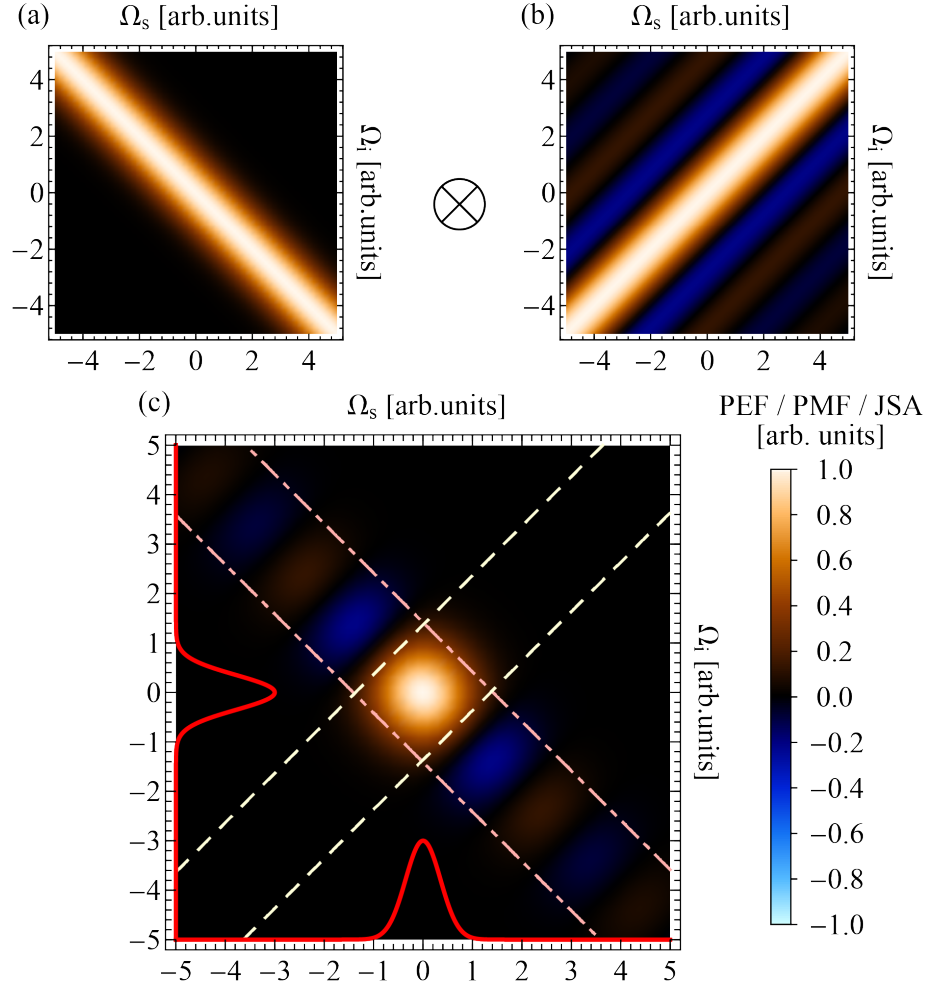


Figure 2.6: Joint spectral amplitude. The joint spectral amplitude (c) is the product of the pump spectrum (a) and the phase-matching function (b). The pink dot-dashed and yellow dashed lines represent the $1/e$ contours of the PEF and PMF, respectively. The red projections represent the marginal spectra (in the intensity domain) of the PDC photons.

multiplying the PEF and PMF to obtain the joint spectral amplitude of the PDC process, as prescribed in Eq. (2.18) and shown in Figure 2.6. The JSA captures the PDC single-photon spectra, defined as the marginals of the *joint spectral intensity* (JSI):

$$\varphi(\omega_1) = \int_{-\infty}^{+\infty} d\omega_2 |f(\omega_1, \omega_2)|^2, \quad (2.28)$$

where we define the JSI as the absolute value squared of the JSA, $|f(\omega_1, \omega_2)|^2$, and $\varphi(\omega_1)$ is the single-photon spectrum, as one would measure with a spectrometer. An example of the single-photon spectra is provided in Figure 2.6. Most importantly, the JSA describes joint spectral properties of the PDC-photons, including in

particular the non-classical correlations that might exist between signal and idler: note that this is true under the (reasonable—as discussed earlier) assumption of the biphoton JSA describing a pure bipartite quantum state. These correlations can be quantified by the amount of *separability* of the JSA, that can be obtained via *Schmidt decomposition* (SD) as discussed in the next Section.

2.2.4 Schmidt decomposition and JSA separability

In this Section we introduce the Schmidt decomposition, i.e. arguably the most useful tool to characterise the joint spectral amplitude. The JSA can be expressed as a sum of orthogonal modes:

$$f(\omega_s, \omega_i) = \sum_k b_k u_k(\omega_s) v_k(\omega_i), \quad (2.29)$$

in what is known as the Schmidt decomposition [67, 68]. The *Schmidt coefficients* $\{b_k\}$ are real numbers such that their absolute values sum to unity if $f(\omega_s, \omega_i)$ is normalised, and the *Schmidt modes* $\{u_k(\omega_s)\}$ and $\{v_k(\omega_i)\}$ are orthonormal single-photon spectral functions, namely *time-frequency modes* (TFM). Likewise, the two-photon state in Eq. (2.13) can be decomposed as

$$|\psi\rangle_{s,i} = \sum_k b_k |u_k\rangle_s |v_k\rangle_i, \quad (2.30)$$

where

$$|u_k\rangle_s = \int d\omega u_k(\omega) |\omega\rangle_s; \quad |v_k\rangle_i = \int d\omega v_k(\omega) |\omega\rangle_i, \quad (2.31)$$

are orthonormal states in the signal and idler subspaces, and $|\omega\rangle_j = \hat{a}_j^\dagger |0\rangle_j$. The states satisfy the orthonormality conditions $\langle u_k | u_{k'} \rangle_s = \delta_{kk'}$ and $\langle v_k | v_{k'} \rangle_i = \delta_{kk'}$, which simplifies expressions for many interesting quantities that can be written just in terms of the Schmidt coefficients.

As we have discussed before, a drawback of PDC is that photon pairs are generated spontaneously, making them difficult to interfere in optical networks. The

spontaneous nature of the down-converted source can be mitigated by placing a photon detector in one of the down-converted modes. Photon-number correlations between the two down-converted modes ensure that detection of a single photon in one mode projects the state in the other mode into a single photon—a process known as *heralding*. The heralded photon can then be stored for future use in a quantum memory or appropriately delayed so that it arrives in the experiment at the right time [23]. While this might seem a weird digression in this Section, we'll see in a few lines why this is instead actually very relevant.

To calculate the heralded state, in say mode s , we model single-photon detection with a flat frequency response, in say mode i , by the projector

$$\hat{P}_i = \int d\omega |\omega\rangle_i \langle\omega|_i = \sum_k |u_k\rangle_i \langle u_k|_i, \quad (2.32)$$

expressed in terms of the Schmidt modes $|v_k\rangle_i$ for convenience. The heralded state is then calculated by applying the Born rule, and tracing out the detected mode:

$$\rho_s = \text{Tr}_i \left[|\psi\rangle_{s,i} \langle\psi|_{s,i} (\hat{\mathbb{I}}_s \otimes \hat{P}_i) \right] \quad (2.33)$$

$$= \sum_k b_k^2 |u_k\rangle_s \langle u_k|_s. \quad (2.34)$$

This result shows that, after detection of a single photon in mode i , the state in mode s is a statistical mixture of single-photon states with orthogonal spectral distributions $u_k(\omega)$. The mixed nature of this state is undesirable because it reduces its interference visibility in an interferometric network, as we will see in [Section 3.2.2](#).

The degree to which the state is mixed can be quantified by the heralded-photon purity:

$$P_s = \text{Tr} \left[\rho_s^2 \right] = \sum_k b_k^4, \quad (2.35)$$

which ranges from $P_s = 1$ for a pure state to $P_s = 1/N$ (where N is the number of Schmidt modes) for a maximally mixed state. The heralded-photon purity only depends on the Schmidt coefficients, and is independent from what PDC photon we

are considering:

$$P_s = P_i = P. \quad (2.36)$$

Similarly, one can define the *Schmidt number* K as the inverse of the heralded-photon purity:

$$K = \frac{1}{P} = \frac{1}{\sum_k b_k^4}, \quad (2.37)$$

that quantifies the amount of spectral entanglement between the PDC photons and, equivalently, the amount of correlations in the JSA [67, 69, 70]. Note that another definition of Schmidt number exists in literature, where Schmidt number is used as a synonym of Schmidt rank, i.e. the minimum number of Schmidt coefficients needed to express a quantum state: however, we do not use such definition in this work.

When the JSA is a separable function of signal and idler frequencies:

$$f(\omega_s, \omega_i) = u_0(\omega_s)v_0(\omega_i), \quad (2.38)$$

then $b_0 = 1$ and all other coefficients $b_{k>0}$ are zero and Eq. (2.30) describes a separable bipartite state:

$$|\psi\rangle_{s,i} = |u_0\rangle_s \otimes |v_0\rangle_i. \quad (2.39)$$

Consequently, the heralded photons are spectrally pure:

$$\begin{aligned} |u_0\rangle_s &= \int d\omega_s u_0(\omega_s) |\omega_s\rangle_s \\ |v_0\rangle_i &= \int d\omega_i v_0(\omega_i) |\omega_i\rangle_i. \end{aligned} \quad (2.40)$$

The SD method discussed in this Section can only be used for pure bipartite states [69], as we assume in Eqs. (2.12),(2.13): a generalisation to mixed states might be possible but it's beyond the scope of this Thesis. As a last remark, we point out that the mathematical procedure prescribed by the Schmidt decomposition is generally hard (and in some cases impossible) to perform analytically. What one

can do instead is to numerically approximate it with what is called the *singular value decomposition* (SVD), by discretising the frequency space, and consequently the joint spectrum and the Schmidt modes. The reader can find an excellent discussion on how to do this in practice in reference [68], while some more advanced details will be discussed in the next Chapter.

Non più ottico ma spacciatore di lenti
per improvvisare occhi contenti,
perché le pupille abituate a copiare
inventino i mondi sui quali guardare

Fabrizio de André, *Un ottico*

CHAPTER 3

Design Considerations for PDC Sources

When building a parametric down-conversion source with a separable joint spectrum, e.g. for making spectrally-pure heralded single photons, two practical issues must be accounted for: the design of the experiment, and its characterisation. Following from and expanding on the results published in

	Contents	
3.1	Designing a down-conversion source . . .	28
3.1.1	Spectral filtering	28
3.1.2	Group-velocity matching	29
3.1.3	Symmetric group-velocity matching	35
3.1.4	Chirped pump pulses and their effect on photon purity	37
3.2	Benchmarking a down-conversion source	40
3.2.1	JSA reconstruction	41
3.2.2	Two-photon interference	46
3.2.3	HOM: the general case	47
3.2.4	Signal-idler interference	48
3.2.5	Heralded-photon interference	51
3.3	Conclusion and discussion	53

Ref. [71], this Chapter is dedicated to discussing these problems in detail. To address experiment design, we study the impact on spectral separability of realistic pump fields combined with the most common phase-matching function shapes; for a comprehensive discussion of realistic crystals, however, we refer the reader to [Chapter 4](#). To address the characterisation of the experiment, we discuss the effect of discretisation and spectral range of the measured joint spectrum, the difference between inferring separability from the joint spectral amplitude vs. the joint spectral intensity, and the advantages of interference experiments for purity characterisation over methods based on the joint spectrum reconstruction.

3.1 Designing a down-conversion source

In the previous Chapter, we have discussed how the joint spectral amplitude captures spectral properties and correlations of the PDC photons. In some cases, correlations in the joint spectrum are desirable (see e.g. [Chapter 6](#)), but more often than not, they are problematic and ought to be minimised. For example, in a heralded single-photon source, a separable JSA ensures high-purity single photons, which are necessary for, e.g., high-visibility interference in optical networks. Being able to tailor the biphoton spectrum accordingly to the specific application is therefore of utmost importance.

Quantifying the temporal-spectral correlation in PDC photon pairs and designing the pump spectrum to reduce them are well-studied problems [[48](#), [53](#), [70](#), [72–85](#)]. In virtually all studies, however, the pump laser is taken to have a transform-limited *Gaussian* spectral amplitude or *delta*-function distribution; when in reality, a pulsed laser has a sech-shaped spectral amplitude that may not be transform limited [[86](#)]. The design of crystal properties for generation of uncorrelated photon pairs is also a well-studied problem. This typically involves matching the group velocities of the fields inside the crystal [[48](#), [70](#), [87](#), [88](#)] as well as shaping the crystal’s nonlinearity profile to approximate a Gaussian function [[89–93](#)].

The first part of this Chapter is dedicated to addressing these practical problems that ought to be considered when designing optimal PDC sources.

3.1.1 Spectral filtering

PDC can be used as a heralded source of single photons, in which one photon of a pair is sacrificed in detection to herald the presence of a photon in the other mode. As we have seen in [Section 2.2.4](#), the heralded photon generally emerges in a spectrally-mixed state due to strong correlation in the joint spectrum of PDC photon pairs resulting from the conservation of energy and momentum. To create pure photons, we therefore need to eliminate correlations without introducing mixture in other degrees of freedom.

The easiest way to reduce spectral correlations is to employ narrowband spectral filters. This approach, however, comes at the price of introducing losses, which severely compromise the heralding efficiency (i.e. the probability of detecting a photon knowing that the other photon of the pair has been detected) of the source even with ideal filters [40], and decreases the absolute flux of the heralded photons. Moreover, spectral filtering acts at the intensity level and can destroy photon-number correlations between the two down-converted modes, and at relatively high pump powers it can also introduce mixing in the photon-number degree of freedom [40, 94–96]. A classic example is the case of heralded sources with photon number resolving detectors: in the case of a lossless source, one can discriminate one- vs multi-photon emission, mitigating the high-order emission problem of PDC sources. However, when a filter introduces losses in the heralding arm, a single-photon click in the trigger detector doesn't necessarily correspond to a heralded single photon, and photon-number-mixed states might be emitted by the source.

It's therefore clear that filtering is not the ideal solution for dealing with unwanted spectral correlations: luckily enough, there exist alternative solutions that are less detrimental on the overall PDC usefulness.

3.1.2 Group-velocity matching

A lossless method to remove (at least part of) frequency correlations is to achieve the so-called group-velocity matching condition [70, 73, 75, 88]. Starting with a set of desired pump, signal and idler wavelengths, one can find phase-matching conditions in certain materials that allow the inverse group velocity of the pump laser in the nonlinear crystal to either match one of the PDC photon's inverse group velocities, or to match the average of the two PDC photons' inverse group velocities, or a value in between the two. This erases some of the spectral correlations that otherwise arises between the PDC photons, which in consequence leads to more separable joint spectra and high purity photons.

What GVM alone cannot address is that, in a standard nonlinear crystal, the nonlinearity that the pump pulse experiences is turned on suddenly as the pump

enters the crystal, and turned off just as suddenly as the pump exists the crystal. This sudden turning-on and turning-off in the nonlinearity can be modelled as a rectangular nonlinearity profile along the direction of propagation. As discussed in [Section 2.2.2](#), the down-conversion spectrum is linked to the Fourier transform of this longitudinal nonlinearity profile, and a rectangular profile results in a sinc-shaped JSA which further restricts photon purity due to its side lobes [94]. To overcome this problem, nonlinearity engineering techniques can be adopted, as discussed in detail in [Chapter 4](#)), allowing one to suppress these side lobes and enhance the JSA separability.

In the following, we will discuss GVM in both ideal and more realistic conditions, considering different possible combinations of PEF and PMF shapes.

Group-velocity matching: the ideal case

It was well-known that, under certain conditions, Gaussian-shaped pump and phase-matching functions can make the joint spectral amplitude separable [70]. Recently, it was shown that Gaussian functions are *conditio sine qua non* to make the JSA separable in standard PDC processes [97]. In this Section, we discuss the conditions for perfect separability, i.e. when both PEF and PMF are Gaussian-shaped.

A Gaussian pump function can be defined as:

$$\alpha_{\text{Gauss}}(\omega_s, \omega_i) = \exp \left[-\frac{(\Omega_s + \Omega_i)^2}{2\sigma_{\text{PEF}}^2} \right]; \quad (3.1)$$

different yet equivalent definitions of Gaussian PEF can also be found in the literature. We also define the *bandwidth* (or simply *width*) of a spectral (or temporal) distribution as its *full width at half maximum* (FWHM). This corresponds to $2\sqrt{2\log 2} \sigma_{\text{PEF}}$ for a Gaussian PEF. It's worth stressing that, when defining the bandwidth, we are considering the spectral *amplitude* of the pump, while there are other conventions that define the bandwidth differently (either with reference to the profile of the spectral *intensity* of the pump, or by considering the $1/e$ width instead of the FWHM [70, 81, 89, 94]). For completeness sake, and for avoiding

any ambiguity in the following lines, we also remind the reader of the obvious fact that functions having the same FWHM in the amplitude domain might not have the same width in the intensity domain (see for example [Figure 3.2](#)).

We can also define a Gaussian PMF as:

$$\phi_{\text{Gauss}}(\omega_s, \omega_i) = \exp \left[-\frac{(\sin(\theta)\Omega_s - \cos(\theta)\Omega_i)^2}{\sigma_{\text{PMF}}^2} \right], \quad (3.2)$$

where θ defines the orientation of the PMF [[80](#), [82](#), [98](#)] and depends on the group velocities according to [Eq. \(2.27\)](#), as already discussed in [Section 2.2.2](#).

Let's study the JSA separability condition, i.e. $f(\omega_s, \omega_i) = u_0(\omega_s)v_0(\omega_i)$, when PEF and PMF are chosen accordingly to [Eq. \(3.1\)](#) and [\(3.2\)](#):

$$f(\omega_s, \omega_i) = \alpha_{\text{Gauss}}(\omega_s, \omega_i)\phi_{\text{Gauss}}(\omega_s, \omega_i). \quad (3.3)$$

We can expand [Eq. \(3.3\)](#) as follows:

$$\begin{aligned} & \exp \left[-\frac{\Omega_s^2 + \Omega_i^2 + 2\Omega_s\Omega_i}{2\sigma_{\text{PEF}}^2} - \frac{\sin(\theta)^2\Omega_s^2 + \cos(\theta)^2\Omega_i^2 - 2\sin(\theta)\cos(\theta)\Omega_s\Omega_i}{\sigma_{\text{PMF}}^2} \right] \\ &= \exp \left[-\frac{\Omega_s^2}{2\sigma_{\text{PEF}}^2} - \frac{\sin(\theta)^2\Omega_s^2}{\sigma_{\text{PMF}}^2} \right] \exp \left[-\frac{\Omega_i^2}{2\sigma_{\text{PEF}}^2} - \frac{\cos(\theta)^2\Omega_i^2}{\sigma_{\text{PMF}}^2} \right] \\ & \quad \exp \left[-\frac{\Omega_s\Omega_i}{\sigma_{\text{PEF}}^2} + \frac{2\sin(\theta)\cos(\theta)\Omega_s\Omega_i}{\sigma_{\text{PMF}}^2} \right]. \end{aligned} \quad (3.4)$$

The JSA in [Eq. \(3.4\)](#) is the product of two separable functions and an additional non-separable one that still depends on both photons' frequencies: $f(\omega_s, \omega_i) = u_0(\omega_s)v_0(\omega_i)p(\omega_s, \omega_i)$. Hence, the condition for having an overall separable joint spectrum translates into the following statement: $p(\omega_s, \omega_i) = 1$. This corresponds to the following condition for perfect separability:

$$\begin{aligned} & \exp \left[-\frac{\Omega_s\Omega_i}{\sigma_{\text{PEF}}^2} + \frac{2\sin(\theta)\cos(\theta)\Omega_s\Omega_i}{\sigma_{\text{PMF}}^2} \right] = 1 \\ & \frac{\Omega_s\Omega_i}{\sigma_{\text{PEF}}^2} = \frac{2\sin(\theta)\cos(\theta)\Omega_s\Omega_i}{\sigma_{\text{PMF}}^2} \\ & \boxed{2\cos(\theta)\sin(\theta) = \sigma_{\text{PMF}}^2/\sigma_{\text{PEF}}^2} \end{aligned} \quad (3.5)$$

which has a solution only when the relation $0 < \theta < \pi/2$ is satisfied. From Eq. (3.5) we can see that, to guarantee perfect separability, the ratio between the widths of PMF and PEF increases from $\theta = 0$ to $\theta = \pi/4$ (where it is exactly equal to one), and then decreases symmetrically between $\theta = \pi/4$ and $\theta = \pi/2$. When the angle θ is outside this range, the separability condition can't be satisfied. In Figure 3.1 we show two examples, where the PMF angle is either $\theta = \pi/4$ or $\theta = 3\pi/7$, and the resulting JSA is perfectly separable (it's indeed the product of two Gaussian functions having either ω_s or ω_i as their only variable).

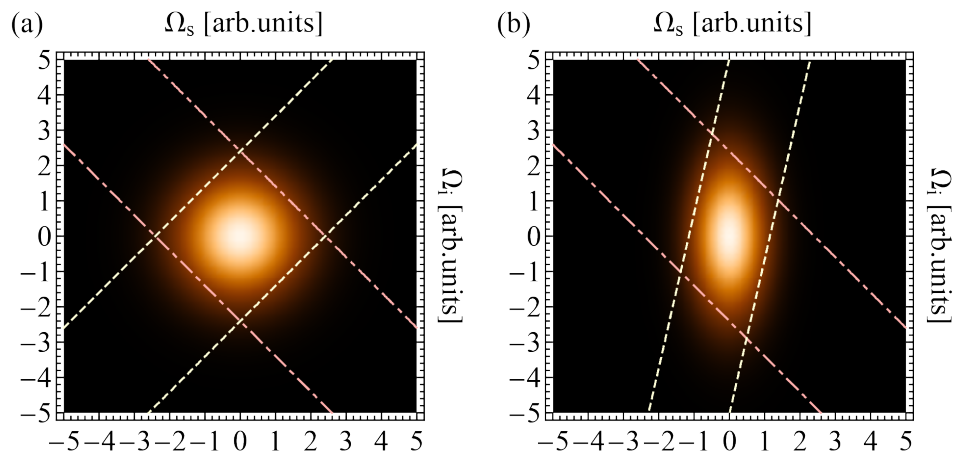


Figure 3.1: JSAs in perfect group-velocity matching condition. Two examples of GVM in the ideal case, where both pump and phase-matching function are Gaussian shaped. On the left, $\theta = \pi/4$ and PEF and PMF have the same width, condition known as symmetric GVM. On the right, $\theta = 3\pi/7$ and the pump spectrum is broader than the PMF to guarantee the JSA separability.

Group-velocity matching: the realistic case

Many studies on the joint spectral properties of down-conversion pairs assume either Gaussian or delta pump-envelope functions. These functions are convenient to work with analytically, but often don't reflect what happens in an experiment. Indeed, most experiments which aim to create more than just one heralded photon, or multiple photon pairs, are performed with mode-locked, ultra-short-pulsed lasers whose temporal intensity function can be described by a squared *hyperbolic secant* (sech) function, $\text{sech}^2(t/\tau)$, where τ is a temporal scaling factor [86]. This yields a PEF

represented, up to an irrelevant linear phase, by a sech function:

$$\alpha_{\text{sech}}(\omega_s, \omega_i) = \text{sech} \left[\frac{1}{2} \pi \tau (\Omega_s + \Omega_i) \right], \quad (3.6)$$

having a bandwidth equal to $4 \cosh^{-1} [2]/(\pi\tau)$. Note that the sech and Gaussian amplitude functions have equal width when $\tau \approx 0.712\sigma_{\text{PEF}}$.

Moreover, we also need to consider sinc-shaped PMFs when discussing standard PDC processes, as we have seen that this is the standard form of the PMF arising from crystals with constant nonlinearity profile, see Eq. (2.24). We can define the sinc PMF in the (ω_s, ω_i) space as:

$$\phi_{\text{sinc}}(\omega_s, \omega_i) = \text{sinc} \left[\sqrt{2}\kappa (\sin(\theta)\Omega_s - \cos(\theta)\Omega_i) \right], \quad (3.7)$$

where κ is the width parameter, and θ defines the PMF's orientation as in Eq. (3.2). The sinc and Gaussian amplitude functions, as defined in Eq. (3.7) and (3.1), have equal width when $\sigma_{\text{PMF}} \approx 1.61/\kappa$. Finally, the sech and sinc functions have equal width when $\tau \approx 0.442\kappa$. These three highly-relevant functions are shown in [Figure 3.2](#), both in their amplitude and intensity (i.e. absolute value squared of the amplitude) forms.

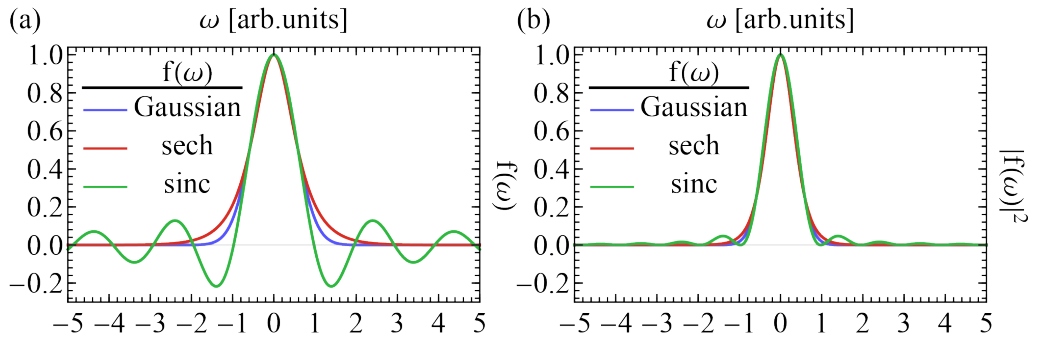


Figure 3.2: Comparison of Gaussian, sech and sinc functions. The width parameters of Gaussian, sech and sinc amplitude functions (a) are chosen to match their FWHM (n.b. the corresponding intensity functions (b), defined as the absolute value squared and shown on the right, have different FWHMs). The sech function has higher tails with respect to the Gaussian function, introducing unwanted correlations in the JSA. The sinc function, on the other hand, presents side lobes near the main peak, even more detrimental for the heralded-photon purity.

We can now analyse how realistic PEFs and PMFs affect the JSA separability. For all four combinations, the spectral purity of heralded photons depends on the relative widths of the functions, in analogy with the Gaussian-Gaussian case discussed analytically in Eq. (3.5). To maximise the purity, we introduce a parameter ξ equal to the ratio between the PEF and PMF widths:

$$\xi = \frac{\sigma_{\text{PMF}}}{\sigma_{\text{PEF}}} \approx 1.40 \sigma_{\text{PMF}} \tau \approx \frac{1.61}{\sigma_{\text{PEF}} \kappa} \approx 2.26 \frac{\tau}{\kappa}, \quad (3.8)$$

and optimise over ξ for each PMF angle θ .

The results of this analysis are shown in Figure 3.3. The angle θ is studied over a range of $[\pi/4, 3\pi/4]$, as the results show symmetric behaviour when studied over the supplementary range $[-\pi/4, \pi/4]$. As expected from Eq. (3.5), optimal purity (relative to each combination of PEF and PMF) can be achieved via GVM only for $\theta \in (0, \pi/4)$, while it drops when the PMF angle is outside this range. At first glance, it's clear that sinc-shaped PMFs are the main cause of the reduction in heralded-photon purity (Chapter 4 is indeed entirely dedicated to solving this issue). Moreover, sech-shaped pump spectra behave very similarly to Gaussian-shaped ones: this is not surprising, as the two functions are both bell-shaped and have very similar profiles. However, the sech function slightly compromises the

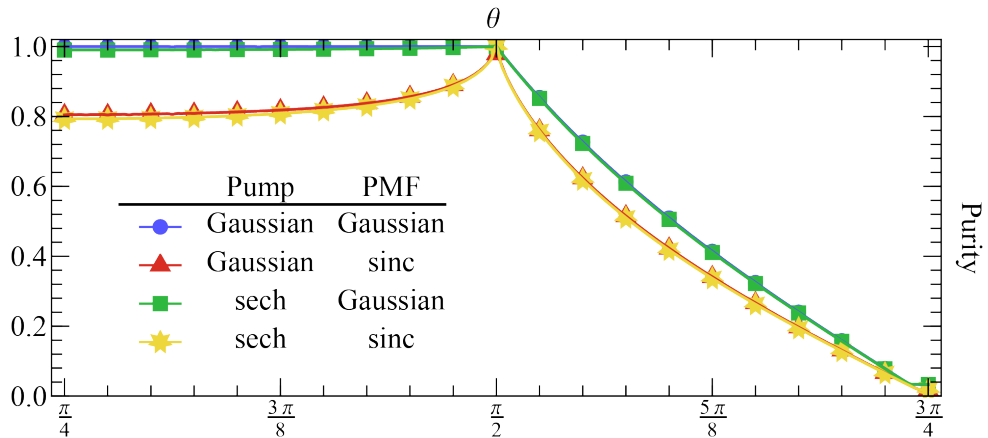


Figure 3.3: Group-velocity matching. GVM condition for different combinations of pump-envelope function and phase-matching function: Gaussian-Gaussian (blue dots), Gaussian-sinc (red triangles), sech-Gaussian (green squares), and sech-sinc (yellow stars).

JSA separability, leaving the Gaussian-Gaussian combination as the only optimal one [97], providing perfect purity whenever the group-velocity matching condition is satisfied. Curiously, in the extreme asymmetric group-velocity matching condition ($\theta \simeq 0$ and $\theta \simeq \pi/2$) all the combinations approximately hit perfect heralded-photon purity. The price to pay is a very small ξ parameter, meaning that the PMF width should be much smaller than the PEF width (see also Eq. (3.5)): a condition hard to implement in actual experiments as it would require extremely short pump pulses combined with extremely long nonlinear crystals.

In an actual experiment, the crystal length determines the phase-matching function width according to Eq. (2.24) and (2.26) (this is not the case for custom-poled crystals discussed in Chapter 4), while the pulse length gives the pump-envelope function bandwidth. Therefore, when designing the experiment, one chooses the crystal length based on the PEF FWHM (or vice-versa) to maximise the purity, as we did in the numerical simulation shown in Figure 3.3. However, the optimal relationship between crystal length and pulse bandwidth differs for different materials, as the Sellmeier equations might not be exactly linear in Δk (see Eq. (2.25)). For this reason, one should always consider their specific case, taking into account the exact pump spectral shape and the nonlinear properties of the crystal, and run simulations with realistic parameters to be sure that the output will approximate sufficiently well the physics of the process. Last but not least, the optimal pulse length for a given PMF is also dependent on eventual filtering that might be applied on the PDC photons: one should also take the filter profile into account when simulating the effective JSA of the overall process, keeping in mind that the filter transmission needs to be translated from the intensity domain to the amplitude domain before applying it to the joint spectrum.

3.1.3 Symmetric group-velocity matching

In this Section, we focus on the special case where $v_p^{-1} = (v_s^{-1} + v_i^{-1})/2$, i.e. $\theta = \pi/4$. In this case, the PMF is perpendicular to the PEF, and is on the main diagonal

of the (ω_s, ω_i) plane:

$$\phi_{\text{Gauss}}^{\text{sym}}(\omega_s, \omega_i) = \exp\left[-\frac{(\Omega_s - \Omega_i)^2}{2\sigma_{\text{PMF}}^2}\right], \quad (3.9)$$

$$\phi_{\text{sinc}}^{\text{sym}}(\omega_s, \omega_i) = \text{sinc}[\kappa(\Omega_s - \Omega_i)].$$

This regime is known as *symmetric* group-velocity matching condition, which for Gaussian functions generates separable photons with equal bandwidths when $\sigma_{\text{PMF}} = \sigma_{\text{PEF}}$. These photons can be used for heralded photon generation, but the photons can also both be fed into an experiment, as they will exhibit perfect two-photon interference if their central wavelengths are chosen to be identical.

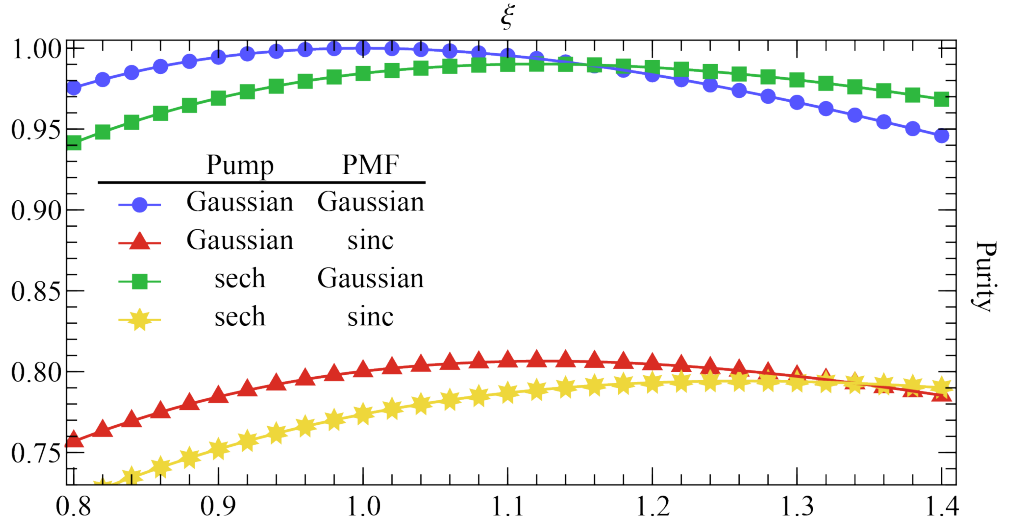


Figure 3.4: Symmetric group-velocity matching. The figure shows the heralded-photon purity as a function of the parameter ξ , defined as the ratio between the PMF and PEF widths, for different combinations of phase-matching function and pump-envelope function. For each combination, there is only one optimal ξ_{opt} that maximises the purity, as shown in Table 3.1, while any other value is sub-optimal and compromises the JSA separability. The only PMF-PEF combination that guarantees perfect purity is Gaussian-Gaussian, as we have already seen in Figure 3.3.

As already mentioned above, the optimal ratio for a Gaussian-Gaussian combination is $\xi = 1$, but we found that for other combinations, this can vary by up to 26%. We can see how, in this symmetric GVM case, a sech PEF reduces the maximum purity only slightly, while a sinc PMF reduces the maximum purity significantly, by approximately 20%. Figure 3.4 shows the dependence of heralded-photon purity on

ξ for all four PEF-PMF combinations here studied, and [Table 3.1](#) shows maximum purities and corresponding ξ for each combination:

PEF	PMF	maximum P_s	optimal ξ
Gaussian	Gaussian	1	1
sech	Gaussian	0.99	1.12
Gaussian	sinc	0.80	1.13
sech	sinc	0.79	1.26

Table 3.1: Maximum purities and corresponding ξ for the most common combinations of pump-envelope functions and phase-matching functions. Due to the low purity arising from a sinc-shaped PMF, spectral filtering on the heralding or both beams is typically used to improve the purity at expense of the overall photon counts.

The optimal JSAs given by the four PEF and PMF combinations are shown in [Figure 3.5](#).

3.1.4 Chirped pump pulses and their effect on photon purity

So far, we have considered Fourier-transform-limited pump-envelope functions, where the temporal and spectral profile of the pump pulses have minimal time-bandwidth product. However, it is possible to have non-transform-limited pulses in an experiment i.e. the temporal duration might exceed the time-bandwidth product, especially when ultra-short pulses are used. This is the scenario we'll discuss in this Section.

When short optical pulses propagate through a transparent medium whose refractive index is wavelength dependent, they acquire a phase that depends nonlinearly on the wavelength, known as frequency *chirp*. To study how a *linear* frequency chirp affects the down-converted photons, we introduce a *quadratic* spectral phase to the PEF to model the group-delay dispersion in the material [86] (the main contribution to the overall dispersion and pulse chirping), i.e., we multiply the PEF by $e^{-ik(\bar{\omega}_p - \omega_p)^2}$ (or, equivalently, multiply the JSA by $e^{-ik(\Omega_s - \Omega_i)^2}$), where k is equal to half of the group delay dispersion. This phase introduces temporal broadening which in turn introduces phase correlations in the JSA, reducing the spectral purity of heralded photons.

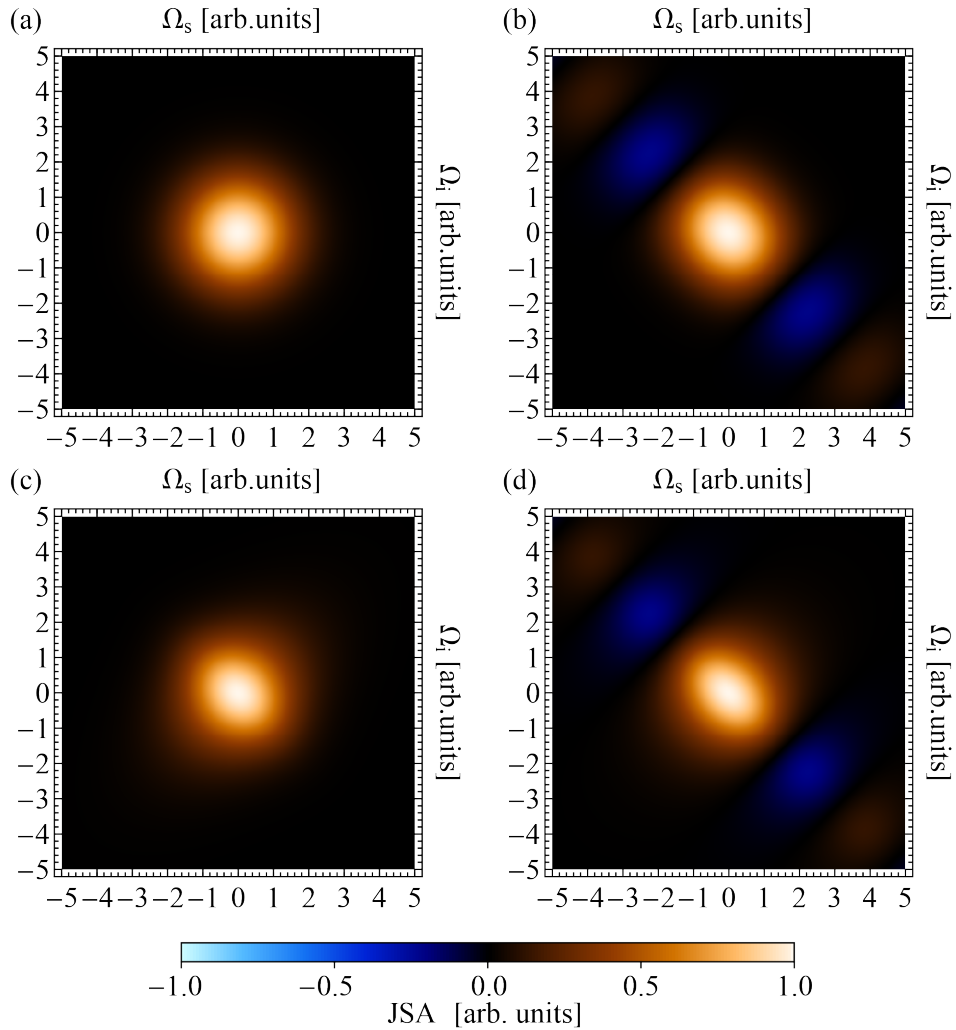


Figure 3.5: Joint spectra in symmetric group-velocity matching. The figure shows the four JSAs corresponding to the four PEF-PMF combinations in symmetric GVM condition, where ξ parameter is chosen individually according to [Table 3.1](#) to maximise the heralded-photon purity. (a) Gauss-Gauss, (b) Gauss-sinc, (c) sech-Gauss, (d) sech-sinc.

The spectral purity of a chirped JSA can be parametrised by the dimensionless parameter kw^2 , where w is the spectral width of the PEF. This tells us that there is a trade-off between the pump width and the amount of chirp that can be tolerated, i.e., increasing the chirp or increasing the square of the pump's width will have the same effect on the purity. We can therefore run numerical simulations to analyse the effect of chirping on the joint spectrum separability. We find that separability decays almost exponentially as chirping increases, as reported in [Figure 3.6](#), where the heralded-photon purity is plotted as a function of kw^2 .

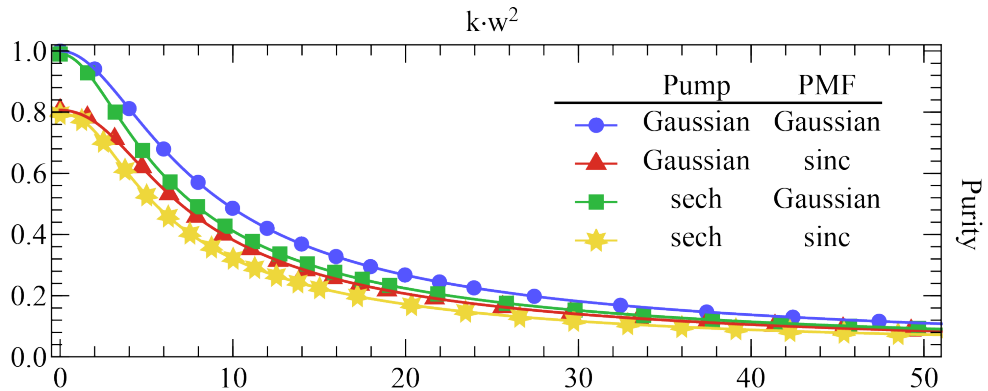


Figure 3.6: Effect of a chirped pump. The figure shows the purity as a function of the chirping parameter, kw^2 , for different combinations of phase-matching function and pump-envelope function. Optimal purity is achieved only in absence of chirping, as correlations between signal and idler arise as soon as $kw^2 > 0$.

To explore the trade-off between k and w^2 , and provide some physical meaning to the numerical result in Figure 3.6, we model sech pulses propagating in optical glass N-BK7—a very common material for optical components. For example, a 400 nm, 50 fs sech pulse (where pulse length is defined as the FWHM of the temporal intensity profile), which is the pulse length of modern GHz repetition rate Ti:sapph lasers, passing through 1 cm of the standard optical substrate of N-BK7 acquires a quadratic phase of $kw^2 \approx 2.1$, decreasing the purity from ~ 0.99 to ~ 0.90 (when the PMF is Gaussian-shaped) or from ~ 0.80 to ~ 0.74 (in the sinc-shaped PMF case). But a 200 fs sech pulse travelling through the same piece of glass acquires a quadratic phase of only $kw^2 \approx 0.13$, decreasing the purity by less than 0.1%. However, if the same 200 fs pulse is sent through 30 cm of fused-silica single-mode fibre, the corresponding chirping is $kw^2 \approx 3.2$ and is therefore not negligible. This shows that while group delay dispersion, and therefore spectral chirping, can be neglected for relatively long pulses (in particular picosecond pulses), it should be taken into account for short (i.e. sub-picosecond) pulses. Figure 3.7 shows values of kw^2 in N-BK7 for a sech pulse at different pulse durations and central wavelengths.

While the frequency chirp introduces correlations in the JSA, these correlations *are not* visible in the JSI, where the absolute value squared of the joint spectral amplitude is considered. Therefore, in the presence of chirp, the JSI is not a good

indicator of heralded photon spectral purity, as discussed in the second half of this Chapter.

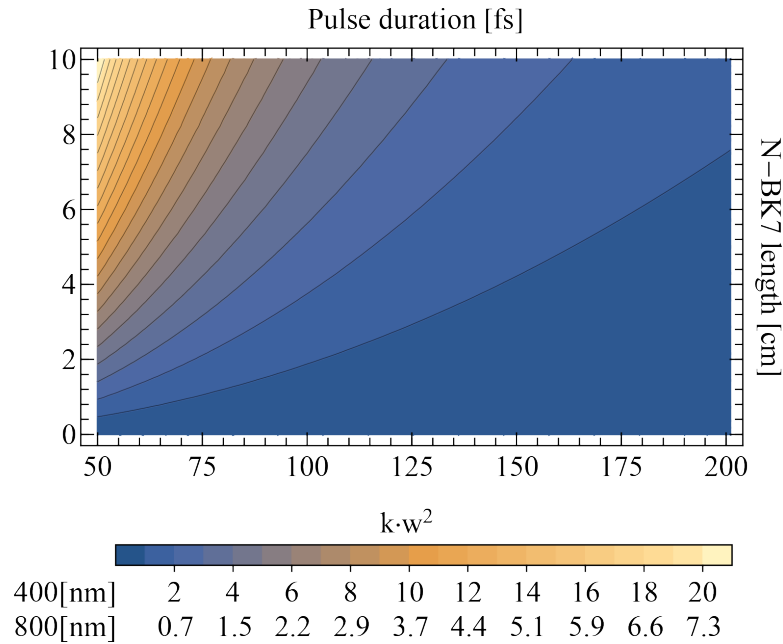


Figure 3.7: Dispersion in N-BK7. Example of chirping parameter, kw^2 , in the optical substrate N-BK7 as a function of pulse duration (assuming a sech-shaped pulse) and glass length. The legend shows kw^2 values for central wavelengths $\lambda = 400$ nm and $\lambda = 800$ nm, where the group velocity dispersion of the material is equal to 122 fs²/mm and 45 fs²/mm, respectively.

3.2 Benchmarking a down-conversion source

In the previous Section, we discussed the design of a heralded single photon source that (aims to) produce spectrally pure photons. In the second part of this Chapter we address the question of how a PDC photon source can be characterised in its spectral properties once it is built. While it can be extremely hard to directly measure the spectral purity of a heralded photon via, e.g., quantum state tomography, this property can be inferred from other measurements, such as those of the JSA, the JSI (in special cases), or HOM interference [41].

Any experimental measurement—as well as any numerical simulation—of the JSA or JSI necessarily yields a discretised approximation over a finite range of signal and idler frequencies. Since poor choice of discretisation and spectral range

can give incorrect results, we will discuss the effect of discretisation and spectral range on the inferred spectral separability. What's more, in many situations only the JSI can be measured directly: common experimental methods such as scanning-monochromator measurements, fibre-spectroscopy techniques or stimulated emission tomography [99–105] lack spectral phase and sign information, and have access to the intensity only. We show that using the square root of the JSI, $\sqrt{\text{JSI}} = |\text{JSA}|$, for purity estimation involves some pitfalls if the JSA has phase-correlations, including sign-changes, and temporal correlation introduced by e.g. a chirped pump. It's worth noting that there are also methods to reconstruct the JSA directly (including phase correlations), such as phase-sensitive stimulated emission tomography [106, 107] or Franson-inspired interferometric schemes [108], but they are experimentally hard and are not widespread techniques.

We will finally discuss why two-photon interference is generally a better benchmark for inferring the PDC heralded-photon purity.

3.2.1 JSA reconstruction

In the first Chapter, we have seen that the purity can be calculated from the Schmidt decomposition of the JSA. To do this in practice, the JSA is discretised into frequency bins, over finite ranges of signal and idler frequencies, then represented as a complex-valued matrix. The Schmidt decomposition is then computed numerically applying SVD [68, 109] to the matrix representation of the JSA.

Whether the discretised JSA is obtained experimentally using, e.g. phase-sensitive stimulated emission tomography, or constructed from the analytical form of the JSA for a numerical simulation, it is crucial to correctly choose the spectral range of both the signal and the idler photons and the number of frequency-bins used for the discretisation. Here, we discuss this matter considering, as an example, a sinc-shaped PMF and Gaussian-shaped pump function in symmetric GVM regime ($\theta = \pi/4$). Clearly, an analogous analysis should be repeated for any given experimental condition: however, the conclusions we'll show in the following pages are general enough to give the reader an idea of how to tackle this problem in any practical case.

Mathematically, we know that only a SVD of the JSA can yield the actual purity. But since others (e.g. [81, 84, 88, 98, 104, 110]) have used the JSI or the $\sqrt{\text{JSI}}$ ($|\text{JSA}|$) to get information about the purity from experiments, we also construct matrix representations of the JSI and $\sqrt{\text{JSI}}$ ($|\text{JSA}|$) and compute a purity-like parameter using the singular values of these matrices. In the following, we'll show that neither the JSI nor the $\sqrt{\text{JSI}}$ provide good estimates of the true purity (with exception of very specific cases).

To study the effect of a finite spectral range, we fix the discretisation (defined as the number of frequency bins) and construct matrix representations of the JSA for increasing spectral ranges. We parameterise the spectral range by the ratio between the spectral range used in the JSA calculation and the average PDC photon bandwidth (defined as the FWHM of the marginal spectral distributions of the photons). We then find the singular values of each matrix and use it to compute the purity according to Eq. (2.35). We find that for a fixed discretisation, the purity starts from near-unity values: this is not surprising, as very small ranges introduce filtering-like effects. As the spectral range increases, more of the “true spectrum” is included in the finite representation of the JSA, and the value of the purity approaches its true value, and in general, as expected, coarser discretisation leads to worse, more unstable results. However, since the number of frequency bins is fixed, each bin gets larger as the spectral range continues to increase, and eventually cannot capture detailed features of the JSA, so the inferred purity diverges from the true purity. This can be seen in Figure 3.8, where the blue dots show the purity computed from the JSA as a function of spectral range for matrix discretisations of 50×50 , 51×51 , and 250×250 . It's worth noting how the purity-like parameter obtained via SVD of the JSI significantly overestimates the separability of the JSA, and also an analysis based on the $\sqrt{\text{JSI}}$ doesn't lead to the correct value, converging to a purity-like parameter about 2.3% higher than the true purity. Curiously, the SVD behaves differently for even and odd discretisations

To study the effect of discretisation, we fix the spectral range and construct matrix representations of the JSA for a range of discretisations. As before, we find

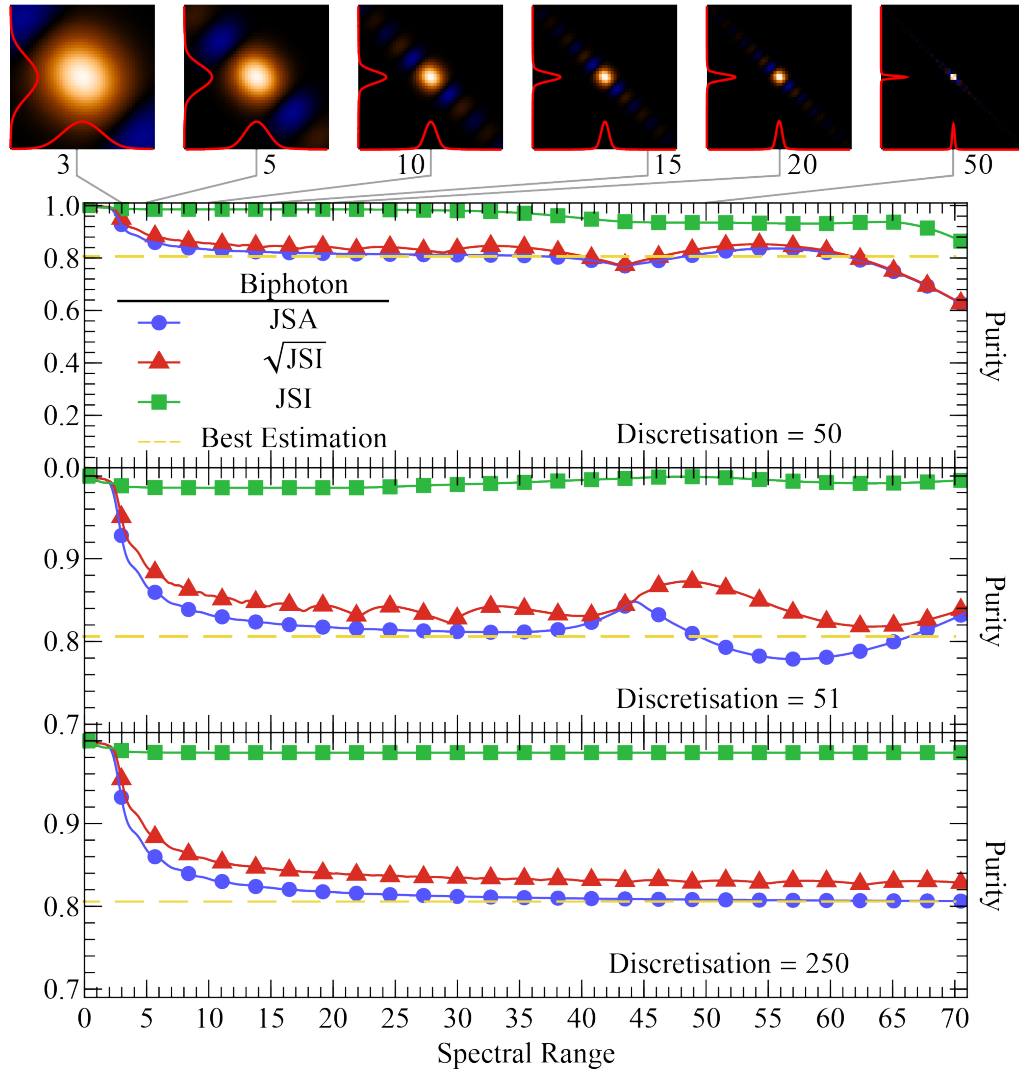


Figure 3.8: JSA separability as a function of spectral range. Blue points, red triangles, and green squares represent the purity-like parameters estimated from the JSA, $|JSA|$ and JSI, respectively, considering (from top to bottom) 50×50 , 51×51 , and 250×250 joint spectral matrices. The yellow dashed line corresponds to the best estimation of the JSA separability, computed from a 3000×3000 matrix over a spectral range larger than 80 times the PDC-photon bandwidth. The density plots at the top represent the JSAs at different spectral ranges, where the PDC-photon spectral bandwidth is highlighted in red.

the singular values of each matrix and use it to compute the purity according to Eq. (2.35). We find that, for a fixed spectral range, the computed purity converges to a fixed value as the discretisation is increased. This can be seen in Figure 3.9, where again the blue dots show the purity computed from the JSA as a function of discretisation for spectral ranges of 5, 15, and 30 times larger of the photons' band-

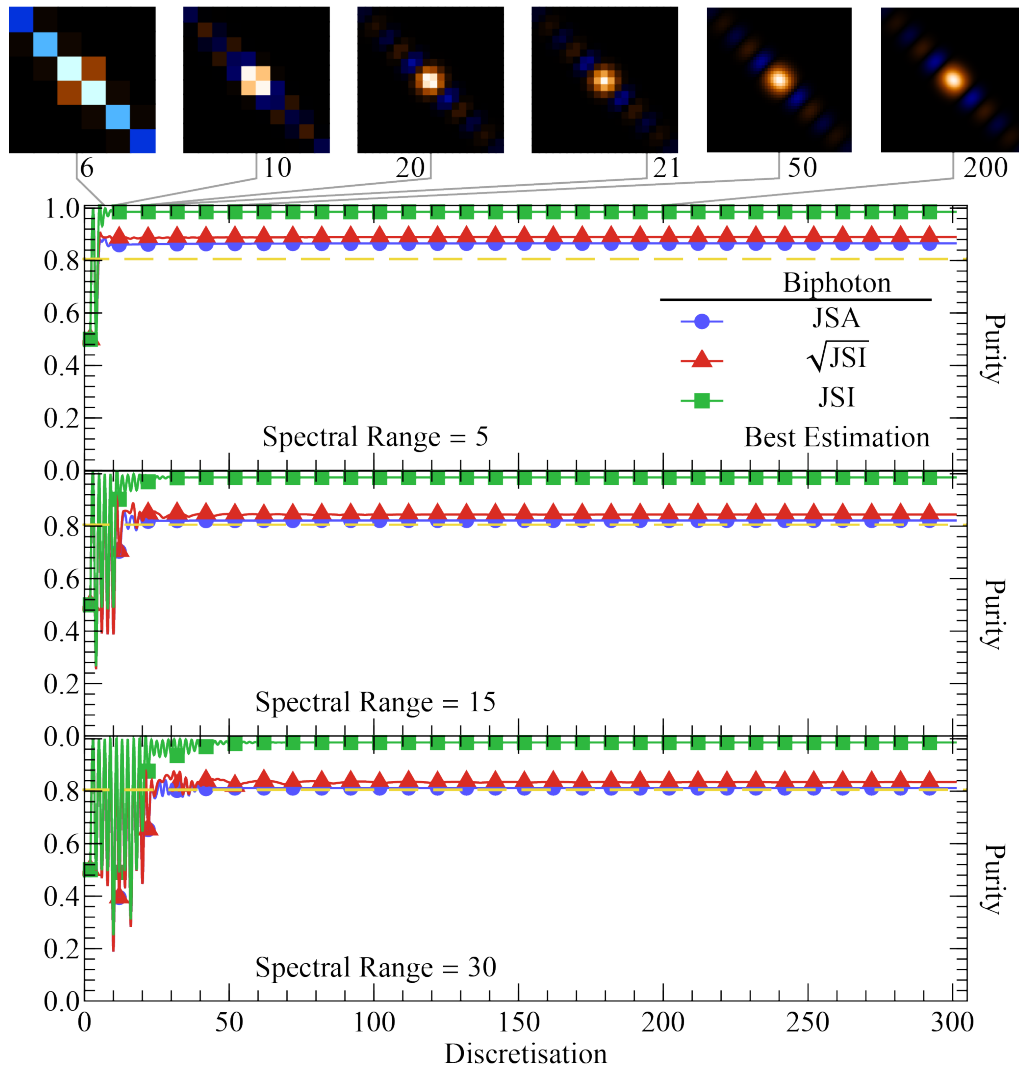


Figure 3.9: JSA separability as a function of spectral discretisation. Blue points, red triangles, and green squares represent the purity-like parameters estimated from the JSA, $|JSA|$ and JSI, respectively, considering (from top to bottom) spectral ranges of 5, 15, and 30 times larger than the photon bandwidth. The yellow dashed line corresponds to the best estimation of the JSA separability, computed from a 3000×3000 matrix over a spectral range larger than 80 times the PDC-photon bandwidth. Density plots at the top represent the JSAs at different discretisations.

widths, respectively. The calculated purity-like parameters are extremely sensitive to relatively small discretisation, and these results aren't suitable for estimating accurately the spectral properties of the PDC photons. At higher discretisations the inferred purity converge to a single value of spectral purity. However, when the spectral range is too small (e.g. in the top plot), the purity converges to an overestimated value, as the corresponding JSA matrix doesn't take into account spectral

correlations existing far from the central peak. As before, we also construct matrix representations of the JSI and $\sqrt{|\text{JSI}|}$ ($|\text{JSA}|$) and compute purity-like parameters using the singular values, shown in [Figure 3.9](#) as green squares and red triangles, respectively. Both converge, but to the wrong value, thus neither provide very good estimates of the true purity. This discrepancy is due to the sinc-shaped PMF having both positive and negative amplitude components. For ideal Gaussian-shaped PEF and PMF, the purity-like parameter would instead converge to the true purity.

To study the interplay between discretisation and spectral range, and to show in what regimes a purity estimation from a measured JSA can be trusted, we compute the JSA separability at different discretisations and spectral ranges, and we show the results in [Figure 3.10](#). The purity is significantly overestimated for small spectral ranges, generally < 10 times the photon bandwidth, while a coarse discretisation leads to noisy results. In general, reliable purity values are obtained in the top-right corner of the plot: while there isn't an optimal recipe for choosing these parameters (as they also depend on the nonlinear properties of the material and on the pump pulse properties), it is advisable to use spectral ranges larger than 10 times the photon bandwidth, and discretisation values of at least 100×100 , for obtaining a good approximation of the real JSA, and therefore of the purity.

In light of this discussion, we conclude that estimating purity from joint spectral measurements has a number of pitfalls. Measurements based on JSA and JSI are impacted by limited spectral range and rough discretisation. In the case of JSI, even if the characterisation is carried out meticulously, the purity-like parameter inferred from the SVD (which, as discussed above, can sometimes correspond to the spectral purity) is at best a rather loose upper bound, and one should seek alternative methods for a more precise purity estimation.

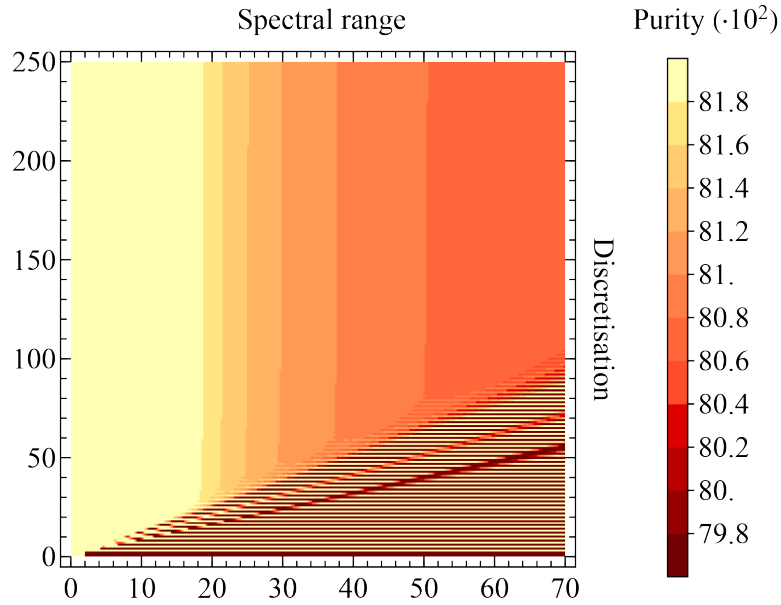


Figure 3.10: Purity estimation at different spectral ranges and discretisations. This contour plot shows the interplay between discretisation the spectral range when estimating the purity from a JSA matrix. As thoroughly discussed in the main text, small spectral ranges overestimate the purity, while small discretisations lead to noisy and unreliable results.

3.2.2 Two-photon interference

If there is reason to believe that the JSA has both positive and negative regions, or if it has additional temporal correlations such as those that come from chirped pulses—and it is not possible to do phase-sensitive stimulated emission tomography—then one ought to find alternative schemes to benchmark the PDC-photons spectral properties.

A more reliable benchmark is HOM two-photon interference. This can be experimentally achieved by interfering the signal and idler photons produced in the same down-conversion process (to gather information on what kind of spectral correlations exist in a given JSA), or two heralded-photons (either signal with signal or idler with idler) produced in the same nonlinear crystal at different times (to infer the heralded-photon spectral purity). The visibility of such process is defined as:

$$V = 1 - \frac{N_{\min}}{N_{\max}}, \quad (3.10)$$

where N_{\max} is the number of photon pairs that exit the BS from opposite ports after arriving at the BS simultaneously, while N_{\min} is the number of photon pairs that exit the BS from opposite ports after arriving at the BS at different times for identical photons. In this last Section, we will discuss how to link the interference pattern and visibility to the PDC spectral properties, and we'll show how two-photon interference predicts the spectral purity even in the case of chirped pulses.

3.2.3 HOM: the general case

Let's consider two spectrally-pure photons entering a BS from the two input modes a and b :

$$|\psi^{\text{in}}\rangle_{a,b} = \int d\omega_a \varphi_a(\omega_a) \hat{a}^\dagger(\omega_a) |0\rangle_a \int d\omega_b \zeta_b(\omega_b) e^{-i\omega_b \Delta t} \hat{b}^\dagger(\omega_b) |0\rangle_b, \quad (3.11)$$

where $e^{-i\omega_b \Delta t}$ is a time delay term indicating a Δt -delay in the arrival times of the two photons at the BS. An ideal 50-50 beam-splitter introduces the following transformations on the creation operators:

$$\begin{cases} \hat{a}^\dagger(\omega_a) \rightarrow \frac{1}{\sqrt{2}} (i\hat{a}^\dagger(\omega_a) + \hat{b}^\dagger(\omega_a)) \\ \hat{b}^\dagger(\omega_b) \rightarrow \frac{1}{\sqrt{2}} (\hat{a}^\dagger(\omega_b) + i\hat{b}^\dagger(\omega_b)) \end{cases}, \quad (3.12)$$

and, consequently, the biphoton state after the BS reads:

$$\begin{aligned} |\psi^{\text{out}}\rangle_{a,b} = & \frac{1}{2} \int d\omega_a \varphi_a(\omega_a) \int d\omega_b \zeta_b(\omega_b) e^{-i\omega_b \Delta t} \\ & (i\hat{a}^\dagger(\omega_a)\hat{a}^\dagger(\omega_b) - \hat{a}^\dagger(\omega_a)\hat{b}^\dagger(\omega_b) + \hat{b}^\dagger(\omega_a)\hat{a}^\dagger(\omega_b) + i\hat{a}^\dagger(\omega_a)\hat{b}^\dagger(\omega_b)) |0\rangle_{a,b}. \end{aligned} \quad (3.13)$$

To calculate the probability of having the two photons exiting opposite outputs of the BS (here labelled as cc , standing for coincident count detected in opposite modes simultaneously), we need to consider the detection projectors on mode k , assuming

flat spectral response to avoid filtering-like effects:

$$\hat{P}_k = \int d\omega \hat{k}^\dagger(\omega) |0\rangle_k \langle 0|_k \hat{k}(\omega), \quad (3.14)$$

and to apply the projectors on the output modes of the BS:

$$p_{cc}(\Delta t) = \text{Tr} \left[|\psi^{\text{out}}\rangle_{a,b} \langle \psi^{\text{out}}|_{a,b} \hat{P}_a \otimes \hat{P}_b \right]. \quad (3.15)$$

Combining Eq. (3.13) and (3.14) with Eq. (3.15), and after a few simplification steps, we obtain the relation [41]:

$$p_{cc}(\Delta t) = \frac{1}{2} - \frac{1}{2} \int d\omega_1 \varphi_a^*(\omega_1) \zeta_b(\omega_1) e^{-i\omega_1 \Delta t} \int d\omega_2 \varphi_a(\omega_2) \zeta_b^*(\omega_2) e^{i\omega_2 \Delta t}. \quad (3.16)$$

When the two photons are spectrally identical, and arrive at the BS simultaneously, the probability of having a coincident count at the two opposite outputs of the BS is 0, meaning that the photons interfere perfectly and always *bunch* at the beam-splitter.

Eq. (3.16) only holds in the case of spectrally-pure photons. However, it can be easily generalised to mixed states summing over the contributions of all the components of the statistical mixture [41]:

$$p_{cc}(\Delta t) = \frac{1}{2} - \frac{1}{2} q_k q_{k'} \sum_{k,k'} \int d\omega_1 \varphi_k^*(\omega_1) \zeta_{k'}(\omega_1) e^{-i\omega_1 \Delta t} \int d\omega_2 \varphi_k(\omega_2) \zeta_{k'}^*(\omega_2) e^{i\omega_2 \Delta t}, \quad (3.17)$$

where $q_k, q_{k'}$ are the weights of the statistical mixture of the two photons, and $\varphi_k(\omega_a), \zeta_{k'}(\omega_b)$ are the corresponding spectra.

3.2.4 Signal-idler interference

Following from the general case described above, we can now discuss the case of interfering signal and idler photons produced in the same parametric down-conversion

process. Starting from the input state:

$$|\psi^{\text{in}}\rangle_{a,b} = \iint d\omega_s d\omega_i f(\omega_s, \omega_i) e^{-i\omega_i \Delta t} \hat{a}^\dagger(\omega_s) \hat{b}^\dagger(\omega_i) |0\rangle_{s,i}, \quad (3.18)$$

we can go through the same steps as above, applying the BS transformations and the projections on the BS output modes. The result is the following relation:

$$p_{\text{cc}}(\Delta t) = \frac{1}{2} - \frac{1}{2} \iint d\omega_1 d\omega_2 f^*(\omega_1, \omega_2) f(\omega_2, \omega_1) e^{i(\omega_2 - \omega_1) \Delta t} \quad (3.19)$$

that can be rewritten in terms of the Schmidt modes of the biphoton state according to Eq. (2.29), with $f(\omega_s, \omega_i) = \sum_k b_k u_k(\omega_s) v_k(\omega_i)$:

$$p_{\text{cc}}(\Delta t) = \frac{1}{2} - \frac{1}{2} \sum_{k,k'} b_k b_{k'} \int d\omega_1 u_k^*(\omega_1) v_{k'}(\omega_1) e^{-i\omega_1 \Delta t} \int d\omega_2 u_{k'}(\omega_2) v_k^*(\omega_2) e^{-i\omega_2 \Delta t}. \quad (3.20)$$

In Figure 3.11 (a) we show the signal-idler interference patterns for the PEF-PMF combinations Gaussian-Gaussian and Gaussian-sinc, obtaining the well known ‘‘Gaussian HOM dip’’ and ‘‘triangular HOM dip’’, respectively.

Conveniently, signal-idler interference can also be used to infer the particle-exchange symmetry properties of the JSA [111, 112]. For example, a JSA of the form $f_1(\omega_s, \omega_i) = \exp[-(\omega_s + \omega_i)^2]$ is perfectly symmetric, as $f_1(\omega_s, \omega_i) = f_1(\omega_i, \omega_s)$, while a JSA equal to $f_2(\omega_s, \omega_i) = \exp[-(\omega_s + \omega_i)^2] (\omega_s - \omega_i)$ is maximally antisymmetric, as $f_2(\omega_s, \omega_i) = -f_2(\omega_i, \omega_s)$. Any JSA can be decomposed in its symmetric and antisymmetric parts as follows:

$$f(\omega_s, \omega_i) = \frac{f(\omega_s, \omega_i) + f(\omega_i, \omega_s)}{2} + \frac{f(\omega_s, \omega_i) - f(\omega_i, \omega_s)}{2} \quad (3.21)$$

$$f(\omega_s, \omega_i) = \gamma f_s(\omega_s, \omega_i) + \delta f_a(\omega_s, \omega_i),$$

where $f_s(\omega_s, \omega_i) = f_s(\omega_i, \omega_s)$, $f_a(\omega_s, \omega_i) = -f_a(\omega_i, \omega_s)$ are normalised functions:

$$\iint d\omega_s d\omega_i |f_s(\omega_s, \omega_i)|^2 = \iint d\omega_s d\omega_i |f_a(\omega_s, \omega_i)|^2 = 1, \quad (3.22)$$

and γ, δ need to satisfy the following condition: $|\gamma|^2 + |\delta|^2 = 1$.

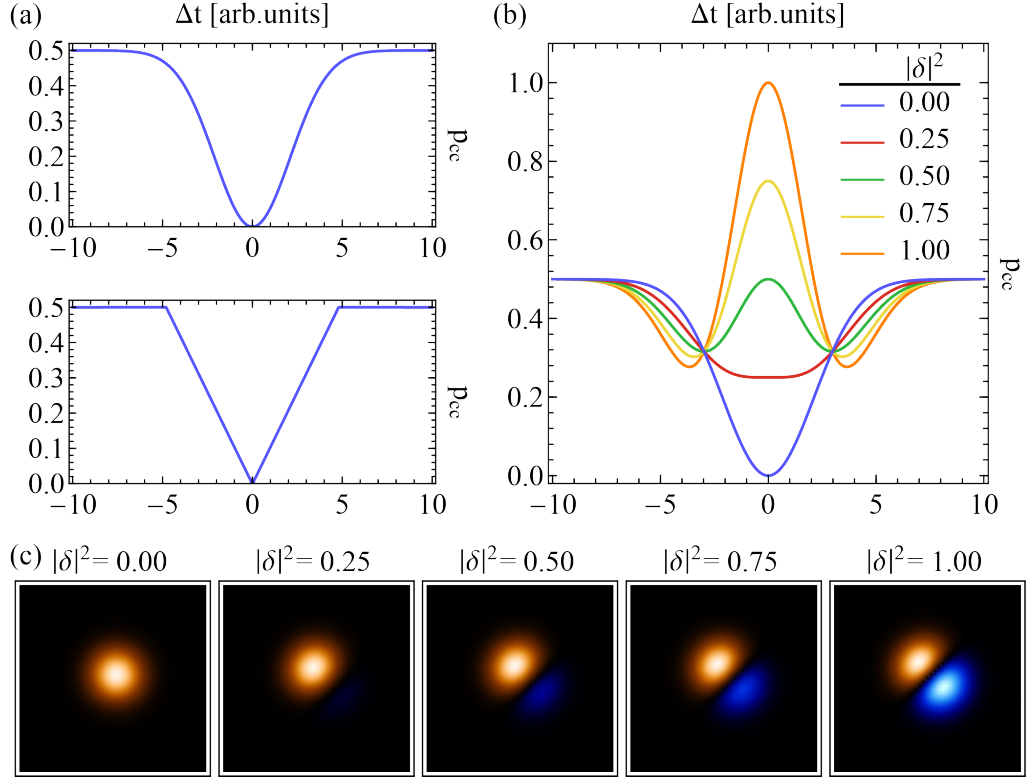


Figure 3.11: Signal-idler interference. (a) Signal-idler interference for a JSA composed of Gaussian pump and Gaussian (top) or sinc (bottom) phase-matching function, respectively. (b) Signal-idler interference at different degrees of antisymmetry of the joint spectrum: perfect bunching occurs when the spectrum is maximally symmetric, perfect antibunching when it's maximally antisymmetric. (c) Corresponding JSAs at different degrees of antisymmetry.

We now replace the JSA in Eq. (3.19) with its decomposition in symmetric and antisymmetric parts, and consider the photons arriving simultaneously at the BS (i.e. we consider $\Delta t = 0$):

$$\begin{aligned}
 p_{cc}(0) = & \frac{1}{2} - \frac{1}{2} \iint d\omega_s d\omega_i (|\gamma|^2 |f_s(\omega_1, \omega_2)|^2 \\
 & - \gamma^* \delta f_s^*(\omega_1, \omega_2) f_a(\omega_1, \omega_2) + \gamma \delta^* f_a^*(\omega_1, \omega_2) f_s(\omega_1, \omega_2) - |\delta|^2 |f_a(\omega_1, \omega_2)|^2),
 \end{aligned} \tag{3.23}$$

where we have rearranged the order of the frequencies and changed sign accordingly to the symmetry/antisymmetry of the function. The integral of the mixed terms is equal to zero because the overall product of f_s and f_a is antisymmetric and integrated over a symmetric interval, and considering the normalisation conditions

in (3.22) the coincidence probability reads:

$$p_{cc}(0) = \frac{1}{2} - \frac{1}{2}(|\gamma|^2 - |\delta|^2) = 1 - |\gamma|^2 = |\delta|^2. \quad (3.24)$$

Equation (3.24) relates the antibunching probability with the antisymmetry of the joint spectrum. As a last step, we can relate the interference visibility with the antisymmetry weight δ :

$$V = 1 - 2p_{cc}(0) = 1 - 2|\delta|^2, \quad (3.25)$$

with $V = 1$ for maximally symmetric biphoton states, and $V = -1$ for maximally antisymmetric ones. As an example, in Figure 3.11 (b,c) we show the signal-idler interference patterns for JSAs having different amount of antisymmetry, showing how the amount of bunching/antibunching depends on the overall symmetry of the joint spectrum.

3.2.5 Heralded-photon interference

We finally consider the interference of heralded PDC photons. Let's consider two independent joint spectra, expanded in terms of the Schmidt modes of the biphoton states: $f(\omega_s, \omega_i) = \sum_k b_k u_k(\omega_s) u'_k(\omega_i)$ and $g(\omega_s, \omega_i) = \sum_k d_k v_k(\omega_s) v'_k(\omega_i)$. Analogously to the previous Sections, we can calculate the probability of having antibunching at the BS as:

$$p_{cc}(\Delta t) = \frac{1}{2} - \frac{1}{2} \sum_{k,k'} b_k^2 d_{k'}^2 \int d\omega_1 u_k^*(\omega_1) v_{k'}(\omega_1) e^{-i\omega_1 \Delta t} \int d\omega_2 u_k(\omega_2) v_{k'}^*(\omega_2) e^{-i\omega_2 \Delta t} \quad (3.26)$$

where we are considering the interference of the signal photons, described by the Schmidt modes $u_k(\omega_s)$ and $v_k(\omega_s)$. An analogous discussion holds for any combination of signal and idler of the two PDC processes.

When we consider two identical JSAs, as for example considering the interference of photons produced by the same crystal at successive time steps, and we consider

$\Delta t = 0$, Eq. (3.26) reduces to:

$$\begin{aligned}
p_{\text{cc}}(0) &= \frac{1}{2} - \frac{1}{2} \sum_{k,k'} b_k^2 b_{k'}^2 \int d\omega_1 u_k^*(\omega_1) u_{k'}(\omega_1) \int d\omega_2 u_k(\omega_2) u_{k'}^*(\omega_2) \\
&= \frac{1}{2} - \frac{1}{2} \sum_{k,k'} b_k^2 b_{k'}^2 \int d\omega_1 u_k^*(\omega_1) u_{k'}(\omega_1) \delta_{kk'} \\
&= \frac{1}{2} - \frac{1}{2} \sum_k b_k^4.
\end{aligned} \tag{3.27}$$

We can finally calculate the interference visibility, as we did in Eq. (3.25), obtaining:

$$V = 1 - 2p_{\text{cc}}(0) = 1 - 2 \left(\frac{1}{2} - \frac{1}{2} \sum_k b_k^4 \right) = \sum_k b_k^4 = P_{s,i}, \tag{3.28}$$

that corresponds exactly to the heralded-photon purity of signal and idler, $P_{s,i}$, as defined in Eq. (2.35). This result is very important as it tells us that, under the assumption of perfect indistinguishability of all the other photon *degrees of freedom* (DOFs), two-photon interference is the perfect tool for measuring the JSA separability or, equivalently, the PDC-photon purity. Unlike techniques based on the JSI reconstruction, HOM interference is intrinsically phase-sensitive, providing the correct estimate of the purity even when non-negligible phases are present in the joint spectrum. [Figure 3.12](#) shows that the two-photon interference is indeed capable of capturing the phase information of the JSA: the visibilities of the interference patterns match the purities obtained via Schmidt decomposition shown in [Figure 3.6](#).

As in any measurement, experimental imperfections (such as for example not-perfectly balanced BS or not-identical sources emitting the interfered photons) might compromise the result, giving a misleading estimate of the single-photon purity. However, these errors are generally small: in the experimental chapters of this Thesis we estimate an error of about 0.2%. Moreover, the main reason why ultimately one wants to characterise pure photons is to use them in quantum information protocols, where two-photon interference is required to implement many quantum operations. Estimating purity via quantum interference is therefore also a direct benchmark of how well the photons will interact when used in real applications.

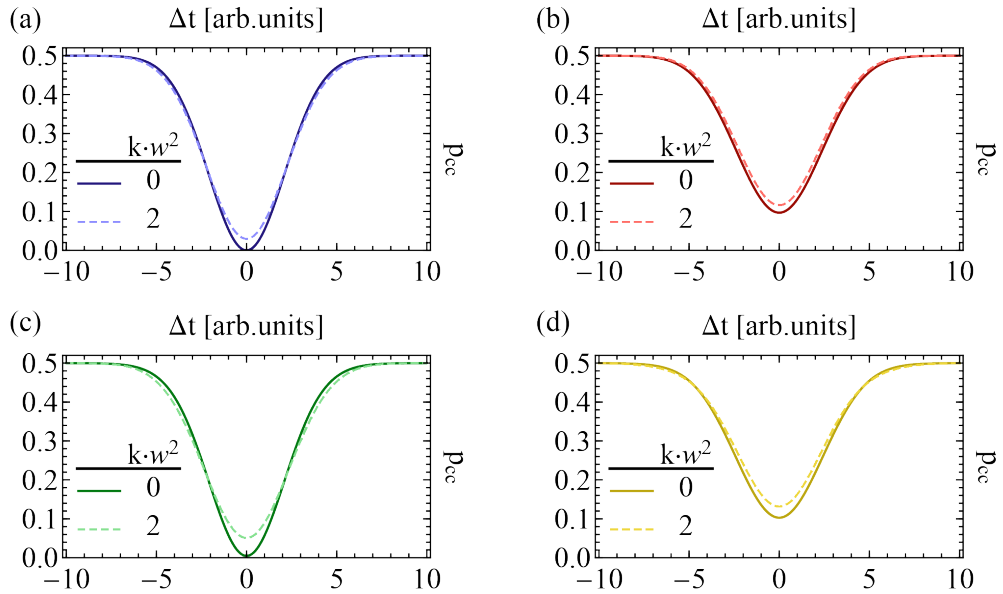


Figure 3.12: Heralded photons’ interference for purity estimation. HOM interference patterns for different combinations of PEF and PMF: Gaussian-Gaussian (a), Gaussian-sinc (b), sech-Gaussian (c), and sech-sinc (d). The solid and dashed lines correspond to different amounts of pump chirping ($kw^2 = 0$ and $kw^2 = 2$, respectively), highlighting the phase sensitivity of the two-photon interference. As expected from [Figure 3.6](#) and the discussion in the first half of this chapter, a chirped pump decreases the spectral purity of the heralded photons and consequently spoils the quality of the interference.

3.3 Conclusion and discussion

In this Chapter, we investigated a number of practical issues relevant to the design and characterisation of single-photon sources based on parametric down-conversion in a group-velocity matching regime. We showed that when realistic laser pulses and phase-matching functions are used, the pulse laser and PDC bandwidths (i.e. choice of crystal length as a function of pulse shape and duration) that optimise heralded photon spectral purity differ to those previously found for ideal Gaussian functions. We examined state characterisation methods based on the joint spectrum of biphotons or two-photon interference, studying how discretisation and spectral range of the joint spectrum play a large role in correctly inferring the heralded photon spectral purity. We also discussed that, in cases where the joint spectral amplitude changes sign or contains non-trivial phases, inferring the purity from the JSI leads to incorrect results. In those cases, if it is not possible to measure the JSA, then

a two-photon HOM interference experiment is a good option to infer the spectral purity. Most importantly, pure single photons are needed in quantum photonics protocols, where the interference quality is usually mapped to the protocol success probability: an additional reason for using two-photon interference as a benchmark for the heralded-photon purity.

The theory developed in this Chapter is for PDC in $\chi^{(2)}$ materials, but the analysis on how the PEF shape and chirp impact the bi-photon properties can be extended to four-wave-mixing processes in $\chi^{(3)}$ materials, which are a building block of integrated nonlinear sources. Furthermore, the results on JSA characterisation apply directly to bi-photons generated via four-wave-mixing.

The sum of these considerations provide a recipe for the correct choice of the experimental parameters for matching laser pulses to PDC bandwidths, and of the parameters for characterising the photon purity. Taking these considerations into account will further improve the quality of PDC photon sources in terms of brightness, spectral purity, and heralding efficiency.

[...] il meglio che ci si può aspettare è di evitare il peggio.

Italo Calvino,
Se una notte d'inverno un viaggiatore

CHAPTER 4

Nonlinearity Engineering

In this Chapter we tackle the problem of sub-optimal, sinc-shaped PMFs typical of standard nonlinear crystals. We start with an introduction to quasi-phase-matching and periodic poling through periodic inversion of the crystal lattice, linking them to the effective nonlinearity of the crystal and the corresponding PMF. We will then move on to the core of this Chapter and of the whole Thesis, discussing how tailored PMFs can

be achieved by means of aperiodic poling. After a brief introduction to pre-existing techniques, we present nonlinearity engineering techniques developed in Ref. [93]. We will discuss the important parameters of this scheme, pointing out the many advantages that it provides over other techniques, and commenting on its limitations and drawbacks. As a case study, we will finally discuss domain engineering in KTP for producing photons at telecom wavelength.

		Contents
4.1	Quasi-phase-matching and periodic poling	56
4.2	Tailoring the PMF: a brief overview . . .	61
4.3	Novel nonlinearity engineering techniques	62
4.3.1	Theory behind the scenes	63
4.3.2	Choosing the width parameter . . .	67
4.3.3	“Two-domain blocks” tracking . . .	70
4.3.4	“One-domain blocks” tracking . . .	72
4.3.5	Simulated annealing algorithm . . .	73
4.3.6	Sub-coherence length domains . . .	77
4.4	Engineering techniques comparison . . .	81
4.5	(A)periodic poling in realistic crystals .	83
4.5.1	Undesirable PDC generation far from central peak	84
4.5.2	Crystal Imperfections	86
4.6	Irregular momentum mismatch: an edge case	90
4.7	Down-conversion in KTP at telecom wavelength: a case study	90
4.8	Conclusion and discussion	93

4.1 Quasi-phase-matching and periodic poling

Let's imagine a nonlinear material with very strong $\chi^{(2)}$ coefficient, that we'd like to use in a nonlinear process, e.g., parametric down-conversion. It might be the case that conservation of momentum is not satisfied at the desired wavelengths, i.e. $\Delta k_0 = \Delta k(\bar{\omega}_s, \bar{\omega}_i) = k_p(\bar{\omega}_p) - k_s(\bar{\omega}_s) - k_i(\bar{\omega}_i) \neq 0$, making the process apparently impossible. This is the case for several materials, as for example potassium titanyl phosphate (KTP) and Lithium Niobate, very common crystals in nonlinear and quantum optics applications at visible, near- and mid-infrared applications. Such problem can be overcome with a technique known as periodic poling, which inverts the crystal lattice periodically to induce *quasi-phase-matching* [113], as shown in [Figure 4.1](#): this shifts the PMF peak in the Δk space to satisfy momentum conservation without significant changes of the PMF shape, enabling the nonlinear process at the desired frequencies.

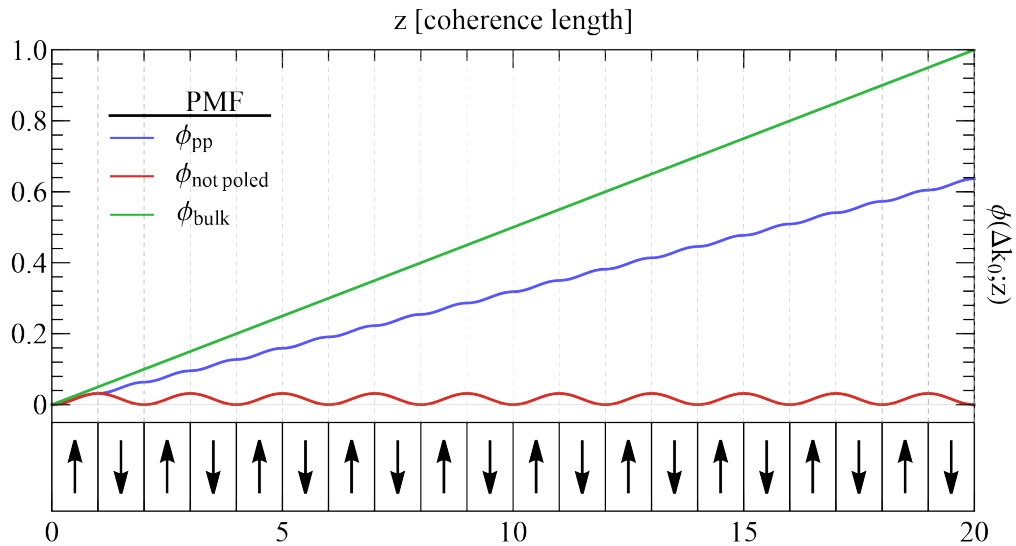


Figure 4.1: Periodic poling. The PMF of a non-phase-matched crystal (red line) reaches a maximum at ℓ_c , where the PDC photons and the pump photon are in counterphase, and then it drops back to 0 at $2\ell_c$: this behaviour is repeated along the crystal, and the PMF keeps oscillating close to 0 and doesn't grow with z . When periodic poling is introduced, the π phase-shift is compensated by a flip in the ferroelectric orientation each domain, and the PMF grows linearly in the crystal (blue line), with a $2/\pi$ scaling factor with respect to a bulk crystal (green line).

Let's start by generalising the phase-matching function definition in Eq. (2.19) to arbitrary longitudinal positions, z , in the crystal:

$$\phi(\Delta k; z) = \int_{-\infty}^{+z} g(z') e^{i\Delta k z'} dz', \quad (4.1)$$

where we omit the dependence of Δk on the signal and idler frequencies, (ω_s, ω_i) , for brevity. When considering a PDC process in a bulk crystal, the normalised nonlinearity along the crystal, $g(z)$, is equal to 1 between $z = 0$ and $z = L$ (where L is the crystal length), and 0 everywhere else. Thanks to the additivity property of our PMF definition, Eq. (2.19) can be rewritten to study the PMF along the crystal at any given position z :

$$\phi_{\text{bulk}}(\Delta k; z) = z e^{i\frac{\Delta k z}{2}} \text{sinc} \left[\frac{\Delta k z}{2} \right]. \quad (4.2)$$

When Δk is centred around 0 at the target frequencies, the PMF grows linearly along the crystal, while its width narrows down also linearly (intuitively, as the crystal gets longer its Fourier transform gets narrower): we show this behaviour in

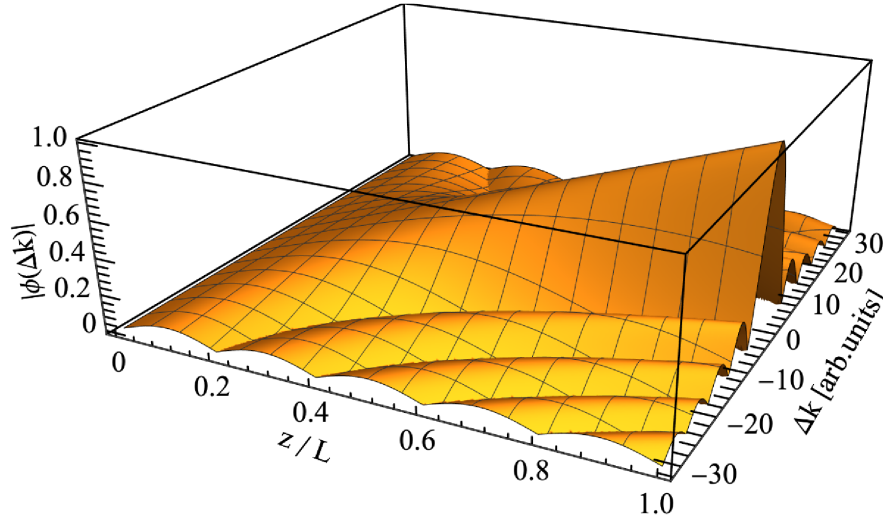


Figure 4.2: 3D phase-matching function of bulk crystal. Three-dimensional plot of the PMF of a bulk crystal, according to Eq. (4.2). As expected, the PMF is 0 at the starting edge of the crystal, it then grows linearly along the longitudinal direction of the crystal while its width narrows down. The plot section at $z/L = 1$ corresponds to the overall PMF of the nonlinear process.

Figure 4.2. However, when the target frequencies correspond to $\Delta k = \Delta k_0 \neq 0$, the PMF follows the relation: $\phi(\Delta k_0; z) = e^{i\frac{\Delta k_0 z}{2}} \sin\left[\frac{\Delta k_0 z}{2}\right] = \frac{i}{2} \left(1 - e^{i\Delta k_0 z}\right)$, that oscillates with period $\Lambda = 2\ell_c = 2\pi/\Delta k_0$ without increasing along the crystal, see plot in **Figure 4.1**. The semi-period ℓ_c is known as the *coherence length*, and represents the distance over which the phase between pump and down-converted photons changes by π , and the $\phi(\Delta k_0; z)$ reaches its maximum value before starting to decrease.

In a periodically-poled crystal, $g(z)$ alternates between $+1$ and -1 every coherence length ℓ_c , to compensate for the π -phase shift between pump and down-converted photons. The corresponding PMF reads:

$$\begin{aligned}
 \phi_{\text{pp}}(\Delta k) &= \sum_{n=1}^N \int_{(n-1)\ell_c}^{n\ell_c} (-1)^{n-1} e^{i\Delta k z} dz \\
 &= i \sum_{n=1}^N \underbrace{(-1)^n}_{e^{in\pi}} e^{i\Delta k n \ell_c} \frac{1 - e^{-i\Delta k \ell_c}}{\Delta k} \\
 &= i \frac{e^{i\Delta k \ell_c} \left(-1 + e^{iN(\Delta k \ell_c + \pi)}\right)}{1 + e^{i\Delta k \ell_c}} \frac{1 - e^{-i\Delta k \ell_c}}{\Delta k} \\
 &= i \left(-1 + \underbrace{e^{iN\ell_c \frac{\pi}{\ell_c}} e^{i\Delta k N \ell_c}}_{e^{i(\Delta k - \frac{\pi}{\ell_c})N \ell_c}} \right) \frac{1}{\Delta k} \frac{e^{i\Delta k \ell_c} - 1}{e^{i\Delta k \ell_c} + 1} \\
 &= i N \ell_c e^{i(\Delta k - \frac{\pi}{\ell_c})\frac{N\ell_c}{2}} \frac{e^{i(\Delta k - \frac{\pi}{\ell_c})\frac{N\ell_c}{2}} - e^{-i(\Delta k - \frac{\pi}{\ell_c})\frac{N\ell_c}{2}}}{2 \left(\Delta k - \frac{\pi}{\ell_c}\right) \frac{N\ell_c}{2}} \frac{\left(\Delta k - \frac{\pi}{\ell_c}\right)}{\Delta k} \frac{e^{i\Delta k \ell_c} - 1}{e^{i\Delta k \ell_c} + 1} \\
 &= \underbrace{L e^{i(\Delta k - \frac{\pi}{\ell_c})\frac{L}{2}} \text{sinc}\left[\left(\Delta k - \frac{\pi}{\ell_c}\right) \frac{L}{2}\right]}_{\text{standard bulk PMF shifted by } \frac{\pi}{\ell_c}} \underbrace{\frac{\left(\Delta k - \frac{\pi}{\ell_c}\right)}{\Delta k} \frac{1 - e^{i\Delta k \ell_c}}{1 + e^{i\Delta k \ell_c}}}_{\text{additional term: } \varphi_{\text{add}}(\Delta k)} \\
 &= \phi_{\text{bulk}}\left(\Delta k - \frac{\pi}{\ell_c}; L\right) \varphi_{\text{add}}(\Delta k), \tag{4.3}
 \end{aligned}$$

where N is the number of domains, ϕ_{bulk} is the PMF as in Eq. (2.24) shifted by π/ℓ_c , and in the second-last step we used $N\ell_c = L$, with L being the total crystal length. Note that Eq. (4.3) considers a crystal centred in $L/2$ and not in 0 along the z -axis, but such shift only corresponds to a negligible phase term. The effects of the additional term, φ_{add} , in Eq. (4.3) are small but non-negligible, and

they make the sinc-shaped PMF slightly asymmetric, as shown in Figure 4.3. The common practice of thinking periodic poling as resulting in an additional term in

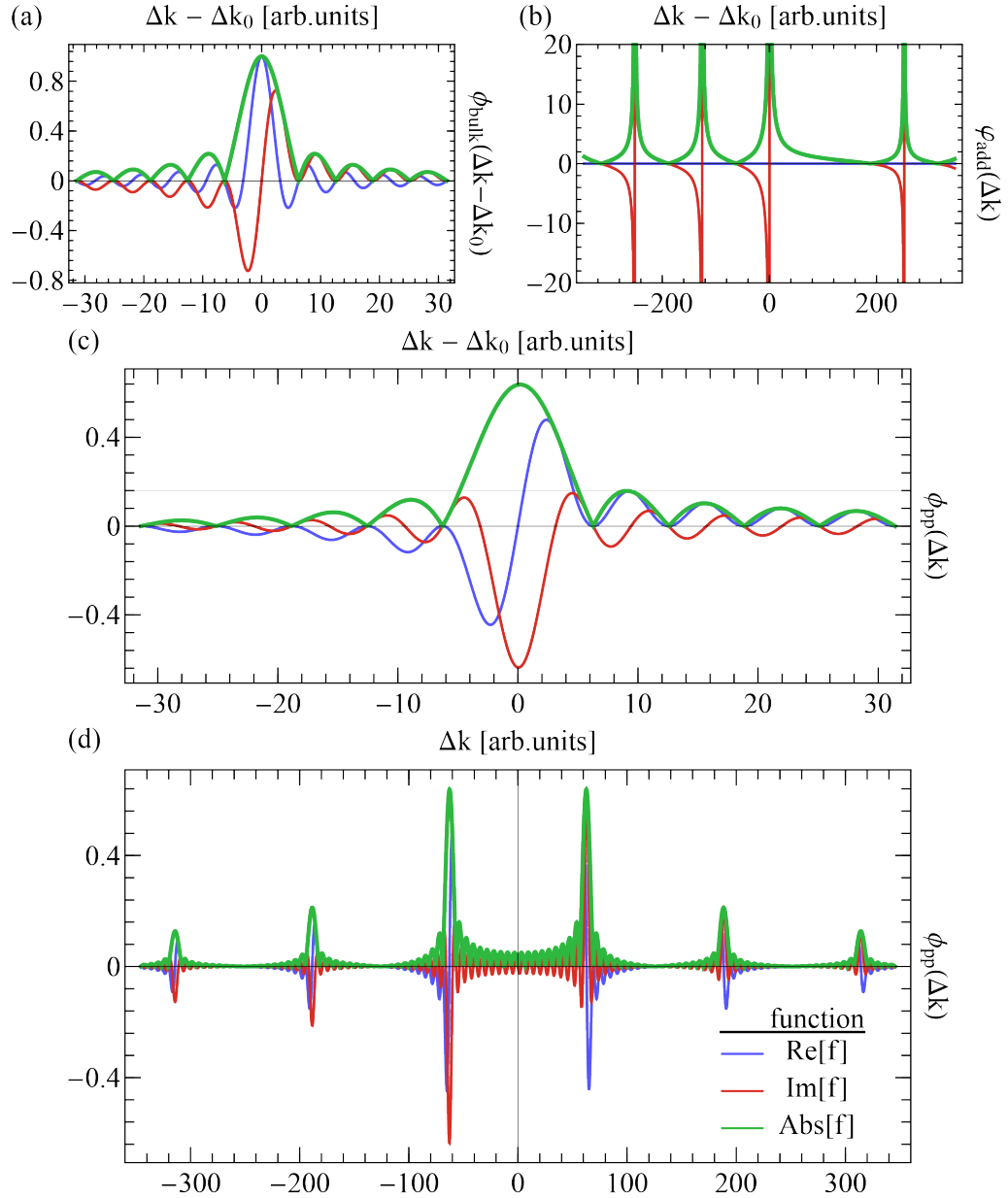


Figure 4.3: Phase-matching function in periodically-poled crystals.

The figure shows (a) the bulk component of the PMF, $\phi_{\text{bulk}}\left(\Delta k - \frac{\pi}{\ell_c}\right)$, and (b) the additional term, $\varphi_{\text{add}}(\Delta k)$. The overall PMF in (c), $\phi_{\text{pp}}(\Delta k)$, is slightly asymmetric: the side lobes on the right of the central peak are slightly higher than the ones on the left. The width of peaks and side lobes depends on the crystal length. The main PMF peak and the higher harmonics, typical of the periodic poling structure, are plotted over a larger Δk range in (d), highlighting the asymmetry. In all the plots, blue, red, and green lines correspond to the real part, imaginary part, and absolute value of the plotted function, respectively.

the momentum mismatch, Δk_{QPM} , that compensates for $\Delta k_0 \neq 0$ and enables the process—a practice that can be found in virtually any nonlinear optics textbook—is not precise because it doesn't take into account the reshaping of the sinc-shaped PMF.

When $\Delta k \rightarrow \Delta k_0 = \pi/\ell_c$, the additional term $|\varphi_{\text{add}}(\Delta k_0)| = 2/\pi$, meaning that the PMF function of a periodically-poled crystal grows linearly with the crystal length, but with a smaller slope with respect to the bulk counterpart: $\phi_{\text{pp}}(\Delta k) = \frac{2}{\pi}\phi_{\text{bulk}}(0)$. This is visualised in Figure 4.1.

By following the reverse reasoning to what we have discussed above, we can think of small variations in the domain widths (introduced via, e.g., temperature tuning of the crystal) as a new coherence length, ℓ_c^{new} , that will lead to a slightly different $\Delta k_0^{\text{new}} \neq \Delta k_0$. This corresponds to a shift of the PMF in the Δk space, allowing one to fine tune the frequencies of the emitted PDC photons, see Figure 4.4 for an example. Such fine tuning works not only for periodic poling, but also for crystals having custom poling structures, and it's crucial when the PDC photons need to exactly match a target frequency for, e.g., achieving perfect interference. In some materials the refractive index also changes significantly with temperature, and both

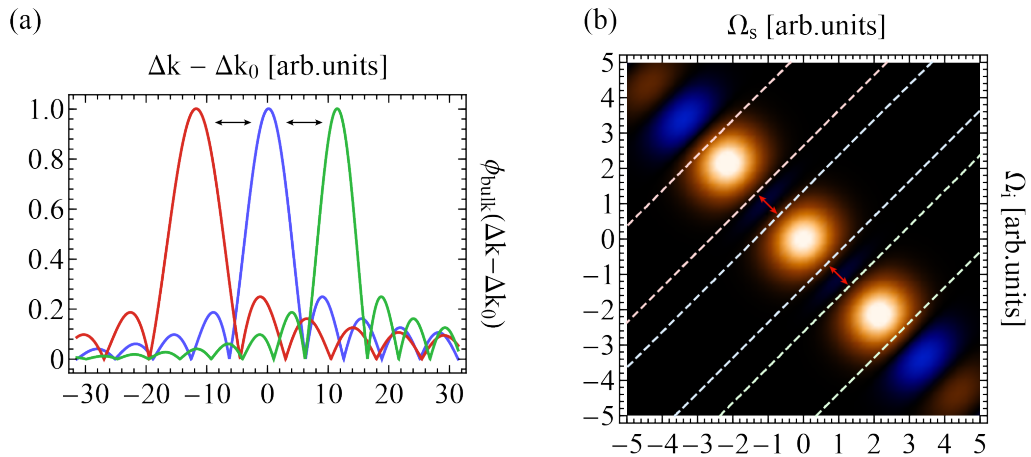


Figure 4.4: Fine-tuning of poled crystal. (a) The PMF can be shifted in Δk by slightly changing the individual domain width (e.g. by varying the temperature of the crystal). (b) In the (ω_s, ω_i) plane, this corresponds to a shift of the PMF parallelly to the Δk contours, enabling the generation of PDC pairs at slightly different frequencies.

domain widening and refractive index change play a role in shifting the PMF when varying the crystal temperature.

4.2 Tailoring the PMF: a brief overview

While periodic poling has been the first attempt to achieve quasi-phase-matching in nonlinear crystals, aperiodic poling is also possible. Domain engineering methods have long been studied in nonlinear optics, for example to compress or shape pulses in second-harmonic generation [114–119].

These techniques have only recently been adapted for single-photon generation, where usually the aim is to reduce the spectral correlations arising from a sinc-shaped PMF (see previous Chapter for details), by tailoring the PMF as a Gaussian. In this context, existing methods for non-trivial poling fall into two categories. Those that vary the domain widths of a predefined poling configuration [90], and those that keep the domain widths equal, but vary their relative orientations [89, 91, 92, 120]. Although such techniques still constrain $g(z)$ to values of $+1$ and -1 , the non-trivial structure makes it possible to shape the effective nonlinearity of the crystal and consequently to customise the PMF.

The first step towards overcoming this issue was proposed by Brańczyk *et al.*, who showed that the nonlinearity profile of the PDC crystal could be suitably shaped via domain engineering [89] in order to achieve a Gaussian PMF. Considering different poling orders along the crystal, it is indeed possible to approximate a Gaussian nonlinearity with rectangular-functions having different amplitudes (i.e. having different heights). Consequently, the corresponding PMF is also approximately Gaussian, as PMF and nonlinearity profile are related via Fourier transformation. A proof-of-principle experiment [89] showed a high overlap between the design and the experimentally determined PMF, proving the feasibility of tailored nonlinearities for this purpose.

This technique was subsequently refined leading to even better approximations to ideal nonlinearity profiles. In [84, 90] the domain-periodicity is restricted to twice the coherence length of the crystal, but the duty-cycle is customised along

the crystal. In [91] a simulated-annealing algorithm is used to randomly flip the domain-orientations (of fixed length ℓ_c) to minimise a cost function that quantifies the difference between the actual and the target PMFs. Similarly, machine-learning frameworks can be used in order to choose domain-orientations along the crystal [120]. Finally, Tambasco *et al.* [92] proposed a fully deterministic, computationally easy algorithm based on tracking the PMF along the crystal. As the results presented in this Chapter follow from [92], I'll discuss this technique in detail in the next Section.

All domain engineering methods mentioned above are intrinsically related to a coherence-length structure typical of periodically-poled crystals. In the following, I'll move beyond the coherence-length domain boundaries to allow for more fine-grained shaping of the nonlinearity. While in the long crystal limit most of these methods provide nearly separable JSAs, we'll see that for short crystal matched with femtosecond lasers, sub-coherence length domain engineering is required to achieve spectrally pure heralded-photons.

4.3 Novel nonlinearity engineering techniques

In the following, we describe two methods for tailoring the phase-matching function by engineering the nonlinearity of the crystal. Both use the method recently introduced by Tambasco *et al.* [92] as a starting point, but deviate from the method by allowing domain widths smaller than the crystal's coherence length. This move toward sub-coherence length structures allows much greater accuracy in tailoring the phase matching function.

In the first approach, we modify the method in Ref. [92] and use it for tailoring a crystal with fixed domain widths: we then shift the boundaries of the domains by means of a previously existing annealing method developed for classical applications in higher-harmonic generation [118, 119]. In the second approach, we generalise the algorithm in [92] to arbitrarily small, but constant domain widths (not necessarily equal to the coherence length) and to a complex target phase-matching function. Both methods lead to a better approximation of the desired PMF and to an enhanced

heralded single-photon purity, especially in the short-crystal regime.

4.3.1 Theory behind the scenes

We begin by discussing and expanding the ideas that lie at the basis of the method introduced by Tambasco *et al.* [92].

Let's start by defining a target phase-matching function: here we consider a Gaussian function, but the following reasoning is completely general and holds for (almost) arbitrary functions:

$$\phi_{\text{target}}(\Delta k) = e^{-\frac{1}{2}(\Delta k - \Delta k_0)^2 \sigma^2}, \quad (4.4)$$

where σ is a width parameter, and Δk_0 is the centre of the PMF, as discussed in the previous Sections for the periodically-poled case. An example of such PMF is given in [Figure 4.6\(a\)](#). A Fourier transformation of Eq. (4.4) leads to the corresponding crystal nonlinearity:

$$\begin{aligned} g_{\text{target}}(z) &= \mathcal{F}[\phi_{\text{target}}(\Delta k)] = \frac{1}{\sqrt{2}} \int_{-\infty}^{\infty} \phi_{\text{target}}(\Delta k) e^{i\Delta k z} d\Delta k \\ &= \frac{e^{-\frac{z^2}{2\sigma^2} + i\Delta k_0 z}}{\sigma}. \end{aligned} \quad (4.5)$$

Note that according to this definition, $g_{\text{target}}(z)$ is centred in $z = 0$, meaning that we are considering a crystal spanning $z \in \left[-\frac{L}{2}, \frac{L}{2}\right]$, as shown in [Figure 4.6\(b\)](#). By definition, a crystal having such nonlinearity would have the PMF described in Eq. (4.4).

The following step might seem counter-intuitive, as it looks like a step back with respect to what we already did. Indeed, we want to find an equation for a target PMF but, unlike Eq. (4.4), we need to know how the PMF behaves along the longitudinal direction of the crystal. To do so, we can perform an inverse Fourier transform of Eq. (4.5) using the beginning of the crystal, $-\frac{L}{2}$, and a generic position in the crystal, $z < \frac{L}{2}$, as boundaries of the integration. This leads to the following

equation:

$$\begin{aligned} \phi_{\text{track}}(\Delta k; z) &= \frac{1}{\sqrt{2}} \int_{-\frac{L}{2}}^z g_{\text{target}}(z') e^{-i\Delta k z'} dz' \\ &= \mathcal{N} \frac{\sqrt{\pi}}{2} e^{-\frac{1}{2}(\Delta k - \Delta k_0)^2 \sigma^2} \left[\text{erf} \left(\frac{z + i(\Delta k - \Delta k_0) \sigma^2}{\sqrt{2}\sigma} \right) - \text{erf} \left(\frac{-\frac{L}{2} + i(\Delta k - \Delta k_0) \sigma^2}{\sqrt{2}\sigma} \right) \right], \end{aligned} \quad (4.6)$$

where we introduce a rescaling constant \mathcal{N} that will be used in the next few lines. Eq. (4.6) describes the PMF as a function of both Δk and z , allowing us to understand how it changes along the crystal. This can be also visualised in a three-dimensional plot, as shown in Figure 4.5. When $z = \frac{L}{2}$, we are looking at the “overall PMF” of the nonlinear process, i.e. we are taking into account the whole crystal when Fourier transforming the nonlinearity. It’s important to notice that $\phi_{\text{track}}(\Delta k; L) \neq \phi_{\text{target}}(\Delta k)$, while the equality holds only in specific cases: this is because the crystal dimension is finite while, mathematically, the function describing its nonlinearity might non-vanish outside the crystal boundaries. More details are provided in a Section 4.3.2, where optimal parameters for engineering techniques will be discussed.

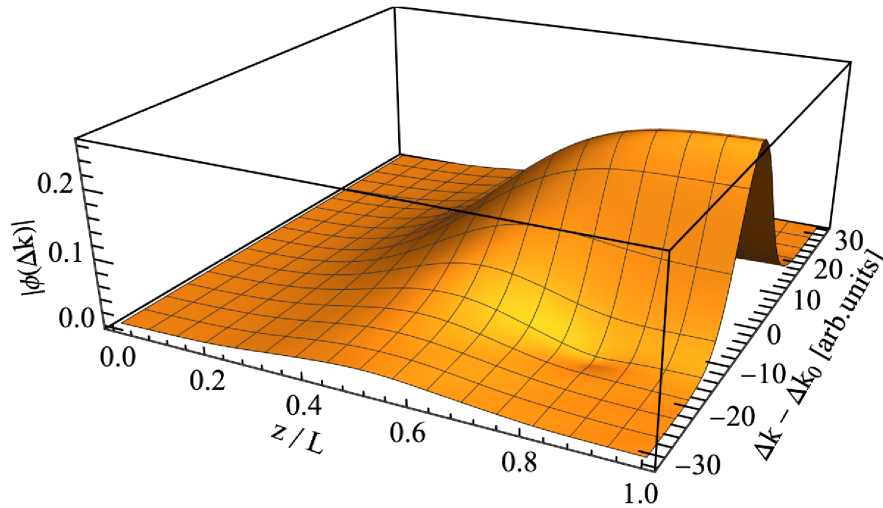


Figure 4.5: 3D phase-matching function. Three-dimensional plot of the PMF $\phi_{\text{track}}(\Delta k; z)$ in Eq. (4.6). As expected, the PMF is zero at the starting edge of the crystal, it then grows with a non-trivial behaviour along the longitudinal direction of the crystal, and finally assumes a Gaussian shape when the whole crystal is considered: $\phi_{\text{track}}(\Delta k; L)$.

We are now close to the finish line. For simplicity, we can translate Eq. (4.6) by $z \rightarrow z - \frac{L}{2}$ to shift the crystal in the region $z \in [0, L]$, and fix the phase mismatch to the quasi-phase-matching condition, $\Delta k = \Delta k_0$, obtaining:

$$\phi_{\text{track}}(\Delta k = \Delta k_0; z - \frac{L}{2}) = \mathcal{N} \sqrt{\frac{\pi}{2}} \left(\text{erf} \left[\frac{L}{2\sqrt{2}\sigma} \right] + \text{erf} \left[\frac{z - \frac{L}{2}}{\sqrt{2}\sigma} \right] \right), \quad (4.7)$$

where “erf” is the error function. This equation describes the PMF along the crystal at Δk_0 , as depicted in Figure 4.6(c).

Following the previous steps backwards, we find that a crystal having a given PMF at Δk_0 , as described in Eq. (4.7), corresponds to a crystal with a well-defined nonlinearity profile, the one in Eq. (4.5), that in turn corresponds to the target PMF in Eq. (4.4) shown in Figure 4.6(d). As mentioned above, this reasoning breaks when the starting parameters are not chosen carefully, as we’ll see in the next Section.

As a last step, we can now choose the domain orientations of a poled crystal so that the corresponding PMF at Δk_0 tracks the one in Eq. (4.7): $\phi_{\text{eff}}(\Delta k = \Delta k_0; z - \frac{L}{2}) \approx \phi_{\text{track}}(\Delta k = \Delta k_0; z - \frac{L}{2})$. However, in the previous Section we have seen how the maximum slope of the normalised PMF in a periodically-poled crystal is $2/\pi$, and we need to rescale the tracking function accordingly:

$$\mathcal{N} = \frac{2}{\pi} \left(\max \left[\frac{d}{dz} \phi_{\text{track}}(\Delta k) \right] \right)^{-1}, \quad (4.8)$$

where the derivative of the tracking function is:

$$\begin{aligned} \frac{d}{dz} \phi_{\text{track}}(\Delta k) &= \frac{e^{-\frac{(z - \frac{L}{2})^2}{2\sigma^2}}}{\sigma} \\ \max \left[\frac{d}{dz} \phi_{\text{track}}(\Delta k) \right] &= \frac{1}{\sigma}. \end{aligned} \quad (4.9)$$

The scaling factor is therefore $\mathcal{N} = \frac{2\sigma}{\pi}$, and the tracking PMF reads:

$$\phi_{\text{track}}(\Delta k = \Delta k_0; z - \frac{L}{2}) = \sqrt{\frac{2}{\pi}} \sigma \left(\text{erf} \left[\frac{L}{2\sqrt{2}\sigma} \right] + \text{erf} \left[\frac{z - \frac{L}{2}}{\sqrt{2}\sigma} \right] \right). \quad (4.10)$$

It's important to keep in mind that the scaling factor \mathcal{N} is not general, but only holds for a Gaussian target phase-matching function, as defined in Eq. (4.4). Whenever one is interested in different shapes of the PMF, the scaling factor should be calculated according to the target function.

We provide a visual representation of all the steps of the procedure described above in Figure 4.6.

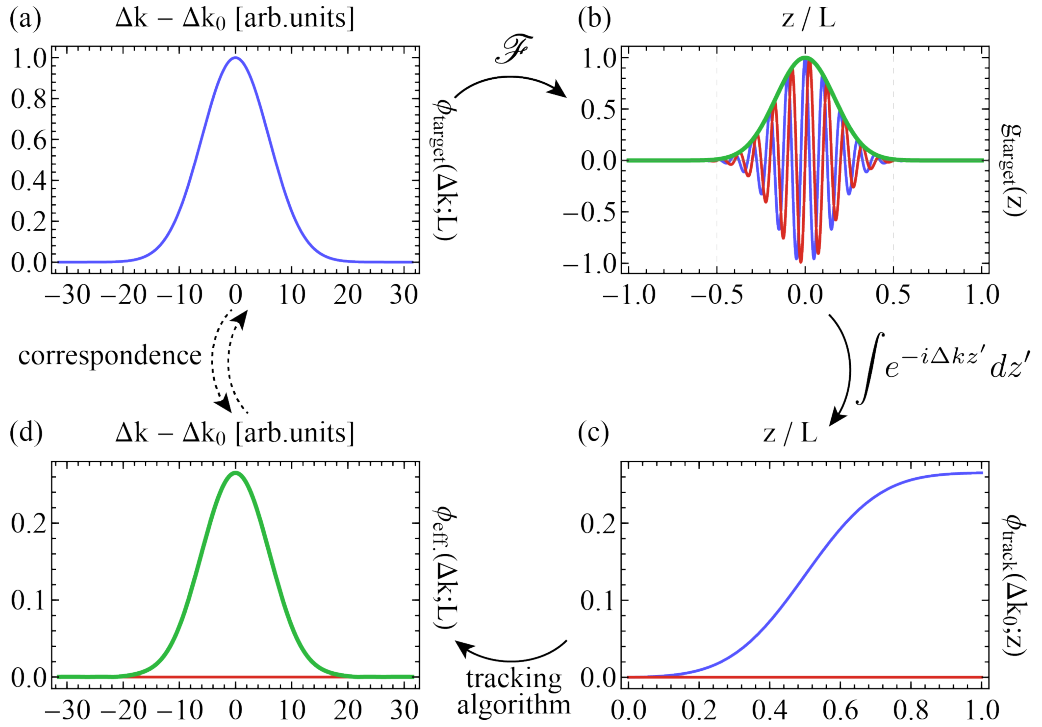


Figure 4.6: Nonlinearity engineering theory. A target PMF (a) corresponds to a nonlinearity profile (b) centred in 0. The vertical dashed lines correspond to the crystal edges. The absolute value of the nonlinearity (green line) is Gaussian shaped, as expected from the Fourier transform of a Gaussian, while the real and imaginary part of the nonlinearity (blue and red lines) oscillates with period $\frac{2\pi}{\Delta k_0} = 2\ell_c$: this is an effect of the target PMF being centred in $\Delta k_0 \neq 0$. Inverse Fourier transform, shifting of the z variable, and rescaling of the function lead to (c), i.e. the PMF that ought to be tracked by choosing an appropriate domain orientation pattern in the poled crystal. The effective PMF corresponding to the engineered crystal is finally shown in (d). In all the plots, blue, red, and green lines correspond to the real part, imaginary part, and absolute value of the plotted function, respectively.

4.3.2 Choosing the width parameter

Equations (4.4) and (4.5) represent the target phase-matching function and the corresponding crystal's nonlinearity. Both equations are parametrised by the width-term, σ , that will be chosen according to the pump-envelope function bandwidth (or vice versa) as discussed in the previous Chapter. However, the nonlinearity profile is also subject to an additional parameter, the crystal length L . Even if the Fourier transform of the target PMF leads to a function that might not be fully contained in the interval $[-\frac{L}{2}, \frac{L}{2}]$, meaning that the corresponding $g_{\text{target}}(z) \neq 0$ when $z < -\frac{L}{2}$ and $z > \frac{L}{2}$, this is physically impossible as the crystal cannot have non-zero nonlinearity outside its edges. This is captured by Eq. (4.6), which is in fact integrated from $z = -\frac{L}{2}$ to a generic position in the crystal $z < \frac{L}{2}$. Whenever $g_{\text{target}}(z)$ is non-zero outside the crystal boundaries, the effective nonlinearity of the crystal abruptly drops to 0 with a step function, giving rise to fluctuations in the Fourier space, i.e. to the side lobes near the main PMF peak.

To understand the importance of a correct choice of the parameter σ , let's rewrite it as a function of the crystal length: $\sigma = \frac{L}{n_\sigma}$. We can therefore rewrite $g_{\text{target}}(z)$ in Eq. (4.5) as:

$$g_{\text{target}}(z; n_\sigma) = \frac{n_\sigma e^{-\frac{z^2 n_\sigma^2}{2L^2} + i\Delta k_0 z}}{L}. \quad (4.11)$$

We can now calculate the area of Eq. (4.11) as a function of the parameter n_σ , both inside the crystal (i.e. the area of the effective nonlinearity):

$$A_{\text{in}}(n_\sigma) = \int_{-\frac{L}{2}}^{\frac{L}{2}} |g_{\text{target}}(z; n_\sigma)| dz = \sqrt{2\pi} \operatorname{erf} \left[\frac{n_\sigma}{2\sqrt{2}} \right], \quad (4.12)$$

and outside the crystal:

$$A_{\text{out}}(n_\sigma) = \int_{-\infty}^{-\frac{L}{2}} |g_{\text{target}}(z; n_\sigma)| dz = \sqrt{2\pi} \operatorname{erfc} \left[\frac{n_\sigma}{2\sqrt{2}} \right], \quad (4.13)$$

where “erfc” is the complementary error function. Finally, we calculate the ratio of

the two areas, obtaining:

$$A_{\text{ratio}}(n_\sigma) = \frac{A_{\text{out}}(n_\sigma)}{A_{\text{in}}(n_\sigma)} = \frac{1}{\text{erf}\left[\frac{n_\sigma}{2\sqrt{2}}\right]} - 1, \quad (4.14)$$

that we plot in [Figure 4.7](#). We see that reasonably small values of $A_{\text{ratio}}(n_\sigma)$ are achieved when $n_\sigma \gtrsim 5$, where the ratio between the areas gets smaller than 1%.

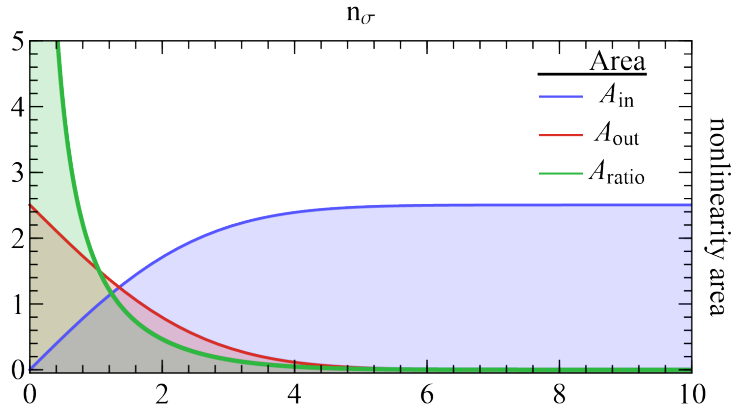


Figure 4.7: Area of the nonlinearity profile. This figure shows the portion of $g_{\text{target}}(z)$ area contained in the crystal (blue), outside of the crystal (red), and the ratio between the two (green). The sum of A_{in} and A_{out} (i.e. the total area) is normalised to $\sqrt{2\pi}$ according to Eq. (4.5).

In light of this discussion, one might think that the optimal parameter choice is a very large n_σ . However, the collateral effect of taking large n_σ values is that the overall nonlinearity of the crystal decreases, meaning that the effective “strength” of the process will be lower: in the case of parametric down-conversion, this means that the source will produce fewer photon pairs. We see this tradeoff in [Figure 4.8](#), where we consider the case of a bulk crystal compared to a periodically-poled one, and to engineered crystals with different width parameters. As we have already seen, bulk crystals have the higher nonlinearity, followed by periodically-poled ones. The PMF in tailored crystals gets more Gaussian as n_σ increases, as the whole g_{target} fits in the crystal’s boundaries and the side lobes get suppressed. However, the PMF’s peak decreases, meaning that there is a tradeoff between PMF “Gaussianity” and amplitude. As mentioned above, $n_\sigma \approx 5$ seems to be a happy medium. Whenever one is not limited in the crystal length, choosing larger L and proportionally larger n_σ is generally the best practise, as it guarantees a better approximation of the Gaussian

function: however, crystal length is often limited for manufacturing limits or by the

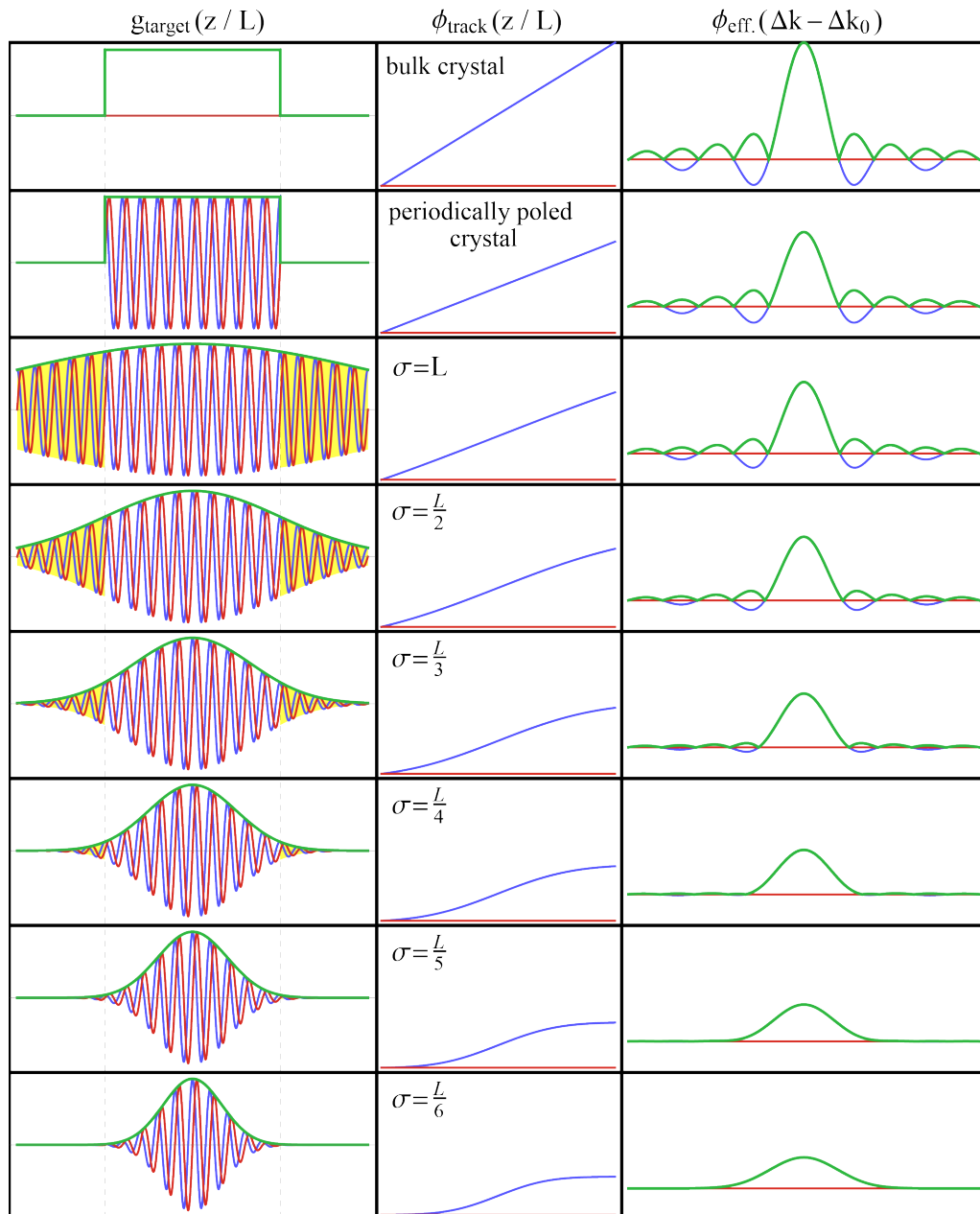


Figure 4.8: Effects of width parameter in nonlinearity engineered crystals. This figure shows a comparison between bulk crystal, periodically-poled crystal, and engineered crystals at different σ values. The real, imaginary parts, and absolute value of the functions are plotted in blue, red, and green, respectively. The vertical dashed lines in the nonlinearity plot represent the crystal edges, while in yellow is highlighted the amount of “artificial” nonlinearity outside the crystal. The PMFs $\phi_{\text{eff.}}$ represented in the third column correspond to an ideal case, where custom poling approximates $\phi_{\text{track.}}$ infinitely well: effects of non-ideal tracking will be discussed in the following Sections.

experimental setup (e.g. when short crystals are needed for matching particular focusing conditions) and therefore the above discussion provides a guideline for an optimal choice of parameters.

4.3.3 “Two-domain blocks” tracking

So far, we have discussed the main idea of nonlinearity engineering, as depicted in [Figure 4.6](#). What is still missing is an algorithm that chooses the domain pattern in order to track ϕ_{track} as defined in Eq. (4.10). For simplicity of notation, in the following we will refer to a ferroelectric domain pointing up by “UP” and to a domain down by “DOWN”.

Tambasco *et al.* [92] originally proposed what we will call here “*two-domain blocks*” tracking method. This method involves three different building blocks which are chosen to track the target function: an UP-UP block leaves the average phase-matching function at Δk_0 unchanged, an UP-DOWN block increases the average $\phi_{\text{eff}}(\Delta k_0; z)$ by a factor $\Delta\phi = \frac{2}{\pi}\ell_c$, while DOWN-UP block decreases it by $-\Delta\phi = -\frac{2}{\pi}\ell_c$. These three possible configurations are graphically represented in [Figure 4.9](#) in green, red, and yellow, respectively.

One can therefore define an error function that will determine which block to use at each step of algorithm:

$$e(z + 2\ell_c) = \phi_{\text{track}}(\Delta k_0; z + 2\ell_c) - \phi_{\text{eff}}(\Delta k_0; z), \quad (4.15)$$

and choose the appropriate block according to the following rules:

- if $-\Delta\phi \leq e(z + 2\ell_c) \leq \Delta\phi$: place an UP-UP block in z
- if $\Delta\phi < e(z + 2\ell_c)$: place an UP-DOWN block in z
- if $-\Delta\phi > e(z + 2\ell_c)$: place a DOWN-UP block in z

[Figure 4.9](#) shows two examples of this tracking algorithm: a Gaussian target PMF (as discuss above) and antisymmetric PMF function, that we’ll meet again in [Chapter 6](#). Being tied to the two-domains blocks means that the domain structure

is not fine-grained enough to track the target function with high accuracy. This translates in sub-optimal results in the case of short crystals, as we'll discuss in [Section 4.4](#).

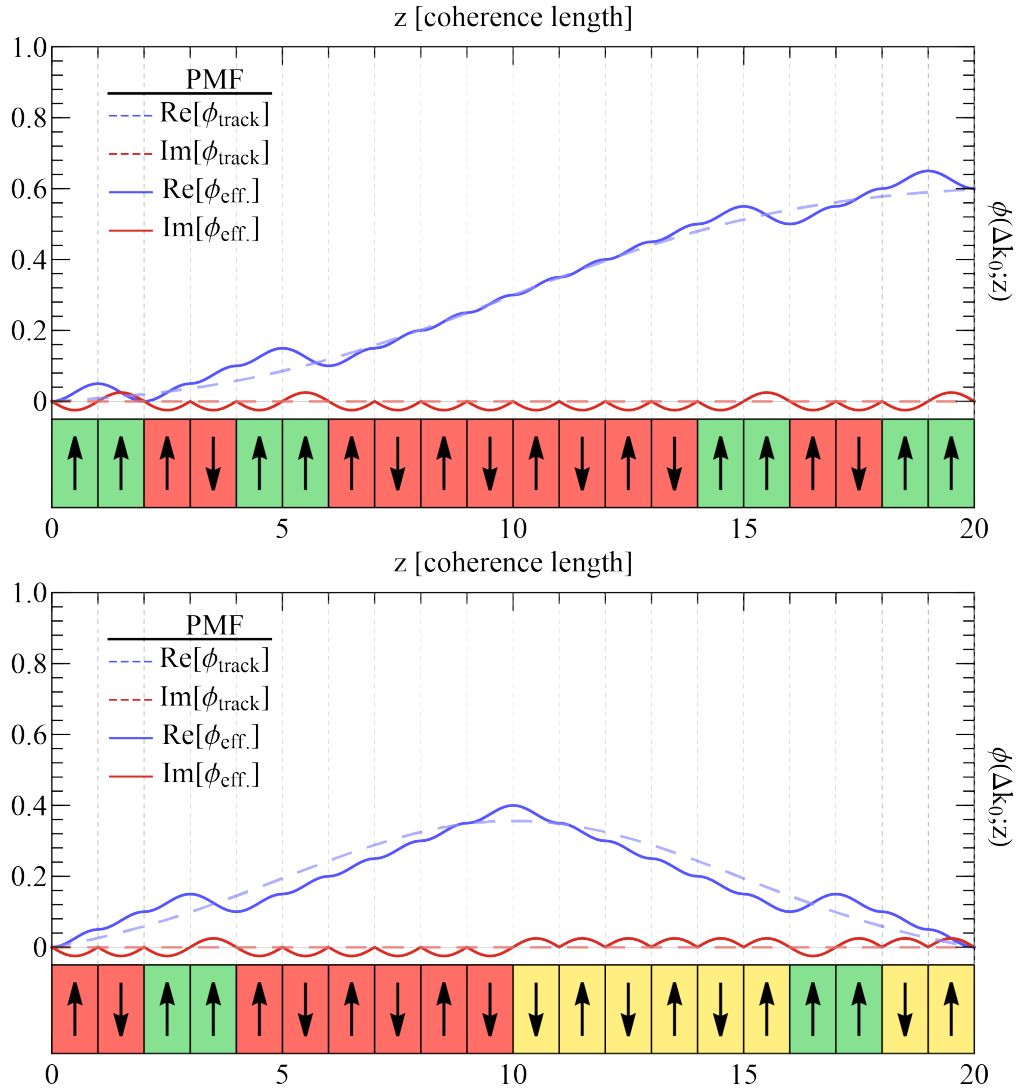


Figure 4.9: “Two-domain blocks” method. The two example target functions are tracked by piecing together three different types of blocks: UP-UP (green), that keeps $\phi_{\text{eff.}}$ approximately constant, UP-DOWN (red), that makes $\phi_{\text{eff.}}$ grow, DOWN-UP (yellow), that makes $\phi_{\text{eff.}}$ decrease. Such rough discretisation doesn't allow $\phi_{\text{eff.}}$ to track the targets ϕ_{track} with high accuracy, especially when the total number of domains is very small.

For comparison, in [Figure 4.10](#) we show the domain structure and corresponding $\phi_{\text{eff.}}(\Delta k_0; z)$ for the duty-cycle modulation technique.

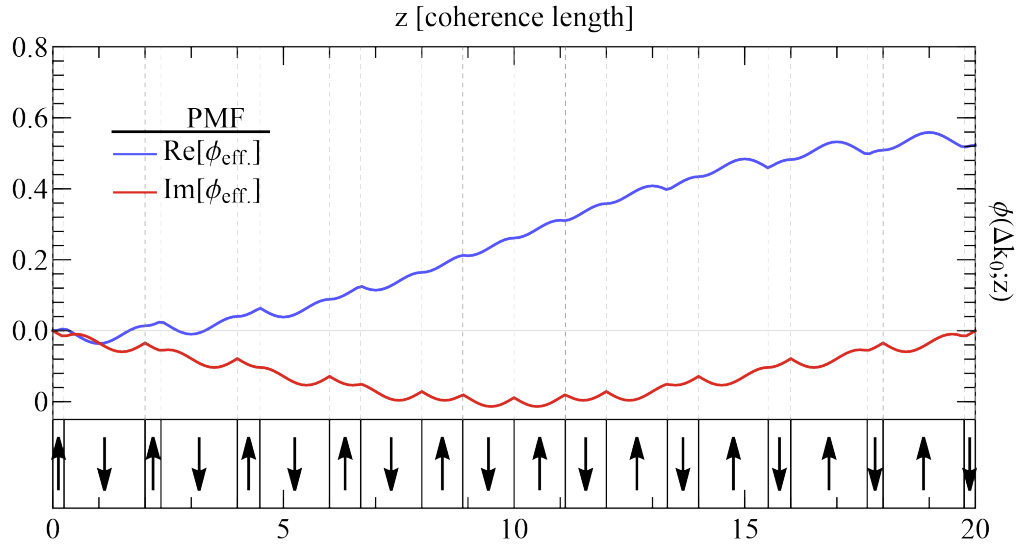


Figure 4.10: Duty-cycle modulation. Here the domain orientation is periodic and blocks of two adjacent domains have fixed width $2\ell_c$. However, the duty-cycle changes along the crystal, meaning that every other domain wall is allowed to shift. Differently from the schemes discussed above, in this method the imaginary part of ϕ_{eff} doesn't stay close to 0 along the whole crystal: however, it converges back to 0 at the end of the crystal.

4.3.4 “One-domain blocks” tracking

Tambasco *et al.* framed their algorithm in terms of two-domain blocks to ensure that the inverted regions were of equal width: this is not a necessary requirement—one might just as well choose each individual domain's orientation. We therefore consider each domain in the grating with fixed width, $w = \ell_c$, and we define the “domain-by-domain” error function:

$$e(z + \ell_c) = \phi_{\text{track}}(\Delta k_0; z + \ell_c) - \phi_{\text{eff}}(\Delta k_0; z), \quad (4.16)$$

which quantifies the difference between the generated ϕ_{eff} at a certain position z and the target ϕ_{track} at $z + \ell_c$ (i.e. after one domain). The decision to flip (or not flip) a given domain is determined by which option gives a closer approximation to the target PMF at that point in the crystal, according to the following algorithm:

- if $e(z + \ell_c) \geq 0$ and $\phi_{\text{track}}(\Delta k_0; z) \geq \phi_{\text{track}}(\Delta k_0; z - \ell_c)$ (i.e. in the previous domain ϕ_{eff} was increasing), flip the domain orientation

with respect to the previous domain: ϕ_{eff} will continue to increase;

- if $e(z + \ell_c) \geq 0$ and $\phi_{\text{track}}(\Delta k_0; z) \leq \phi_{\text{track}}(\Delta k_0; z - \ell_c)$ (i.e. in the previous domain ϕ_{eff} was decreasing), keep the same orientation of the previous domain: ϕ_{eff} will start increasing;
- if $e(z + \ell_c) < 0$ and $\phi_{\text{track}}(\Delta k_0; z) \geq \phi_{\text{track}}(\Delta k_0; z - \ell_c)$, keep the same orientation of the previous domain: ϕ_{eff} will start decreasing;
- if $e(z + \ell_c) < 0$ and $\phi_{\text{track}}(\Delta k_0; z) \leq \phi_{\text{track}}(\Delta k_0; z - \ell_c)$, flip the domain orientation with respect to the previous domain: ϕ_{eff} will continue to decrease.

We show two examples of the “one-domain blocks” method in [Figure 4.11](#), considering the same target PMFs of [Figure 4.9](#). Thanks to the ability of choosing each domain orientation individually, the algorithm allows for higher flexibility, and the effective PMFs at Δk_0 stay closer to the target functions with respect to the “two-domain blocks” method, leading to higher purities—see [Section 4.4](#).

4.3.5 Simulated annealing algorithm

The previous methods consider the case of a poled crystal with constant domain width, allowing an easy approach to the problem. However, there is no evidence to suggest that a fixed-domain structure leads to an optimal result, and it is reasonable to ask if it is possible to improve the PMF shape by slightly varying the width of each domain. To this aim, we use an adapted version of the simulated annealing algorithm introduced by Reid *et al.* in [118, 119] to introduce domain-width variation to a pre-defined poling pattern. Annealing algorithms are commonly exploited for finding a global minimum of a given function dependent on multiple parameters [121, 122] by slightly perturbing the system from a suitable starting point, calculating the relative cost function (commonly called energy in analogy with the internal energy in a physical annealing process) and accepting the change with some probability—the higher the energy the lower is the probability of accepting the new configuration. These kinds of algorithms are probabilistic and may require several runs to get an

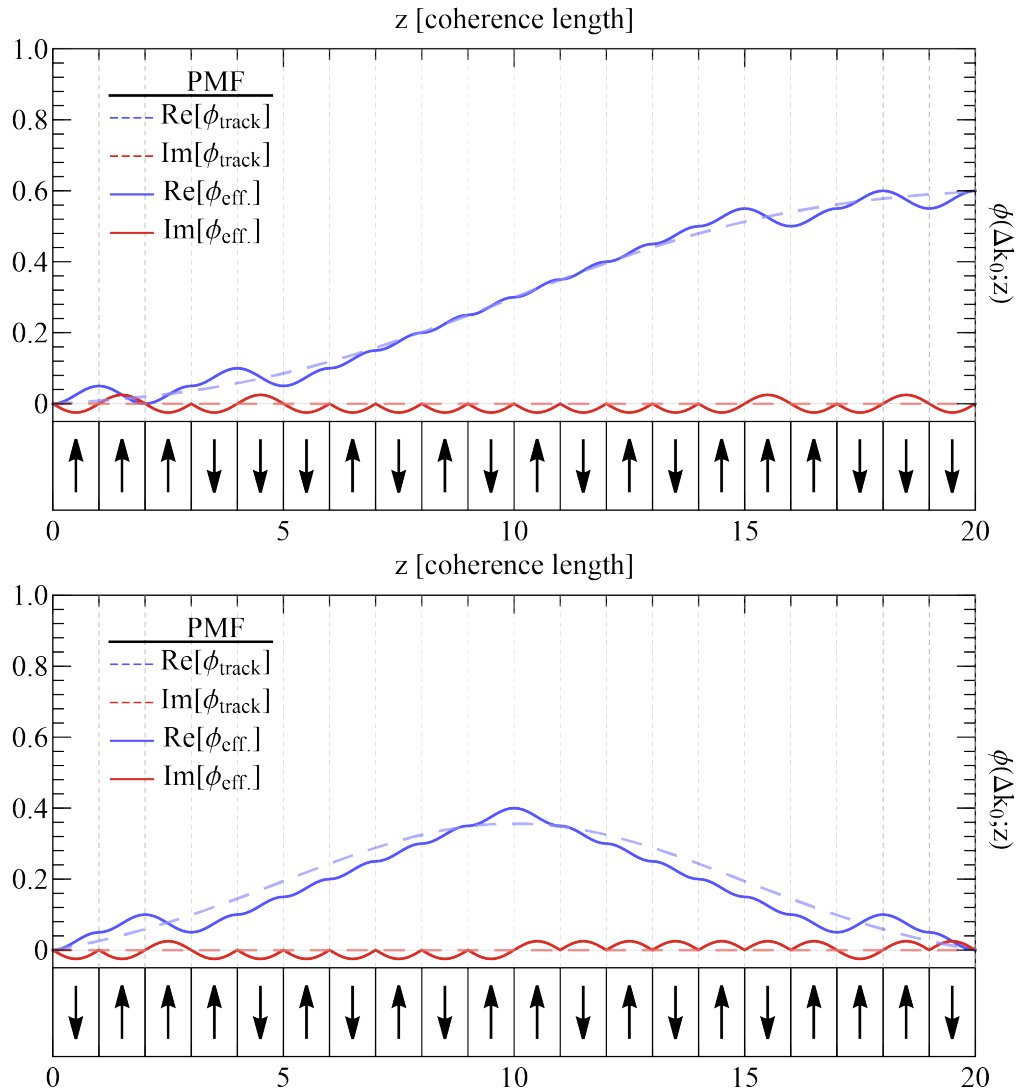


Figure 4.11: “One-domain blocks” method. Here the each domain orientation is chosen individually to achieve higher accuracy in tracking the targets ϕ_{track} , and we can already see an improvement respect to the “two-domain blocks” method in [Figure 4.9](#), especially in tracking the top function.

optimal result.

Given a target PMF $\phi_{\text{target}}(\Delta k)$, we first find the initial configuration of domain orientations by means of the “one-domain blocks” method described above. Adjacent domains with the same orientation are grouped together into bigger blocks. Secondly, we define a starting temperature T and a temperature step ΔT for the annealing algorithm: we found that a value of $T \in \{0.1; 10\}$ and $\Delta T = T/100000$ works well for the configurations that we tested. The width of each block is then perturbed by up to 1% and the relative PMF is computed. The perturbation value

1% is empirically determined: too small values would lead to slow convergence of the algorithm, while if the perturbation is too big the algorithm is unstable and doesn't converge. It is then possible to find the system energy defined as

$$E = \left(\sum_{\Delta k} [|\phi_{\text{target}}(\Delta k)| - |\phi_{\text{annealing}}(\Delta k)|]^2 \right)^{1/2}. \quad (4.17)$$

If this energy is smaller than the minimum energy recorded so far, the new domain widths are recorded as the best configuration and they are accepted with a probability of $\exp(-E/T)$ (even if they are not the optimal configuration). Finally, the temperature is decreased by ΔT and the algorithm is repeated until the energy becomes smaller than a chosen threshold or the temperature reaches 0. A block diagram of the algorithm is shown in [Figure 4.12](#), and is described below:

1. Define target phase-matching function, $\phi_{\text{target}}(\Delta k)$, and initial domain configuration.
2. Group together all the adjacent domains in bigger blocks having the same orientation.
3. Define algorithm temperature T , temperature step ΔT and energy threshold E_t (used for accepting a given configuration as the optimal one).
4. Compute the energy for the initial configuration and store it in the variable E_{min} .
5. Apply a random perturbation to the blocks' width of up to 1% of their current width.
6. Calculate the new phase-matching function.
7. Compute the corresponding energy E .
8. If $E < E_{\text{min}}$, accept the current block configuration as the best configuration, update $E_{\text{min}} = E$ and go to step 11.
9. Else if $E > E_{\text{min}}$, accept the new configuration with probability $\exp[-E/T]$.
10. If the new configuration is not accepted, return to the best configuration and decrement T by ΔT .
11. Iterate 5 to 10 until $E_{\text{min}} < E_t$ or $T = 0$.

This algorithm is computationally demanding and may require a few hours for converging to a solution for a crystal having a large number of domains.

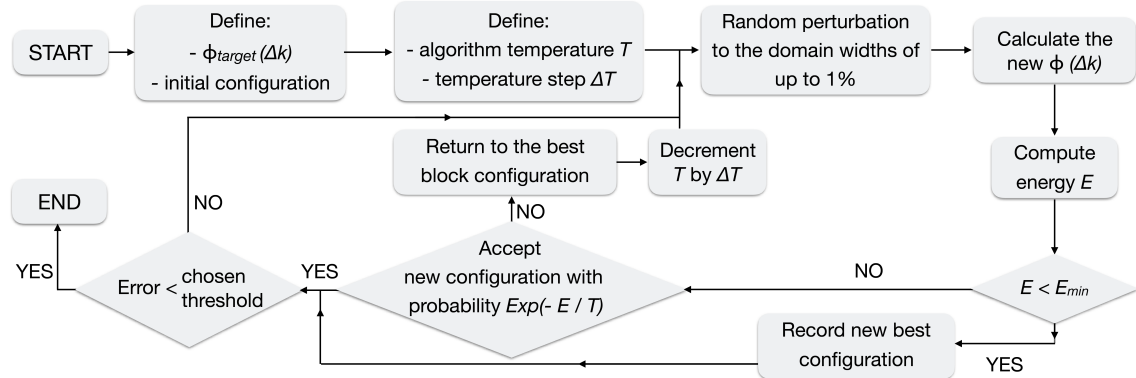


Figure 4.12: Simulated annealing algorithm. Block diagram of the algorithm.

One may think to directly use the annealing procedure without using a pre-processed initial configuration as a seed: however, our annealing algorithm doesn't allow the flipping of domain orientations, and thus a near-optimal result cannot be obtained without a suitable starting configuration. Moreover, it's reasonable to think that the “one-domain blocks” method discussed above provides a good initial domain orientation because we know that the corresponding PMF is already approximating the target reasonably well.

When we first developed the simulated annealing algorithm, we obtained some improvement in the heralded-photon purity of the order of 1% (or slightly less) with respect to the “one-domain blocks” method. However, after a thorough study of the domain engineering techniques and having obtained a better understanding of the parameter choice discussed in [Section 4.3.2](#), we realised that simulated annealing doesn't provide a significant improvement in the PMF quality (generally less than 0.1%). Moreover, in light of the following Section—where a more sophisticated algorithm is proposed and implemented—I believe that there is no reason in exploring this technique in more detail. It's also worth noting that better algorithms, based e.g. on stochastic gradient descent, can perform multiparameter minimisations in a much more efficient way [120], rendering our simulated annealing approach obsolete.

4.3.6 Sub-coherence length domains

Until now we have considered domain widths equal to the coherence length, ℓ_c , with small variations of this configuration. In this Section, we will see that pushing the algorithm beyond this constraint by allowing a finer discretisation of the domain-structure leads to an even better approximation of the target function.

Analogously to what we have seen for the periodically-poled crystal in Eq. (4.3), we consider the PMF at the end of the m -th domain:

$$\begin{aligned}\phi_{\text{cp}}(\Delta k; \{s_n\}_{n=1}^m) &= \sum_{n=1}^m s_n \int_{(n-1)w}^{nw} e^{i\Delta k z} dz \\ &= \sum_{n=1}^m s_n \frac{i \left(e^{i\Delta k(n-1)w} - e^{i\Delta k n w} \right)}{\Delta k} \\ &= \frac{i \left(e^{-i\Delta k w} - 1 \right)}{\Delta k} \sum_{n=1}^m s_n e^{i\Delta k n w},\end{aligned}\tag{4.18}$$

where ‘‘cp’’ stands for custom poling, w is the domain width and $s_n = \pm 1$ is the orientation of the n -th domain. Note that $\phi_{\text{cp}}(\Delta k; \{s_n\}_{n=1}^m)$ depends on the orientations of all domains that come before it (but not those that come after). Calculating the PMF value at an arbitrary point in the crystal, z , and not necessarily at the end of a given domain, is as simple as adding to Eq. (4.18) an additional piece that takes into account the contribution of the portion of crystal after the last crystal wall:

$$\begin{aligned}\phi_{\text{cp}}(\Delta k; z) &= \phi_{\text{cp}}(\Delta k; \{s_n\}_{n=1}^m) + \int_{nw}^z e^{i\Delta k z} dz \\ &\text{with: } m = \text{Floor} \left[\frac{z}{w} \right].\end{aligned}\tag{4.19}$$

As we have discussed before, for domain widths equal to the coherence length, the imaginary part of the PMF is always zero at the domain boundaries, and therefore it always oscillates about zero. If the domain widths differ from the coherence length, however, the phase might get flipped at a place where the imaginary part is non-zero, providing control over both the real and imaginary parts of the phase-matching function. With this modification, it is now possible to approximate complex PMFs.

To account for the complex nature of the PMF, we define a cost function that

we want to minimise at each domain:

$$e_m(\{s_n\}_{n=1}^m) = |\phi_{\text{track}}(\Delta k_0; mw) - \phi_{\text{cp}}(\Delta k; \{s_n\}_{n=1}^m)|. \quad (4.20)$$

Since the target function for tailoring a Gaussian PMF has a zero imaginary part (see Eq. (4.10)), the algorithm with the new cost function will force the imaginary component close to zero. However, different target functions might have a non-zero imaginary part, and the error function in Eq. (4.20) would also include these cases.

The algorithm can be summarised as follows. First, define a domain width w , the coherence length ℓ_c , and the number of domains N . Note that the total crystal length will therefore be $L = Nw$. Then, starting from a crystal having just one domain, compute the cost function e_{UP} for the case where a domain UP is added and the cost function e_{DOWN} when a domain DOWN is added. Next, compare the two cost functions: if $e_{\text{UP}} < e_{\text{DOWN}}$ keep the configuration where the UP domain was added, otherwise keep the configuration where the DOWN domain was added. Repeat for each subsequent domain. Below the step-by-step procedure:

1. Define complex ϕ_{track} .
2. Define parameters w , ℓ_c , and the number of domains N .
3. Initialize an empty list $S = \{\}$ for storing the domain orientation.
4. Define $m = 1$.
5. Create two trial lists that are identical except for the last element:
 $S_{\text{UP}} = S + \{\text{UP}\}$ and $S_{\text{DOWN}} = S + \{\text{DOWN}\}$
6. Compute cost functions for the two trial lists:
 $e_{\text{UP}} = e_m(S_{\text{UP}})$ and $e_{\text{DOWN}} = e_m(S_{\text{DOWN}})$.
7. If $e_{\text{UP}} < e_{\text{DOWN}}$, update $S = S_{\text{UP}}$.
8. Else if $e_{\text{UP}} > e_{\text{DOWN}}$, update $S = S_{\text{DOWN}}$.
9. Update $m = m + 1$.
10. Iterate Steps 4 to 9 until $m = N + 1$.

With this technique, it is possible to generate a wide range of PMF shapes, as long as the corresponding ϕ_{track} does not vary too quickly. When the domain width is equal to the coherence length, $w = \ell_c$, this algorithm corresponds to the

“one-domain blocks” method.

We show two examples of this algorithm in action in [Figure 4.13](#), considering the same target PMFs of [Figure 4.9](#) and [4.11](#). Using small domains without being bounded to ℓ_c -long domains means that this algorithm can achieve arbitrarily-high accuracy in tracking ϕ_{track} , corresponding in better approximations of the target

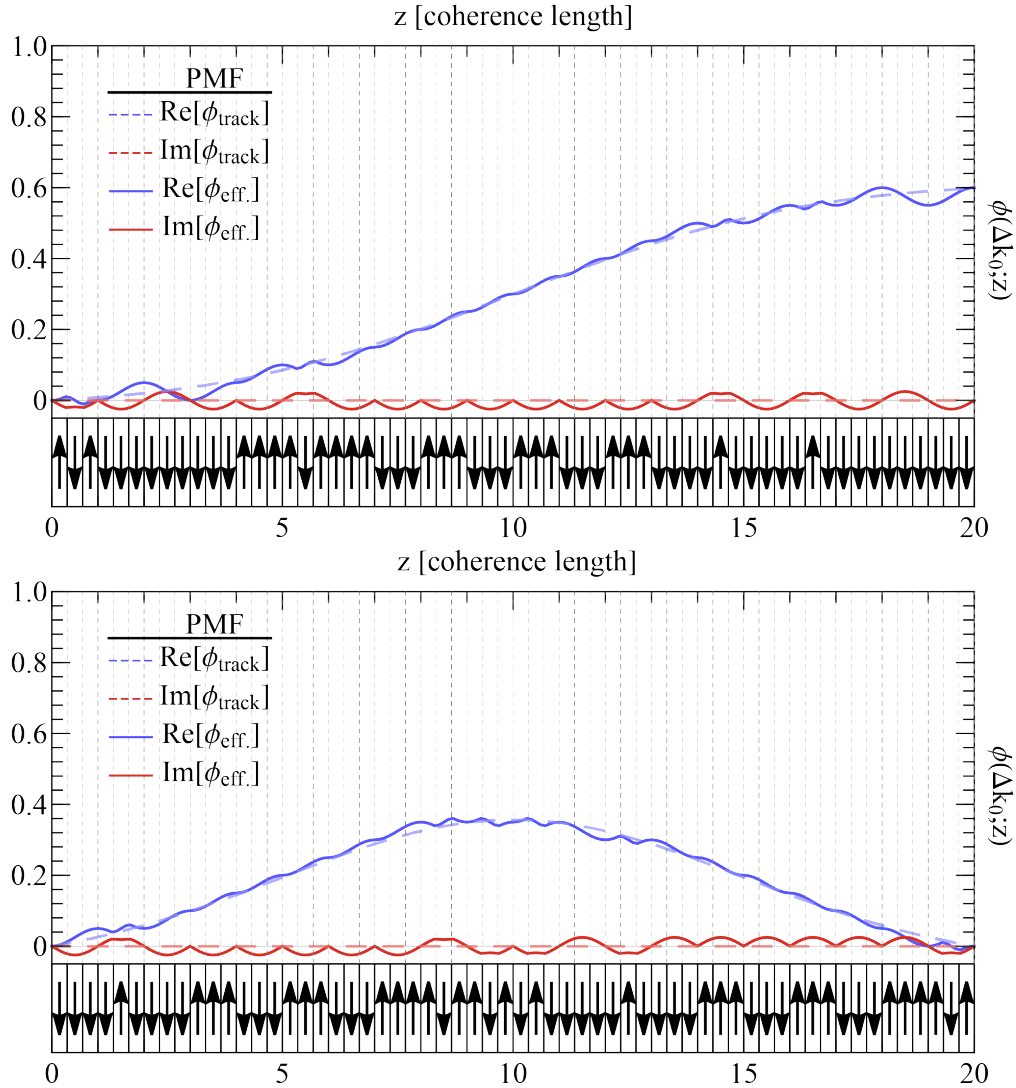


Figure 4.13: Sub-coherence length poling. As in “one-domain blocks” method, here the each domain orientation is chosen individually: however, the domains can be arbitrarily small. In this example, we choose a domain width of $w = \ell_c/3$, that already provide a significant improvement in accuracy respect to “one-domain blocks” and “two-domain blocks” methods shown in [Figure 4.9](#) and [4.11](#). We can see that the imaginary part of ϕ_{eff} might be slightly above or below 0 at the domain boundaries: however, the algorithm actively keeps this value small, unless one wants to track a complex function with non-zero imaginary part.

PMF.

The choice of a correct domain width should be done on a case-by-case basis. If a crystal is “long” respect to the coherence length, the ratio ℓ_c/L is small, and ϕ_{track} can be tracked efficiently regardless of the specific choice of w (even if $w = \ell_c$ and the “one-domain blocks” method is used). However, when the crystal is “short”, smaller domain widths need to be considered to approximate correctly the target function. We show an example in Figure 4.14, where a crystal long $L = 20\ell_c$ is considered. When $w = \ell_c$, the crystal only has 20 domains, and the algorithm can’t approximate the target function sufficiently well. Decreasing the domain size down to $w \leq \ell_c/15$, allows one to approximate the wanted PMF with increasing

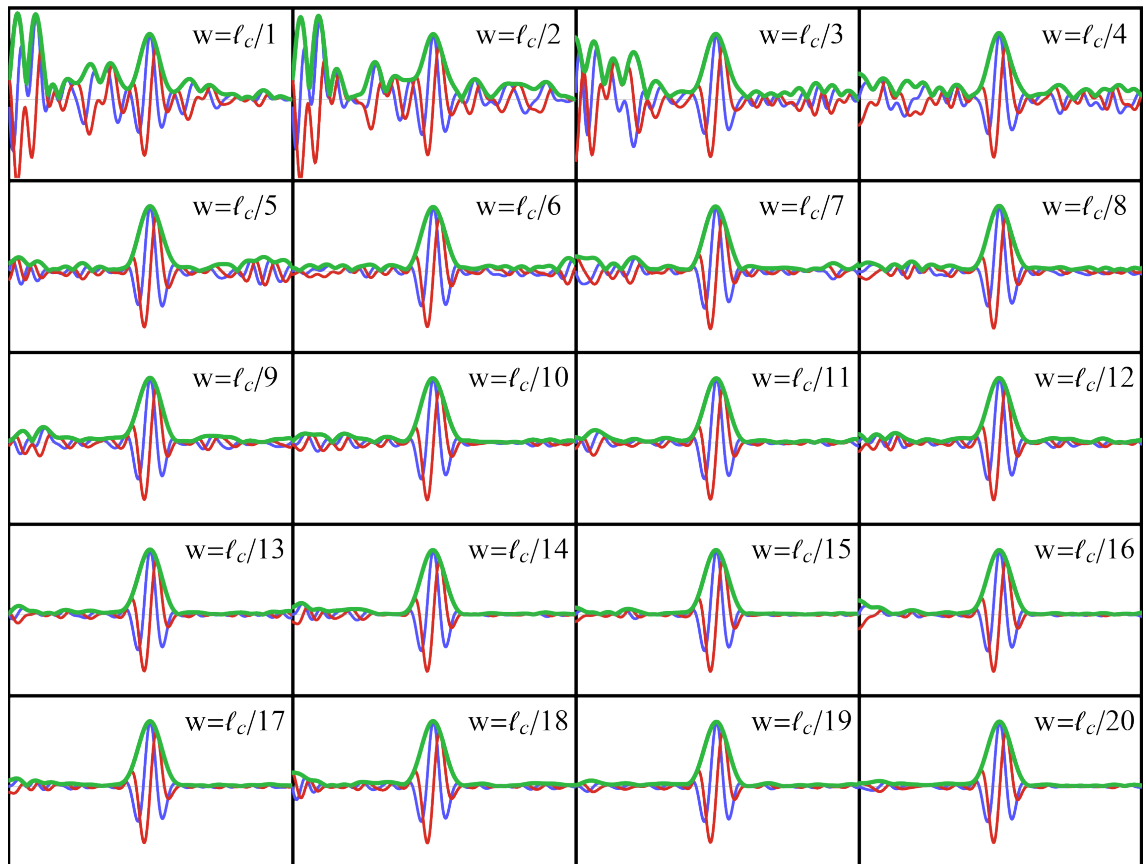


Figure 4.14: Effects of domain width on very short crystals. When very short crystals are considered, tracking the target PMF can be tricky. Here we show how the choice of the domain width in sub-coherence length poling algorithm affects the resulting PMF for a crystal having only 20 domains. $w = \ell_c/1$ corresponds to the “one-domain blocks” method, and it’s not fine-grained enough to correctly shape the PMF. Acceptable results are achieved when $w < \ell_c/15$.

accuracy. Obviously, there are physical limits that might prevent one from being able to fabricate crystals with such a small poling period, and this depends on the material as well as on the target frequencies. For example, type-II PDC in KTP for producing telecom wavelength photons (as discussed later on in this Thesis) requires a poling period of $\sim 46 \mu\text{m}$: in this case, a domain size of $w \leq \ell_c/20$ would correspond to $\sim 1 \mu\text{m}$, which is achievable with the current fabrication capabilities. However, producing 800 nm photons in the same material would require a poling period of $\sim 10 \mu\text{m}$, making a domain size of $w \leq \ell_c/20$ infeasible.

4.4 Engineering techniques comparison

In this Section we compare the performances of different poling methods. [Figure 4.15](#) shows a comparison of the PMFs for periodic poling, duty-cycle modulation, two- and one-domain blocks methods, and sub-coherence length poling for a crystal of length $L = 100 \ell_c$. The width parameter for the tracking-based algorithms is chosen to be $\sigma = L/5$, and the domain width for the sub-coherence length technique is taken as ten times smaller than the coherence length: $w = \ell/10$. We can see that duty-cycle modulation is not able to completely suppress the PMF side lobes, while other methods do a better job in approximating a Gaussian PMF, with the sub-coherence length method achieving the best result.

We can quantify this by looking at the heralded-photon purity in [Figure 4.16](#), where we numerically simulate 125×125 JSA matrices with spectral ranges 10 and 40 times larger than the PDC photon bandwidths. We find that for crystals longer than $200 \ell_c$, all methods converge to a fixed value of the purity, as shown in [Table 4.1](#).

poling	purity (larger spectral range)	purity (smaller spectral range)
periodic	0.817	0.870
duty-cycle modulation	0.969	0.978
two-domain blocks	0.995	0.999
one-domain blocks	0.998	1.000
sub-coherence length	0.999	1.000

Table 4.1: Asymptotic purities for crystal longer than 200 coherence lengths.

Two-, one-domain blocks and sub-coherence length methods all behave similarly, surpassing the duty-cycle modulated poling by a few percent. The difference between the algorithms is more drastic when short crystals are considered, where $L < 200 \ell_c$. While the sub-coherence length poling always achieves an almost optimal result, the other techniques are quite sensitive respect to small number of domains. It's worth mentioning that periodic poling and duty-cycle modulation are less affected by short crystals.

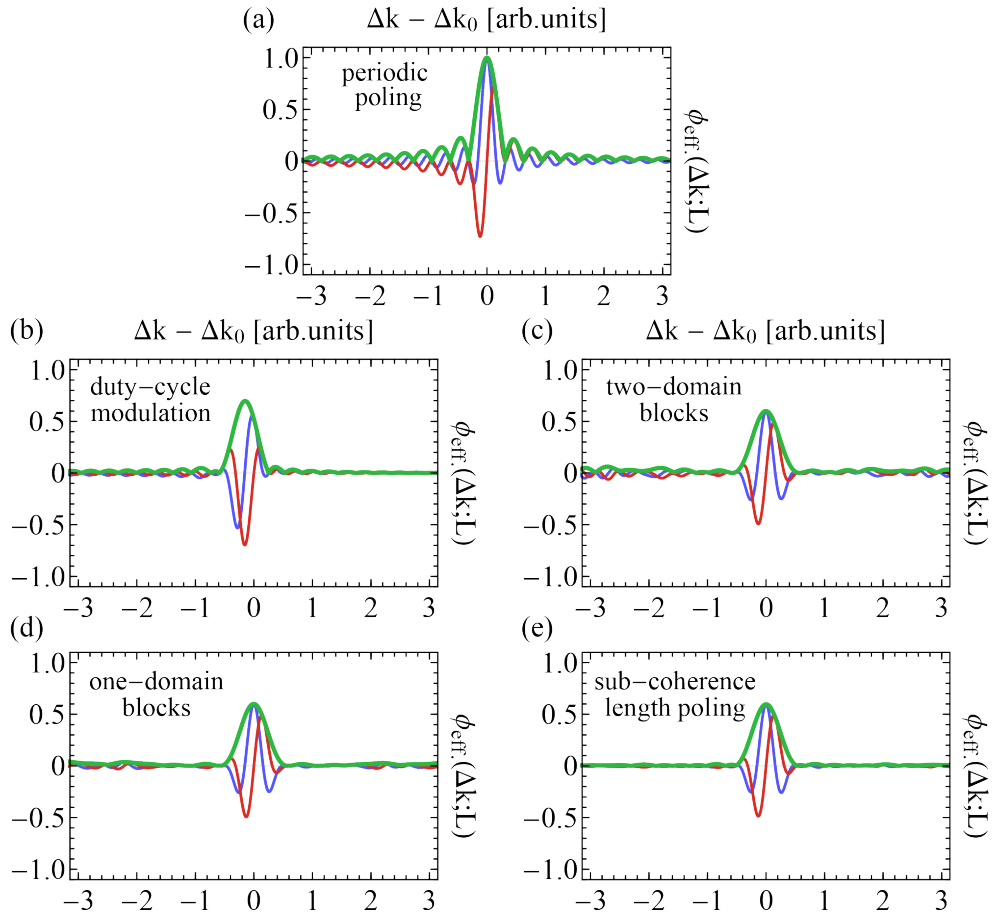


Figure 4.15: PMF comparison. Comparison of PMFs for different poling schemes, considering crystals length $L = 100 \ell_c$. All PMFs are normalised respect to the periodic poling case (a), which is sinc-shaped. Duty-cycle modulation (b) is not able to completely suppress the side lobes, while “two-domain blocks” method (c) does a better job. However, the PMF still shows some noise away from the central peak, due to a sub-optimal tracking of the target function. This can be fixed using the “one-domain blocks” method (d) or, in the extreme case, with sub-coherence length poling (e).

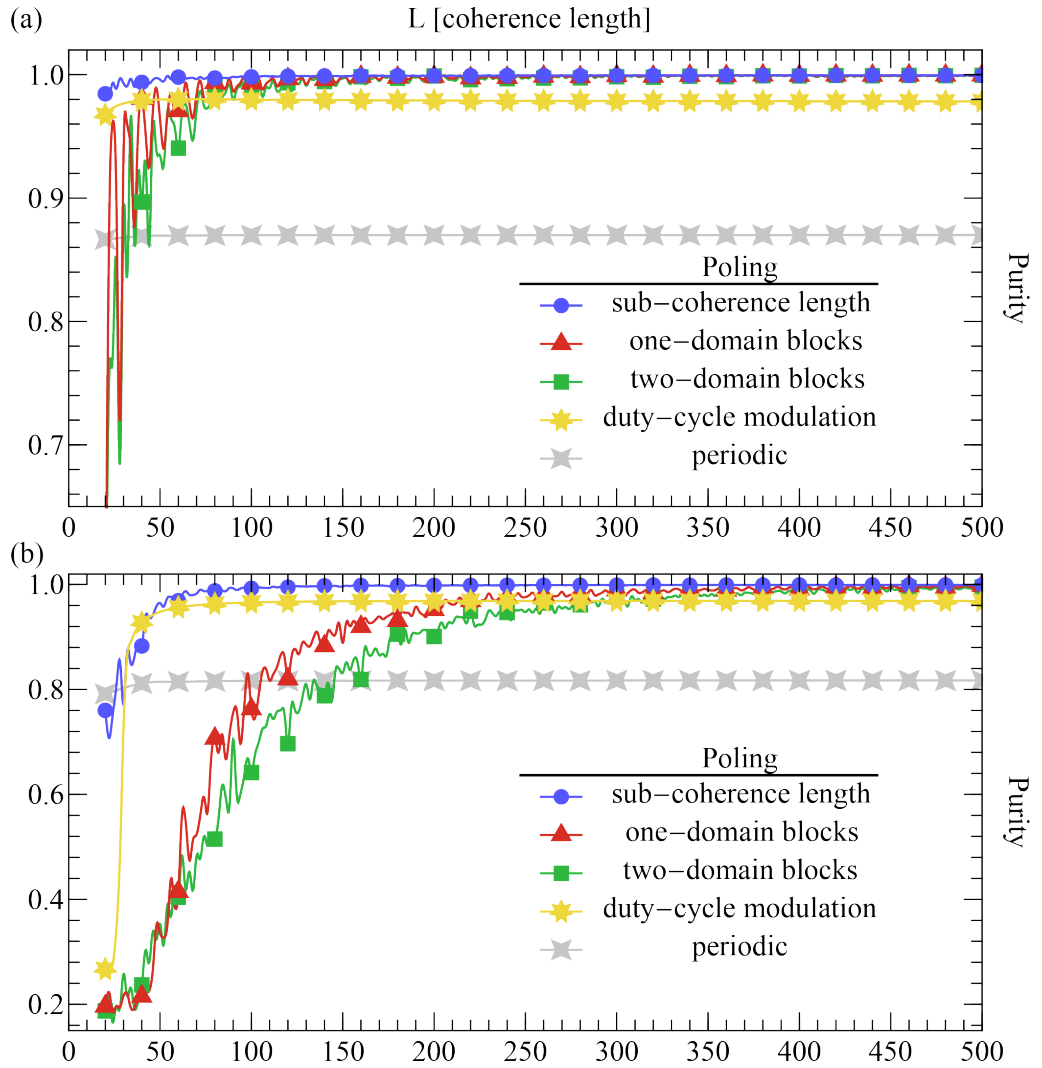


Figure 4.16: Purity for different engineering methods. The purities are calculated for spectral ranges 10 (a) and 40 (b) times larger than the PDC photon bandwidths.

4.5 (A)periodic poling in realistic crystals

Existing work on tailoring crystal nonlinearities for JSA separability assumed ideal crystal fabrication [89–93, 120], and for the most part neglected discussion of undesirable PDC generation that arises from nonlinearity shaping methods. In this Section, we discuss how fabrication imperfections in nonlinearity shaping impact JSA separability and pair generation probability, and discuss the implications of undesired PDC generation [71]. Having already discussed how the “two-domain blocks” method is similar to and outperformed by the algorithms discussed above,

we won't consider this case in the following numerical simulations.

4.5.1 Undesirable PDC generation far from central peak

The nonlinearity engineering techniques discussed so far shape the PMF through “interference” between the PMFs of individual domains. The PMF is shaped as desired only within a certain spectral range of interest, but outside this range the nature of interference can generate undesired PMF amplitude, leading to what we call here “undesirable PDC generation”.

Undesirable PDC generation far from the central PMF peak arises in all poling techniques, but the nature of this amplitude differs. [Figure 4.17](#) shows the undesirable PDC generation for four poling patterns, compared with an unpoled crystal. We consider a periodically-poled crystal with $L = 300 \ell_c$, a duty-cycle modulated crystal with $L = 362 \ell_c$, and two crystals with $L = 476 \ell_c$ shaped with the “one-domain block” and sub-coherence length methods, respectively. In the latter two cases, the width parameter is chosen as $\sigma = L/5$, and the sub-coherence length domain is $w = \ell_c/5$, and in all cases, the main PMF peak is in $\Delta k_0 = \pi/\ell_c$. The crystal lengths are chosen to provide PMFs having the same bandwidths. In periodically poled crystals these regions are concentrated at $\Delta k = \pm n\pi/\ell_c$. When duty-cycle modulation is used there is additional amplitude peaked at $\Delta k = 0$. Finally, for the “one-domain blocks” and the sub-coherence length poling techniques, the additional amplitude is more spread out in Δk .

For periodic poling and the customised duty-cycle method, the undesirable PDC generation is typically far outside the spectral range of the detectors and therefore gets filtered out automatically. For the customised domain orientation methods, such generation is closer to the spectral range of interest: choosing small domains in the sub-coherence length poling case can both suppress and push this undesirable amplitude away from the main PMF peak, but it might still need to be filtered out deliberately. This raises the question: when the motivation for nonlinearity shaping is to avoid destruction of photon-number correlations caused by filtering, is nonlinearity shaping a good idea when filtering is required anyway? The answer lies

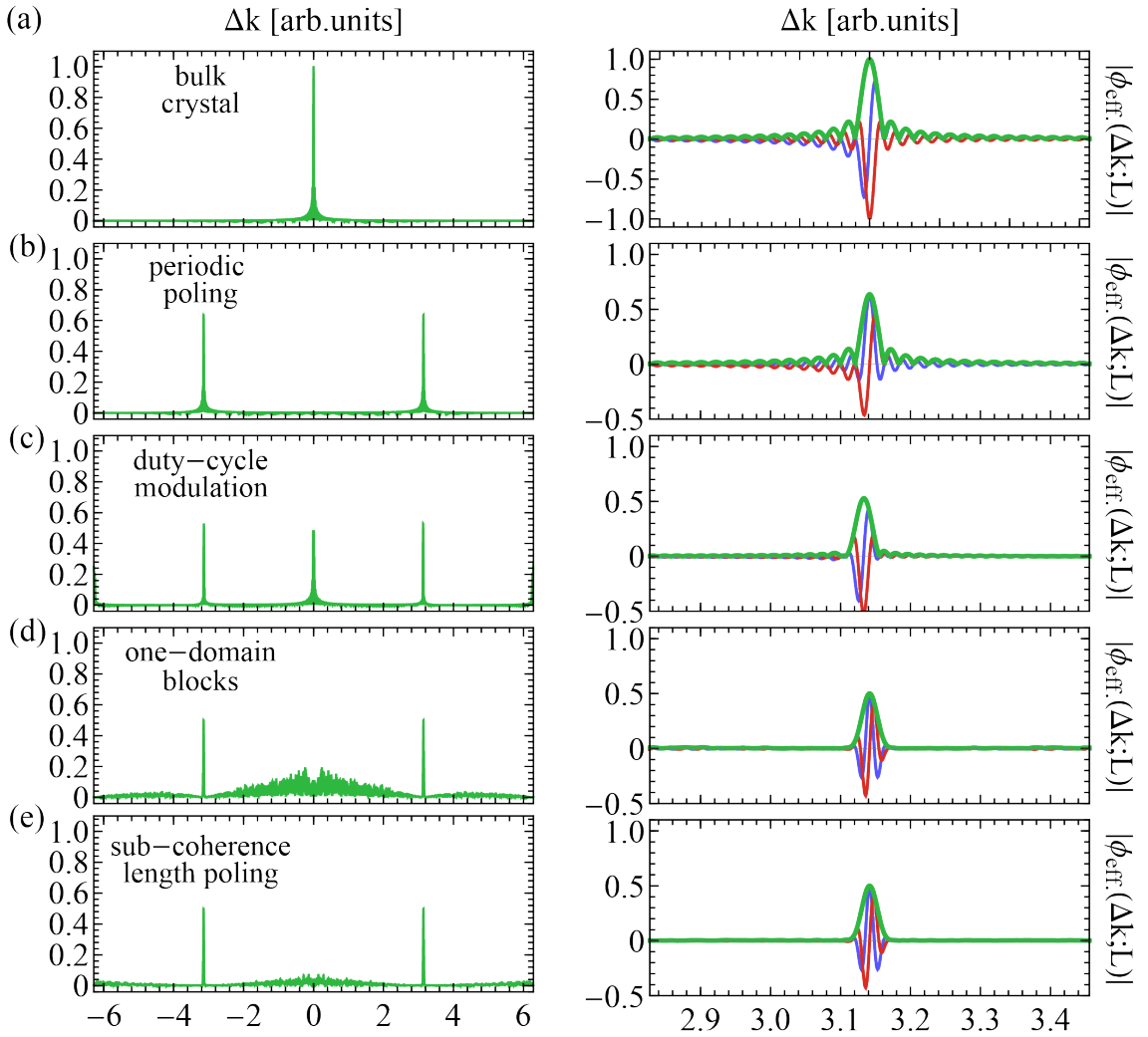


Figure 4.17: PDC generation far from central peak. PMF over a large (left column) and smaller (right column) Δk range, for bulk (a), periodically-poled (b), and duty-cycle modulated (c) crystals, as well as two crystals shaped with the “one-domain blocks” method (d) and sub-coherence length poling (e) ($w = \ell_c/5$). The main PMF peaks are centred in $\Delta k_0 = \pi/\ell_c$, and the crystal lengths are chosen to match the PMFs bandwidths. We note that non-zero PMF far from the main peak in (d) and (e) can be further suppressed by choosing smaller values for the width parameter σ , as shown in Figure 4.8. All PMFs are normalised respect to the bulk crystal case.

in the nature of the filtering. Filtering preserves photon number correlations if the filter is partially transmissive *only* at frequencies for which the JSA is negligible (the special case of this is a filter described by a top-hat function with unit transmittance, which can be used in any region of the JSA). If the region containing undesirable PDC generation is far enough away from the region of interest to ensure no overlap between where the JSA is non-negligible and where the filter is partially transmissive,

then the undesired PDC generation can be safely filtered out without destroying photon-number correlations [40, 94–96, 123, 124]. We can conclude that, as long as the undesired PDC generation is sufficiently far away from the desired PDC generation, nonlinearity shaping is indeed a good idea.

4.5.2 Crystal Imperfections

A popular method for generating poled crystals is ferroelectric poling, in which the spontaneous polarisation of a ferroelectric crystal can be reversed under the influence of a sufficiently large electric field that is applied using lithographically defined periodic electrodes [125]. This process is susceptible to various fabrication imperfections: timing errors in applying the field may systematically over- or under-pole inverted domains, roughness in electrode lithography may introduce random variations in domain walls, and failure of the crystal to nucleate may prevent inversion, resulting in missed domains. These imperfections are sketched in [Figure 4.18](#) for the periodic and aperiodic poling.

Impact of imperfections on conversion efficiency has been studied for periodically-poled crystals (e.g random variations in domain walls [126], missed domains [127], and deviations in duty-cycle [128]). Expanding on the analysis conducted in Ref. [71], here we study how fabrication errors affect custom poled crystals, studying the relation between crystal imperfections, heralded-photon spectral purity and overall nonlinearity. To gain information about photon pair generation, we compute the peak of the PMF, defined as $\phi_{\text{eff}}(\Delta k_0; L)$, and compare it with that generated by a periodically-poled crystal.

We consider a periodically-poled crystal with $L = 300 \ell_c$, a duty-cycle modulated crystal with $L = 362 \ell_c$, and two crystals with $L = 476 \ell_c$ shaped with the “one-domain block” and sub-coherence length methods, respectively. In the latter two cases, the width parameter is chosen as $\sigma = L/5$, and the sub-coherence length domain is $w = \ell_c/2$. All PMFs are centred in $\Delta k_0 = \pi/\ell_c$. We run numerical simulations generating 200×200 JSA matrices, considering a spectral range of about 25 times the PDC photons bandwidth (smaller spectral range is discussed in

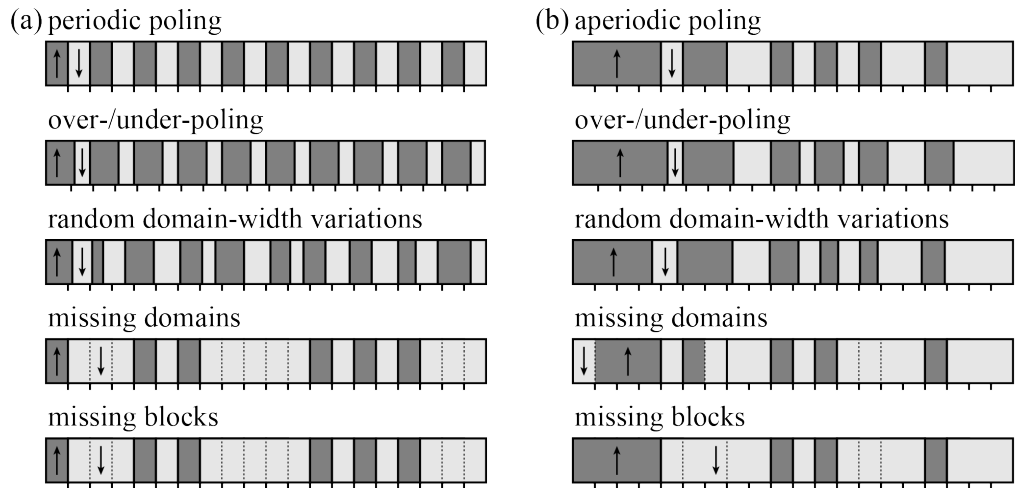


Figure 4.18: Different types of poling errors. Sketch of poling errors in periodic (a) and aperiodic (b) poling, where the aperiodic poling emulates a crystal shaped with the one-domain blocks method. From top to bottom are represented the effects of over- and under-poling, random variations in the wall positions, missing domains (i.e. crystal’s section of elementary width w , where $w = \ell_c$ in the sketch, that aren’t poled in the correct direction), and missing blocks (i.e. whole uniformly-poled crystal blocks are not poled correctly). In the periodic poling case the last two types of errors have the same effect, but this is not the case for aperiodic poling, where blocks might be composed of more than one domain poled in the same direction, forming uniformly-poled blocks larger than w . The dashed lines represent the walls of the missing domains/blocks.

Appendix A). The results are shown in Figure 4.19.

Under/over-poling

Simulations for over- and under-poling are analogous, we thus restricted our simulations to over-poling. We systematically increased the widths of UP blocks while proportionally decreasing the DOWN segments, considering variations of the domain width up to a 20% of the coherence length ℓ_c (note that deviations of around 5% were reported in [128]). We find that the heralded-photon purity is not affected in the case of periodic poling and “one-domain blocks” apodisation, while it decreases up to 15% in the case of duty-cycle modulation and sub-coherence length poling. In all cases, the PMF amplitude decreases in amplitude as the over-poling increases. Results are shown in Figure 4.19(a).

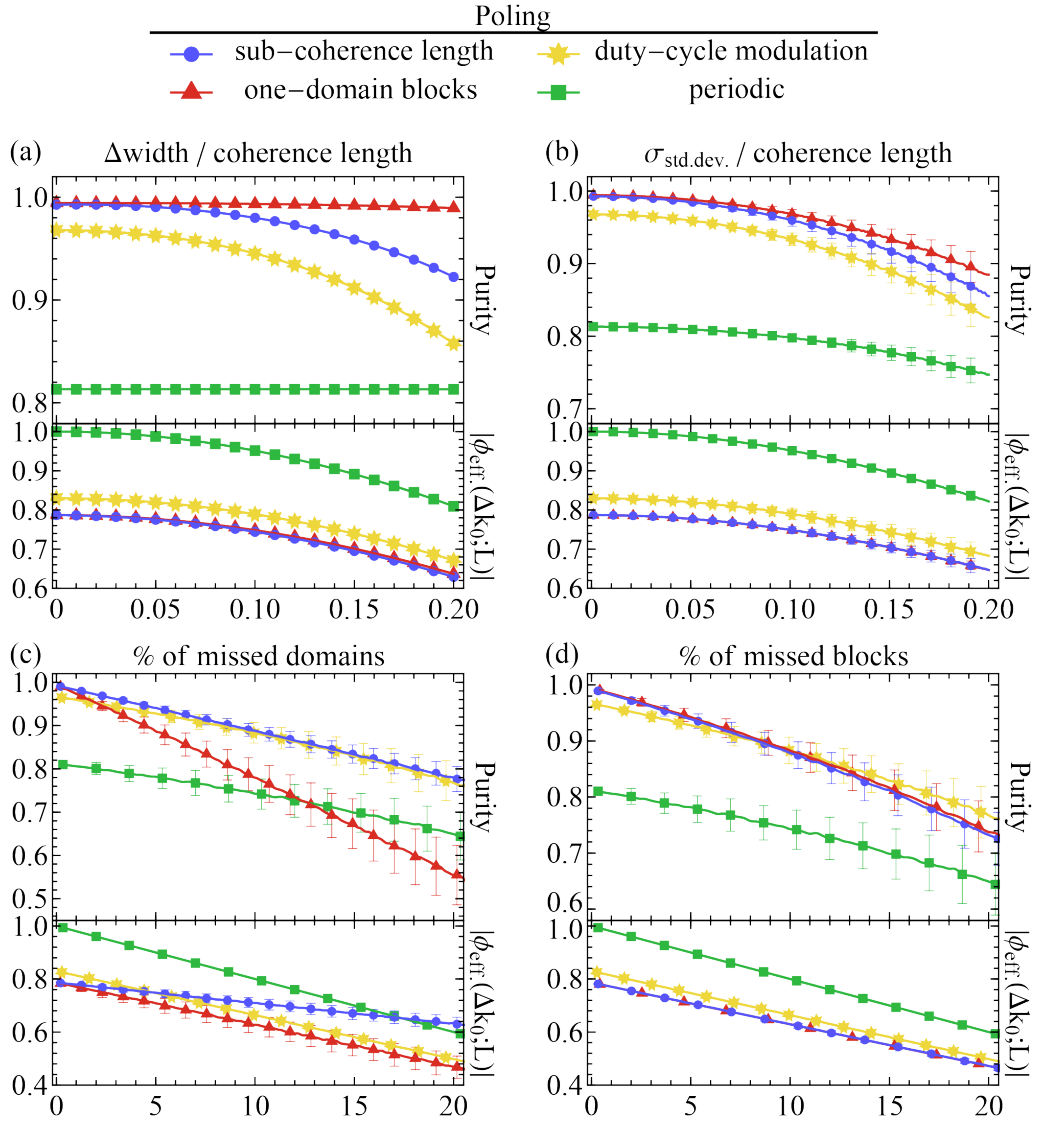


Figure 4.19: Poling errors. Effect of poling errors on different poling methods: periodic (green squares), duty-cycle modulation (yellow stars), “one-domain blocks” (red triangles), and sub-coherence length poling (blue points). Each panel represents the purity (top) and PMF amplitude (bottom) as a function of the amount of (a) under- and over-poling, (b) domain-width variation, (c) missing domains, and (d) missing blocks.

Random variations in wall positions

We ran Monte Carlo simulations averaged over 1000 data samples, where we shift the wall position of each uniformly-poled block. The amount of shift is based on a Gaussian distribution parameterised by its standard deviation normalised to the coherence length: $\sigma_{\text{std.dev.}}/\ell_c$, and we considered variations up to a 20%. Errors in standard crystals made by established manufacturers will typically be on the

low end of this range, but others have reported errors of $\sigma_{\text{std.dev.}} = 0.08 \ell_c$ in two different experiments involving lithium niobate waveguides [129, 130]. This kind of error makes the purity decrease in all cases, but the periodically-poled one is slightly less affected. The PMF amplitude decreases similarly to the under- and over-poling case. Results are shown in [Figure 4.19\(b\)](#).

Missing domains

We model missing domains by considering crystal segments of length ℓ_c pointing in one direction, then flipping the sign of a randomly selected subset of these, up to 20%. We average over 1000 data points for each % value. Both purities and PMF amplitudes drop linearly as the percentage of missed domains increases, but the purity of “one-domain blocks” poling seems to be effected more strongly than the other poling methods. Results are shown in [Figure 4.19\(c\)](#).

Missing blocks

We model missing blocks by considering uniformly-poled crystal blocks pointing in one direction, then flipping the sign of a randomly selected subset of these, up to 20%. This is analogous to the missing domains error in the case of periodic poling and duty-cycle modulation, as the ferroelectric orientation is reversed every domain. However, in the case of “one-domain blocks” and sub-coherence length poling, adjacent domains might have the same ferroelectric orientation, forming uniformly-poled blocks. Again, we average over 1000 data points for each percentage of flipped blocks, and we find a linear drop of both purities and PMF amplitudes as the amount of errors increases. Results are shown in [Figure 4.19\(d\)](#).

In summary, we can say that the fabrication imperfections considered here impact all poling methods approximately in an equivalent way.

4.6 Irregular momentum mismatch: an edge case

This Section is a speculation on a possible (but probably unlikely) problem that domain engineering wouldn't be able to entirely solve. In all previous simulations we have considered linear momentum mismatch, meaning that the $\Delta k(\omega_s, \omega_i)$ contours are linear in the (ω_s, ω_i) space, and the contours are equally spaced (meaning that the momentum mismatch is also linear perpendicularly to the contours). This is clearly true when considering relatively small frequency ranges, as we have seen for KTP crystals in [Figure 2.5](#).

However, let's imagine a material where this is not the case. Two possible cases might occur: the $\Delta k(\omega_s, \omega_i)$ contours might not be linearly spaced, or they might not be linear themselves. An exaggerated example of such cases is provided in [Figure 4.20](#) (a) and (b) to highlight the nature of this problem, and examples of the corresponding sinc-shaped PMFs are depicted in (c) and (d).

While nonlinearity engineering can shape the PMF pattern, such PMF is then applied to each Δk value in the considered frequency range, and the effects of "non-linear Δk " will compromise the shape of the tailored PMF. In the first case, where the $\Delta k(\omega_s, \omega_i)$ contours are not linearly spaced, one can compensate this effect with nonlinearity engineering, by considering a target PMF ϕ_{target} that takes into account the non-linear nature of Δk . In the second case, however, nonlinearity engineering cannot compensate for the non-linear contours of the momentum mismatch, and optimal PMFs cannot be achieved.

4.7 Down-conversion in KTP at telecom wavelength: a case study

So far we have analysed nonlinearity engineering in an ideal scenario, where Δk dependence on signal and idler frequencies was perfectly linear, and the pump was Gaussian shaped. We now consider a more realistic case, and we numerically simulate the spectral properties of parametric down-conversion in KTP crystals to gen-

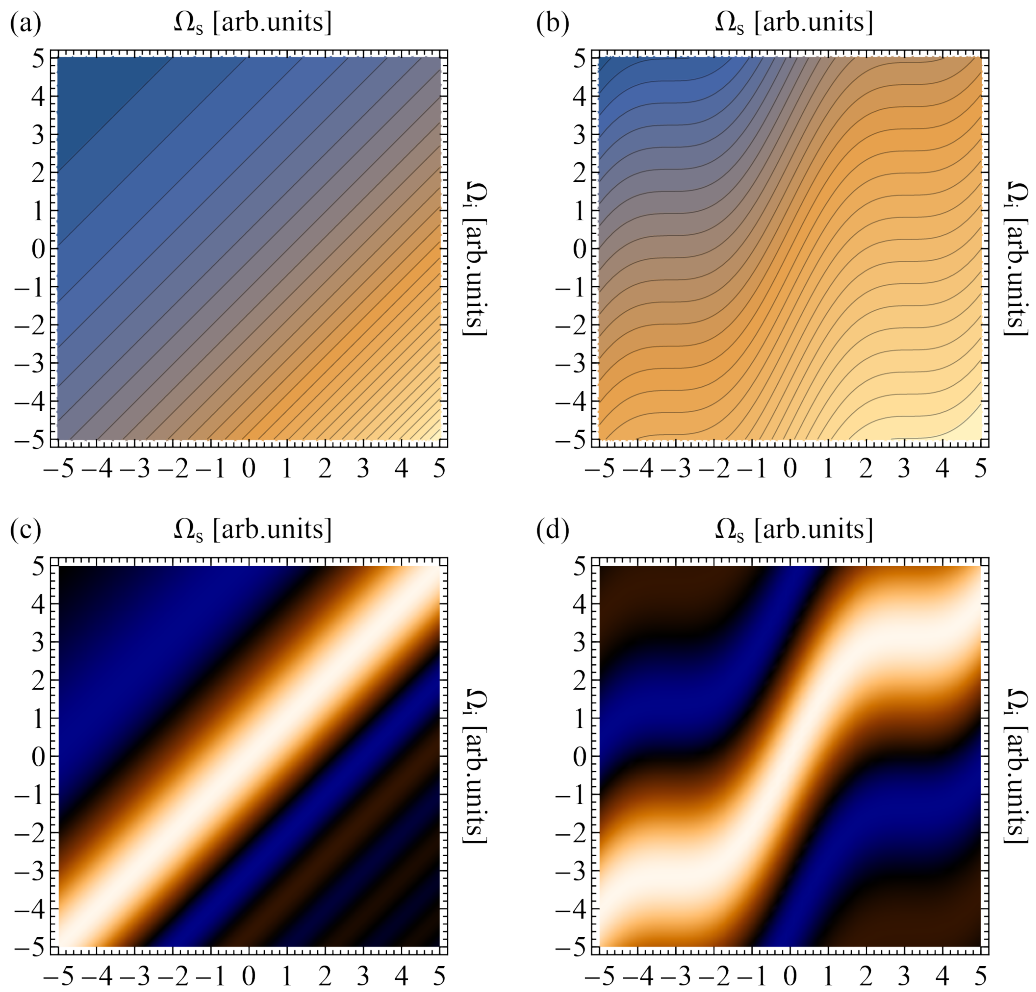


Figure 4.20: Momentum mismatch matrices. The momentum mismatch contours might not be equally spaced (a), or they might not be linear (b). The corresponding PMFs in (c) and (d) follow the $\Delta k(\omega_s, \omega_i)$ contours.

erate telecom-wavelength photons.

We compare periodically-poled crystals (where the crystal length is chosen to maximise the JSA separability) with apodised crystals designed with one-domain blocks and sub-coherence length poling techniques, where we have chosen the width parameter as $\sigma = L/5$. We consider sech-shaped pump pulses, centred at 775 nm, that generate photon pairs at 1550 nm in a type-II PDC process. Conservation of momentum is achieved by considering a coherence length $\ell_c = 23.1 \mu\text{m}$, corresponding to a poling period of $\lambda = 46.2 \mu\text{m}$ in the periodic poling case.

We generate 150×150 JSA matrices considering spectral ranges 20 and 8 times larger than the PDC photon bandwidth. This choice of spectral ranges allows us

to examine the “unfiltered case” (20), as well as the “gentle-filtering case” (8): two scenarios that are quite common in numerical simulations and actual experiments.

We find that the optimal crystal length (in millimetres) for a given pump pulse duration (in femtoseconds) is given by the following linear relations:

$$\begin{aligned} L_{\text{pp}} [\text{mm}] &\simeq 0.01374 \cdot \text{sech}^2 \text{ pulse duration} [\text{fs}] \\ L_{\text{ap}}^{\sigma=L/5} [\text{mm}] &\simeq 0.02432 \cdot \text{sech}^2 \text{ pulse duration} [\text{fs}], \end{aligned} \quad (4.21)$$

as also shown in Figure 4.21(a). It’s important to keep in mind that it’s very unlikely that a periodically poled crystal will be used in a multi-photon experiment without any kind of narrowband filtering, or the interference quality would be very low (unless one consider extremely asymmetric GVM conditions, where the use of strong filtering can be somehow avoided). For this reason, when choosing the experiment parameters, one should also consider the bandpass filter bandwidth in their simulations, and optimise the periodically-poled crystal length not only with

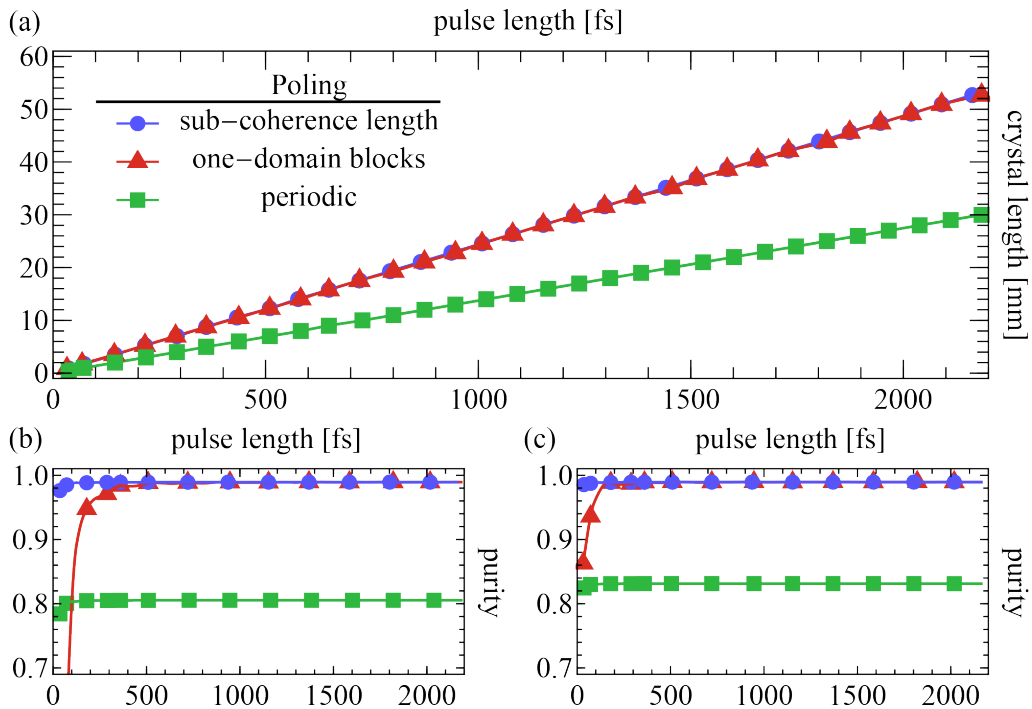


Figure 4.21: Nonlinearity engineering in KTP crystals. The optimal KTP crystal length grows linearly with the pulse duration (a). Corresponding purities are calculated for spectral ranges 20 (b) and 8 (c) times larger than the PDC photon bandwidths.

respect to the pulse duration, but also with respect to the filter parameters. Taking filtering into account typically results in crystals that are slightly longer than in the unfiltered case.

We also find that optimal purity of 0.99 is achieved for pulse lengths longer than 500 fs independently from the chosen engineering method, but for shorter pulses (i.e. shorter crystals) the finite-domain effects arise and sub-coherence length poling is required to maximise JSA separability. These results are shown in [Figure 4.21](#) (b) and (c) for the one-domain blocks and sub-coherence length poling methods, respectively.

4.8 Conclusion and discussion

This Chapter was entirely devoted to tailoring the PMF of nonlinear crystals via domain engineering. We have seen how such technique promises to make narrow-band filtering in PDC sources obsolete—it has indeed been proven that apodized crystals would significantly reduce the overhead source-costs in boson-sampling experiments [131]—as well as enabling access to more exotic PMFs (more of this in [Chapter 6](#)). We compared different engineering methods, and discussed how manufacturing errors might affect their performances. Overall, it appears evident that nonlinearity engineering is the simplest solution for making efficient PDC sources and, in the next Chapters, we'll see several experimental demonstrations of this technique.

[...] Yes we know what's written in the books,
but now let's see what our eyes tell us.

Bertolt Brecht, *A Life of Galileo*

CHAPTER 5

Pure Single Photon Generation Enabled Via Nonlinearity Engineering

In [Chapter 3](#) we have discussed the desirable properties of a PDC source, while in [Chapter 4](#) we introduced a state-of-the-art nonlinearity engineering technique that promises to significantly enhance the usefulness of PDC sources. In

this Chapter, we report the first experimental demonstration of our technique, as presented in Ref. [24]. In the first Section, we will introduce a reliable method for characterising the spectral purity of heralded PDC photons, based on two-photon interference. We will then proceed to describe the experimental setup and parameters that we used for benchmarking our nonlinearity engineering technique. We will discuss the results we obtained, and we will finally report the latest results that we recently measured in an improved version of our original experiment.

	Contents
5.1	Heralded-photons interference for purity estimation 95
5.2	Experiment 99
5.2.1	Experimental setup 99
5.2.2	Signal-idler interference 104
5.2.3	Heralded-photons interference . . . 104
5.3	Sneak peek at the latest results 107
5.4	Conclusion and discussion 109

5.1 Heralded-photons interference for purity estimation

In Chapter 3 we have discussed how interfering heralded PDC photons is arguably the most reliable way of measuring their spectral purity. However, the relation between interference visibility and spectral purity derived in Eq. (3.28) only takes into account the first-order term of the PDC state defined in Eq. (2.12). Clearly, higher-order PDC terms are detrimental for quantum interference, spoiling the direct correspondence between visibility and purity. Here we provide a simple way of modelling high-order contribution to HOM interference visibility, and we introduce a reliable method for estimating a lower-bound on the heralded-photon spectral purity.

In Eq. (3.10) we defined the interference visibility as $V = 1 - \frac{N_{\min}}{N_{\max}}$, where N_{\max} (N_{\min}) is the maximum (minimum) number of coincident counts recorded during the two-photon interference scan at opposite beam-splitter output ports, and in which the arrival time of the photons at the BS from its two inputs is varied by means of a delay line. In a standard HOM experiment, N_{\max} corresponds to counts recorded when the photons arrive at the BS at perfectly distinguishable times: no quantum interference occurs, as the photons are distinguishable in the temporal degree of freedom. In line with the wide-spread quantum optics slang, we will refer to this configuration as “outside the dip”.

N_{\min} is instead the number of coincidences recorded when the photons arrive simultaneously at the BS: in this case quantum interference effects occurs and, when two and only two indistinguishable photons enter the BS, we have perfect two-photon bunching. We will refer to this configuration as “in the dip”.

The visibility can be written in terms of the probabilities of having a coincidence “outside the dip” (p_{cc}^{out}) and “in the dip” (p_{cc}^{in}):

$$V(\lambda) = \frac{p_{cc}^{\text{out}}(\lambda) - p_{cc}^{\text{in}}(\lambda)}{p_{cc}^{\text{out}}(\lambda)}, \quad (5.1)$$

where the brightness parameter $\lambda = \sqrt{P\tau}$ has been defined in Eq. (2.14). In order to find the visibility dependence on the λ parameter (which translates to its dependence on the pump power), we need to consider the BS action on the higher-order terms of the PDC states.

We rewrite the PDC state in the Fock space (Eq. (2.14)) in terms of the creation operators \hat{a}^\dagger and \hat{b}^\dagger :

$$\begin{aligned} |\psi_{\text{PDC}}\rangle &= \sqrt{1 - |\lambda|^2} \sum_{n=0}^{\infty} \lambda^n |n\rangle_s |n\rangle_i \\ &= \sqrt{1 - |\lambda|^2} \sum_{n=0}^{\infty} \lambda^n \frac{(\hat{a}^\dagger \hat{b}^\dagger)^n}{n!} |0\rangle_s |0\rangle_i. \end{aligned} \quad (5.2)$$

In this framework, the probability of having coincidences after the BS corresponds to the amplitudes squared of the $|n > 0\rangle_c |m > 0\rangle_d$ terms in the BS-output Fock-state, i.e. all the terms where both the \hat{a}^\dagger and \hat{b}^\dagger operators occur. This probability is calculated as $\sum_{n,m>0} |\langle n, m | \psi_{\text{BS}} \rangle|^2$, where $|\psi_{\text{BS}}\rangle$ is the state after the BS. In the “outside the dip” case, an additional term has to be taken into account for a correct estimation of $p_{\text{cc}}^{\text{out}}$, as discussed in the next Section.

Signal estimate outside the interference region

We can write the state after the BS by means of the transformations in Eq. (3.12) applied to one PDC state in the case of signal-idler interference:

$$|\psi_{\text{BS}}^{\text{out}}\rangle = \sqrt{1 - |\lambda|^2} \sum_{n=0}^{\infty} \lambda^n \frac{(\hat{a}_1^\dagger + i \hat{b}_1^\dagger)^n (i \hat{a}_2^\dagger + \hat{b}_2^\dagger)^n}{2^n n!} |0\rangle_s |0\rangle_i, \quad (5.3)$$

or heralded PDC photons:

$$|\psi_{\text{BS}}^{\text{out}}\rangle = (1 - |\lambda|^2) \sum_{n,m=0}^{\infty} \lambda^{n+m} \frac{(\hat{a}_1^\dagger + i \hat{b}_1^\dagger)^n (i \hat{a}_2^\dagger + \hat{b}_2^\dagger)^m}{2^{n+m} n! m!} \hat{c}^\dagger \hat{d}^\dagger |0\rangle_a |0\rangle_b |0\rangle_c |0\rangle_d, \quad (5.4)$$

where we have used the subscripts 1 and 2 to indicate the different arrival time at the BS of the input photons \hat{a}_1^\dagger and \hat{b}_2^\dagger , while \hat{c}^\dagger , \hat{d}^\dagger are the heralding photons. For simplicity, we use the same λ parameter for both the PDC processes.

We can then calculate the probability of having coincidences “outside the dip”. We assume a lossless setup, and that the detectors and the logic can’t resolve the detection time of the photons: this is reasonable for an actual experimental setup because the difference in the photons’ detection time is usually narrower than the counting logic resolution. Under this assumptions, we calculate p_{cc}^{out} as follows:

$$p_{cc}^{\text{out}} = \sum_{\substack{n>1, m>1 \\ t_1, t_2 = \{1, 2\}}} |\langle n_{t_1}, m_{t_2} | \psi_{\text{BS}}^{\text{out}} \rangle_{s,i}|^2, \quad (5.5)$$

for the signal-idler interference, and

$$p_{cc}^{\text{out}} = \sum_{\substack{n>1, m>1, l>1, k>1, \\ t_1, t_2 = \{1, 2\}}} |\langle n_{t_1}, m_{t_2}, l, k | \psi_{\text{BS}}^{\text{out}} \rangle_{a,b,c,d}|^2, \quad (5.6)$$

for the heralded-photon interference.

Signal estimate within the interference region

We can also calculate the probability of having coincidences “in the dip” by considering the state after the BS when the photons from the two inputs arrive simultaneously at the BS. In the case of signal-idler interference, the output state reads:

$$\begin{aligned} |\psi_{\text{BS}}^{\text{in}}\rangle &= \sqrt{1 - |\lambda|^2} \sum_{n=0}^{\infty} \lambda^n \frac{(\hat{a}^\dagger + i \hat{b}^\dagger)^n (i \hat{a}^\dagger + \hat{b}^\dagger)^n}{2^n n!} |0\rangle_s |0\rangle_i \\ &= \sqrt{1 - |\lambda|^2} \sum_{n=0}^{\infty} \lambda^n i^n \frac{(\hat{a}^{\dagger 2} + \hat{b}^{\dagger 2})^n}{2^n n!} |0\rangle_s |0\rangle_i, \end{aligned} \quad (5.7)$$

while in the heralded-PDC-photons case it reads:

$$|\psi_{\text{BS}}^{\text{in}}\rangle = (1 - |\lambda|^2) \sum_{n,m=0}^{\infty} \lambda^{n+m} \frac{(\hat{a}^\dagger + i \hat{b}^\dagger)^n (i \hat{a}^\dagger + \hat{b}^\dagger)^m}{2^{n+m} n! m!} \hat{c}^\dagger \hat{d}^\dagger |0\rangle_a |0\rangle_b |0\rangle_c |0\rangle_d. \quad (5.8)$$

In this configuration we don’t have the subscripts 1 and 2 as in Eq. (5.3) and (5.4) because it’s impossible to distinguish the arrival time of the photons at the BS.

The probability of having coincidences reads:

$$p_{\text{cc}}^{\text{in}} = \sum_{n>1, m>1} |\langle n, m | \psi_{\text{BS}}^{\text{in}} \rangle_{s,i}|^2, \quad (5.9)$$

for the signal-idler interference, and

$$p_{\text{cc}}^{\text{in}} = \sum_{n>1, m>1, l>1, k>1} |\langle n, m, l, k | \psi_{\text{BS}}^{\text{in}} \rangle_{a,b,c,d}|^2, \quad (5.10)$$

for the heralded-photon interference.

Interference visibility

We can finally find the two-photon interference visibility by plugging Eq. (5.5) and (5.9) (for the signal-idler HOM) or Eq. (5.6) and (5.10) (for heralded-photon HOM) into the visibility relation in Eq. (5.1). In Figure 5.1 (a) we show the visibilities as a function of the brightness parameter λ : as expected, visibilities start from 1 at $\lambda \approx 0$, and then drop approximately quadratically as the brightness increases. Consequently, visibilities decrease approximately linearly with the pump power, as shown in Figure 5.1 (b). Note that the visibility drop is quicker for the heralded-photon interference with respect to the signal-idler case.

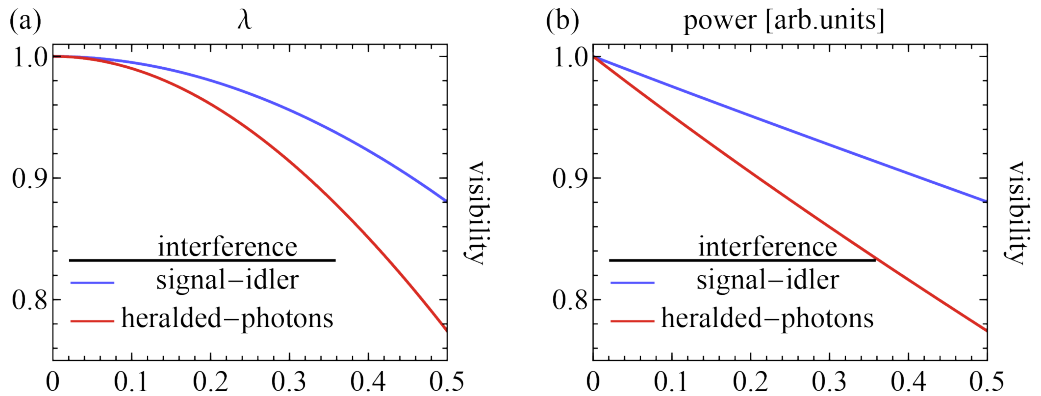


Figure 5.1: Interference visibility. HOM interference visibility as a function of the λ parameter (a) and the pump power (b).

This result gives us a tool to estimate the heralded-photon purity. Indeed, one can perform two-photon interference scans at different pump powers, find the corresponding visibilities and extrapolate a visibility at 0 power, $V(0)$, with a linear

fit. This value will be equal to 1 if the heralded-photons are spectrally pure and our experimental setup is perfect. However, $V(0) < 1$ when interfering spectrally-mixed heralded photons: in this case, $V(0)$ will give us an estimate of the single-photon purity according to Eq. (3.28). As experimental imperfections, detrimental for the HOM interference quality, are inevitable, it is reasonable to assume that $V(0)$ represents a lower-bound to the heralded-photon spectral purity. It's also worth noticing that this model neglects dark counts, that at very low powers (hence low counts) would lead to a drop of the visibility.

5.2 Experiment

In this Section we discuss the experiment where an enhancement of heralded-photons' interference visibility enabled by nonlinearity engineering has been observed for the first time [24].

5.2.1 Experimental setup

PDC source

A 80 MHz repetition rate Ti-Sapphire laser, with 775 nm, 1.7 ps sech^2 -shaped pulses, is filtered in power and polarisation with a *half-wave plate* (HWP) and a Glan-Taylor polariser. The beam is then focused into KTP crystals (more details below), phase-matched for degenerate type-II parametric down-conversion, producing orthogonally polarised photons with central wavelength of 1550 nm. The PDC photons are filtered from the pump with a dichroic mirror, and are then separated to two orthogonal paths by means of a PBS. Finally, signal and idler pass through a long-pass filter (for removing residual pump light) and, in some of the measurements, a “gentle” band-pass filter (for suppressing noise far from the main JSA peak discussed in Chapter 4), before being coupled into single-mode fibres with aspheric lenses. The photons can then be used in interference experiments (as discussed in the next Section) or sent straight to *superconducting nanowire single-photon detectors* (SNSPDs) for characterising source brightness and heralding efficiency. The PDC source is shown

in Figure 5.2.

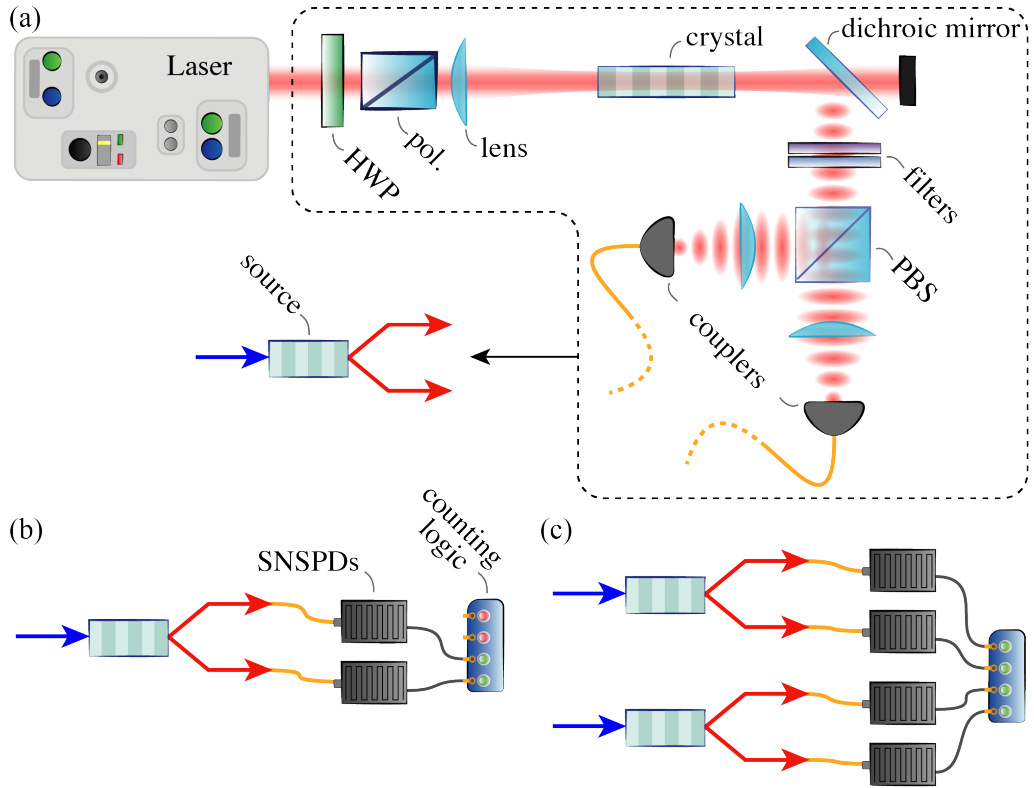


Figure 5.2: Photon source setup. Collinear parametric down-conversion source (a) and setup for measuring brightness and heralding efficiency (b) as well as four-fold coincidences (c).

Details on the crystals under study are provided below. We designed a 29 mm-long apodized KTP crystal (fabricated by Raicol Crystals Ltd.) using the annealing-algorithm combined with a preliminary version of the one-domain blocks method. However, when the crystal was designed, we didn’t have a full understanding of the engineering algorithm parameters. Consequently, we designed “sub-optimal” crystals, where the tracking function wasn’t rescaled as discussed in Eq. (4.8) for maximising the crystal nonlinearity, and the width parameter was chosen as $\sigma = L/4$, slightly larger than optimal (see Figure 4.8). Moreover, we chose a seed poling period for the algorithm equal to $46.22\ \mu\text{m}$, according to the Sellmeier equations in Ref. [64–66], but it ended up being slightly too long, meaning that the degeneracy PDC emission was achieved below room temperature, making the experiment hard to keep stable. Last but not least, our crystal was designed for being optimally

group-velocity matched with 1.4 ps pulses, while the laser we used in this experiment wasn't stable when pulses were shorter than 1.7 ps, further compromising the JSA separability. Nonetheless, despite these problems, we numerically estimated a JSA separability of 95.3% for our experimental settings, and we managed to measure very high heralded-photon purities. For comparison with a standard PDC source, we benchmarked the apodised crystal performances against a 22 mm-long periodically-poled KTP crystal, with numerically-estimated JSA separability of 80.1%. JSAs, PMFs, and poling patterns of periodically-poled and apodised crystals are shown in [Figure 5.3](#).

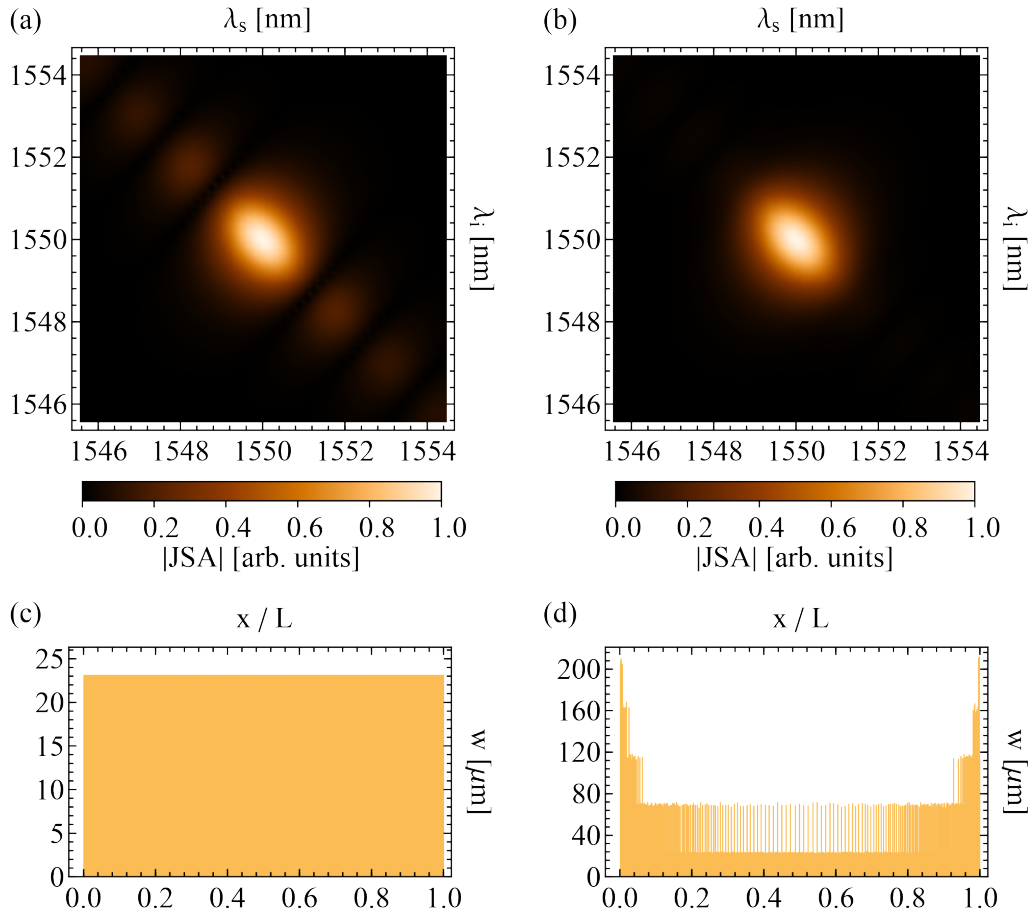


Figure 5.3: JSAs and crystal structures. The apodised crystal's JSA in (b) is slightly elliptical, due to a too long laser pulse resulting in a narrower spectral width, while 1.7 ps pulses are almost optimal for the unfiltered periodically-poled case (a). The poling pattern is uniform for the periodically-poled KTP (c), while it is composed of longer uniformly-poled blocks at the edges of the crystals, and shorter blocks in the centre (d).

As shown in Figure 5.2 (b,c), we send the PDC photons straight to the detectors and collect singles counts (s_i) detected by the SNSPDs and collected by a timing logic, as well as coincident counts (cc) within a 1 ns time window between different channels of the timing logic (i.e. corresponding to different detectors). With the setup in Figure 5.2 (b), we measure a source brightness (defined as the number of coincident counts in unit of time and power) of (11.25 ± 0.08) kHz/mW and (4.02 ± 0.04) kHz/mW detected pairs for periodically-poled and apodised crystals, respectively, and a four-photon rate (Figure 5.2 (c)) for two independent PDC sources of (1.52 ± 0.02) Hz/mW² and (0.19 ± 0.01) Hz/mW². We estimate a symmetric heralding-efficiency $\eta = cc/(\sqrt{s_1 s_2})$ of 53% in the configuration used for the experiment, but a value of η up to 68% is achieved with the same crystals under loose focusing conditions [16, 132–134], at expense of the brightness: this corresponds to a collection efficiency of 88.5% once detector efficiency (nominally 80%) and known optical losses of (7.6%) are accounted for.

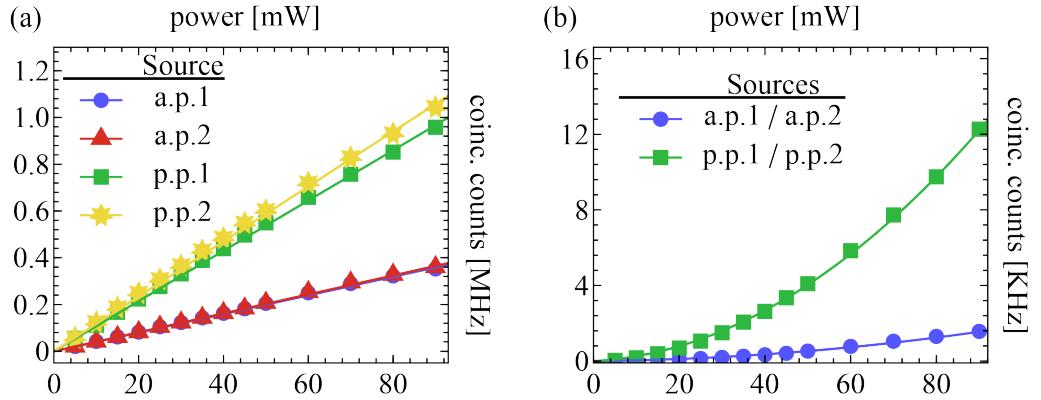


Figure 5.4: Source brightness. Pairwise (each source) (a) and four-folds (across two sources) (b) coincident counts within 1 ns window for the periodically-poled (p.p.) and apodised (a.p.) crystals.

Interference setup

Signal-idler indistinguishability is measured via HOM interference of PDC photons in a two-photon experiment, as shown in Figure 5.5 (a).

Ideally, measuring the spectral purity of a PDC photon requires interfering two copies of the same photon. However, the quantum state of a photon cannot be

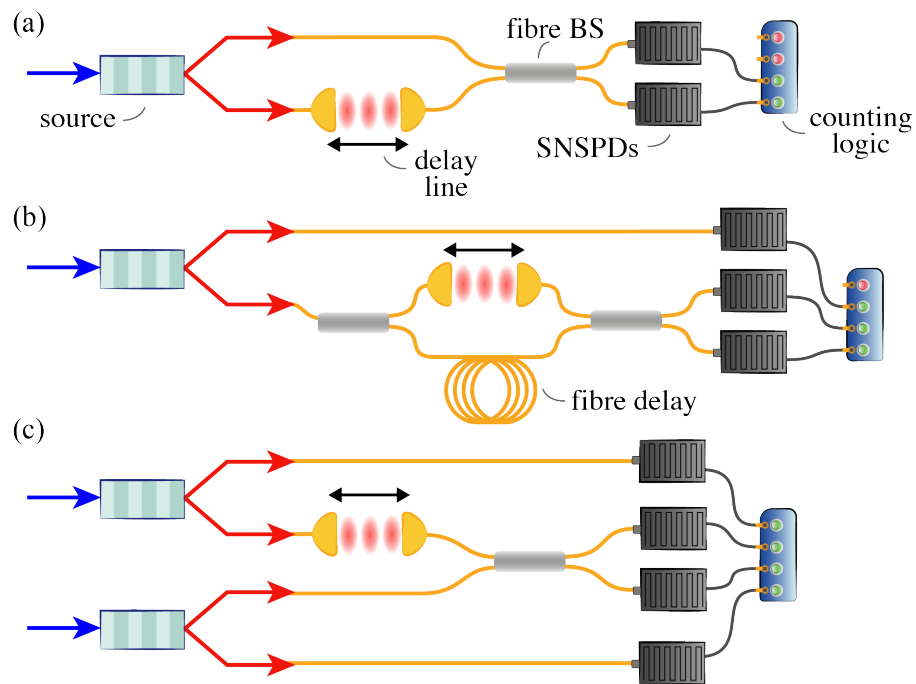


Figure 5.5: Interference setups. Signal-idler interference setup (a), heralded-photons interference schemes of delayed photons produced by the same source (b) and of photons produced by independent sources (c).

cloned, and a faithful purity estimate can be obtained from interfering two photons emitted in short succession from the same crystal pumped with the same laser. In our setup, [Figure 5.5 \(b\)](#), we send the first heralded photon into a fibre delay-line and a second into a shorter fibre before superposing them on a fibre BS. This scheme succeeds with probability $1/4$, and we chose a delay of five pump pulses to exceed the ~ 60 ns SNSPDs reset time. The two interfering photons are heralded by their respective twins, and four-photon coincidences are recorded.

We finally interfere photons produced by two different crystals, [Figure 5.5 \(c\)](#) to show that our technique is feasible for multi-photon experiments. We detect the idler photons as a heralding trigger and interfere the signal photons, collecting the overall number of four-fold coincidences from the four SNSPDs connected to the timing logic.

5.2.2 Signal-idler interference

We first estimate the signal-idler indistinguishability with the setup in [Figure 5.5](#) (a): when interfering signal-idler, the indistinguishability is equal to the symmetry of the JSA, as discussed in [Section 3.2.4](#). According to the model introduced in [Section 5.1](#), we interfere the PDC pairs produced at different pump powers, P , to extrapolate the HOM visibility “at 0 power”, $V(0)$, that gives us a lower-bound to the photons’ indistinguishability. Being close to symmetric GVM condition, the interference pattern can be approximated by the convolution of the phase-matching function with itself [83]: as expected, it is almost triangular for the standard crystal [111], and Gaussian for the custom design, as shown in [Figure 5.6](#). We find indistinguishabilities of $V(0) = (99.7 \pm 0.1) \%$ for the periodically-poled crystal, and $V(0) = (98.7 \pm 0.1) \%$ for the apodised one, where we use the interference visibility as a metric for the signal-idler indistinguishability. By the time of publication, to our knowledge, this signal-idler indistinguishability was the highest reported so far with an unfiltered nonlinearity-engineered crystal.

The interference visibility can be further increased by introducing an additional “gentle” spectral filtering stage. We use a band-pass filter with a spectral transmission of the form: $\exp\left[-\frac{(\omega-\omega_0)^4}{2\sigma^4}\right]$, centred at 1550 nm and having nominal FWHM of 7.4 nm (roughly five times larger than the PDC bandwidth). This kind of filtering decreases heralding efficiency by less than 1 %, and we measure a signal-idler indistinguishability of $(99.7 \pm 0.1) \%$ for loosely-filtered apodised crystals. This value is close to the maximum visibility we can achieve (99.8 %) due to imperfect optics. In fact, the fibre BS has a reflectivity (transmissivity) 49.2 % (50.8 %), and the PBS leaks 0.5 % of opposite polarised photons, corresponding to a visibility decrease of $\sim 0.2 \%$.

5.2.3 Heralded-photons interference

The interference model for PDC photons discussed in [Section 5.1](#) assumes a perfect setup, with negligible losses, no detector dark counts or other sources of noise. In the case of lossy detectors and non-negligible background noise, the photon num-

ber purity not only decreases at high pump powers (i.e. high values of λ in the PDC state), but it is also compromised at very low powers, where the number of detected single-photons is comparable to the background noise counts [135]. In our experiment, the background noise rate is about 300 Hz, the chosen power range corresponds approximatively to a λ -range of 0.05 - 0.3, and the coincidence window is 1 ns. Under these assumptions, according to Eq. (17) in Ref. [135], we work in a regime where the number-photon purity decreases linearly as the power increases, but we are away from the region where number-purity drops at very low power: this translates to linear behaviour of the visibility, as predicted by our model and experimentally verified by the linear trend of the data points.

By interfering PDC photons emitted by successive pulses (Figure 5.5 (b)), we extrapolate a $V_0 = (79.6 \pm 0.1)\%$ for the standard periodically-poled crystal (a value that matches theory expectations discussed above), and we measure $V_0 =$

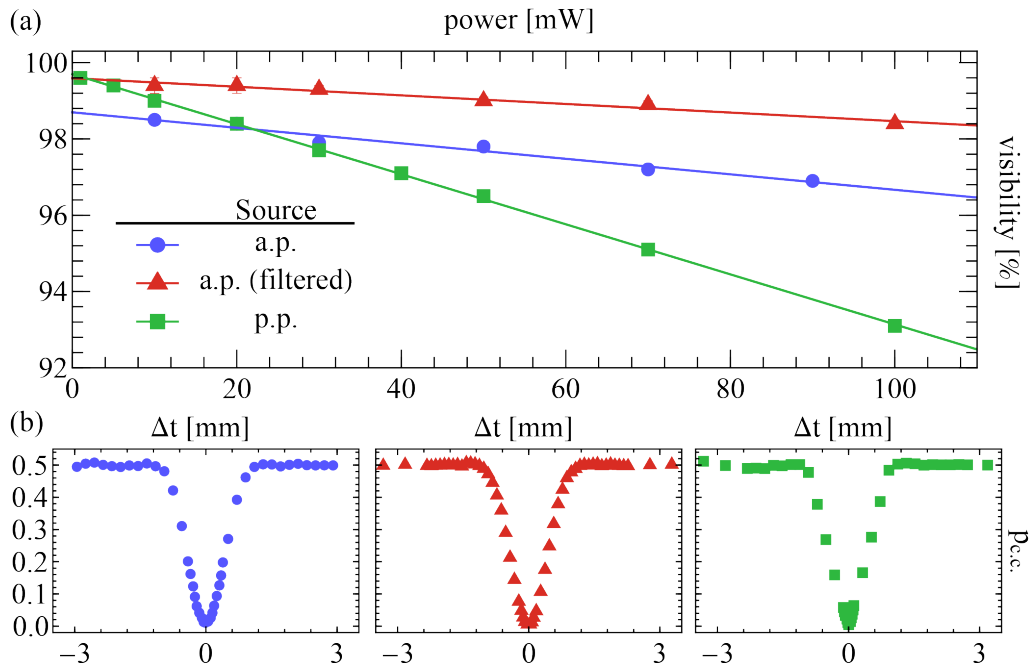


Figure 5.6: Signal-idler interference Signal-idler interference visibilities at different pump powers (a), and three examples of HOM scans dips (b) for the unfiltered and filtered apodised crystals—a.p., blue dots, and a.p. (filtered), red triangles, respectively—as well as the periodically-poled case (p.p., green squares). As expected, the apodised crystals have a Gaussian-shaped interference pattern, while the periodically-poled one shows a triangular dip.

$(90.7 \pm 0.3) \%$ for the apodised crystals. Results are shown in Figure 5.7. As we did in the signal-idler interference case, we can increase the JSA separability by applying “gentle” spectral filtering, achieving a heralded-photon purity of $(92.7 \pm 0.2) \%$. Finally, we measure $V_0 = (89.8 \pm 0.2) \%$ when interfering heralded-photons produced in different crystals: a slightly lower value with respect to the interference of photons produced by the same crystal, probably due to fabrication imperfections and small discrepancies between the two sources.

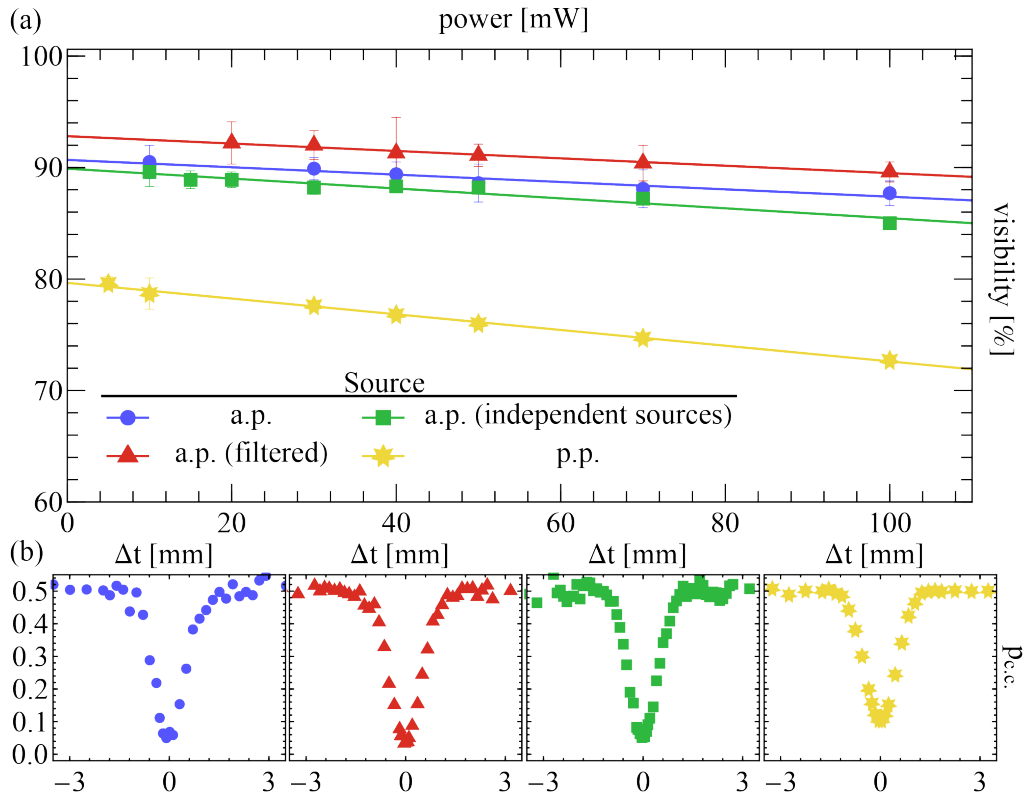


Figure 5.7: Heralded-photons interference. Heralded-photons interference visibilities at different pump powers (a), and four examples of HOM scans dips (b) for unfiltered and filtered apodised crystals—a.p., blue dots, and a.p. (filtered), red triangles, respectively, two independent apodised crystals (a.p. (independent sources), green squares), as well as the periodically-poled case (p.p., yellow stars).

The V_0 values corresponding to the apodised crystals shown in Figure 5.7 (a) are definitely higher than for the standard periodically-poled case: however, they are still somewhat short of expectations by $\sim 3\%$. Some degradation may be due to poling errors, as discussed in Chapter 4. Imperfect BS and components also

compromises the HOM visibility, as discussed for the signal-idler interference case. Laser instability (in both pulse duration and central wavelength) might also have impacted negatively the interference quality. Finally, the imperfect indistinguishability of the unfiltered signal-idler photons, and its increase under “gentle” filtering, suggests the presence of undesirable PDC-generation far from the central JSA peak, which is not present in standard crystals.

5.3 Sneak peek at the latest results

The original paper on experimental nonlinearity engineering [24] ended with the following sentence:

By fixing all known minor problems—fine tuning the domain-engineering algorithm, shaping a Gaussian pump pulse at 791 nm, and suppressing PDC noise—we are confident we can push the lower bound on spectral purity to at least 95 % in the near future.

Indeed, I’m happy to say that this is exactly what happened. We used the one-domain block engineering technique to design 30 mm-long crystals with a width parameter of $\sigma = L/4.7$ —a width of $\sigma = L/5$ would have probably been the optimal choice, however KTP crystals longer than 30 mm aren’t commercially available. We also used a new, more stable laser (Tsunami Spectra-Physics), with 1.3 ps pulses, group-velocity-matched with the crystals above, and improved some setup components (e.g. a more balanced fibre BS). We compare these apodised crystals with periodically-poled crystals with narrow-band filters, where filtering width of 2.8 nm is chosen to filter out most of the JSA side lobes without compromising the source brightness and heralding efficiency too much. JSAs and crystal patterns are shown in [Figure 5.8](#) (a) and (b), respectively. Numerical simulations, according to the above parameters, suggest that apodised crystal JSA would have 0.989 separability, while the filtered standard crystal would have 0.984 separability.

As discussed above, we perform heralded-photons HOM scans at different pump powers, and we show the results in [Figure 5.9](#). Here, however, we don’t consider

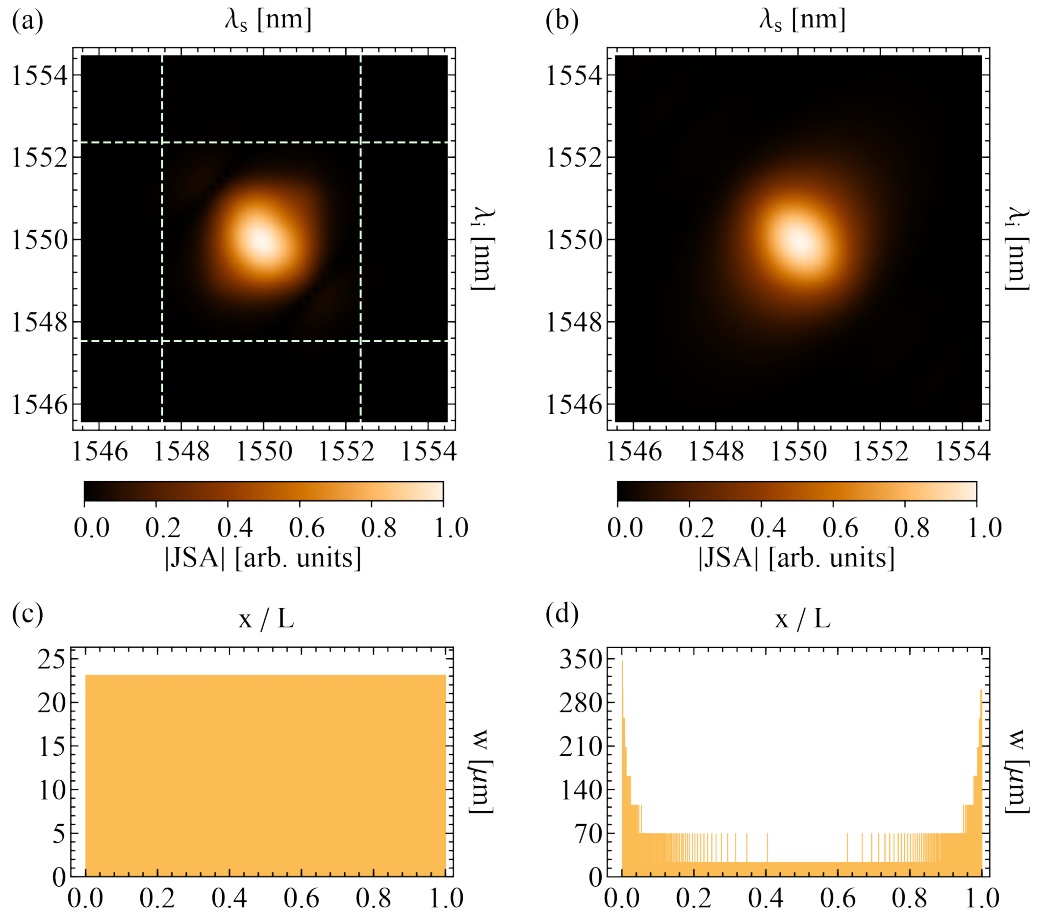


Figure 5.8: JSAs and crystal structure in latest experiment. The periodically-poled crystal JSA (a) doesn't show strong side lobes, as they are suppressed with narrowband filters ($1/e$ filter contours are represented with green-dashed lines). The apodised crystal JSA is circular, meaning that it is close to perfect separability. The poling pattern is uniform for the periodically-poled case (c), while it is composed of longer uniformly-poled blocks at the edges of the crystals, and shorter blocks in the centre (d).

delayed photons from the same source, but we interfere photons produced in two different crystals, as we are more interested into the scalability of this approach to multiple sources. We measure $V_0 = 0.980 \pm 0.001$ for the apodised crystals, while filtered periodically-poled crystals achieve $V_0 = 0.967 \pm 0.001$ —with a 15% reduction of the heralding efficiency. Such V_0 values represent a lower-bound to the heralded-photon purities, and as we have seen in the previous Sections, it could be further enhanced by interfering photons produced by the same crystal.

These latest results represent what I think is safe to consider as being a conclusive proof of the success of nonlinearity engineering for producing spectrally pure

photons.

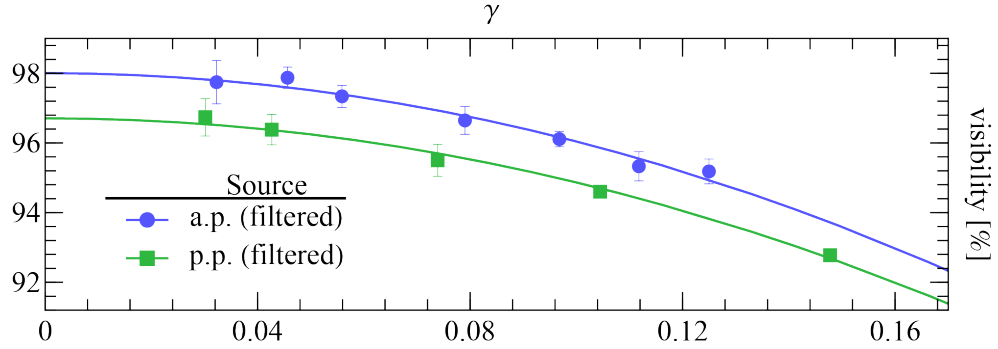


Figure 5.9: Heralded-photons interference in new apodised crystals. Heralded-photons interference at different pump powers. Here, the visibilities of both apodised crystal (blue dots) and filtered periodically-poled crystal (green squares) are plotted as a function of the PDC parameter γ , in order to provide a more fair comparison between the two sources. In fact, equal γ means equal amount of squeezing, and factoring out discrepancies in the effective nonlinearity of the crystals. The visibility decreases approximately quadratically as λ increases.

5.4 Conclusion and discussion

Using parametric down-conversion successfully in actual applications, such as building deterministic single-photon sources [123] or proving a true quantum advantage in Boson sampling experiments [131], requires minimising losses to reduce the number-of-sources overhead cost. In this Chapter, we have experimentally proven that nonlinearity engineering can indeed improve PDC performances significantly, increasing heralded-photon purities without compromising the heralding efficiency.

As a last remark, we conclude by assessing the impact of spectral filtering on the heralding efficiency and the single-photon purity of our photon sources (considering sech^2 pulses) to stress the relevance of nonlinearity engineering. In Figure 5.10, the normalised heralding represents the maximum heralding achievable, factoring out known losses, detection and collection efficiency, while the x-axis is the ratio between filter and single-photon bandwidth. The data corresponds to our experimental results discussed in the previous Sections: filtered and unfiltered, standard and apodised KTP crystals. We see a drastic trade-off between spectral purity and

heralding efficiency for photons created in standard crystals. A purity of 0.99 can be achieved when a filter with twice the PDC bandwidth is applied. However, even ideal filters with 100 % peak transmission would decrease the heralding efficiency to 80 %, and the source brightness to 60 %, which in a modest six-photon experiment would amount to a drop in observed rates to just 22 %. In contrast, our apodised crystal sources operate at, or at least very close to, 100 % heralding efficiency, overcoming this tradeoff: this is particularly evident in the red-triangle data points, representing the latest results obtained with domain engineering, where both heralding and purity are close to 100 %.

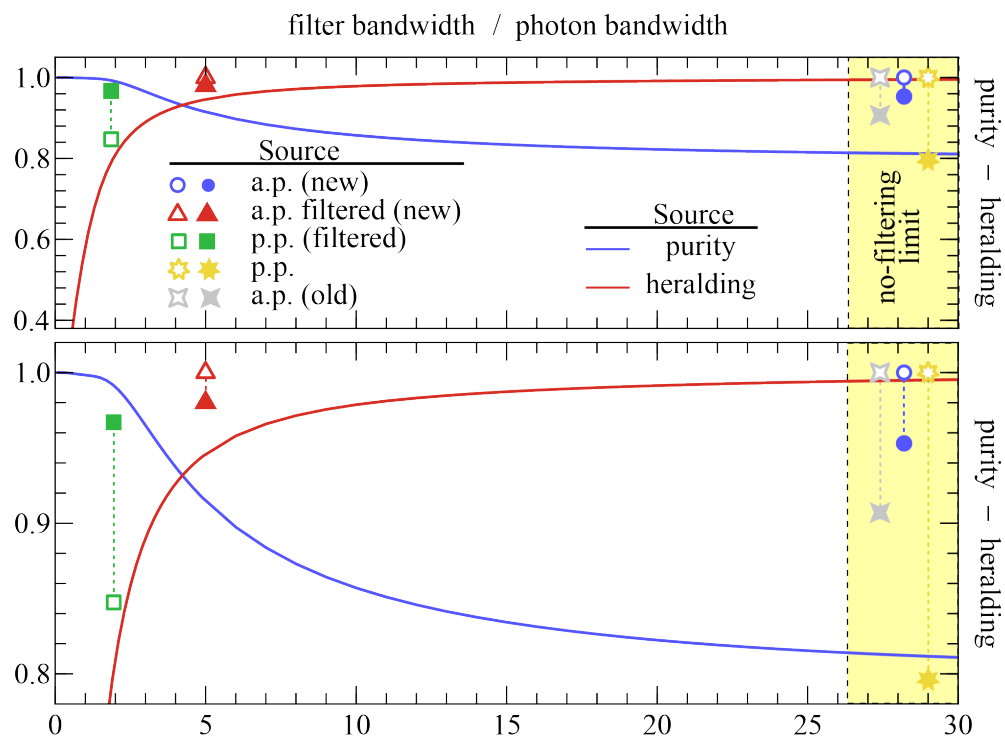


Figure 5.10: Filtering effects. Empty (filled) data points represent heralding (purity) of each source. The bottom plot zooms over the region with purity and heralding $>80\%$.

Time is an illusion. Lunchtime doubly so.

Douglas Adams,
The Hitchhiker's Guide to the Galaxy

CHAPTER 6

Generation of Time-Frequency Mode Entanglement

While generating pure heralded single-photons is the original and arguably the main application of nonlinearity engineering, its capabilities go much beyond this. Shaping the phase-matching function of nonlinear processes enables direct generation and manipulation of spectrally-tailored photonic states.

Contents	
6.1	TFM framework 112
6.2	Nonlinearity engineering for TFM encoding 115
6.3	Experimental TFM entanglement generation 118
6.3.1	Target TFM-entangled state 118
6.3.2	Experimental setup 120
6.3.3	Dispersive fibre spectroscopy 122
6.3.4	Two-photon interference 123
6.3.5	Effective JSA reconstruction 126
6.4	TFM entanglement swapping 129
6.5	Conclusion and future directions 132

We briefly discuss this in the first part of this Chapter, where we introduce what we call the time-frequency modes framework. We will then move on to the main part of this Chapter, reporting an experiment where we generate maximally-entangled biphoton states encoded in the TFM degree of freedom [112]. We describe the characterisation techniques and the novel analysis tools that allowed us to certify the authenticity of the produced TFM entangled state, and we report the experimental implementation of a TFM entanglement-swapping scheme as a proxy for multiphoton time-frequency modes protocols. Finally, we will conclude this Chapter with a brief discussion on upcoming projects following this line of research.

6.1 TFM framework

In the previous Chapter, nonlinearity engineering was used to generate spectrally pure single photons. For implementing photonic quantum information processing tasks, one needs to encode quantum information into these photons, in the form of, e.g., polarisation, transverse and longitudinal spatial modes [136, 137], time and frequency bins [138–141], etc. While this has been the most common choice for nearly three decades, the last few years have seen increasing interest into encoding quantum information directly into the complex spectral (temporal) envelope of the single-photon wavefunction: the time-frequency modes, that we have already discussed in the Schmidt decomposition Section of Chapter 2. Figure 6.1 shows the first five TFMs encoded in the Hermite-Gauss modes basis, that is the most common basis for describing such encoding. As for other high-dimensional encodings (e.g. orbital angular momentum), different bases can be obtained with linear superposition of the HG functions.

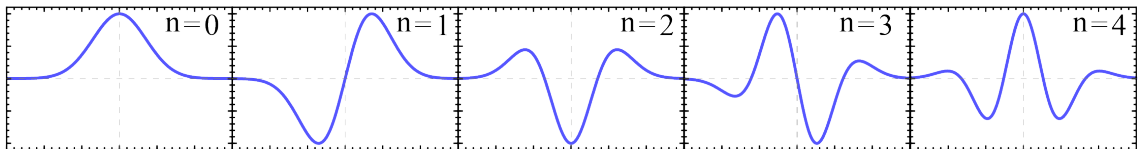


Figure 6.1: Example of Hermite-Gauss TFMs. This Figure represents the first five (not-normalised) HG time-frequency modes.

Time-frequency modes arise naturally in parametric down-conversion processes, as they are eigenstates of the PDC Hamiltonian spanning an infinite-dimensional Hilbert space. These modes possess highly desirable properties: being centred around a target wavelength makes them compatible with waveguide integration and fibre networks, they are robust against noise [142] and chromatic dispersion [143], their pulsed nature enables synchronisation and therefore multi-photon protocols, and they offer intrinsically high dimensionality [144]. Manipulation and detection of TFMs is enabled by the quantum-pulse toolbox, where engineered sum- and difference-frequency generation are used for reshaping and projecting the quantum

states, composing a complete framework for linear optical quantum computing based on time-frequency modes encoding [144, 145].

Generating spectrally-pure heralded TFM-encoded states requires PDC in asymmetric group-velocity matching condition, as depicted in Figure 6.2 for the case of a vertical phase-matching function. In this configuration, a spectrally broad pump

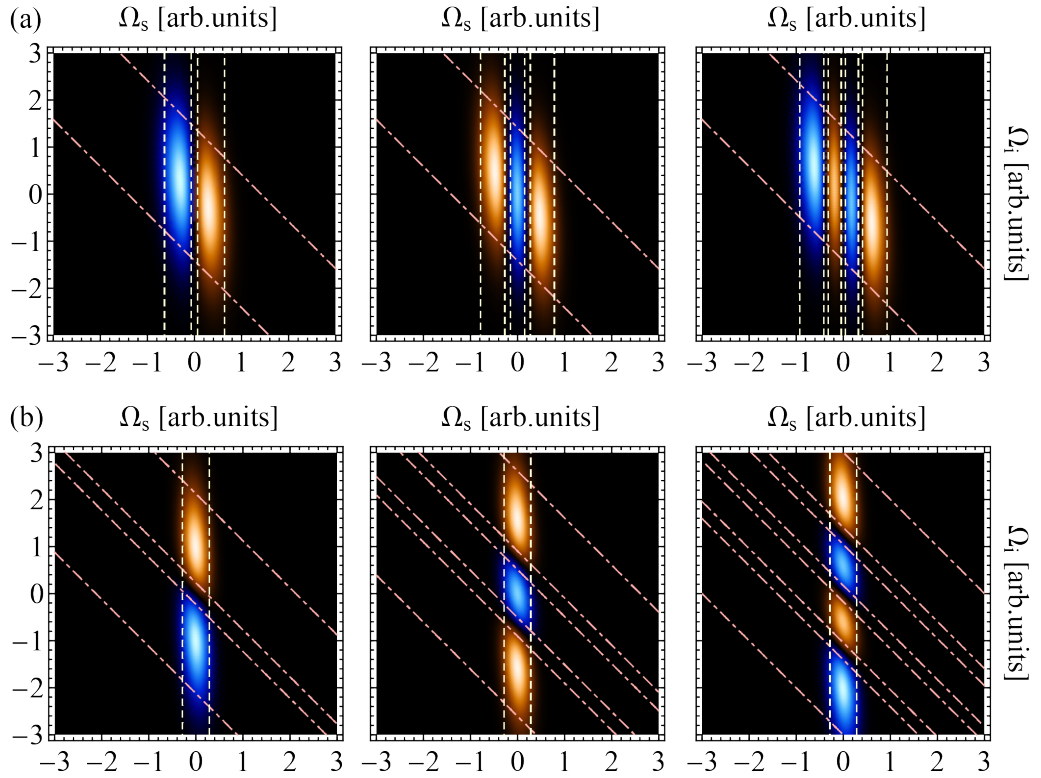


Figure 6.2: Heralded TFMs in asymmetric group-velocity matching. Heralded spectrally-pure TFMs can be generated in engineered PDC sources by either shaping the PMF (a) or the pump envelope (b). In both cases the pump function has to be much broader than the PMF to guarantee separability of the JSA. From left to right, we show HG modes of order 1, 2, and 3. The same JSA matrices shown in this picture also correspond to transfer matrices in a DFG process, meaning that one could use the same crystal to perform mode-selective TFM measurements. The red dot-dashed lines are the $1/e$ contours of the pump, while the yellow dashed lines are the PMF contours.

pulse is combined with a narrower PMF and leads to a nearly separable JSA. Unlike what we have seen in previous Chapters, however, in this case the joint spectrum is not Gaussian, as either the pump spectrum or the phase-matching function are chosen as a HG mode function (or other non-Gaussian functions that might be relevant for specific applications). This results in one of the two photons having an

approximately Gaussian spectral envelope, while the other one will have a tailored spectrum. One can therefore measure the Gaussian-shaped photon to herald the TFM-encoded one.

Incidentally, the same matrices depicted in [Figure 6.2](#) also correspond to the transfer matrix of the frequency conversion process, where one of the two axes corresponds to the input photon spectrum, and the other one to the output, as described by the interaction Hamiltonian:

$$\hat{H}_{\text{int}} = \theta \int d\omega_{\text{in}} d\omega_{\text{out}} F(\omega_{\text{in}}\omega_{\text{out}}) \hat{a}_{\text{in}} \hat{b}_{\text{out}}^\dagger + \text{h.c.}, \quad (6.1)$$

where \hat{a} and \hat{b} are the annihilation operators of the input and output modes, θ is the coupling constant, and $F(\omega_{\text{in}}\omega_{\text{out}})$ is the transfer matrix. The quantum-pulse toolbox requires engineered transfer matrices to manipulate TFM states (e.g., Hadamard and Pauli gates can be implemented with cascades of three or four frequency conversion stages), as well as to perform mode-selective projective measurements on specific TFM-encoded states. [Figure 6.2](#) shows that tailored transfer matrices can be obtained by shaping the pump as a Hermite-Gauss mode (as originally proposed in [\[145\]](#)), but equivalently one can also tailor a HG-shaped phase-matching function via domain engineering to achieve the same goal.

Parametric down-conversion also enables the generation of TFM entanglement. In this case one can work in symmetric GVM, where pump and PMF are perpendicular, and shape one of them as HG mode function, as shown in [Figure 6.3](#). The output biphoton state will exhibit time-frequency-mode entanglement, however the amplitudes of the TFM basis states might not be perfectly balanced [\[145\]](#): whenever this could be a problem for specific applications, tailoring different PEF or PMF shapes can easily overcome this problem and lead to balanced entangled TFM states [\[144\]](#).

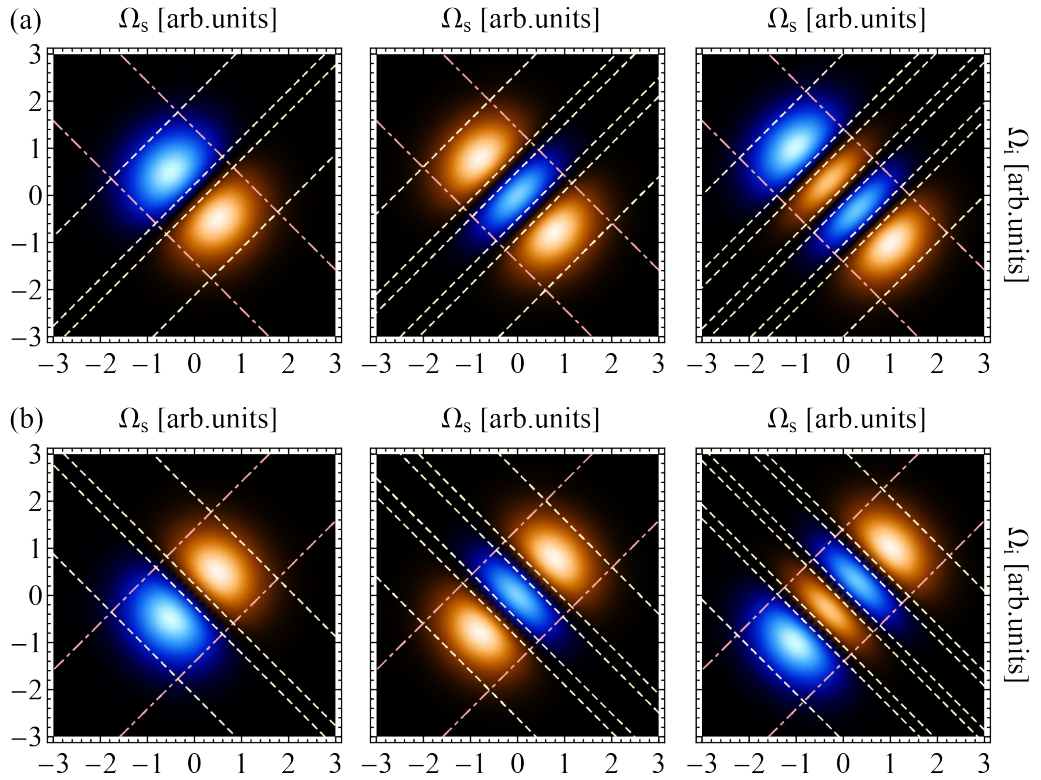


Figure 6.3: Entangled TFMs in symmetric group-velocity matching. parametric down-conversion can be engineered for producing entangled biphoton states in TFM encoding by either shaping the PMF (a) or the pump envelope (b) in symmetric GVM. From left to right, we show HG modes of order 1, 2, and 3. The red dot-dashed lines are the $1/e$ contours of the pump, while the yellow dashed lines are the PMF contours.

6.2 Nonlinearity engineering for TFM encoding

Nonlinearity engineering can be used for tailoring the PMF as an Hermite-Gauss mode function to enable TFM encoding in parametric down-conversion, as shown for example in [Figure 6.2](#) and [6.3](#). As we did for the Gaussian nonlinearity, we analyse step by step the engineering algorithm. Take for example the first-order HG mode as a target PMF (see [Figure 6.5\(a\)](#)):

$$\phi_{\text{target}}(\Delta k) = 2(\Delta k - \Delta k_0) \sigma e^{-\frac{1}{2}(\Delta k - \Delta k_0)^2 \sigma^2}. \quad (6.2)$$

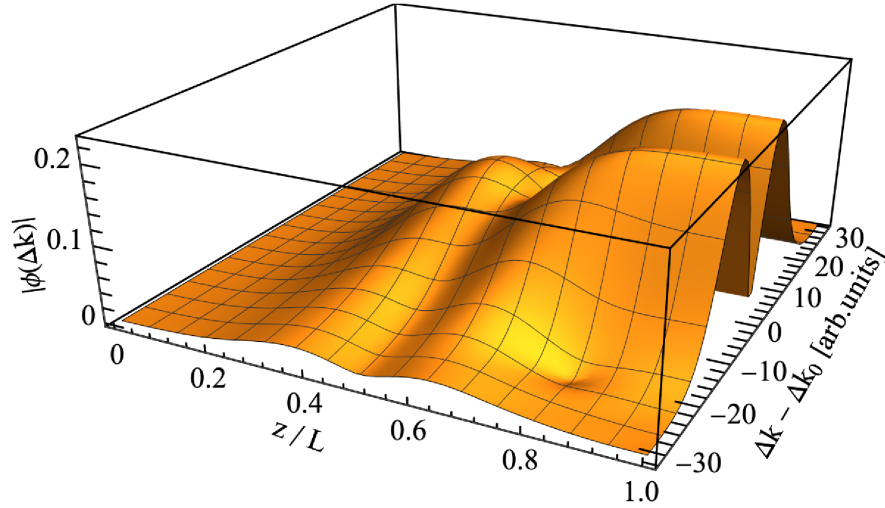


Figure 6.4: 3D phase-matching function Three-dimensional plot of the PMF $\phi_{\text{track}}(\Delta k; z)$. As expected, the PMF is 0 at the starting edge of the crystal, it then grows with a non-trivial behaviour along the longitudinal direction of the crystal, and finally assumes a first-order HG mode shape when the whole crystal is considered: $\phi_{\text{track}}(\Delta k; L)$.

The corresponding nonlinearity profile reads:

$$\begin{aligned} g_{\text{target}}(z) &= \mathcal{F}[\phi_{\text{target}}(\Delta k)] = \frac{1}{\sqrt{2}} \int_{-\infty}^{\infty} \phi_{\text{target}}(\Delta k) e^{i\Delta k z} d\Delta k \\ &= -\frac{2z e^{-\frac{z^2}{2\sigma^2} + i\Delta k_0 z}}{\sigma^2}, \end{aligned} \quad (6.3)$$

and is depicted in [Figure 6.5\(b\)](#). Then, we perform the inverse Fourier transform of Eq. (6.3): the output $\phi_{\text{track}}(\Delta k; z)$ is too complex to write down here, but we plot its envelope in [Figure 6.4](#).

We finally fix the phase mismatch to the quasi-phase-matching condition, $\Delta k = \Delta k_0$, obtaining the tracking function shown in [Figure 6.5\(c\)](#):

$$\phi_{\text{track}}\left(\Delta k = \Delta k_0; z - \frac{L}{2}\right) = \frac{2}{\pi} \sigma e^{\frac{1}{2} - \frac{L^2 + 4z^2}{8\sigma^2}} \left(e^{\frac{Lz}{2\sigma^2}} - e^{\frac{z^2}{2\sigma^2}} \right), \quad (6.4)$$

where we have already included a scaling factor (in this case equal to $\frac{\sqrt{2e}\sigma}{\pi}$), as discussed in [Chapter 4](#) for a Gaussian PMF. When the poling structure of a nonlinear crystal is chosen to track Eq. (6.4) accordingly to one of the tracking methods discussed in [Chapter 4](#), the corresponding PMF approximates the target function,

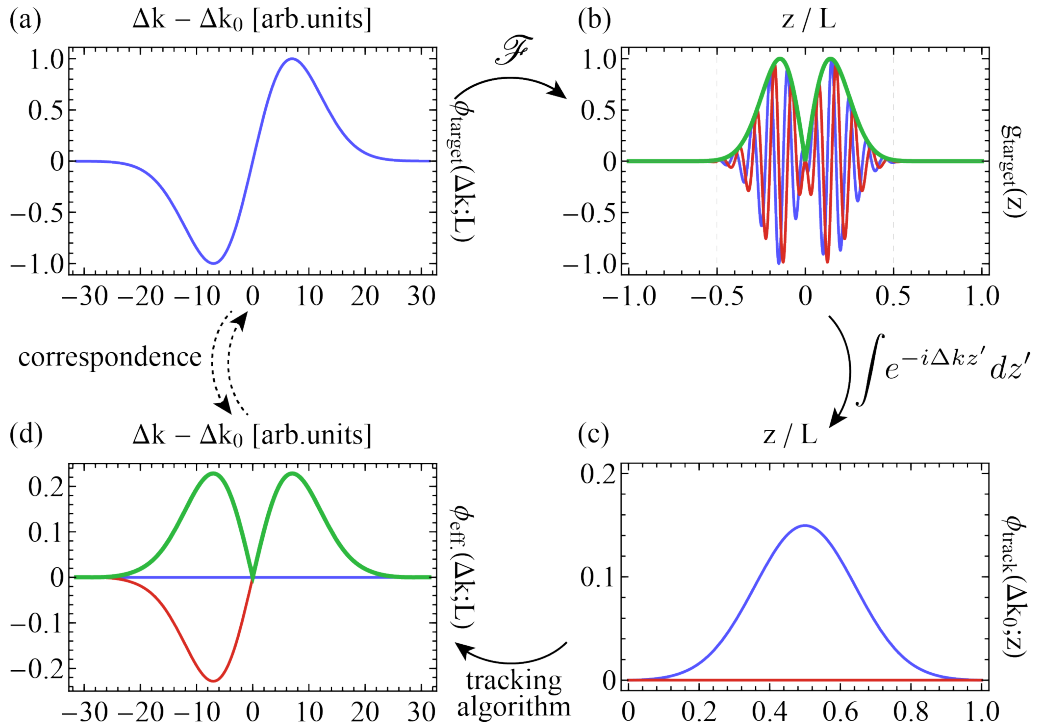


Figure 6.5: First order HG mode PMF engineering. The target PMF (a) corresponds to a nonlinearity profile (b) centred in 0. The vertical dashed lines correspond to the crystal edges. The absolute value of the nonlinearity (green line) is also shaped as the absolute value of a first order HG mode, while the real and imaginary part of the nonlinearity (blue and red lines) oscillates with period $\frac{2\pi}{\Delta k_0} = 2\ell_c$: this is an effect of the target PMF being centred in $\Delta k_0 \neq 0$. Inverse Fourier transform, shifting of the z variable, and rescaling of the function lead (c), i.e. the PMF that ought to be tracked by choosing an appropriate domain orientation pattern in the poled crystal. The effective PMF corresponding to the engineered crystal is finally shown in (d). In all the plots, blue, red, and green lines correspond to the real part, imaginary part, and absolute value of the plotted function, respectively.

as shown in [Figure 6.5\(d\)](#).

This procedure can be applied to any order of HG modes. In [Figure 6.6](#) we show target nonlinearity profile $g_{\text{target}}(z)$, tracking function $\phi_{\text{track}}\left(\Delta k = \Delta k_0; z - \frac{L}{2}\right)$ and corresponding PMF shaped as the first seven HG modes.

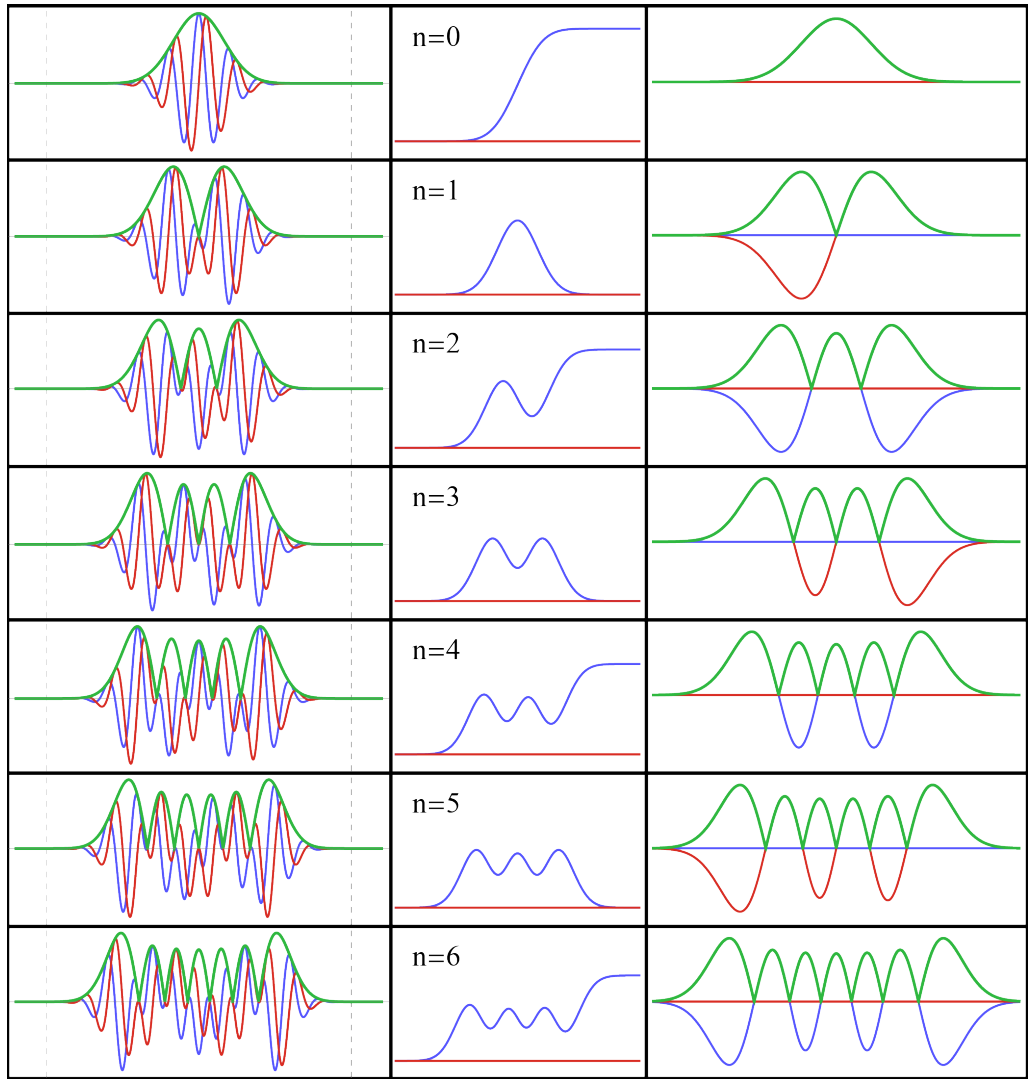


Figure 6.6: Nonlinearity engineering for TFM generation. Nonlinear-profile (left), tracking function (centre) and corresponding PMF (right) for first seven orthogonal HG modes.

6.3 Experimental TFM entanglement generation

6.3.1 Target TFM-entangled state

Let's consider a Gaussian pump-envelope function combined with a first-order HG mode phase-matching function:

$$\begin{aligned}
 \alpha(\omega_s, \omega_i) &= e^{-\frac{(\omega_s + \omega_i)^2}{2\sigma^2}} \\
 \phi(\omega_s, \omega_i) &= e^{-\frac{(\omega_s - \omega_i)^2}{2\sigma^2}} (\omega_s - \omega_i) .
 \end{aligned} \tag{6.5}$$

The corresponding PDC first-order biphoton state reads:

$$\begin{aligned}
 |\psi^-\rangle_{s,i} &= \iint d\omega_s d\omega_i \alpha(\omega_s, \omega_i) \phi(\omega_s, \omega_i) a_s^\dagger(\omega_s) a_i^\dagger(\omega_i) |0\rangle_{s,i} \\
 &= \iint d\omega_s d\omega_i \exp\left[-\frac{\omega_s^2 + \omega_i^2}{\sigma^2}\right] (\omega_s - \omega_i) a_s^\dagger(\omega_s) a_i^\dagger(\omega_i) |0\rangle_{s,i},
 \end{aligned} \tag{6.6}$$

where we are omitting the wavefunction normalisation, and the corresponding joint spectrum is shown in [Figure 6.7](#) (a).

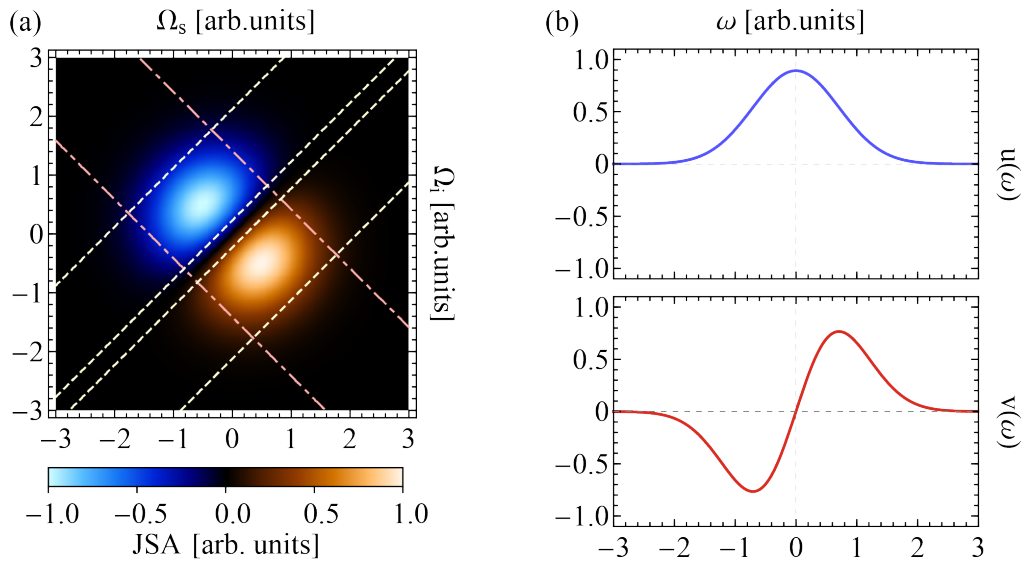


Figure 6.7: JSA and time-frequency modes. Joint spectrum (a) and corresponding TFMs (b) that compose the PDC state.

Eq. (6.6) can be decomposed via Schmidt decomposition considering the zero- and first-order HG modes:

$$\begin{aligned}
 |u\rangle_j &\equiv |\wedge\rangle_j = \int d\omega_j \exp\left[-\frac{\omega_j^2}{\sigma^2}\right] a_j^\dagger(\omega_j) |0\rangle_j \\
 |v\rangle_j &\equiv |\vee\rangle_j = \int d\omega_j \exp\left[-\frac{\omega_j^2}{\sigma^2}\right] \omega_j a_j^\dagger(\omega_j) |0\rangle_j,
 \end{aligned} \tag{6.7}$$

with $j = s, i$, and where we are neglecting the normalisation constants. The shape of the two spectral modes is shown in [Figure 6.7](#) (b). Following from (6.7), the

biphoton state can be therefore written as follows:

$$\begin{aligned} |\psi^-\rangle_{s,i} &= \frac{1}{\sqrt{2}} (|u\rangle_s |v\rangle_i - |v\rangle_s |u\rangle_i) \\ &= \frac{1}{\sqrt{2}} (|\wedge\rangle_s |\vee\rangle_i - |\vee\rangle_s |\wedge\rangle_i), \end{aligned} \quad (6.8)$$

where $\wedge = u(\omega)$ and $\vee = v(\omega)$ in [Figure 6.7\(a\)](#). The state in [Eq. \(6.8\)](#) is a maximally entangled singlet state in the spectral-temporal mode basis.

To approximate the ideal case in [Eq. \(6.8\)](#), we use nonlinearity engineering to tailor a first-order HG-shaped PMF, as discussed in detail in the previous Section. We design an apodised 30 mm-long KTP crystal for close-to-symmetric GVM (the PMF is at $\sim 48^\circ$ in the (ω_s, ω_i) plane). The fundamental domain width is $\sim 23.1 \mu\text{m}$, equal to the coherence length of a 775 nm pump down-converted into two 1550 nm photons. The domain structure, [Figure 6.8 \(b\)](#), is quite different from the ones shown in [Figure 5.3](#) and [Figure 5.8](#) for Gaussian-shaped PMFs: the domain pattern of “longer - shorter - longer blocks” is now replaced with a pattern of the kind “longer - shorter - longer - shorter - longer blocks”, due to the very nature of the tracking function that has a flat section in the middle of the crystal. The absolute value of the PMF, [Figure 6.8 \(c\)](#), has the expected shape, and the phase is linear where the amplitude is not non-negligible, with a π shift in Δk_0 , as expected from the first-order HG function. We’ll discuss again the nature of this linear phase in the next Sections.

By considering a 1.3 ps pump pulse, we can also numerically simulate the $|\text{JSA}|$ of the process, that we show in [Figure 6.8 \(a\)](#).

6.3.2 Experimental setup

The photon-pair source is exactly the same as described for pure heralded photons generation in [Chapter 5](#), and depicted in [Figure 5.2](#), where the Gaussian shaped crystals are replaced with TFM crystals

1.3 ps-long, 775 nm laser pulses with 80 MHz repetition rate are focused into the tailored KTP crystal to create orthogonally-polarised 1550 nm photon pairs via

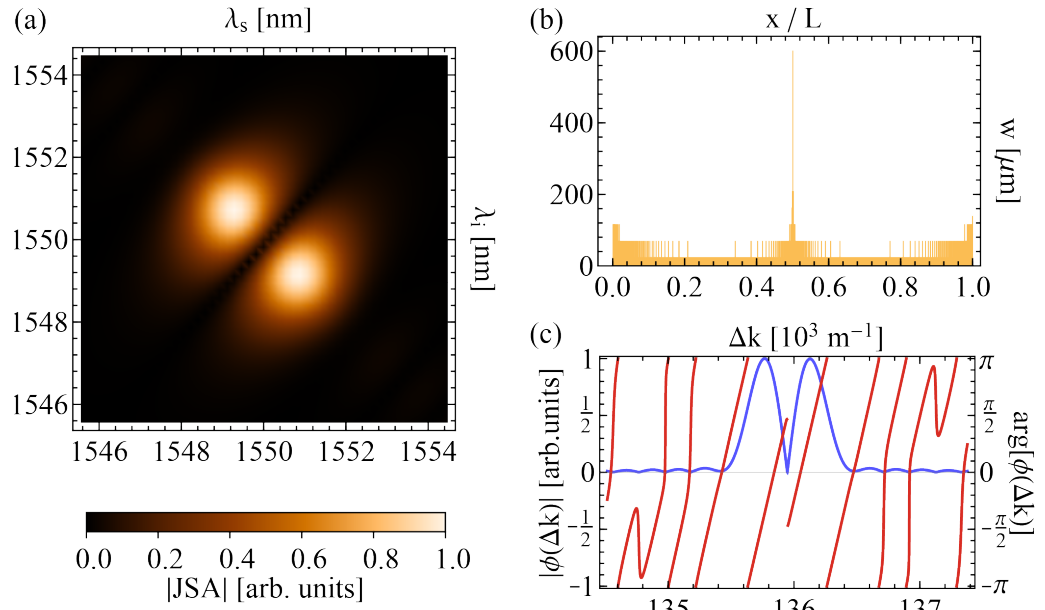


Figure 6.8: Crystal design. Simulated $|JSA|$ (a), poling pattern in the crystal (b), and simulated PMF (absolute value in blue, phase in red).

type-II PDC. The photons are loosely filtered with a band-pass filter (~ 3 times broader than the PDC photons' bandwidth). A polarising BS separates them before they are coupled into single-mode fibres. When the source is sent to the SNSPDs, we measure a brightness of ~ 4 kHz/mW photon pairs with a symmetric heralding efficiency higher than 60%, a reasonable trade-off achieved by optimising the pump, signal and idler focusing conditions [16, 132–134].

A full characterisation of the biphoton quantum state could be obtained via quantum state tomography in the TFM basis, which requires projective measurements onto three mutually unbiased bases using cascades of tailored nonlinear processes [146–148], or by reconstructing the JSA including its phase, which assumes a pure biphoton state and involves complex interferometric techniques [106, 108, 149]. We instead characterise the PDC state using an indirect approach that exploits joint spectral intensity reconstruction via dispersive fibre spectroscopy [101] and two-photon interference to infer information on populations and entanglement of the quantum state, respectively. The experimental setups for the biphoton characterisation is shown in Figure 6.9.

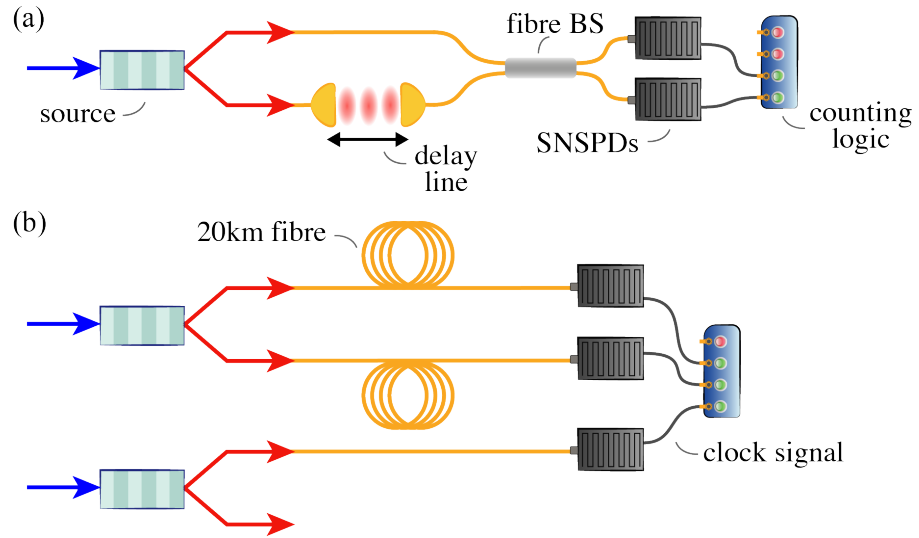


Figure 6.9: Experimental setup. Two-photon interference setup (a) and dispersive fibre spectroscopy setup (b).

6.3.3 Dispersive fibre spectroscopy

The setup for the JSI reconstruction is shown in [Figure 6.9 \(b\)](#). Each photon is sent through ~ 20 km single-mode fibre to convert spectral to temporal information exploiting the fibre dispersion of ~ 18 ps/km/nm at 1550 nm. The photons are then detected with SNSPDs with nominal 80% detection efficiency and < 50 ps timing jitter. Arrival times are recorded as time tags by a *Picoquant HydraHarp* in 1 ps bins for offline processing. We collected $\sim 2.8 \times 10^6$ two-photon coincidence counts with respect to a clock signal, used to centre the JSI matrices, in 24 hours. The clock consisted of a third SNSPD triggered by an independent PDC source (at ~ 0.9 MHz count rate) synchronously pumped by the same laser pulse. We reconstruct 12250×12250 JSI matrices, where each bin has a size of 1×1 ps, corresponding to the timing logic's resolution. We calibrate our dispersive-fibre spectrometer with a reference signal with respect to a commercial single-photon CCD spectrometer, obtaining a scaling factor of ~ 2.94 pm/ps (centred around 1550 nm). This corresponds to a 36 nm spectral range, ~ 12 times larger than the PDC photons' bandwidth, to ensure reliable estimation of the JSI properties as discussed in [Chapter 3](#). We down-sample the JSI matrices to 40×40 ps bins for reducing the sparsity of the data and computing the singular value decomposition as numerical implementation

of the Schmidt decomposition.

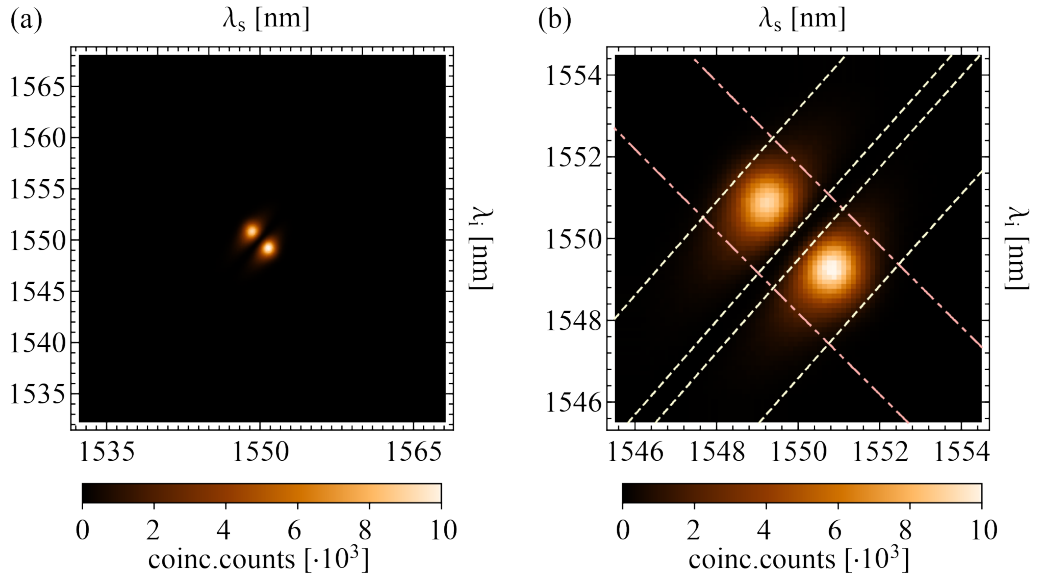


Figure 6.10: JSI matrices via fibre spectroscopy. Reconstructed JSI matrix over the whole 36 nm spectral range (a), and focusing on a reduced 12 nm range (b). The red dot-dashed lines represent the $1/e^2$ contours of the PEF, while the yellow dashed lines the PMF ones.

Results are shown in [Figure 6.10](#) over the whole (a) and reduced (b) spectral range. The overlay contours show the theoretical pump spectrum and the numerically calculated PMF, assuming the ideal crystal domain structure and a sech^2 pump function. There is excellent correspondence between the theoretical target and the measured JSIs, which faithfully reproduces not only the two main peaks but also the spectral bandwidth.

6.3.4 Two-photon interference

In [Section 3.2.2](#) we have seen how signal-idler HOM interference can be used to infer the antisymmetry of the biphoton down-converted state. Here we use this result to study the spectral properties of the target state in [Eq. \(6.8\)](#), that ideally is maximally antisymmetric in the photon spectra.

We can calculate the signal-idler interference pattern in [Eq. \(3.19\)](#) for the anti-

symmetric normalised JSA of the biphoton state:

$$f(\omega_s, \omega_i) = \frac{2}{\sqrt{\pi}\sqrt{\sigma^4}} e^{-\frac{\omega_i^2 + \omega_s^2}{\sigma^2}} (\omega_s - \omega_i), \quad (6.9)$$

and we obtain the following equation:

$$p_{cc}(\Delta t) = \frac{1}{2} - \frac{1}{4} e^{-\frac{1}{4}\sigma^2\Delta t^2} (\sigma^2\Delta t^2 - 2), \quad (6.10)$$

where p_{cc} is the coincidence-count probability after interference, σ depends on the biphoton bandwidth and Δt is the relative arrival time of the two photons at the BS. As expected from a maximally antisymmetric joint spectrum, the coincidence probability when the photons arrive simultaneously at the BS is 1, meaning that they always anti-bunch. Remarkably, for a biphoton state that is separable in all other degrees of freedom, anti-bunching at a BS corresponds to entanglement in the biphoton spectrum, and we can use this result to verify TFM entanglement in our generated state [111, 150–152].

Using the setup in [Figure 6.9](#) (a), we measure the interference pattern by delaying one photon with respect to the other before they interfere in a fibre BS. We show the experimental data for two apodised crystals in [Figure 6.11\(a\)](#): the fitted HOM visibility is equal to $(99.4 \pm 0.4)\%$, where we use Eq. (6.10) with an additional visibility scaling factor to fit the data, certifying a high degree of spectral entanglement of the PDC biphoton state.

Small variations in the crystal domain widths can be introduced by changing the crystals temperature. This results in a shift of the PMF in the (ω_s, ω_i) plane, as discussed in [Chapter 2](#), producing frequency non-degenerate photons and therefore compromising the antisymmetry of the biphoton wavefunction. Surprisingly, this doesn't affect the Schmidt number of the quantum state: the biphoton state structure remains intact, but the signal and idler TFMs will be centred around different frequencies. This enables the capability of switching between an antisymmetric state to a non-antisymmetric one without spoiling the spectral modal structure. We observe the biphoton antisymmetry-breaking by performing HOM scans at different

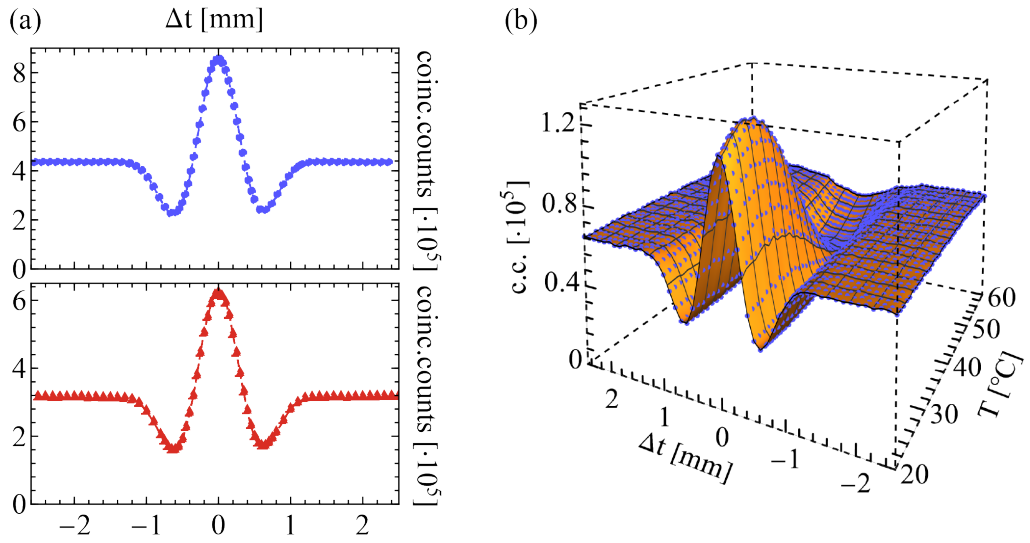


Figure 6.11: Signal-idler interference. (a) Signal-idler interference for two apodised crystals with antisymmetric PMF. (b) Signal-idler interference varying crystal temperature. The HOM visibility has a maximum at 25°C , while no antibunching occurs above 39°C . Error bars assuming Poissonian counting statistics are smaller than the symbol size.

temperatures, from 20° to 60° at 1° intervals. We show the results in Figure 6.11(b): anti-bunching (and therefore antisymmetry) is maximal for perfectly degenerate PDC and it reduces as we tune away from degeneracy, until no anti-bunching occurs above a certain centre-frequency offset, as expected from theory.

In Chapter 3 we have seen that the spectral purity (and, consequently, the Schmidt number) of the JSA can be mapped to the interference visibility in an heralded-photon HOM experiment between two identical PDC sources. We can use the same experimental scheme described in Figure 5.5 (c) for estimating the heralded-photon purity: two (nearly) identical PDC sources emit simultaneously two photon pairs, one photon of each pair is detected to provide a heralding signal for its twin photon, and the heralded photons are finally interfered on a fibre BS. Since the $|\psi^-\rangle$ state in Eq. (6.8) is composed of two equally-weighted TFM basis states, the corresponding Schmidt number is expected to be equal to 2. We can in fact calculate the heralded interference pattern according to the HOM equation (3.26) calculated for the antisymmetric JSA in Eq. (6.9), obtaining the following relation:

$$p_{cc}(\Delta t) = \frac{1}{2} - \frac{1}{128} e^{-\frac{1}{4}\Delta t^2 \sigma^2} (\Delta t^4 \sigma^4 + 32), \quad (6.11)$$

where the visibility of the interference pattern is equal to $1 - 2p_{cc}(0) = 1/2$, corresponding to a Schmidt number equal to 2.

We experimentally measure an interference visibility of $(48.8 \pm 1.2)\%$ at 30 mW of average pump power, which corresponds to a Schmidt number of 2.05 ± 0.05 , in excellent agreement with theory. The interference data are shown in [Figure 6.12](#).

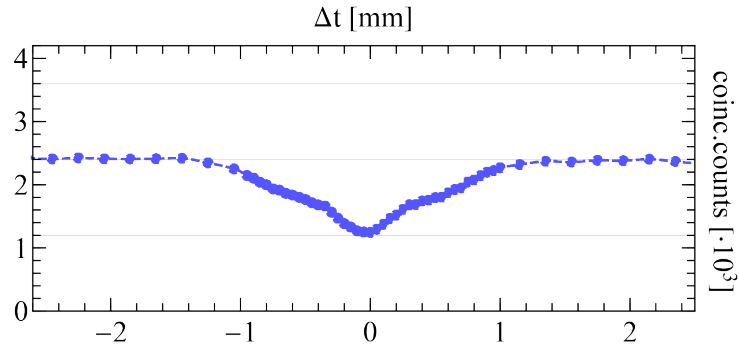


Figure 6.12: Heralded-photons interference. Heralded-photon interference pattern for estimating the JSA Schmidt number. Error bars assuming Poissonian counting statistics are smaller than the symbol size.

6.3.5 Effective JSA reconstruction

The JSI reconstruction provides full information on the absolute value of the JSA, but it doesn't give any information on the phase of the biphoton state. In the case of Eq. (6.8), the value of $|JSA|$ corresponds to:

$$|f(\omega_s, \omega_i)| = \exp \left[-\frac{\omega_s^2 + \omega_i^2}{\sigma^2} \right] |\omega_s - \omega_i|, \quad (6.12)$$

which is in good agreement with the JSI we measured and showed in [Figure 6.10](#).

While the JSI reconstruction doesn't contain any phase information, we can exploit our knowledge of the antisymmetry and Schmidt number of the biphoton wavefunction to reconstruct an "effective" JSA. Specifically, to guarantee antisymmetry and bi-modal structure of the quantum state (that we measured via signal-idler and heralded-photon HOM interference), we impose a $e^{i\pi}$ sign shift between the two peaks of the square root of the measured JSI. This antisymmetric phase shift matches, up to an additional linear phase, the output of the nonlinearity-engineering

algorithm that generates the state in Eq. (6.8).

Any additional phase that multiplies Eq. (6.12) has to provide an antisymmetric state in the signal and idler frequencies, otherwise it wouldn't produce a HOM peak: moreover, it also has to preserve the very specific interference pattern we derived in Eq. (6.10) and measured (see Figure 6.11). In particular, we restrict our analysis on JSA phase to a function of the form $(\omega_s - \omega_i)$: this is a good approximation for the symmetric group-velocity matching condition, where the dependence of Δk on the signal and idler frequencies rising from the phase-matching function is linear and perpendicular to the pump field, as we discussed and showed in Chapter 2, Figure 2.5 (a).

We consider an additional linear phase, as this is the expected PMF structure produced by the nonlinearity engineering scheme used to design the crystal, as shown in Figure 6.8. Under this assumption, the JSA reads:

$$f(\omega_s, \omega_i) = \exp \left[-\frac{\omega_s^2 + \omega_i^2}{\sigma^2} \right] (\omega_s - \omega_i) \exp [i \text{const} (\omega_s - \omega_i)], \quad (6.13)$$

where “const” is the gradient of the phase, and the Schmidt decomposition provides the corresponding orthonormal modes:

$$\begin{aligned} |u\rangle_j &\equiv |\wedge\rangle_j = \int d\omega_j \exp \left[-\frac{\omega_j^2}{\sigma^2} \pm i \text{const} \omega_j \right] a_j^\dagger(\omega_j) |0\rangle_j \\ |v\rangle_j &\equiv |\vee\rangle_j = \int d\omega_j \exp \left[-\frac{\omega_j^2}{\sigma^2} \pm i \text{const} \omega_j \right] \omega_j a_j^\dagger(\omega_j) |0\rangle_j, \end{aligned} \quad (6.14)$$

where the $+$ ($-$) sign is used for the signal (idler) photon, and we are neglecting the normalisation constants. The Schmidt number corresponding to Eq. (6.14) is 2, as for the antisymmetric JSA without linear phase, and the overall JSA is still antisymmetric. The corresponding HOM pattern reads:

$$p_{\text{cc}}(\Delta t) = \frac{1}{2} - \frac{1}{4} e^{-\frac{1}{4}\sigma^2(\Delta t + 2\text{const})^2} (\sigma^2(\Delta t + 2\text{const})^2 - 2), \quad (6.15)$$

which still exhibits perfect antibunching and the same interference shape (only translated by twice the value of the constant). This phase is therefore a suitable candidate

for describing the measured quantum state, as expected from the crystal engineering technique used to tailor the PMF and consequently the JSA of the PDC process. Other phase structures might, in principle, give rise to a JSA having a Schmidt number equal to 2 while preserving the same HOM structure: testing this possibility would require a phase-sensitive JSA reconstruction [106, 108, 149].

As a result of the analysis above, we only apply a $e^{i\pi}$ sign shift between the two peaks of the $|JSA|$, as an additional linear phase factor is negligible. The effective JSA obtained in this way is depicted in Figure 6.13. It qualitatively matches the theoretical target JSA shown in Figure 6.7(a) and has an effective Schmidt number of 2.026 ± 0.001 , consistent with the HOM measurement and with our numerical simulations. The error on the extracted Schmidt numbers represents 3σ statistical confidence regions obtained via Monte-Carlo re-sampling (10k runs of the algorithm) assuming a Poissonian statistics on the coincident counts distribution.

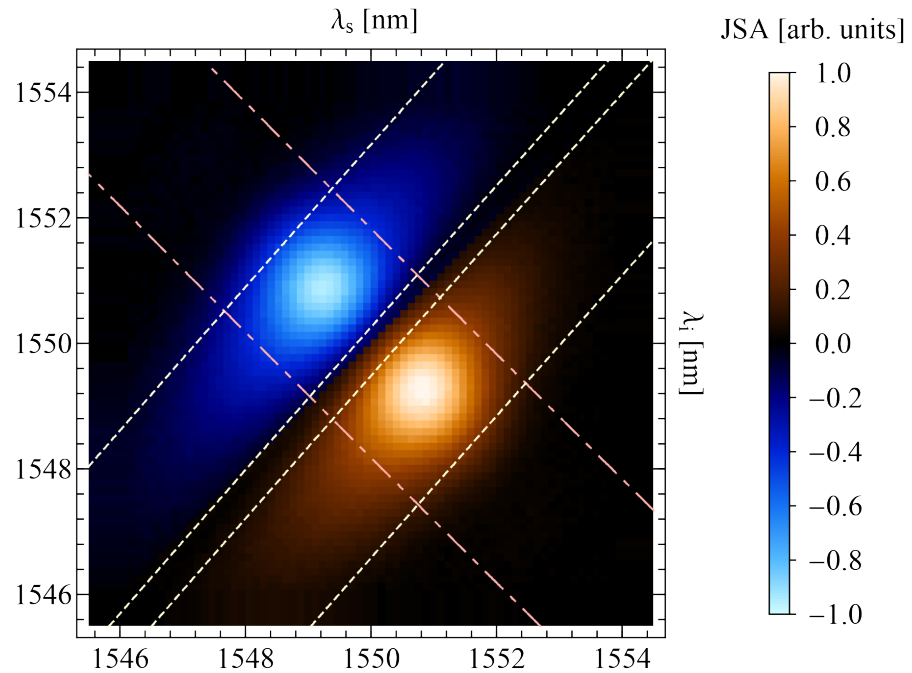


Figure 6.13: Effective JSA. Joint spectral amplitude reconstructed with dispersive fibre spectroscopy and HOM interference to infer the phase structure of the biphoton spectrum.

6.4 TFM entanglement swapping

Multiphoton protocols using TFMs will require the ability to interfere and swap independently generated TFM-encoded photons. While a generalised entanglement swapping for TFM has been proposed, it relies on a nonlinear process between two single photons and therefore has very low success probability [153]. Here, instead, we implement the standard entanglement swapping scheme with the setup shown in Figure 6.14. A similar experiment has been reported slightly after ours [154] where TFM entanglement swapping is heralded by a frequency-resolved Bell-state measurement, and verified using a similar scheme.

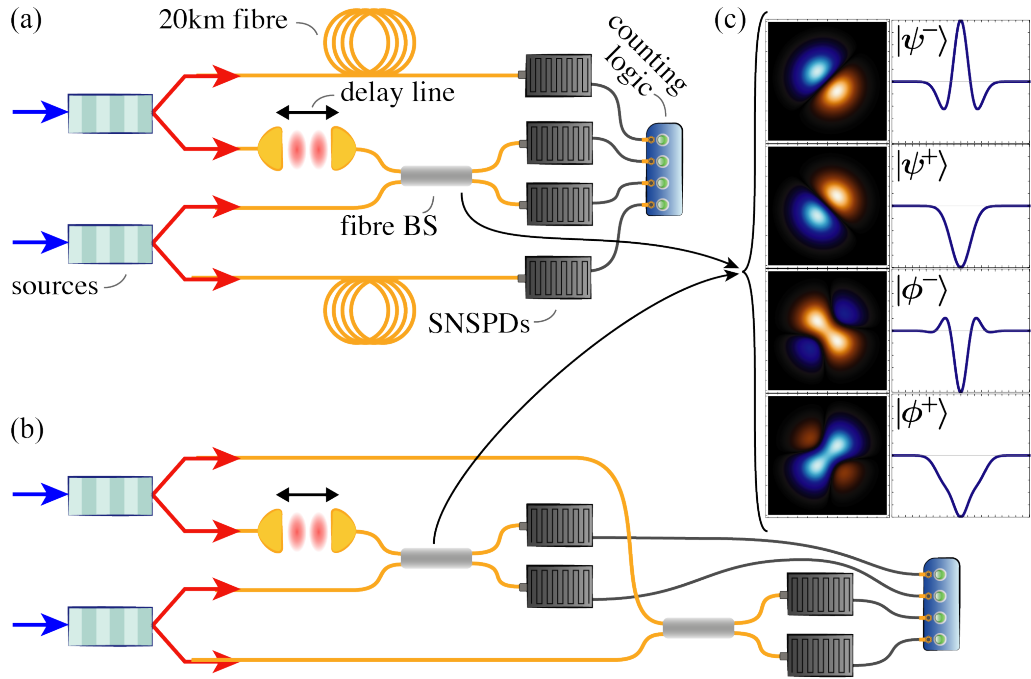


Figure 6.14: TFM entanglement swapping setup. Fibre spectroscopy (a) and double HOM interference (b) setups for implementing the TFM entanglement swapping scheme.

Two entangled $|\psi^-\rangle$ states are produced via two independent engineered TFM-entangled pair sources:

$$|\Psi\rangle = |\psi^-\rangle_{1,2} |\psi^-\rangle_{3,4}, \quad (6.16)$$

where $|\dots\rangle_{1,2}$ are the mode indices of the first source, while $|\dots\rangle_{3,4}$ corresponds to the second source.

The overall four-photon state in Eq. (6.16) can be rewritten as:

$$|\Psi\rangle = \frac{1}{2}(|\phi^+\rangle_{1,4}|\phi^+\rangle_{2,3} + |\phi^-\rangle_{1,4}|\phi^-\rangle_{2,3} + |\psi^+\rangle_{1,4}|\psi^+\rangle_{2,3} - |\psi^-\rangle_{1,4}|\psi^-\rangle_{2,3}), \quad (6.17)$$

where we are grouping together the heralding modes $|\dots\rangle_{1,4}$ and the interfering modes $|\dots\rangle_{2,3}$. The four Bell states in Eq. (6.17) are defined as:

$$\begin{aligned} |\psi^\pm\rangle &= \frac{1}{\sqrt{2}}|\wedge\rangle|\vee\rangle \pm |\vee\rangle|\wedge\rangle \\ |\phi^\pm\rangle &= \frac{1}{\sqrt{2}}|\wedge\rangle|\wedge\rangle \pm |\vee\rangle|\vee\rangle. \end{aligned} \quad (6.18)$$

The joint spectra for all four Bell states and the corresponding HOM patterns are shown in Figure 6.14(c): perfect antibunching at the BS occurs only for the singlet state $|\psi^-\rangle$, while triplet states $\{|\psi^-\rangle, |\phi^+\rangle, |\phi^-\rangle\}$ bunch due to the symmetry of their wavefunctions. We use this knowledge to discern a successful projection on $|\psi^-\rangle_{2,3}$ from all the other outcomes after the (first) fibre BS: a two-photon coincidence detection at the two BS outputs corresponds to a projection on the singlet state, and heralds swapping of the TFM $|\psi^-\rangle$ state from the two original photon pairs to the two non-interacting photons.

We benchmark the heralded swapped state via fibre spectroscopy and HOM interference, as shown in Figure 6.14, (a) and (b) respectively.

The JSI of the swapped $|\psi^-\rangle_{1,4}$ state is measured by sending the two photons through a pair of 20 km single-mode fibres, as we did in the previous Sections. Unlike the standard biphoton JSI reconstruction discussed before, where an external clock signal is needed to reference the arrival time of signal and idler, in this entanglement swapping scheme a two-clicks event in the SNSPDs at the output of the BS acts both as herald of a successful projection on $|\psi^-\rangle_{2,3}$, and as a clock signal for the arrival time of the photons in modes (1, 4). This is possible because the photons in modes (2, 3) after the BS are not sent through long fibres, and their arrival time is well defined in time (and within the detector jitter window): therefore, there is no need for an additional clock signal.

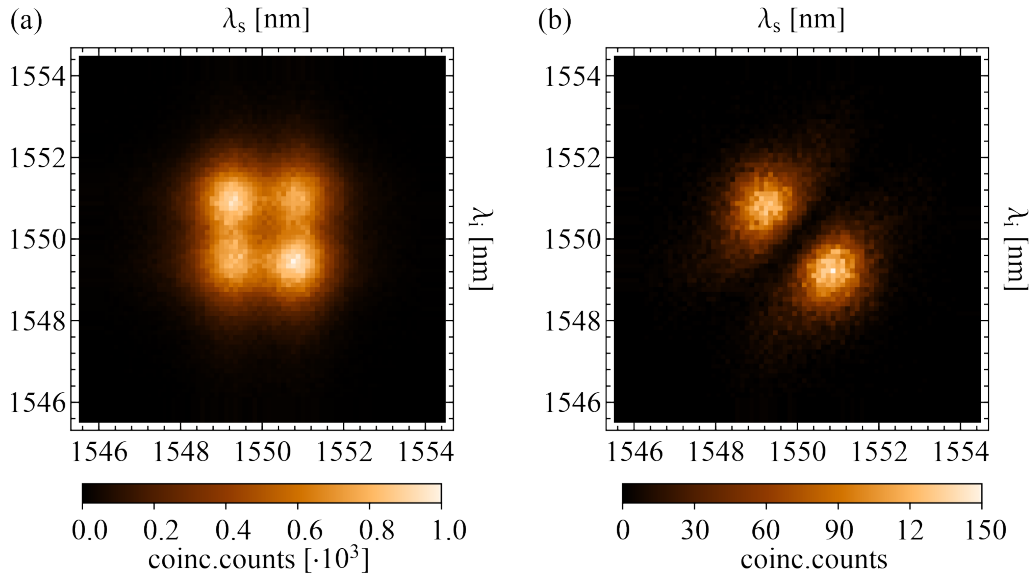


Figure 6.15: TFM entanglement swapping: fibre spectroscopy. Reconstructed JSIs corresponding to the mixed state (a) and the swapped $|\psi^-\rangle$ state (b).

In [Figure 6.15\(a\)](#) we show the measured joint spectrum of the two-photon state without post-selection, where we consider as heralding signal either one or two detection events after the BS, corresponding to 3-fold and 4-fold coincidence counts, respectively. We collect 670k 3-fold and 46k 4-fold coincident counts in 72 hours of integration time. We observe 4 peaks, arising from a mixture of the four equally weighted Bell state JSAs (depicted in [Figure 6.14\(c\)](#)). When we instead record only 4-fold coincident counts, we measure the spectrum of the swapped $|\psi^-\rangle$ biphoton state, recovering the two main peaks on the JSI's diagonal, as shown in [Figure 6.15 \(b\)](#).

We then measure two-photon interference of the swapped state with the setup in [Figure 6.14 \(b\)](#), where we add an additional HOM stage for the modes $|\dots\rangle_{1,4}$. Because the probability of generating photon pairs independently in two sources equals that of a double-pair emission in each source, the maximal theoretical HOM visibility is 25%. This is not a fundamental limitation of the scheme, but it only occurs when both photons of two PDC pairs are interfered, which is not required in realistic applications as, e.g., repeater protocols. We obtain an interference visibility of $(24.5 \pm 0.5)\%$, as shown in [Figure 6.16\(a\)](#). We subtract the multi-photon

background by recording the counts when either of the two photon sources are blocked. The corrected interference pattern in Figure 6.16(c) yields a HOM visibility of $97.1 \pm 1.7\%$, certifying success of the TFM entanglement swapping protocol.

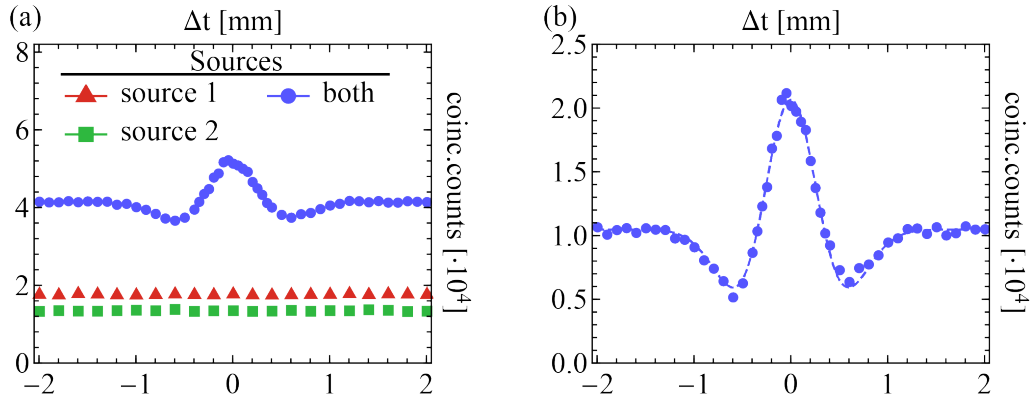


Figure 6.16: TFM entanglement swapping: two-photon interference. HOM interference for benchmarking the TFM entanglement swapping scheme. In (a) we show 4-fold coincidences at the outputs of the two BSs in Figure 6.14 (b), looking at contributions from source 1 (red triangles), source 2 (green squares) or both sources (blue dots). In (b) we subtract the single-source contributions from the overall recorded counts to correct for higher-order PDC emission.

We can finally reconstruct the effective JSA of the swapped state under the assumptions discussed earlier, imposing the $e^{i\pi}$ sign shift between the two peaks of the square root of the measured JSI. We calculate a Schmidt number of 2.15 ± 0.01 : a value slightly higher than for the single-source scenario, as expected due to discrepancies between independent sources that affect the interference quality.

6.5 Conclusion and future directions

The controlled generation and detection of TFM entanglement is a very challenging task [155–159], limiting its usefulness in realistic scenarios. Here, we have discussed how nonlinearity engineering can help us tackling this challenge, enabling generation of TFM entanglement from standard ultrafast laser pulses in single-pass PDC sources. We experimentally validate this technique by benchmarking a maximally antisymmetric state at telecom wavelength with near unity fidelity, and implement

a four-photon entanglement swapping scheme. Our work complements the pulse-gate toolbox [144, 145] for TFM quantum information processing, and establishes a standard for the generation of TFM quantum states of light while paving the way for more complex frequency encoding.

Due to its simplicity and quality, we expect this technique to be used in a host of different quantum information tasks. The flexibility in tailoring the PMF lends itself to the generation of high-dimensional TFM entanglement: not only can one use higher-order Hermite-Gaussian PMFs to up-scale to qudits, as discussed in the beginning of this Chapter, but one can also aim at different PMF shapes for targeting specific applications, such as frequency multiplexing [160].

The natural step forward will be using quantum pulse gates to implement projective measurements in the TFM space, enabling TFM-encoded quantum information processing protocols. This can be achieved working in asymmetric group-velocity matching condition, by either shaping the pump pulse or the PMF, as we have seen in this Chapter. Moreover, the advent of reconfigurable functional materials [161] would make this technique even more appealing for practical applications in generation and detection of TFMs.

Finally, the ability to customise biphoton spectra could be useful for multiphoton quantum metrology applications in which measurement precision depends on the shape and steepness of the HOM pattern [162].

Er senso della vita è la vita.
Er fine della vita è la fine.

Corrado Guzzanti, *Don Pizarro*

CHAPTER 7

Conclusion

We are finally at the end of this Thesis, and I believe there is not much to add to what has been said in the previous (and following) pages. I hope to have convinced the reader that, if photonics aims to be the leading platform for quantum information applications, a lot of work in engineering reliable and high-performance single photon sources has yet to be done, but the foundations have already been laid.

Parametric down-conversion (or other probabilistic sources based on nonlinear processes) has the potential to fulfil this role as efficient source, if its three major drawbacks are overcome: probabilistic emission, photon number purity, and spectral purity. Both PDC probabilistic nature and photon number purity problems still require quite some engineering to be considered solved, but I think that either source multiplexing [20] with improved low-loss fast switches, or optimised temporal multiplexed sources [23], (or a combination of the two) will be able to address these problems sufficiently well. On the other hand, the challenge of increasing the photon spectral purity has been intensively discussed in this manuscript, and I believe it is fair to say that it has been in large part solved.

What would now be of utmost importance, is to start combining these solutions into a single device that can actually fulfil all the requirements of a single photon source. The simplicity of nonlinearity engineering allows one to easily combine it with the aforementioned multiplexed schemes, and building a prototype of a high efficient source under all aspects should now be near at hand.

While such a source would probably already meet industry standards for useful

applications in fields where not many photons are required (e.g. two-party quantum communication), it would only be another milestone in the route towards a photonic device for quantum information processing. In that sense, the natural following step would be to start implementing nonlinearity engineering in photonic chips, where miniaturisation of optical components would enable scalability to many photons quantum architectures.

Moving beyond these technological aspects, there are a few topics that would require further investigation.

For example, it is known that focusing and collection conditions in a bulk PDC source affect both efficiency and spatial/spectral properties of the PDC photons [16, 53, 132–134]. A thorough study that considers crystal structure (when nonlinearity engineering is used), spectral properties and overall source efficiency in relation to the focusing parameters is, to my knowledge, still missing, and it would be relevant from both a scientific and a technological point of view.

Another open question is how nonlinearity engineering would behave when used to tailor the nonlinearity of (integrated) waveguides. From a fundamental point of view, there shouldn't be any substantial difference with the bulk crystal case. However, waveguide geometry and fabrication errors influence (in some case significantly) the material dispersion and the overall phase-matching function of the process [163], and I believe an in-depth analysis is required to understand whether nonlinearity engineering and field propagation in the waveguide can be treated independently (e.g. use the latter to find the fundamental poling period and feed it into the engineering algorithm), or if there is an interplay between the two that needs to be taken into account in a generalised framework.

As most of the analysis of the joint spectral amplitude properties can be directly mapped to the four-wave mixing case, it is natural to ask if (the ideas behind) nonlinearity engineering can be applied to this nonlinear process. In this regard, there are already proposals and proof-of-principle experiments addressing this questions. For example, one could think of modifying the tapering structure of periodically tapered waveguides [164] introducing an effective tailored nonlinearity, as we did

in this work for the ferroelectric domains of poled crystals. Another solution, that has been recently demonstrated [26] is to use dual-mode pump-delayed excitation in spiralled waveguides to increase the output photons' purity without narrowband filtering: this solution, despite sharing the same underlying purpose of nonlinearity engineering, is based on a quite different physical implementations.

Finally, it would be very interesting to use nonlinearity engineering in frequency-conversion schemes to complement the quantum pulse gate framework, implementing direct manipulation and projection of the time-frequency modes-encoded photons and, in the long-term, building TFM-based devices for useful quantum photonics applications.

Like all people who try to exhaust a subject, he exhausted his listeners.

Oscar Wilde, *The Picture of Dorian Gray*

APPENDIX A

Poling errors effects at smaller spectral range

Analogously to the analysis conducted in Chapter 4, in Appendix we report the effects of poling errors on different types of poling. Instead of considering a very wide spectral range (as I did previously, where a spectral range ~ 25 larger than the PDC photons bandwidth was taken into account), here we consider the effect of poling errors on a reduced JSA, where I consider a spectral range only ~ 7.5 larger than the PDC photons bandwidth. This is to emulate the effect of “gentle” filtering, that is often used in combination with nonlinearity engineered crystals. We run numerical simulations generating 60×60 JSA matrices.

The results of this analysis are shown in Figs. [A.1](#), [A.2](#), [A.3](#), and [A.4](#).

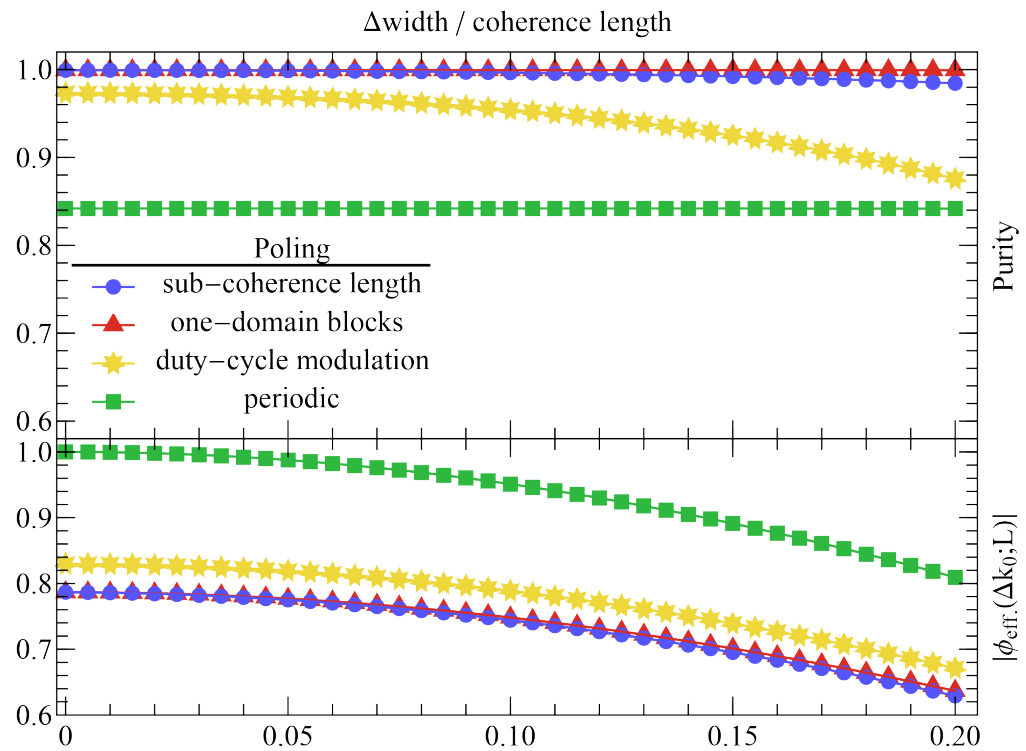


Figure A.1: Under/over poling. Both sub-coherence length and one-domain blocks method are more robust to errors than the duty-cycle modulation method.

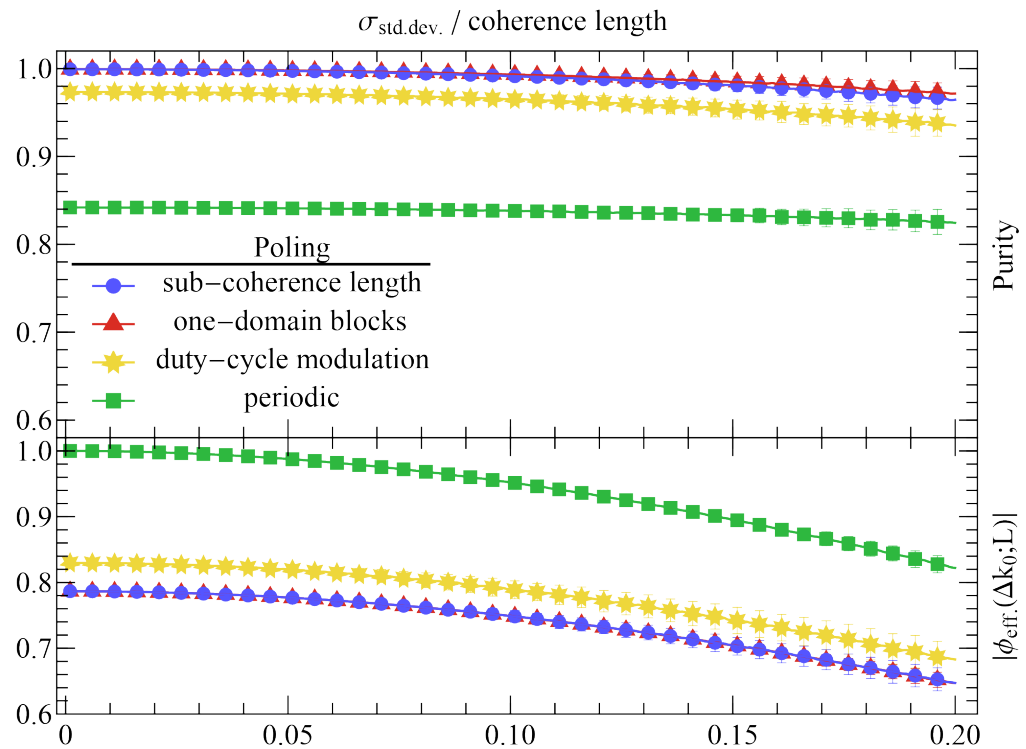


Figure A.2: Domain-width variation. All poling techniques are similarly affected by the domain-width variation error.

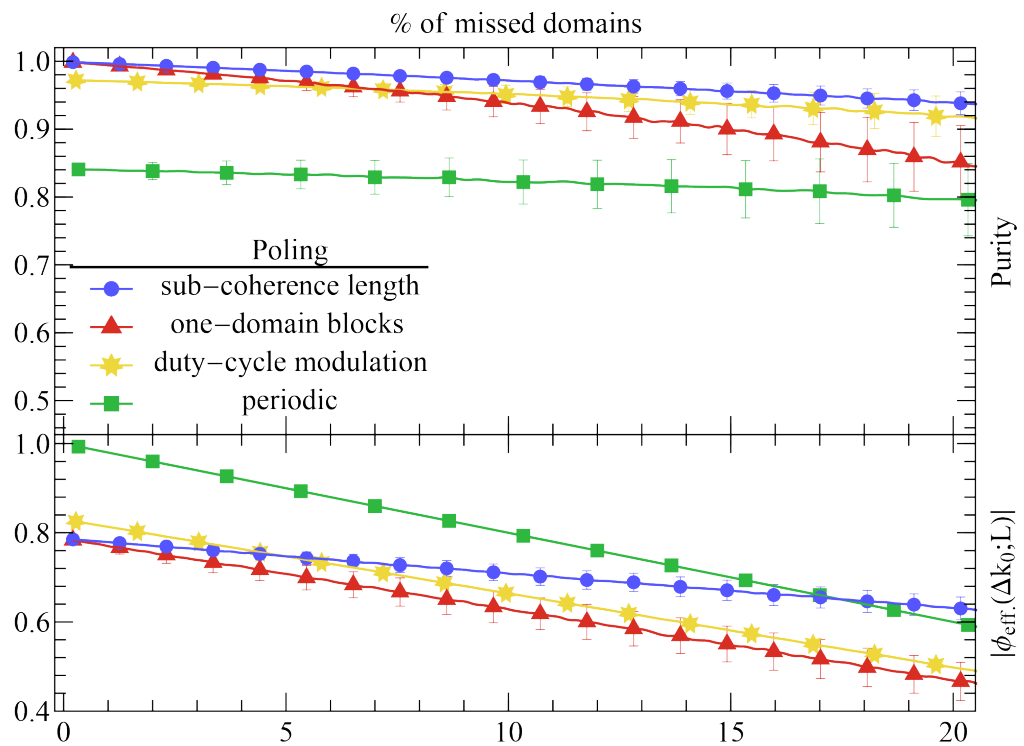


Figure A.3: Missing domains. Different poling techniques exhibit different behaviours when missing domain errors occur in the crystal.

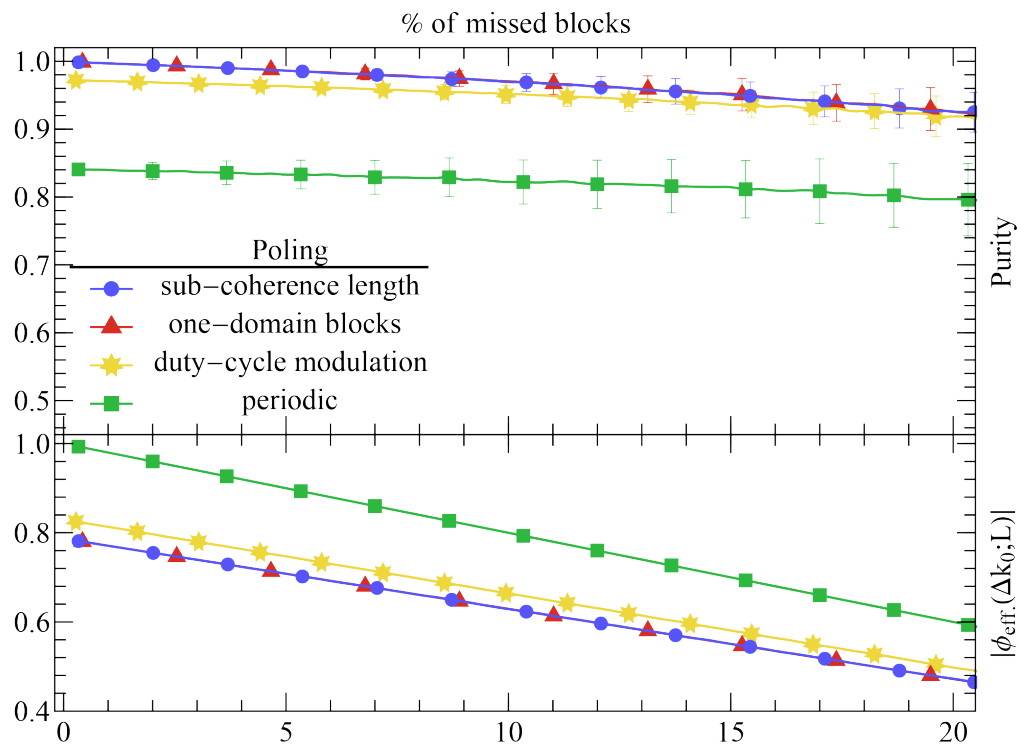


Figure A.4: Missing blocks. All poling techniques are similarly affected by the domain-width variation error.

Goat butts against the hedge and its horns
become entangled.

Egg Shen, *Big Trouble in Little China*

APPENDIX B

Hyperentanglement in Structured Quantum Light

As I already mentioned in the introduction, this Appendix should be considered as a the seventh Chapter of this manuscript: the reason why it appears at the end of this Thesis is simply bureaucratic.

In their “Roadmap on structured light” (2016) [165], Rubinsztein-Dunlop *et al.* posed a somewhat challenging question:

Going forward one wonders what exciting prospects await the expansion of structured light concepts beyond the spatial domain, for example, the shaping of light’s time envelop [sic] and frequency control. Could we see optical fields structured in all dimensions and in all degrees of freedom?





In this Chapter, we address this question by bridging the gap between spatially- and spectrally-structured light.

To this aim, we exploit nonlinearity-engineering compatibility with different photonic quantum encodings, such as polarisation and orbital angular momentum, that makes it a versatile tool for multi-DOF quantum photonics applications. By combining the TFM entanglement scheme discussed in Chapter 6 with a polarisation to OAM conversion technique, we experimentally demonstrate hyperentanglement between vector vortex beam and time-frequency modes: a quantum state of light that, to our knowledge, has never been observed before.

This result presents foundational interests arising from the non-trivial structure of entanglement coexisting in three different forms within the same biphoton state: hyperentanglement of biphoton entangled TFMs and VVBs, which in turn carry single-particle entanglement between polarisation and OAM. However, it also holds promise for direct applications in quantum technologies. Hyperentanglement of the form discussed here can indeed leverage features of structured light, which offers noise robustness and intrinsically high dimensionality to enhance existing protocols.

Unlike the other Chapters, here I attach the original manuscript to this Thesis, as I don't have additional material and/or comments on the results already published.

Hyperentanglement in structured quantum light

Francesco Graffitti ^{1,*} Vincenzo D'Ambrosio^{2,†} Massimiliano Proietti,¹ Joseph Ho ¹ Bruno Piccirillo,²
Corrado de Lisio ^{2,3} Lorenzo Marrucci ² and Alessandro Fedrizzi¹

¹*Institute of Photonics and Quantum Sciences, School of Engineering and Physical Sciences, Heriot-Watt University, Edinburgh EH14 4AS, Scotland, United Kingdom*

²*Dipartimento di Fisica, Università di Napoli Federico II, Complesso Universitario di Monte Sant'Angelo, Via Cintia, 80126 Napoli, Italy*

³*Consiglio Nazionale delle Ricerche–SPIN U.O.S. di Napoli, Via Cintia 2, 80126 Napoli, Italy*



(Received 15 May 2020; accepted 16 November 2020; published 9 December 2020)

Entanglement in high-dimensional quantum systems, where one or more degrees of freedom of light are involved, offers increased information capacities and enables new quantum protocols. Here, we demonstrate a functional source of high-dimensional, noise-resilient hyperentangled states encoded in time-frequency and vector vortex structured modes, which in turn carry single-particle entanglement between polarization and orbital angular momentum. Pairing nonlinearity-engineered parametric downconversion in an interferometric scheme with spin-to-orbital-angular-momentum conversion, we generate highly entangled photon pairs at telecom wavelength that we characterize via two-photon interference and quantum state tomography, achieving near-unity visibilities and fidelities. While hyperentanglement has been demonstrated before in photonic qubits, here we present a rich entanglement structure involving spectrally and spatially structured light, where three different forms of entanglement coexist in the same biphoton state.

DOI: [10.1103/PhysRevResearch.2.043350](https://doi.org/10.1103/PhysRevResearch.2.043350)

I. INTRODUCTION

Photonic platforms are a natural choice for many quantum applications owing to their advantages as low-noise quantum systems with high-fidelity control and suitability for long-distance transmission. The ubiquity of binary encoding in many proof-of-principle demonstrations, even for contemporary experiments, has in part been motivated by their simplicity in implementation. However, there are scenarios that benefit from expanding the system dimensionality, e.g., for enhancing information capacity, noise resilience, and robustness against external attacks in quantum cryptography [1,2]. Intrinsically high-dimensional degrees of freedom (DOFs) of light—such as orbital angular momentum (OAM), time, and frequency—enable a larger quantum alphabet in a single-photon state. The combination of two or more DOFs of light—including entanglement across them, namely, *hyperentanglement* [3,4]—allows further expansion of the Hilbert space while providing easy access to the individual subsystems for selective control and measurements, improving existing protocols or enabling new ones [5,6]. Hyperentanglement in particular enables protocols like complete Bell-state analysis [7–9] and logic gates simplification [10], and has

been used in cluster state generation [11,12] as well as in testing quantum foundations [13]. Moreover, hyperentangled systems have been successfully used for demonstrations of quantum dense coding [14] and teleportation of multiple DOFs of a single photon [15,16].

Photonic hyperentangled states have been demonstrated in different encoding regimes, such as polarization, time and frequency bins, path, and OAM [4,9,17]. While entanglement of three DOFs has been demonstrated [4,18] the generation of hyperentanglement in spatially and spectrally structured light having nontrivial polarization and OAM patterns and temporal/spectral envelopes [19] (as discussed below in detail) remains elusive owing to the complexity of accessing such encoding regimes. Notably, structured light modes—where one or more DOFs are modulated into custom light fields—are highly sought after in quantum photonics applications spanning communication, metrology, and imaging [19]. In this paper, we fill this gap combining a nonlinearity engineering technique [20,21] with a spin-to-orbital-angular-momentum conversion scheme [22] to generate and characterize a biphoton state that exhibits complex entanglement between spectrally and spatially structured light. We produce hyperentanglement between time-frequency modes (TFMs)—temporal/spectral envelopes of the electric field of the photons [6,21], and vector vortex beams (VVBs)—spatially structured beams characterized by a nonuniform polarization pattern on their transverse profile [23–25]. Due to their resilience to different noise sources, both TFMs [26,27] and VVBs [5,28] are ideal encodings for free-space communication schemes. Meanwhile sources that generate polarization-TFM hyperentanglement could be immediately deployed in telecom networks, as both DOFs are suitable for long-distance

*Corresponding author: fraccalo@gmail.com

†Corresponding author: vincenzo.dambrosio@unina.it

Published by the American Physical Society under the terms of the [Creative Commons Attribution 4.0 International license](https://creativecommons.org/licenses/by/4.0/). Further distribution of this work must maintain attribution to the author(s) and the published article's title, journal citation, and DOI.

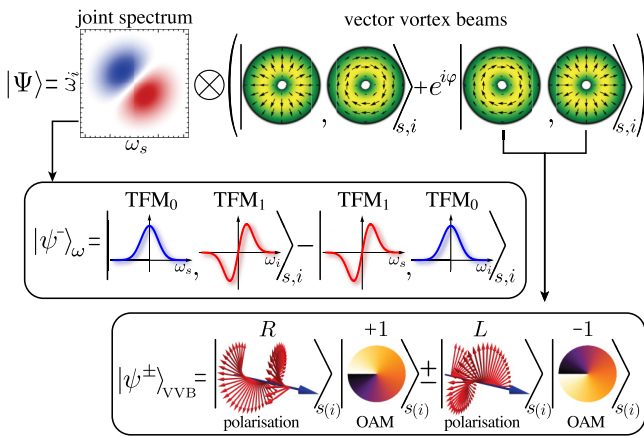


FIG. 1. Sketch of the biphoton hyperentangled state. The overall quantum state $|\Psi\rangle$ (first row) exhibits hyperentanglement between spectrally and spatially structured light. Signal and idler are encoded in the $|\psi^-\rangle_\omega$ state of the TFM basis, represented with the biphoton joint spectrum and the corresponding expansion in TFMs (first box), and in any Bell states of the VVB basis (we only display $|\psi^-\rangle$ -type states for compactness). Each photon is also in a single-particle entangled state between polarization and OAM, giving rise to a VVB (second box). The plus (minus) sign corresponds to the radially (azimuthally) polarized beams, respectively.

transmission in fiber. Furthermore, a recent demonstration on quantum transmission of VVBs in specialized fibers [29] bolsters future prospects for fiber-based networks exploiting the full capabilities of our scheme. Finally, silicon based quantum photonics is compatible with periodically poled sources [30] and has been recently proven capable of generating spatially structured light [31], paving the way towards the integration of TFM-VVB hyperentanglement sources into photonics chips.

The generation of hyperentanglement between time-frequency modes and vector vortex beams implies the ability to independently create spectrally and spatially structured light. TFM encoding can be achieved via nonlinearity engineering, a technique that tailors the phase-matching function in parametric downconversion (PDC) processes by modifying the ferroelectric structure of periodically poled nonlinear crystals. Originally used for generating spectrally pure heralded single photons [20,32,33], nonlinearity engineering has since been applied to generate TFM entanglement with high fidelity [21]. Vector vortex beams on the other hand can be efficiently created by converting polarization into polarization-OAM entanglement by means of birefringent liquid-crystal devices known as q-plates [22,24]. Our scheme combines these two techniques with an interferometric Sagnac scheme [34,35] for generating the highly entangled state with the nontrivial structure sketched in Fig. 1.

II. HYPERENTANGLEMENT GENERATION

We describe the experimental implementation of our state generation scheme in Fig. 2(a). A Ti-sapphire laser produces a train of near transform-limited, 1.3-ps pulses centered at 775 nm with 80-MHz repetition rate. A plano-convex lens focuses the laser beam (30-mW average power) to a spot size

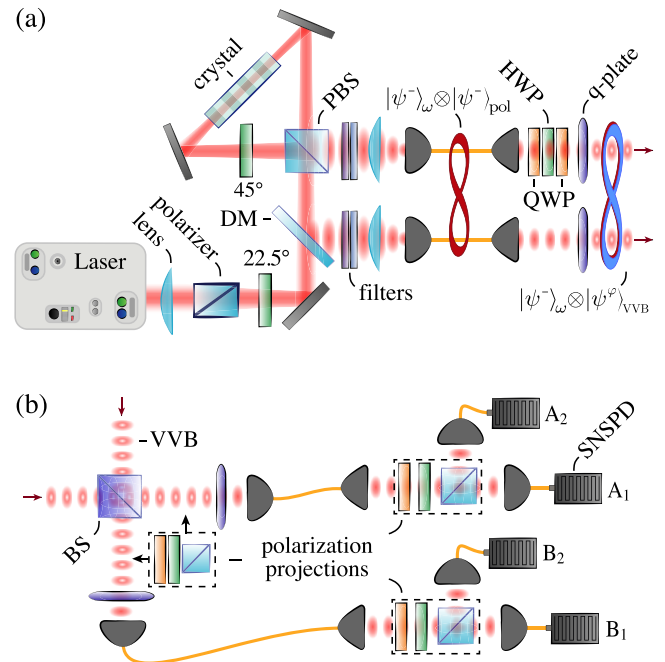


FIG. 2. Experimental setup. (a) State preparation: interferometric scheme to produce hyperentangled biphoton states in TFM and VVB encoding. (b) Characterization setup to measure the overall state via two-photon interference and tomographic reconstruction. A set of QWP, HWP, and QWP is used to prepare any maximally entangled state in the radial/azimuthal VVB basis. When the fast axis of the QWPs is aligned, a rotation of the HWP corresponds to changing the phase factor of the Bell-like state. The polarization projection stages in the dashed boxes, each consisting of the QWP, HWP, and polarizer, are used to perform projective measurements on the polarization of the photons for the 16-dimensional polarization-OAM biphoton state reconstruction.

of $\approx 220 \mu\text{m}$ into a Sagnac interferometer PDC source for generating a polarization entangled state [34,35]:

$$|\psi^-\rangle_{\text{pol}} = \frac{1}{\sqrt{2}}(|H\rangle_s|V\rangle_i - |V\rangle_s|H\rangle_i). \quad (1)$$

The PDC crystal in the Sagnac loop is a nonlinearity engineered potassium titanyl phosphate (KTP) poled crystal (details in Ref. [21]), that simultaneously enables the generation of TFM entanglement in a tailored PDC process. The phase-matching function of the engineered crystal is indeed shaped as a first-order Hermite-Gauss mode, leading to a highly correlated joint spectrum of the form $f_{s,i}(\omega_s, \omega_i) \propto \exp[-(\omega_s^2 + \omega_i^2)]$, which we show in Fig. 1, and consequently a TFM-entangled singlet state:

$$|\psi^-\rangle_\omega = 1/\sqrt{2}(|\wedge\rangle_s|\vee\rangle_i - |\vee\rangle_s|\wedge\rangle_i), \quad (2)$$

where $|\wedge\rangle$ and $|\vee\rangle$ are the orthonormal zeroth- and first-order Hermite-Gauss TFM modes spanning a two-dimensional TFM subspace (see Sec. 1 of Supplemental Material for more details on the state generation [36]).

The PDC pair (signal “s” and idler “i”) is separated at a polarizing beamsplitter (PBS), and the signal is filtered from the pump with a dichroic mirror (DM). The photons are then spectrally filtered with a long-pass filter (cutoff wavelength

at 1400 nm) and a “loose” bandpass filter (10-nm nominal bandwidth), about four times larger than the photons’ bandwidth of ≈ 2.4 nm, defined as the full width at half maximum of the marginal photon’s spectral intensity. The photon pair is therefore coupled into single-mode fibers for spatial mode filtering. At this stage of the scheme, the quantum state carries hyperentanglement between the maximally antisymmetric TFM Bell state and a polarization Bell state, $|\Psi\rangle_{\omega, \text{pol.}} = |\psi^-\rangle_{\omega} \otimes |\psi^-\rangle_{\text{pol.}}$, that is already potentially useful for fiber-based quantum photonic protocols, as both polarization and TFM are readily compatible with long-distance transmission over an optical network. We measure a source brightness of ≈ 4 -KHz/mW detected photon pairs using superconducting nanowire single-photon detectors (SNSPDs) with 80% nominal detection efficiency, with symmetric heralding efficiency of $\approx 60\%$. However, brightness and heralding can be easily varied by changing the focusing and collection parameters of the source.

The photons are then out-coupled and collimated in free space, and a set of quarter-wave plate (QWP), half-wave plate (HWP), and QWP is used to prepare any maximally entangled polarization state via local operations. Each photon is finally sent through a q-plate for converting polarization encoding into VVB encoding, producing the target TFM-VVB hyperentangled state. A q-plate with topological charge q (with $q = 0.5$ in our setup) implements the following transformation: $\alpha|R, 0\rangle + \beta|L, 0\rangle \rightarrow \alpha|L, -2q\rangle + \beta|R, 2q\rangle$ where the first and second label correspond to polarization and OAM value, respectively. If the input polarization is linear, a VVB in a linear superposition of the basis states $|\hat{r}\rangle$ (radially polarized) and $|\hat{\theta}\rangle$ (azimuthally polarized) is produced in the process. When each photon of the polarization-entangled biphoton state is sent through a q-plate, the overall system consists of two entangled vector vortex beams [37]. The q-plates used in our setup are electrically tunable, and have a transmittance of 70 to 75%, that could be improved by coating the inner and outer surfaces of the devices, or by different engineering techniques (e.g., nontunable q-plates with near-unity transmission are already commercially available).

At the output of the q-plates, the biphoton state shows a nontrivial entanglement structure, where three different forms of entanglement coexist in the same quantum state: hyperentanglement between TFMs and VVBs, which is in turn composed of single-particle (intrasystem) entanglement [25,37–39]—polarization and OAM of each photon—and two distinct sets of intersystem entanglement—between the two VVBs and between the two TFMs, as sketched in Fig. 1 and shown in its full form below:

$$|\Psi\rangle_{\omega, \text{VVB}} = |\psi\rangle_{\omega} \otimes \underbrace{\frac{1}{\sqrt{2}}(|\hat{r}\rangle_s |\hat{\theta}\rangle_i - |\hat{\theta}\rangle_s |\hat{r}\rangle_i)}_{|\psi^-\rangle_{\text{VVB}}}, \quad (3)$$

with $|\hat{r}\rangle_{\text{VVB}} = \frac{1}{\sqrt{2}}(|R\rangle_{\text{pol.}}|+1\rangle_{\text{OAM}} + |L\rangle_{\text{pol.}}|-1\rangle_{\text{OAM}})$ and $|\hat{\theta}\rangle_{\text{VVB}} = \frac{1}{\sqrt{2}}(|R\rangle_{\text{pol.}}|+1\rangle_{\text{OAM}} - |L\rangle_{\text{pol.}}|-1\rangle_{\text{OAM}})$. We note that this scheme allows one to generate states within a two-dimensional VVB subspace of order 1, while additional HWPs after the q-plates enable the generation of any VVB state in the four-dimensional space [37].

III. HYPERENTANGLEMENT CHARACTERIZATION

The analysis stage consists of two main steps, as shown in Fig. 2(b). First, we send the two photons on a BS to check for quantum interference depending on the symmetry of the full state [21]. After the BS, a set of two additional q-plates (with $q = 0.5$) and polarization optics (QWP, HWP, and PBS for each photon) are used to perform tomographic projections in the VVB space, and the photons are finally detected with SNSPDs. An additional tomographic projection set can be added before the measurement q-plates to perform a four-qubit tomography in the polarization and OAM subspaces, simultaneously certifying the intrasystem entangled structure of each VVB and the intersystem entanglement between the two photons [37], and verifying the Greenberger-Horne-Zeilinger (GHZ)-type structure of the state [40].

The synergy of the quantum interference and tomographic parts of the setup allows us to demonstrate the hyperentangled nature of the biphoton state. The tomographic stages are decoupled from the spectral degree of freedom and only act on the polarization and OAM components of the state, providing full reconstruction of the VVB-encoded quantum state: this means that our setup is capable of preparing and measuring unambiguously the spatial component of the state. On the other hand, while the visibility depends on the overall state’s symmetry, the shape of the interference pattern only depends on the biphoton joint spectrum (see Sec. 2 of Supplemental Material for proof [36]). Consequently, the knowledge of the VVB component of the state combined with the measured interference pattern allows us to decouple spatial and spectral contributions of the overall measurement, and to use the interference results to certify the TFM entanglement, as proven in Ref. [21].

IV. RESULTS

To benchmark our scheme, we produce states of the form

$$|\Psi\rangle_{\omega, \text{VVB}} = |\psi^-\rangle_{\omega} \otimes |\psi^{\varphi}\rangle_{\text{VVB}},$$

where $|\psi^{\varphi}\rangle_{\text{VVB}} = 1/\sqrt{2}(|\hat{r}\rangle, \hat{\theta}\rangle + e^{i\varphi}|\hat{\theta}\rangle, \hat{r}\rangle)$ is a ψ -type maximally entangled state in the VVB basis. By changing the state preparation HWP angle we can change the phase φ of the VVB part of the state and hence the symmetry of the overall wave function. The phase factors e^{i0} and $e^{i\pi}$ correspond to the $|\psi^-\rangle_{\omega} \otimes |\psi^+\rangle_{\text{VVB}}$ and $|\psi^-\rangle_{\omega} \otimes |\psi^-\rangle_{\text{VVB}}$ states, i.e., to a maximally antisymmetric and symmetric state, respectively. This translates into different interference behavior at the BS, where moving from an antisymmetric to a symmetric state corresponds to moving from photon antibunching to photon bunching, as we show in Fig. 3. When the spatial contribution is symmetric ($|\psi^+\rangle_{\text{VVB}}$) the interference exhibits perfect antibunching, while when it is antisymmetric ($|\psi^-\rangle_{\text{VVB}}$) it exhibits bunching: this certifies the maximal antisymmetry of the spectral part of the state, and consequently verifies the TFM singlet state $|\psi^-\rangle_{\omega}$ (see Ref. [21] for details).

We monitor coincident counts between detectors $\{A_1, B_1\}$, $\{A_1, B_2\}$, $\{A_2, B_1\}$, and $\{A_2, B_2\}$, corresponding to the photons exiting from both outputs of the BS, and between the detectors $\{A_1, A_2\}$ and $\{B_1, B_2\}$, corresponding to the photons exiting the same outputs of the BS, to reconstruct the

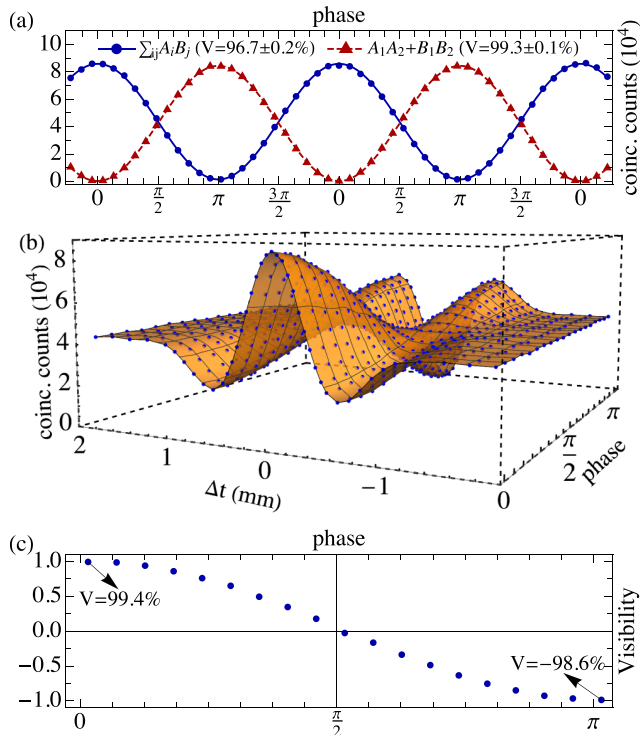


FIG. 3. Two-photon interference results. (a) The interference fringes depend on the phase in the VVB-encoded part of the hyperentangled state: A maximum in the coincident counts at the two outputs of the BS (labeled as $\sum_{ij} A_i B_j$, where A_i, B_j are the detectors in Fig. 2) corresponds to a minimum in the coincident counts at each BS output (labeled as $A_1 A_2 + B_1 B_2$), and vice versa. Interference patterns measured by collecting coincident counts at the two outputs of the BS (b) and corresponding visibilities (c) changing phase and relative arrival time of the photons at the BS. By controlling the phase of the $|\psi\rangle$ type we can move from almost perfect antibunching to bunching, i.e., from an overall antisymmetric state to a symmetric one. The acquisition time is 30 s per data point.

interference fringes as a function of the state's phase φ . We show the results in Fig. 3(a): the fringes corresponding to antibunching (blue dots) and to bunching (red triangles) are in antiphase, and have high visibilities (96.7 ± 0.2 and $99.3 \pm 0.1\%$, respectively) certifying a high quality of the generated state. By varying both the state's phase and the relative arrival time of signal and idler at the BS, we can reconstruct the full biphoton interference pattern for states with different amounts of antisymmetry. The three-dimensional plot in Fig. 3(b) shows how the interference pattern changes from perfect antibunching (corresponding to $\varphi = 0$) to perfect bunching ($\varphi = \pi$), in excellent agreement with the theoretical model we discuss in Sec. 2 of Supplemental Material [36]. Finally, Fig. 3(c) shows the interference visibilities of each scan, where plus and minus 100% correspond to perfect antibunching and bunching, respectively.

The two-photon interference allows us to measure the overall antisymmetry of the biphoton state, but it does not provide any information on its spatial structure. The VVB state can instead be measured via quantum state tomography after the interference at the BS. We prepare the symmetric state

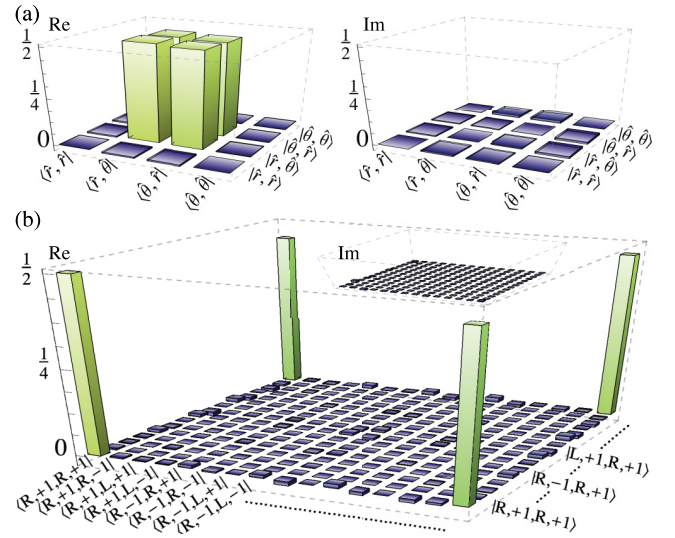


FIG. 4. Tomography results. (a) Tomographic reconstruction of the biphoton $|\psi^+\rangle$ state in the VVB subspace $\{|\hat{r}\rangle, |\hat{\theta}\rangle\}$. We record $\approx 1.6 \times 10^6$ coincident counts in nine different settings (corresponding to the two-photon Pauli projections), with 60 s of acquisition time per setting. (b) Tomographic reconstruction of the biphoton GHZ state encoded in polarization and OAM. We record $\approx 11 \times 10^6$ coincident counts in 324 different settings (corresponding to a combination of 36 projective measurements on the OAM basis and nine Pauli projections on the polarization basis), with 220 s of acquisition time per setting.

$|\psi^-\rangle_\omega \otimes |\psi^+\rangle_{\text{VVB}}$, which antibunches at the BS. We then convert the VVB information into polarization information, and we perform a overcomplete quantum state tomography of the state. We measure a purity and fidelity of (99.26 ± 0.07) and ($99.57 \pm 0.03\%$), respectively, in the VVB subspace $\{|\hat{r}\rangle, |\hat{\theta}\rangle\}$ [see Fig. 4(a)]. Introducing an additional tomographic projection before each measurement q-plate allows us to investigate the polarization-OAM intrasystem entanglement and, at the same time, the two-photon intersystem entanglement [37]. With this scheme, we measure a two-photon, four-qubit purity of ($92.4 \pm 0.1\%$) and a fidelity of ($95.0 \pm 0.1\%$) with the GHZ state $1/\sqrt{2}(|R, +1, R, +1\rangle + |L, -1, L, -1\rangle)$: we show the corresponding density matrix in Fig. 4(b). Errors on the extracted purities and fidelities calculated from the reconstructed density matrices represent 3σ statistical confidence regions obtained via Monte Carlo resampling (1000 runs of the algorithm) assuming a Poissonian statistics on the coincident counts distribution.

The high interference visibility measured in both the bunching and antibunching configuration, combined with the high state quality obtained via tomographic reconstruction of the VVB-encoded state, testifies to an unprecedented capability of generating and manipulating structured light encoded in three different degrees of freedom with very high efficiency and precision.

V. DISCUSSION AND CONCLUSIONS

Many photonic quantum protocols rely on entanglement to carry out their tasks efficiently, therefore the capability

of generating and manipulating complex entangled states of light with high precision is a fundamental requirement and a key challenge of quantum technologies. Here, we tackled this problem by introducing and experimentally demonstrating a scheme for efficient generation of a complex entanglement structure between three DOFs of light: polarization, orbital angular momentum, and time-frequency modes. In particular, we combine TFM encoding and VVB encoding introducing a simple yet high-quality source of TFM-VVB hyperentanglement. We expect our scheme will find applications in quantum communication schemes (where increased information capacity and noise resilience are obvious advantages) but also in different areas of quantum technologies, such as metrology or imaging, where both TFM and VVB encoding have already been independently used as resources [41,42].

There are two main routes to go beyond the results of this paper in the future. On the one hand, it would be ideal to explore the intrinsic high dimensionality of these DOFs, generating higher-order OAM and TFM states to increase the information capacity of the biphoton state and investigate

even more complex entanglement structures. This could be achieved by expanding either the TFM subspace (e.g., by engineering higher-order Hermite-Gauss modes as nonlinearity patterns, or by introducing spectral tailoring of the pump's spectral profile) or the VVB subspace (e.g., using q-plates of different singularity order in interferometric schemes), or a combination of the two. On the other hand, implementing quantum pulse gates or other schemes [6,43–45] for performing TFM manipulation and measurements would allow one to fully exploit the potential of our technique.

ACKNOWLEDGMENTS

This work was supported by the Engineering and Physical Sciences Research Council (EPSRC Grants No. EP/N002962/1, No. EP/T001011/1, and No. EP/L015110/1); the Italian Ministry of Education, University, and Research through the PRIN Project INPhoPOL; and the European Union Horizon 2020 program, within European Research Council Grant No. 694683, PHOSPhOR.

-
- [1] M. Erhard, R. Fickler, M. Krenn, and A. Zeilinger, Twisted photons: New quantum perspectives in high dimensions, *Light: Science & Applications* **7**, 17146 (2018).
- [2] D. Cozzolino, B. Da Lio, D. Bacco, and L. K. Oxenløwe, High-dimensional quantum communication: Benefits, progress, and future challenges, *Adv. Quantum Technol.* **2**, 1900038 (2019).
- [3] P. G. Kwiat, Hyper-entangled states, *J. Mod. Opt.* **44**, 2173 (1997).
- [4] J. T. Barreiro, N. K. Langford, N. A. Peters, and P. G. Kwiat, Generation of Hyperentangled Photon Pairs, *Phys. Rev. Lett.* **95**, 260501 (2005).
- [5] V. D'Ambrosio, E. Nagali, S. P. Walborn, L. Aolita, S. Slussarenko, L. Marrucci, and F. Sciarrino, Complete experimental toolbox for alignment-free quantum communication, *Nat. Commun.* **3**, 961 (2012).
- [6] B. Brecht, D. V. Reddy, C. Silberhorn, and M. G. Raymer, Photon temporal modes: A complete framework for quantum information science, *Phys. Rev. X* **5**, 041017 (2015).
- [7] S. P. Walborn, S. Pádua, and C. H. Monken, Hyperentanglement-assisted Bell-state analysis, *Phys. Rev. A* **68**, 042313 (2003).
- [8] C. Schuck, G. Huber, C. Kurtsiefer, and H. Weinfurter, Complete Deterministic Linear Optics Bell State Analysis, *Phys. Rev. Lett.* **96**, 190501 (2006).
- [9] M. Barbieri, G. Vallone, P. Mataloni, and F. De Martini, Complete and deterministic discrimination of polarization Bell states assisted by momentum entanglement, *Phys. Rev. A* **75**, 042317 (2007).
- [10] B. P. Lanyon, M. Barbieri, M. P. Almeida, T. Jennewein, T. C. Ralph, K. J. Resch, G. J. Pryde, J. L. O'Brien, A. Gilchrist, and A. G. White, Simplifying quantum logic using higher-dimensional hilbert spaces, *Nat. Phys.* **5**, 134 (2009).
- [11] G. Vallone, G. Donati, R. Ceccarelli, and P. Mataloni, Six-qubit two-photon hyperentangled cluster states: Characterization and application to quantum computation, *Phys. Rev. A* **81**, 052301 (2010).
- [12] M. A. Ciampini, A. Orieux, S. Paesani, F. Sciarrino, G. Corrielli, A. Crespi, R. Ramponi, R. Osellame, and P. Mataloni, Path-polarization hyperentangled and cluster states of photons on a chip, *Light: Science & Applications* **5**, e16064 (2016).
- [13] M. Barbieri, F. De Martini, P. Mataloni, G. Vallone, and A. Cabello, Enhancing the Violation of the Einstein-Podolsky-Rosen Local Realism by Quantum Hyperentanglement, *Phys. Rev. Lett.* **97**, 140407 (2006).
- [14] J. T. Barreiro, T.-C. Wei, and P. G. Kwiat, Beating the channel capacity limit for linear photonic superdense coding, *Nat. Phys.* **4**, 282 (2008).
- [15] Y.-B. Sheng, F.-G. Deng, and G. L. Long, Complete hyperentangled-Bell-state analysis for quantum communication, *Phys. Rev. A* **82**, 032318 (2010).
- [16] X.-L. Wang, X.-D. Cai, Z.-E. Su, M.-C. Chen, D. Wu, L. Li, N.-L. Liu, C.-Y. Lu, and J.-W. Pan, Quantum teleportation of multiple degrees of freedom of a single photon, *Nature (London)* **518**, 516 (2015).
- [17] Z. Xie, T. Zhong, S. Shrestha, X. Xu, J. Liang, Y.-X. Gong, J. C. Bienfang, A. Restelli, J. H. Shapiro, F. N. C. Wong, and C. Wei Wong, Harnessing high-dimensional hyperentanglement through a biphoton frequency comb, *Nat. Photonics* **9**, 536 (2015).
- [18] X.-L. Wang, Y.-H. Luo, H.-L. Huang, M.-C. Chen, Z.-E. Su, C. Liu, C. Chen, W. Li, Y.-Q. Fang, X. Jiang, J. Zhang, L. Li, N.-L. Liu, C.-Y. Lu, and J.-W. Pan, 18-Qubit Entanglement with Six Photons' Three Degrees of Freedom, *Phys. Rev. Lett.* **120**, 260502 (2018).
- [19] H. Rubinsztein-Dunlop, A. Forbes, M. V. Berry, M. R. Dennis, D. L. Andrews, M. Mansuripur, C. Denz, C. Alpmann, P. Banzer, T. Bauer, E. Karimi, L. Marrucci, M. Padgett, M. Ritsch-Marte, N. M. Litchinitser, N. P. Bigelow, C. Rosales-Guzmán, A. Belmonte, J. P. Torres, T. W. Neely, M. Baker, R. Gordon, A. B. Stilgoe, J. Romero, A. G. White, R. Fickler, A. E. Willner, G. Xie, B. McMorran, and A. M. Weiner, Roadmap on structured light, *J. Opt.* **19**, 013001 (2016).

- [20] F. Graffitti, D. Kundys, D. T. Reid, A. M. Brańczyk, and A. Fedrizzi, Pure down-conversion photons through sub-coherence-length domain engineering, *Quantum Sci. Technol.* **2**, 035001 (2017).
- [21] F. Graffitti, P. Barrow, A. Pickston, A. M. Brańczyk, and A. Fedrizzi, Direct Generation of Tailored Pulse-Mode Entanglement, *Phys. Rev. Lett.* **124**, 053603 (2020).
- [22] L. Marrucci, C. Manzo, and D. Paparo, Optical Spin-to-Orbital Angular Momentum Conversion in Inhomogeneous Anisotropic Media, *Phys. Rev. Lett.* **96**, 163905 (2006).
- [23] M. R. Dennis, K. O’Holleran, and M. J. Padgett, *Chapter 5 Singular Optics: Optical Vortices and Polarization Singularities* (Elsevier, Amsterdam, 2009), pp. 293–363.
- [24] F. Cardano, E. Karimi, S. Slussarenko, L. Marrucci, C. de Lisio, and E. Santamato, Polarization pattern of vector vortex beams generated by q-plates with different topological charges, *Appl. Opt.* **51**, C1 (2012).
- [25] A. Selyem, C. Rosales-Guzmán, S. Croke, A. Forbes, and S. Franke-Arnold, Basis-independent tomography and nonseparability witnesses of pure complex vectorial light fields by Stokes projections, *Phys. Rev. A* **100**, 063842 (2019).
- [26] A. Eckstein, B. Brecht, and C. Silberhorn, A quantum pulse gate based on spectrally engineered sum frequency generation, *Opt. Express* **19**, 13770 (2011).
- [27] Q. Ding, R. Chatterjee, Y. Huang, and T. Yu, High-dimensional temporal mode propagation in a turbulent environment, *arXiv:1907.02321* (2019).
- [28] O. J. Farías, V. D’Ambrosio, C. Taballione, F. Bisesto, S. Slussarenko, L. Aolita, L. Marrucci, S. P. Walborn, and F. Sciarrino, Resilience of hybrid optical angular momentum qubits to turbulence, *Sci. Rep.* **5**, 8424 (2015).
- [29] D. Cozzolino, E. Polino, M. Valeri, G. Carvacho, D. Bacco, N. Spagnolo, L. K. K. Oxenløwe, and F. Sciarrino, Air-core fiber distribution of hybrid vector vortex-polarization entangled states, *Adv. Photonics* **1**, 046005 (2019).
- [30] S. Atzeni, A. S. Rab, G. Corrielli, E. Polino, M. Valeri, P. Mataloni, N. Spagnolo, A. Crespi, F. Sciarrino, and R. Osellame, Integrated sources of entangled photons at the telecom wavelength in femtosecond-laser-written circuits, *Optica* **5**, 311 (2018).
- [31] Y. Chen, K.-Y. Xia, W.-G. Shen, J. Gao, Z.-Q. Yan, Z.-Q. Jiao, J.-P. Dou, H. Tang, Y.-Q. Lu, and X.-M. Jin, Vector Vortex Beam Emitter Embedded in a Photonic Chip, *Phys. Rev. Lett.* **124**, 153601 (2020).
- [32] A. M. Brańczyk, A. Fedrizzi, T. M. Stace, T. C. Ralph, and A. G. White, Engineered optical nonlinearity for quantum light sources, *Opt. Express* **19**, 55 (2011).
- [33] F. Graffitti, P. Barrow, M. Proietti, D. Kundys, and A. Fedrizzi, Independent high-purity photons created in domain-engineered crystals, *Optica* **5**, 514 (2018).
- [34] T. Kim, M. Fiorentino, and F. N. C. Wong, Phase-stable source of polarization-entangled photons using a polarization Sagnac interferometer, *Phys. Rev. A* **73**, 012316 (2006).
- [35] A. Fedrizzi, T. Herbst, A. Poppe, T. Jennewein, and A. Zeilinger, A wavelength-tunable fiber-coupled source of narrowband entangled photons, *Opt. Express* **15**, 15377 (2007).
- [36] See Supplemental Material at <http://link.aps.org/supplemental/10.1103/PhysRevResearch.2.043350> for details on the state generation and characterization schemes.
- [37] V. D’Ambrosio, G. Carvacho, F. Graffitti, C. Vitelli, B. Piccirillo, L. Marrucci, and F. Sciarrino, Entangled vector vortex beams, *Phys. Rev. A* **94**, 030304(R) (2016).
- [38] A. Aiello, F. Töppel, C. Marquardt, E. Giacobino, and G. Leuchs, Quantum-like nonseparable structures in optical beams, *New J. Phys.* **17**, 043024 (2015).
- [39] M. McLaren, T. Konrad, and A. Forbes, Measuring the non-separability of vector vortex beams, *Phys. Rev. A* **92**, 023833 (2015).
- [40] G. Carvacho, F. Graffitti, V. D’Ambrosio, B. C. Hiesmayr, and F. Sciarrino, Experimental investigation on the geometry of GHZ states, *Sci. Rep.* **7**, 13265 (2017).
- [41] V. D’Ambrosio, N. Spagnolo, L. Del Re, S. Slussarenko, Y. Li, L. C. Kwek, L. Marrucci, S. P. Walborn, L. Aolita, and F. Sciarrino, Photonic polarization gears for ultra-sensitive angular measurements, *Nat. Commun.* **4**, 2432 (2013).
- [42] J. M. Donohue, V. Ansari, J. Řeháček, Z. Hradil, B. Stoklasa, M. Paúr, L. L. Sánchez-Soto, and C. Silberhorn, Quantum-Limited Time-Frequency Estimation through Mode-Selective Photon Measurement, *Phys. Rev. Lett.* **121**, 090501 (2018).
- [43] Y.-P. Huang and P. Kumar, Mode-resolved photon counting via cascaded quantum frequency conversion, *Opt. Lett.* **38**, 468 (2013).
- [44] V. Ansari, J. M. Donohue, M. Allgaier, L. Sansoni, B. Brecht, J. Roslund, N. Treps, G. Harder, and C. Silberhorn, Tomography and Purification of the Temporal-Mode Structure of Quantum Light, *Phys. Rev. Lett.* **120**, 213601 (2018).
- [45] D. V. Reddy and M. G. Raymer, High-selectivity quantum pulse gating of photonic temporal modes using all-optical Ramsey interferometry, *Optica* **5**, 423 (2018).

Hyperentanglement in structured quantum light - Supplemental Material

Francesco Graffitti,¹ Vincenzo D'Ambrosio,² Massimiliano Proietti,¹ Joseph Ho,¹
Bruno Piccirillo,² Corrado de Lisio,² Lorenzo Marrucci,² and Alessandro Fedrizzi¹

¹*Institute of Photonics and Quantum Sciences, School of Engineering and Physical Sciences,
Heriot-Watt University, Edinburgh EH14 4AS, United Kingdom*

²*Dipartimento di Fisica, Università di Napoli Federico II,
Complesso Universitario di Monte S. Angelo, Via Cintia, 80126 Napoli, Italy*

This document provides Supplemental Material to “Hyperentanglement in structured quantum light”. The document is structured as follows: In Section 1 we discuss the hyperentangled-state generation; In Section 2 we derive the two-photon interference pattern for the hyperentangled state.

I. HYPERENTANGLED-STATE GENERATION

Frequency entanglement

The PDC biphoton state, neglecting the multipair emission, reads:

$$|\psi\rangle_\omega = \iint d\omega_s d\omega_i f(\omega_s, \omega_i) a_s^\dagger(\omega_s) a_i^\dagger(\omega_i) |0\rangle_{s,i}, \quad (\text{S1})$$

where $f(\omega_s, \omega_i)$ is the joint spectral amplitude (JSA) and contains the spectral properties of the PDC biphoton state. The JSA is the product of the pump envelope function $\alpha(\omega_s, \omega_i)$, describing the pump spectrum, and the phasematching function (PMF) $\phi(\omega_s, \omega_i)$, depending on the nonlinear properties of the crystal that mediates the PDC process. Here, we work in symmetric group-velocity matching condition (i.e. pump and PMF are perpendicular in the (ω_s, ω_i) plane [1]), and we consider a Gaussian-shaped pump pulse and a PMF equal to the first order Hermite-Gauss function multiplied by a Gaussian envelope (deviations from the ideal case are discussed in details in Ref. [2]). The corresponding JSA is shown in Fig. S1 (left).

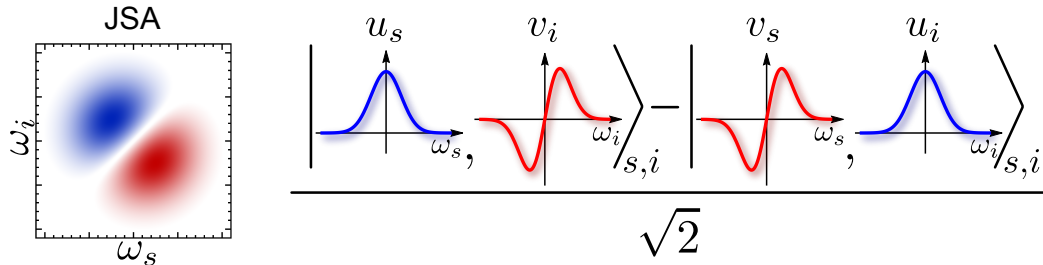


FIG. S1. **PDC biphoton state in frequency space.** Joint spectral amplitude (left) and corresponding decomposed quantum state (right) encoded in two equally-weighted, orthonormal TFM.

This corresponds to the following PDC state:

$$|\psi\rangle_\omega = \iint d\omega_s d\omega_i \frac{2(\omega_s - \omega_i)}{\sqrt{\pi} \sigma^2} e^{-\frac{\omega_s^2 + \omega_i^2}{\sigma^2}} a_s^\dagger(\omega_s) a_i^\dagger(\omega_i) |0\rangle_{s,i}. \quad (\text{S2})$$

We can perform the Schmidt decomposition on the state in Eq. (S2) to obtain the TFMs composing the biphoton state, obtaining:

$$\begin{aligned} |u\rangle_{\omega,j} &\equiv |\wedge\rangle_j = \left(\frac{2}{\pi\sigma^2}\right)^{\frac{1}{4}} \int d\omega_j e^{-\frac{\omega_j^2}{\sigma^2}} a_j^\dagger(\omega_j) |0\rangle_j \\ |v\rangle_{\omega,j} &\equiv |\vee\rangle_j = \left(\frac{2^5}{\pi\sigma^6}\right)^{\frac{1}{4}} \int d\omega_j e^{-\frac{\omega_j^2}{\sigma^2}} \omega_j a_j^\dagger(\omega_j) |0\rangle_j, \end{aligned} \quad (\text{S3})$$

where j can label either the signal s or the idler i photon, and there are only two non-null, balanced Schmidt

coefficients, both equal to $\frac{1}{\sqrt{2}}$. Hence, the decomposed PDC state can be written as the maximally entangled singlet state:

$$|\psi^-\rangle_\omega = \frac{1}{\sqrt{2}} \left(|u\rangle_{\omega,s} |v\rangle_{\omega,i} - |v\rangle_{\omega,s} |u\rangle_{\omega,i} \right) = \frac{1}{\sqrt{2}} (|\wedge\rangle_s |\vee\rangle_i - |\vee\rangle_s |\wedge\rangle_i) . \quad (\text{S4})$$

In Figure S1 (right) we show the two orthonormal TFMs in a balanced superposition.

Polarisation-frequency hyperentanglement

We now consider the case of a Sagnac interferometer source, commonly used for generating polarisation entanglement in the two photon state [3], where the standard ppKTP is replaced by the nonlinearity-engineered crystal in the Sagnac loop. This enables the generation of an hyperentangled state in polarisation and frequency (as discussed in details in the next paragraph):

$$|\Psi\rangle_{\omega,\text{pol.}} = \frac{1}{\sqrt{2}} (|\wedge\rangle_s |\vee\rangle_i - |\vee\rangle_s |\wedge\rangle_i) \otimes \frac{1}{\sqrt{2}} (|H\rangle_s |V\rangle_i - |V\rangle_s |H\rangle_i) = |\psi^-\rangle_\omega \otimes |\psi^-\rangle_{\text{pol.}} , \quad (\text{S5})$$

where the polarisation state $|\psi^-\rangle_{\text{pol.},s,i}$ can be easily manipulated via linear optical components (half- and quarter-wave plates) to generate any maximally entangled state.

Let's first consider both the clockwise and the anticlockwise cases where a pump photon is down-converted in two PDC photons having an antisymmetric joint spectral amplitude:

$$\begin{aligned} |\psi_{\text{clockwise}}\rangle_{\omega,\text{pol.}} &= \iint d\omega_s d\omega_i f_{s,i}(\omega_s, \omega_i) c_{s,H}^\dagger c_{i,V}^\dagger |0\rangle \\ |\psi_{\text{anticlockwise}}\rangle_{\omega,\text{pol.}} &= \iint d\omega_s d\omega_i f_{s,i}(\omega_s, \omega_i) d_{s,H}^\dagger d_{i,V}^\dagger |0\rangle , \end{aligned} \quad (\text{S6})$$

where we omit the frequency dependence of the creation operators c^\dagger (clockwise) and d^\dagger (anticlockwise). The half-wave plate (HWP) and polarising beam splitter (PBS) introduce following transformations:

$$\begin{aligned} \text{HWP} : & \begin{cases} d_{\dots,H}^\dagger \rightarrow d_{\dots,V}^\dagger \\ d_{\dots,V}^\dagger \rightarrow d_{\dots,H}^\dagger \end{cases} \\ \text{PBS} : & \begin{cases} c_{\dots,H}^\dagger \rightarrow a_{\dots,H}^\dagger \\ c_{\dots,V}^\dagger \rightarrow b_{\dots,V}^\dagger \\ d_{\dots,H}^\dagger \rightarrow b_{\dots,H}^\dagger \\ d_{\dots,V}^\dagger \rightarrow a_{\dots,V}^\dagger \end{cases} , \end{aligned} \quad (\text{S7})$$

where a^\dagger, b^\dagger corresponds to the two outputs of the PBS. The state before entering the polarising beam splitter (PBS) reads:

$$\begin{aligned} |\psi_{\text{clockwise}}\rangle_{\omega,\text{pol.}}^{\text{IN}} &= \iint d\omega_s d\omega_i f_{s,i}(\omega_s, \omega_i) c_{s,H}^\dagger c_{i,V}^\dagger |0\rangle \\ |\psi_{\text{anticlockwise}}\rangle_{\omega,\text{pol.}}^{\text{IN}} &= \iint d\omega_s d\omega_i f_{s,i}(\omega_s, \omega_i) d_{s,V}^\dagger d_{i,H}^\dagger |0\rangle , \end{aligned} \quad (\text{S8})$$

while at the output of the PBS the state is:

$$\begin{aligned} |\psi_{\text{clockwise}}\rangle_{\omega,\text{pol.}}^{\text{OUT}} &= \iint d\omega_s d\omega_i f_{s,i}(\omega_s, \omega_i) a_{s,H}^\dagger b_{i,V}^\dagger |0\rangle \\ |\psi_{\text{anticlockwise}}\rangle_{\omega,\text{pol.}}^{\text{OUT}} &= \iint d\omega_s d\omega_i f_{s,i}(\omega_s, \omega_i) a_{s,V}^\dagger b_{i,H}^\dagger |0\rangle . \end{aligned} \quad (\text{S9})$$

We note that in the Sagnac scheme the signal (idler) photons produced in both clockwise and anticlockwise paths exit the PBS from the same port, hence the labels s, a (and i, b) are interchangeable. Being the clockwise and

anticlockwise cases in a coherent superposition [3], we can write the output state as:

$$\begin{aligned}
|\Psi\rangle_{\omega,\text{pol.}} &= \frac{1}{\sqrt{2}} \left(\iint d\omega_s d\omega_i f_{s,i}(\omega_s, \omega_i) a_{s,H}^\dagger b_{i,V}^\dagger |0\rangle + \iint d\omega_s d\omega_i f_{s,i}(\omega_s, \omega_i) a_{s,V}^\dagger b_{i,H}^\dagger |0\rangle \right) \\
|\Psi\rangle_{\omega,\text{pol.}} &= \frac{1}{\sqrt{2}} \left(|\psi^-(\omega_s, \omega_i)\rangle_{s,i} |H\rangle_s |V\rangle_i + |\psi^-(\omega_s, \omega_i)\rangle_{s,i} |V\rangle_s |H\rangle_i \right) \\
|\Psi\rangle_{\omega,\text{pol.}} &= |\psi^-(\omega_s, \omega_i)\rangle_{s,i} \otimes \frac{1}{\sqrt{2}} (|H\rangle_s |V\rangle_i + |V\rangle_s |H\rangle_i) = |\psi^-(\omega_s, \omega_i)\rangle_{s,i} \otimes |\psi_{\text{pol.}}^+\rangle_{s,i}
\end{aligned} \tag{S10}$$

where $|\psi_{\text{pol.}}^+(\omega_s, \omega_i)\rangle_{s,i}$ is the symmetric polarisation-encoded Bell state. From this state, one can prepare any state of the polarisation Bell basis by means of local operations:

$$\begin{aligned}
|\Psi^+\rangle_{\omega,\text{pol.}} &= |\psi^-\rangle_\omega \otimes |\psi^+\rangle_{\text{pol.}} \\
|\Psi^-\rangle_{\omega,\text{pol.}} &= |\psi^-\rangle_\omega \otimes |\psi^-\rangle_{\text{pol.}} \\
|\Phi^+\rangle_{\omega,\text{pol.}} &= |\psi^-\rangle_\omega \otimes |\phi^+\rangle_{\text{pol.}} \\
|\Phi^-\rangle_{\omega,\text{pol.}} &= |\psi^-\rangle_\omega \otimes |\phi^-\rangle_{\text{pol.}} .
\end{aligned} \tag{S11}$$

Ψ^+ , Φ^+ and Φ^- are antisymmetric states, because they result from the product of an antisymmetric state (in TFM encoding) and a symmetric one (in polarisation encoding). Ψ^- is the only symmetric state, being the product of two antisymmetric states.

Polarisation to vector vortex beam conversion and final state

When a polarisation-encoded photon is sent through a q-plate, the circular component of the polarisation is flipped and the photon acquires orbital angular momentum (OAM) according to the following transformation:

$$\begin{aligned}
|L\rangle |0\rangle &\rightarrow |R\rangle | +2q\rangle \\
|R\rangle |0\rangle &\rightarrow |L\rangle | -2q\rangle ,
\end{aligned} \tag{S12}$$

where the first and second ket state represent polarisation and OAM, respectively, and q is the topological charge of the q-plate [4]. If the input polarisation of the photon is linear, the output photon is a vector vortex beam (VVB), i.e. polarisation and orbital angular momentum are entangled, giving rise to a non-uniform polarisation pattern in the transverse plane [5]. In particular, by sending H and V polarised light through the q-plate one can generate the so called $|\hat{r}\rangle$ and $|\hat{\theta}\rangle$ states, respectively, defined as [6]:

$$\begin{aligned}
|H\rangle &\rightarrow |\hat{r}\rangle = \frac{1}{\sqrt{2}} (|R\rangle | +2q\rangle + |L\rangle | -2q\rangle) \\
|V\rangle &\rightarrow |\hat{\theta}\rangle = \frac{1}{\sqrt{2}} (|R\rangle | +2q\rangle - |L\rangle | -2q\rangle) .
\end{aligned} \tag{S13}$$

The other two state of the four-dimensional VVB basis, namely $|\hat{\pi}^+\rangle$ and $|\hat{\pi}^-\rangle$, can be generated with an additional HWP after the q-plate:

$$\begin{aligned}
|\hat{\pi}^+\rangle &= \frac{1}{\sqrt{2}} (|L\rangle | +2q\rangle + |R\rangle | -2q\rangle) \\
|\hat{\pi}^-\rangle &= \frac{1}{\sqrt{2}} (|L\rangle | +2q\rangle - |R\rangle | -2q\rangle) .
\end{aligned} \tag{S14}$$

By sending a polarisation-TFM hyperentangled state (i.e. the one described in Eq. (S5)) through the q-plates, the following state is produced:

$$|\Psi\rangle_{\omega,\text{VVB}} = \frac{1}{\sqrt{2}} (|\wedge\rangle_s |\vee\rangle_i - |\vee\rangle_s |\wedge\rangle_i) \otimes \frac{1}{\sqrt{2}} (|\hat{r}\rangle_s |\hat{\theta}\rangle_i - |\hat{\theta}\rangle_s |\hat{r}\rangle_i) = |\psi\rangle_\omega \otimes |\psi^-\rangle_{\text{VVB}} , \tag{S15}$$

which is an hyperentangled between the TFM space and VVB space. In such system, intersystem hyperentanglement

(between VVB and TFM encoded in signal and idler) and intrasystem entanglement (between polarisation and OAM of each individual photon) coexist in the same biphoton state.

2. TWO-PHOTON INTERFERENCE OF THE HYPERENTANGLED STATE

In this section we discuss the two-photon interference for the polarisation-TFM hyperentangled state. We note that the same procedure can be used for the VVB-TFM hyperentanglement, where the polarisation indices H and V needs to be replaced by the VVB indices \hat{r} and $\hat{\theta}$.

Let's consider the hyperentangled state:

$$|\Psi\rangle_{\omega, \text{pol.}} = |\psi^-\rangle_{\omega} \otimes \frac{1}{\sqrt{2}} (|H\rangle_s |V\rangle_i + e^{i\varphi} |V\rangle_s |H\rangle_i) : \quad (\text{S16})$$

depending on the value of the phase φ , the overall quantum state can be maximally symmetric ($\varphi = \pi$), maximally antisymmetric ($\varphi = 0$), or a combination of the two cases (for any other value of φ). The signal and idler photon enter the ports a and b of a beam splitter (BS), which introduce the following transformations:

$$\text{BS} : \begin{cases} a_p^\dagger(\omega_s) \rightarrow \frac{1}{\sqrt{2}} (ia_p^\dagger(\omega_s) + b_p^\dagger(\omega_s)) \\ b_p^\dagger(\omega_i) \rightarrow \frac{1}{\sqrt{2}} (a_p^\dagger(\omega_i) + ib_p^\dagger(\omega_i)) \end{cases} \quad (\text{S17})$$

where p is the polarisation index. The state after the BS reads:

$$\begin{aligned} |\Psi\rangle_{\omega, \text{pol.}} &= \frac{1}{\sqrt{2}} \iint d\omega_s d\omega_i f_{s,i}(\omega_s, \omega_i) e^{-i\omega_i \tau} \left(a_H^\dagger(\omega_s) b_V^\dagger(\omega_i) + e^{i\varphi} a_V^\dagger(\omega_s) b_H^\dagger(\omega_i) \right) |0\rangle \\ &\quad \Downarrow \text{BS} \\ |\Psi\rangle_{\omega, \text{pol.}} &= \frac{1}{2\sqrt{2}} \iint d\omega_s d\omega_i f_{s,i}(\omega_s, \omega_i) e^{-i\omega_i \tau} \\ &\quad \left(\left(ia_H^\dagger(\omega_s) + b_H^\dagger(\omega_s) \right) \left(a_V^\dagger(\omega_i) + ib_V^\dagger(\omega_i) \right) + e^{i\varphi} \left(ia_V^\dagger(\omega_s) + b_V^\dagger(\omega_s) \right) \left(a_H^\dagger(\omega_i) + ib_H^\dagger(\omega_i) \right) \right) |0\rangle ; \end{aligned} \quad (\text{S18})$$

where we added a delay τ on the arrival time of the idler photon respect to the signal, and we decomposed the state in Eq. (S16) in its spectral and polarisation components. We can expand (S18) to:

$$\begin{aligned} |\Psi\rangle_{\omega, \text{pol.}} &= \frac{1}{2\sqrt{2}} \iint d\omega_s d\omega_i f_{s,i}(\omega_s, \omega_i) e^{-i\omega_i \tau} \\ &\quad \times \left(ia_H^\dagger(\omega_s) a_V^\dagger(\omega_i) - a_H^\dagger(\omega_s) b_V^\dagger(\omega_i) + b_H^\dagger(\omega_s) a_V^\dagger(\omega_i) + ib_H^\dagger(\omega_s) b_V^\dagger(\omega_i) + \right. \\ &\quad \left. + e^{i\varphi} ia_V^\dagger(\omega_s) a_H^\dagger(\omega_i) - e^{i\varphi} a_V^\dagger(\omega_s) b_H^\dagger(\omega_i) + e^{i\varphi} b_V^\dagger(\omega_s) a_H^\dagger(\omega_i) + e^{i\varphi} ib_V^\dagger(\omega_s) b_H^\dagger(\omega_i) \right) |0\rangle . \end{aligned} \quad (\text{S19})$$

We now project on the all possible coincidence cases:

$$\hat{P}_{s,i} = \iint d\omega_a \omega_b \left(a_H^\dagger(\omega_a) b_V^\dagger(\omega_b) |0\rangle \langle 0| a_H(\omega_a) b_V(\omega_b) + a_V^\dagger(\omega_a) b_H^\dagger(\omega_b) |0\rangle \langle 0| a_V(\omega_a) b_H(\omega_b) \right) , \quad (\text{S20})$$

where we neglect the cases where the operators have the same label ((H, H) and (V, V)) because they are not present

in the state.

$$\begin{aligned}
p_{cc}(\tau) &= \text{Tr} \left[|\Psi\rangle \langle \Psi|_{\omega, \text{pol.}} \hat{P}_{s,i} \right] = \langle \Psi | \hat{P}_{s,i} | \Psi \rangle_{\omega, \text{pol.}} \\
&= \frac{1}{8} \iint d\omega_s d\omega_i f_{s,i}^*(\omega_s, \omega_i) e^{i\omega_i \tau} \langle 0 | (-i a_H(\omega_s) a_V(\omega_i) - a_H(\omega_s) b_V(\omega_i) + b_H(\omega_s) a_V(\omega_i) - i b_H(\omega_s) b_V(\omega_i) + \\
&\quad - e^{-i\varphi} i a_V(\omega_s) a_H(\omega_i) - e^{-i\varphi} a_V(\omega_s) b_H(\omega_i) + e^{-i\varphi} b_V(\omega_s) a_H(\omega_i) - e^{-i\varphi} i b_V(\omega_s) b_H(\omega_i)) \\
&\quad \times \iint d\omega_a \omega_b \left(a_H^\dagger(\omega_a) b_V^\dagger(\omega_b) |0\rangle \langle 0| a_H(\omega_a) b_V(\omega_b) + a_V^\dagger(\omega_a) b_H^\dagger(\omega_b) |0\rangle \langle 0| a_V(\omega_a) b_H(\omega_b) \right) \\
&\quad \times \iint d\omega'_s d\omega'_i f_{s,i}(\omega'_s, \omega'_i) e^{-i\omega'_i \tau} \\
&\quad \left(i a_H^\dagger(\omega'_s) a_V^\dagger(\omega'_i) - a_H^\dagger(\omega'_s) b_V^\dagger(\omega'_i) + b_H^\dagger(\omega'_s) a_V^\dagger(\omega'_i) + i b_H^\dagger(\omega'_s) b_V^\dagger(\omega'_i) + \right. \\
&\quad \left. + e^{i\varphi} i a_V^\dagger(\omega'_s) a_H^\dagger(\omega'_i) - e^{i\varphi} a_V^\dagger(\omega'_s) b_H^\dagger(\omega'_i) + e^{i\varphi} b_V^\dagger(\omega'_s) a_H^\dagger(\omega'_i) + e^{i\varphi} i b_V^\dagger(\omega'_s) b_H^\dagger(\omega'_i) \right) |0\rangle .
\end{aligned} \tag{S21}$$

We can rearrange the terms obtaining:

$$\begin{aligned}
p_{cc}(\tau) &= \frac{1}{8} \iint d\omega_s d\omega_i d\omega'_s d\omega'_i d\omega_a \omega_b \\
&\quad \times f_{s,i}^*(\omega_s, \omega_i) f_{s,i}(\omega'_s, \omega'_i) e^{i(\omega_i - \omega'_i) \tau} \\
&\quad \times \left(-\langle 0 | a_H(\omega_s) b_V(\omega_i) a_H^\dagger(\omega_a) b_V^\dagger(\omega_b) |0\rangle \right. \\
&\quad \left. + \langle 0 | b_H(\omega_s) a_V(\omega_i) a_V^\dagger(\omega_a) b_H^\dagger(\omega_b) |0\rangle \right. \\
&\quad \left. - e^{-i\varphi} \langle 0 | a_V(\omega_s) b_H(\omega_i) a_V^\dagger(\omega_a) b_H^\dagger(\omega_b) |0\rangle \right. \\
&\quad \left. + e^{-i\varphi} \langle 0 | b_V(\omega_s) a_H(\omega_i) a_H^\dagger(\omega_a) b_V^\dagger(\omega_b) |0\rangle \right) \\
&\quad \times \left(-\langle 0 | a_H(\omega_a) b_V(\omega_b) a_H^\dagger(\omega'_s) b_V^\dagger(\omega'_i) |0\rangle \right. \\
&\quad \left. + \langle 0 | a_V(\omega_a) b_H(\omega_b) b_H^\dagger(\omega'_s) a_V^\dagger(\omega'_i) |0\rangle \right. \\
&\quad \left. - e^{i\varphi} \langle 0 | a_V(\omega_a) b_H(\omega_b) a_V^\dagger(\omega'_s) b_H^\dagger(\omega'_i) |0\rangle \right. \\
&\quad \left. + e^{i\varphi} \langle 0 | a_H(\omega_a) b_V(\omega_b) b_V^\dagger(\omega'_s) a_H^\dagger(\omega'_i) |0\rangle \right)
\end{aligned} \tag{S22}$$

where we have already neglected all the terms where the polarisation of the creation and annihilation operators don't match, and where both the creation operator/annihilation operators are in one mode (as we are considering coincidences between the two modes).

$$\begin{aligned}
p_{cc}(\tau) &= \frac{1}{8} \iint d\omega_s d\omega_i d\omega'_s d\omega'_i d\omega_a \omega_b f_{s,i}^*(\omega_s, \omega_i) f_{s,i}(\omega'_s, \omega'_i) e^{i(\omega_i - \omega'_i) \tau} \\
&\quad \times (-\delta_H(\omega_s - \omega_a) \delta_V(\omega_i - \omega_b) + \delta_H(\omega_s - \omega_b) \delta_V(\omega_i - \omega_a) - e^{-i\varphi} \delta_V(\omega_s - \omega_a) \delta_H(\omega_i - \omega_b) + e^{-i\varphi} \delta_V(\omega_s - \omega_b) \delta_H(\omega_i - \omega_a)) \\
&\quad \times (-\delta_H(\omega'_s - \omega_a) \delta_V(\omega'_i - \omega_b) + \delta_H(\omega'_s - \omega_b) \delta_V(\omega'_i - \omega_a) - e^{i\varphi} \delta_V(\omega'_s - \omega_a) \delta_H(\omega'_i - \omega_b) + e^{i\varphi} \delta_V(\omega'_s - \omega_b) \delta_H(\omega'_i - \omega_a))
\end{aligned} \tag{S23}$$

Integrating over ω_a and ω_b we get:

$$\begin{aligned}
p_{cc}(\tau) &= \frac{1}{8} \iint d\omega_s d\omega_i d\omega'_s d\omega'_i f_{s,i}^*(\omega_s, \omega_i) f_{s,i}(\omega'_s, \omega'_i) e^{i(\omega_i - \omega'_i) \tau} \\
&\quad \times (\delta_H(\omega_i - \omega'_i) \delta_V(\omega_s - \omega'_s) - e^{i\varphi} \delta_H(\omega_s - \omega'_i) \delta_V(\omega_i - \omega'_s) + \delta_H(\omega_s - \omega'_s) \delta_V(\omega_i - \omega'_i) - e^{i\varphi} \delta_H(\omega_s - \omega'_i) \delta_V(\omega_i - \omega'_s) + \\
&\quad - e^{-i\varphi} \delta_V(\omega_s - \omega'_i) \delta_H(\omega_i - \omega'_s) + \delta_V(\omega_s - \omega'_s) \delta_H(\omega_i - \omega'_i) - e^{-i\varphi} \delta_V(\omega_s - \omega'_i) \delta_H(\omega_i - \omega'_s) + \delta_V(\omega_s - \omega'_s) \delta_H(\omega_i - \omega'_i))
\end{aligned} \tag{S24}$$

where we have neglected all the terms where the polarisation of the delta functions doesn't match. Let's now integrate over ω'_s and ω'_i (and we can also get rid of the polarisation labels as are now irrelevant):

$$\begin{aligned}
p_{cc}(\tau) &= \frac{1}{8} \iint d\omega_s d\omega_i \left(4 |f_{s,i}(\omega_s, \omega_i)|^2 - 2 f_{s,i}^*(\omega_s, \omega_i) f_{s,i}(\omega_i, \omega_s) e^{i(\omega_i - \omega_s) \tau} e^{i\varphi} - 2 f_{s,i}^*(\omega_s, \omega_i) f_{s,i}(\omega_i, \omega_s) e^{i(\omega_i - \omega_s) \tau} e^{-i\varphi} \right) \\
&= \frac{1}{2} \iint d\omega_s d\omega_i \left(|f_{s,i}(\omega_s, \omega_i)|^2 - \cos(\varphi) f_{s,i}^*(\omega_s, \omega_i) f_{s,i}(\omega_i, \omega_s) e^{i(\omega_i - \omega_s) \tau} \right) \\
&= \frac{1}{2} \iint d\omega_s d\omega_i \left(1 - \cos(\varphi) f_{s,i}^*(\omega_s, \omega_i) f_{s,i}(\omega_i, \omega_s) e^{i(\omega_i - \omega_s) \tau} \right) .
\end{aligned} \tag{S25}$$

We can finally write the JSA in terms of the Schmidt modes:

$$\begin{aligned}
 p_{cc}(\tau) &= \frac{1}{2} \iint d\omega_s d\omega_i \left(1 - \cos(\varphi) \left(\sum_k d_k u_k^*(\omega_s) v_k^*(\omega_i) \right) \left(\sum_{k'} d_{k'} u_{k'}(\omega_i) v_{k'}(\omega_s) \right) e^{i(\omega_i - \omega_s)\tau} \right) \\
 &= \frac{1}{2} \left(1 - \cos(\varphi) \left(\sum_{k,k'} d_k d_{k'} \int d\omega_s u_k^*(\omega_s) v_{k'}(\omega_s) e^{-i\omega_s \tau} \int d\omega_i v_k^*(\omega_i) u_{k'}(\omega_i) e^{i\omega_i \tau} \right) \right).
 \end{aligned} \tag{S26}$$

Replacing u and v with the corresponding Schmidt modes in Eq. (S3) we obtain the following interference pattern:

$$p_{cc}(\tau) = \frac{1}{2} - \frac{1}{4} e^{-\frac{1}{4}\sigma^2\tau^2} (\sigma^2\tau^2 - 2) \cos(\varphi), \tag{S27}$$

that we plot in Fig. S2. $\varphi = 0$ corresponds to perfect antibunching, as expected by a maximally antisymmetric state, while for $\varphi = \pi$ leads to perfect bunching, as the state is symmetric.

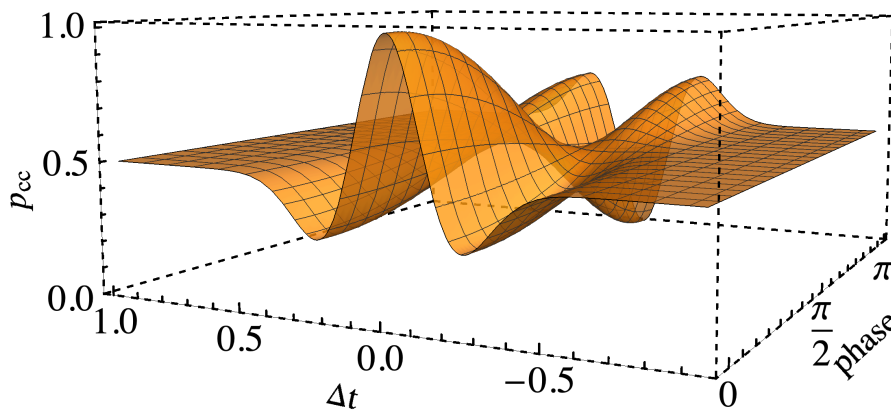


FIG. S2. **Two-photon interference pattern.** Probability of having coincidences after the BS as a function of the state's phase, varying the relative arriving time of signal and idler.

-
- [1] F. Graffitti, J. Kelly-Massicotte, A. Fedrizzi, and A. M. Brańczyk, Design considerations for high-purity heralded single-photon sources, *Phys. Rev. A* **98**, 053811 (2018).
 - [2] F. Graffitti, P. Barrow, A. Pickston, A. M. Brańczyk, and A. Fedrizzi, Direct generation of tailored pulse-mode entanglement, *Phys. Rev. Lett.* **124**, 053603 (2020).
 - [3] A. Fedrizzi, T. Herbst, A. Poppe, T. Jennewein, and A. Zeilinger, A wavelength-tunable fiber-coupled source of narrowband entangled photons, *Opt. Express* **15**, 15377 (2007).
 - [4] L. Marrucci, C. Manzo, and D. Paparo, Optical spin-to-orbital angular momentum conversion in inhomogeneous anisotropic media, *Phys. Rev. Lett.* **96**, 163905 (2006).
 - [5] F. Cardano, E. Karimi, S. Slussarenko, L. Marrucci, C. de Lisio, and E. Santamato, Polarization pattern of vector vortex beams generated by q-plates with different topological charges, *Appl. Opt.* **51**, C1 (2012).
 - [6] V. D'Ambrosio, G. Carvacho, F. Graffitti, C. Vitelli, B. Piccirillo, L. Marrucci, and F. Sciarrino, Entangled vector vortex beams, *Phys. Rev. A* **94**, 030304 (2016).

Bibliography

- [1] D. Magde and H. Mahr, Study in Ammonium Dihydrogen Phosphate of Spontaneous Parametric Interaction Tunable from 4400 to 16 000 Å, *Phys. Rev. Lett.* **18**, 905–907 (1967).
- [2] S. Akhmanov, V. Fadeev, R. Khokhlov, and O. Chunaev, Quantum noise in parametric light amplifiers, *ZhETF Pisma Redaktsiiu* **6**, 575 (1967).
- [3] R. L. Byer and S. E. Harris, Power and Bandwidth of Spontaneous Parametric Emission, *Phys. Rev.* **168**, 1064–1068 (1968).
- [4] D. C. Burnham and D. L. Weinberg, Observation of Simultaneity in Parametric Production of Optical Photon Pairs, *Phys. Rev. Lett.* **25**, 84–87 (1970).
- [5] B. Y. Zel’dovich and D. N. Klyshko, Field statistics in parametric luminescence, *ZhETF Pisma Redaktsiiu* **9**, 69 (1969).
- [6] R. Ghosh and L. Mandel, Observation of nonclassical effects in the interference of two photons, *Phys. Rev. Lett.* **59**, 1903–1905 (1987).
- [7] C. K. Hong, Z. Y. Ou, and L. Mandel, Measurement of subpicosecond time intervals between two photons by interference, *Phys. Rev. Lett.* **59**, 2044–2046 (1987).
- [8] P. G. Kwiat, K. Mattle, H. Weinfurter, A. Zeilinger, A. V. Sergienko, and Y. Shih, New High-Intensity Source of Polarization-Entangled Photon Pairs, *Phys. Rev. Lett.* **75**, 4337–4341 (1995).
- [9] M. Barbieri, F. De Martini, G. Di Nepi, P. Mataloni, G. M. D’Ariano, and C. Macchiavello, Detection of Entanglement with Polarized Photons: Experimental Realization of an Entanglement Witness, *Phys. Rev. Lett.* **91**, 227901 (2003).
- [10] M. Barbieri, C. Cinelli, P. Mataloni, and F. De Martini, Polarization-momentum hyperentangled states: Realization and characterization, *Phys. Rev. A* **72**, 052110 (2005).
- [11] A. Mair, A. Vaziri, G. Weihs, and A. Zeilinger, Entanglement of the orbital angular momentum states of photons, *Nature* **412**, 313–316 (2001).

- [12] X.-L. Wang, L.-K. Chen, W. Li, H.-L. Huang, C. Liu, C. Chen, Y.-H. Luo, Z.-E. Su, D. Wu, Z.-D. Li, H. Lu, Y. Hu, X. Jiang, C.-Z. Peng, L. Li, N.-L. Liu, Y.-A. Chen, C.-Y. Lu, and J.-W. Pan, Experimental Ten-Photon Entanglement, *Phys. Rev. Lett.* **117**, 210502 (2016).
- [13] H.-S. Zhong, Y. Li, W. Li, L.-C. Peng, Z.-E. Su, Y. Hu, Y.-M. He, X. Ding, W. Zhang, H. Li, L. Zhang, Z. Wang, L. You, X.-L. Wang, X. Jiang, L. Li, Y.-A. Chen, N.-L. Liu, C.-Y. Lu, and J.-W. Pan, 12-Photon Entanglement and Scalable Scattershot Boson Sampling with Optimal Entangled-Photon Pairs from Parametric Down-Conversion, *Phys. Rev. Lett.* **121**, 250505 (2018).
- [14] A. Fedrizzi, T. Herbst, A. Poppe, T. Jennewein, and A. Zeilinger, A wavelength-tunable fiber-coupled source of narrowband entangled photons, *Opt. Express* **15**, 15377–15386 (2007).
- [15] P. G. Evans, R. S. Bennink, W. P. Grice, T. S. Humble, and J. Schaake, Bright Source of Spectrally Uncorrelated Polarization-Entangled Photons with Nearly Single-Mode Emission, *Phys. Rev. Lett.* **105**, 253601 (2010).
- [16] L. K. Shalm, E. Meyer-Scott, B. G. Christensen, P. Bierhorst, M. A. Wayne, M. J. Stevens, T. Gerrits, S. Glancy, D. R. Hamel, M. S. Allman, K. J. Coakley, S. D. Dyer, C. Hodge, A. E. Lita, V. B. Verma, C. Lambrocco, E. Tortorici, A. L. Migdall, Y. Zhang, D. R. Kumor, W. H. Farr, F. Marsili, M. D. Shaw, J. A. Stern, C. Abellán, W. Amaya, V. Pruneri, T. Jennewein, M. W. Mitchell, P. G. Kwiat, J. C. Bienfang, R. P. Mirin, E. Knill, and S. W. Nam, Strong Loophole-Free Test of Local Realism, *Phys. Rev. Lett.* **115**, 250402 (2015).
- [17] M. Giustina, M. A. M. Versteegh, S. Wengerowsky, J. Handsteiner, A. Hochrainer, K. Phelan, F. Steinlechner, J. Kofler, J.-A. Larsson, C. Abellán, W. Amaya, V. Pruneri, M. W. Mitchell, J. Beyer, T. Gerrits, A. E. Lita, L. K. Shalm, S. W. Nam, T. Scheidl, R. Ursin, B. Wittmann, and A. Zeilinger, Significant-Loophole-Free Test of Bell’s Theorem with Entangled Photons, *Phys. Rev. Lett.* **115**, 250401 (2015).
- [18] X.-S. Ma, S. Zotter, J. Kofler, T. Jennewein, and A. Zeilinger, Experimental generation of single photons via active multiplexing, *Phys. Rev. A* **83**, 043814 (2011).
- [19] M. A. Broome, M. P. Almeida, A. Fedrizzi, and A. G. White, Reducing multiphoton rates in pulsed down-conversion by temporal multiplexing, *Opt. Express* **19**, 22698–22708 (2011).
- [20] M. J. Collins, C. Xiong, I. H. Rey, T. D. Vo, J. He, S. Shahnian, C. Reardon, T. F. Krauss, M. J. Steel, A. S. Clark, and B. J. Eggleton, Integrated spatial multiplexing of heralded single-photon sources, *Nature Communications* **4**, 2582 (2013).
- [21] R. J. A. Francis-Jones, R. A. Hoggarth, and P. J. Mosley, All-fiber multiplexed source of high-purity single photons, *Optica* **3**, 1270–1273 (2016).

- [22] C. Xiong, X. Zhang, Z. Liu, M. J. Collins, A. Mahendra, L. G. Helt, M. J. Steel, D.-Y. Choi, C. J. Chae, P. H. W. Leong, and B. J. Eggleton, Active temporal multiplexing of indistinguishable heralded single photons, *Nature Communications* **7**, 10853 (2016).
- [23] F. Kaneda, F. Xu, J. Chapman, and P. G. Kwiat, Quantum-memory-assisted multi-photon generation for efficient quantum information processing, *Optica* **4**, 1034–1037 (2017).
- [24] F. Graffitti, P. Barrow, M. Proietti, D. Kundys, and A. Fedrizzi, Independent high-purity photons created in domain-engineered crystals, *Optica* **5**, 514–517 (2018).
- [25] O. Cohen, J. S. Lundeen, B. J. Smith, G. Puentes, P. J. Mosley, and I. A. Walmsley, Tailored Photon-Pair Generation in Optical Fibers, *Phys. Rev. Lett.* **102**, 123603 (2009).
- [26] S. Paesani, M. Borghi, S. Signorini, A. Mañnos, L. Pavesi, and A. Laing, Near-ideal spontaneous photon sources in silicon quantum photonics, *Nature Communications* **11**, 2505 (2020).
- [27] P. Senellart, G. Solomon, and A. White, High-performance semiconductor quantum-dot single-photon sources, *Nature Nanotechnology* **12**, 1026–1039 (2017).
- [28] T. Gaebel, I. Popa, A. Gruber, M. Domhan, F. Jelezko, and J. Wrachtrup, Stable single-photon source in the near infrared, *New Journal of Physics* **6**, 98–98 (2004).
- [29] C. Maurer, C. Becher, C. Russo, J. Eschner, and R. Blatt, A single-photon source based on a single Ca^{+} ion, *New Journal of Physics* **6**, 94–94 (2004).
- [30] J. McKeever, A. Boca, A. D. Boozer, R. Miller, J. R. Buck, A. Kuzmich, and H. J. Kimble, Deterministic Generation of Single Photons from One Atom Trapped in a Cavity, *Science* **303**, 1992–1994 (2004).
- [31] B. Lounis and W. E. Moerner, Single photons on demand from a single molecule at room temperature, *Nature* **407**, 491–493 (2000).
- [32] B. Hensen, H. Bernien, A. E. Dréau, A. Reiserer, N. Kalb, M. S. Blok, J. Ruitenberg, R. F. L. Vermeulen, R. N. Schouten, C. Abellán, W. Amaya, V. Pruneri, M. W. Mitchell, M. Markham, D. J. Twitchen, D. Elkouss, S. Wehner, T. H. Taminiau, and R. Hanson, Loophole-free Bell inequality violation using electron spins separated by 1.3 kilometres, *Nature* **526**, 682–686 (2015).
- [33] H. Wang, J. Qin, X. Ding, M.-C. Chen, S. Chen, X. You, Y.-M. He, X. Jiang, L. You, Z. Wang, C. Schneider, J. J. Renema, S. Höfling, C.-Y. Lu, and J.-W. Pan, Boson Sampling with 20 Input Photons and a 60-Mode Interferometer in a 10^{14} -Dimensional Hilbert Space, *Phys. Rev. Lett.* **123**, 250503 (2019).

- [34] J. Yin, Y. Cao, Y.-H. Li, S.-K. Liao, L. Zhang, J.-G. Ren, W.-Q. Cai, W.-Y. Liu, B. Li, H. Dai, G.-B. Li, Q.-M. Lu, Y.-H. Gong, Y. Xu, S.-L. Li, F.-Z. Li, Y.-Y. Yin, Z.-Q. Jiang, M. Li, J.-J. Jia, G. Ren, D. He, Y.-L. Zhou, X.-X. Zhang, N. Wang, X. Chang, Z.-C. Zhu, N.-L. Liu, Y.-A. Chen, C.-Y. Lu, R. Shu, C.-Z. Peng, J.-Y. Wang, and J.-W. Pan, Satellite-based entanglement distribution over 1200 kilometers, *Science* **356**, 1140–1144 (2017).
- [35] S.-K. Liao, W.-Q. Cai, W.-Y. Liu, L. Zhang, Y. Li, J.-G. Ren, J. Yin, Q. Shen, Y. Cao, Z.-P. Li, F.-Z. Li, X.-W. Chen, L.-H. Sun, J.-J. Jia, J.-C. Wu, X.-J. Jiang, J.-F. Wang, Y.-M. Huang, Q. Wang, Y.-L. Zhou, L. Deng, T. Xi, L. Ma, T. Hu, Q. Zhang, Y.-A. Chen, N.-L. Liu, X.-B. Wang, Z.-C. Zhu, C.-Y. Lu, R. Shu, C.-Z. Peng, J.-Y. Wang, and J.-W. Pan, Satellite-to-ground quantum key distribution, *Nature* **549**, 43–47 (2017).
- [36] S.-K. Liao, W.-Q. Cai, J. Handsteiner, B. Liu, J. Yin, L. Zhang, D. Rauch, M. Fink, J.-G. Ren, W.-Y. Liu, Y. Li, Q. Shen, Y. Cao, F.-Z. Li, J.-F. Wang, Y.-M. Huang, L. Deng, T. Xi, L. Ma, T. Hu, L. Li, N.-L. Liu, F. Koidl, P. Wang, Y.-A. Chen, X.-B. Wang, M. Steindorfer, G. Kirchner, C.-Y. Lu, R. Shu, R. Ursin, T. Scheidl, C.-Z. Peng, J.-Y. Wang, A. Zeilinger, and J.-W. Pan, Satellite-Relayed Intercontinental Quantum Network, *Phys. Rev. Lett.* **120**, 030501 (2018).
- [37] A. Villar, A. Lohrmann, X. Bai, T. Vergoossen, R. Bedington, C. Perumangatt, H. Y. Lim, T. Islam, A. Reezwana, Z. Tang, R. Chandrasekara, S. Sachidananda, K. Durak, C. F. Wildfeuer, D. Griffin, D. K. L. Oi, and A. Ling, Entanglement demonstration on board a nano-satellite, *Optica* **7**, 734–737 (2020).
- [38] M. Gimeno-Segovia, P. Shadbolt, D. E. Browne, and T. Rudolph, From Three-Photon Greenberger-Horne-Zeilinger States to Ballistic Universal Quantum Computation, *Phys. Rev. Lett.* **115**, 020502 (2015).
- [39] Y. Li, S. D. Barrett, T. M. Stace, and S. C. Benjamin, Fault Tolerant Quantum Computation with Nondeterministic Gates, *Phys. Rev. Lett.* **105**, 250502 (2010).
- [40] E. Meyer-Scott, N. Montaut, J. Tiedau, L. Sansoni, H. Herrmann, T. J. Bartley, and C. Silberhorn, Limits on the heralding efficiencies and spectral purities of spectrally filtered single photons from photon-pair sources, *Phys. Rev. A* **95**, 061803 (2017).
- [41] A. M. Brańczyk, Hong-Ou-Mandel Interference, (2017), [arXiv:1711.00080](https://arxiv.org/abs/1711.00080) [quant-ph] .
- [42] F. Graffitti, V. D’Ambrosio, M. Proietti, J. Ho, B. Piccirillo, C. de Lisio, L. Marrucci, and A. Fedrizzi, Hyperentanglement in structured quantum light, *Phys. Rev. Research* **2**, 043350 (2020).

- [43] A. Migdall, S. V. Polyakov, J. Fan, and J. C. Bienfang, *Single-photon generation and detection: physics and applications* (Academic Press, Cambridge, Massachusetts, 2013).
- [44] P. J. Mosley, *Generation of heralded single photons in pure quantum states*, Ph.D. thesis, University of Oxford, Oxford, United Kingdom (2007).
- [45] G. Harder, *Optimized down-conversion source and state-characterization tools for quantum optics*, Ph.D. thesis, University of Paderborn, Paderborn, Germany (2016).
- [46] R. W. Boyd, *Nonlinear optics*, 3rd ed. (Academic Press, Cambridge, Massachusetts, 2008).
- [47] R. Loudon, *The quantum theory of light* (Oxford University Press, Oxford, 2000).
- [48] W. P. Grice and I. A. Walmsley, Spectral information and distinguishability in type-II down-conversion with a broadband pump, *Phys. Rev. A* **56**, 1627–1634 (1997).
- [49] A. M. Brańczyk, T. M. Stace, and T. C. Ralph, Time Ordering in Spontaneous Parametric Down-conversion, in *AIP Conference Proceedings*, Vol. 1363 (AIP, 2011) pp. 335–338.
- [50] A. Christ, B. Brecht, W. Mauerer, and C. Silberhorn, Theory of quantum frequency conversion and type-II parametric down-conversion in the high-gain regime, *New Journal of Physics* **15**, 053038 (2013).
- [51] N. Quesada and J. E. Sipe, Effects of time ordering in quantum nonlinear optics, *Phys. Rev. A* **90**, 063840 (2014).
- [52] N. Quesada and J. E. Sipe, Time-Ordering Effects in the Generation of Entangled Photons Using Nonlinear Optical Processes, *Phys. Rev. Lett.* **114**, 093903 (2015).
- [53] N. Bruno, A. Martin, T. Guerreiro, B. Sanguinetti, and R. T. Thew, Pulsed source of spectrally uncorrelated and indistinguishable photons at telecom wavelengths, *Opt. Express* **22**, 17246–17253 (2014).
- [54] M. Avenhaus, H. B. Coldenstrodt-Ronge, K. Laiho, W. Mauerer, I. A. Walmsley, and C. Silberhorn, Photon Number Statistics of Multimode Parametric Down-Conversion, *Phys. Rev. Lett.* **101**, 053601 (2008).
- [55] W. Wasilewski, C. Radzewicz, R. Frankowski, and K. Banaszek, Statistics of multiphoton events in spontaneous parametric down-conversion, *Phys. Rev. A* **78**, 033831 (2008).
- [56] W. Mauerer, M. Avenhaus, W. Helwig, and C. Silberhorn, How colors influence numbers: Photon statistics of parametric down-conversion, *Phys. Rev. A* **80**, 053815 (2009).

- [57] J. Schneeloch, S. H. Knarr, D. F. Bogorin, M. L. Levangie, C. C. Tison, R. Frank, G. A. Howland, M. L. Fanto, and P. M. Alsing, Introduction to the absolute brightness and number statistics in spontaneous parametric down-conversion, *Journal of Optics* **21**, 043501 (2019).
- [58] G. Triginer, M. D. Vidrighin, N. Quesada, A. Eckstein, M. Moore, W. S. Kolthammer, J. E. Sipe, and I. A. Walmsley, Understanding high gain twin beam sources using cascaded stimulated emission, (2019), [arXiv:1911.05708 \[quant-ph\]](https://arxiv.org/abs/1911.05708) .
- [59] R.-B. Jin, M. Fujiwara, T. Yamashita, S. Miki, H. Terai, Z. Wang, K. Wakui, R. Shimizu, and M. Sasaki, Efficient detection of an ultra-bright single-photon source using superconducting nanowire single-photon detectors, *Optics Communications* **336**, 47 – 54 (2015).
- [60] C. Greganti, P. Schiansky, I. A. Calafell, L. M. Procopio, L. A. Rozema, and P. Walther, Tuning single-photon sources for telecom multi-photon experiments, *Opt. Express* **26**, 3286–3302 (2018).
- [61] F. Kaneda and P. G. Kwiat, High-efficiency single-photon generation via large-scale active time multiplexing, *Science Advances* **5**, eaaw8586 (2019).
- [62] A. L. Migdall, D. Branning, and S. Castelletto, Tailoring single-photon and multiphoton probabilities of a single-photon on-demand source, *Phys. Rev. A* **66**, 053805 (2002).
- [63] W. Sellmeier, About the vibrations of the body particles excited by the ether vibrations and their reaction to the former, especially to explain the dispersion and its anomalies, *Annals of Physics* **223**, 386–403 (1872).
- [64] K. Fradkin, A. Arie, A. Skliar, and G. Rosenman, Tunable midinfrared source by difference frequency generation in bulk periodically poled KTiOPO₄, *Applied Physics Letters* **74**, 914–916 (1999).
- [65] S. Emanuelli and A. Arie, Temperature-dependent dispersion equations for KTiOPO₄ and KTiOAsO₄, *Appl. Opt.* **42**, 6661–6665 (2003).
- [66] F. König and F. N. C. Wong, Extended phase matching of second-harmonic generation in periodically poled KTiOPO₄ with zero group-velocity mismatch, *Applied Physics Letters* **84**, 1644–1646 (2004).
- [67] C. K. Law, I. A. Walmsley, and J. H. Eberly, Continuous Frequency Entanglement: Effective Finite Hilbert Space and Entropy Control, *Phys. Rev. Lett.* **84**, 5304–5307 (2000).
- [68] F. Laudenbach, H. Hübel, M. Hentschel, P. Walther, and A. Poppe, Modeling parametric down-conversion yielding spectrally pure photon pairs, *Opt. Express* **24**, 2712–2727 (2016).

- [69] J. H. Eberly, Schmidt analysis of pure-state entanglement, *Laser Physics* **16**, 921–926 (2006).
- [70] A. B. U'Ren, C. Silberhorn, R. Erdmann, K. Banaszek, W. P. Grice, I. A. Walmsley, and M. G. Raymer, Generation of Pure-State Single-Photon Wavepackets by Conditional Preparation Based on Spontaneous Parametric Down-conversion, (2006), [arXiv:quant-ph/0611019](https://arxiv.org/abs/quant-ph/0611019) [quant-ph] .
- [71] F. Graffitti, J. Kelly-Massicotte, A. Fedrizzi, and A. M. Brańczyk, Design considerations for high-purity heralded single-photon sources, *Phys. Rev. A* **98**, 053811 (2018).
- [72] M. H. Rubin, D. N. Klyshko, Y. H. Shih, and A. V. Sergienko, Theory of two-photon entanglement in type-II optical parametric down-conversion, *Phys. Rev. A* **50**, 5122–5133 (1994).
- [73] T. E. Keller and M. H. Rubin, Theory of two-photon entanglement for spontaneous parametric down-conversion driven by a narrow pump pulse, *Phys. Rev. A* **56**, 1534–1541 (1997).
- [74] R. Erdmann, D. Branning, W. Grice, and I. A. Walmsley, Restoring dispersion cancellation for entangled photons produced by ultrashort pulses, *Phys. Rev. A* **62**, 053810 (2000).
- [75] W. P. Grice, A. B. U'Ren, and I. A. Walmsley, Eliminating frequency and space-time correlations in multiphoton states, *Phys. Rev. A* **64**, 063815 (2001).
- [76] Y.-H. Kim and W. P. Grice, Generation of pulsed polarization-entangled two-photon state via temporal and spectral engineering, *Journal of Modern Optics* **49**, 2309–2323 (2002).
- [77] V. Giovannetti, L. Maccone, J. H. Shapiro, and F. N. C. Wong, Extended phase-matching conditions for improved entanglement generation, *Phys. Rev. A* **66**, 043813 (2002).
- [78] V. Giovannetti, L. Maccone, J. H. Shapiro, and F. N. C. Wong, Generating Entangled Two-Photon States with Coincident Frequencies, *Phys. Rev. Lett.* **88**, 183602 (2002).
- [79] A. Christ, A. Eckstein, P. J. Mosley, and C. Silberhorn, Pure single photon generation by type-I PDC with backward-wave amplification, *Opt. Express* **17**, 3441–3446 (2009).
- [80] F. Kaneda, K. Garay-Palmett, A. B. U'Ren, and P. G. Kwiat, Heralded single-photon source utilizing highly nondegenerate, spectrally factorable spontaneous parametric downconversion, *Opt. Express* **24**, 10733–10747 (2016).
- [81] M. M. Weston, H. M. Chrzanowski, S. Wollmann, A. Boston, J. Ho, L. K. Shalm, V. B. Verma, M. S. Allman, S. W. Nam, R. B. Patel, S. Slussarenko, and G. J. Pryde, Efficient and pure femtosecond-pulse-length source of polarization-entangled photons, *Opt. Express* **24**, 10869–10879 (2016).

- [82] F. Laudenbach, R.-B. Jin, C. Greganti, M. Hentschel, P. Walther, and H. Hübel, Numerical Investigation of Photon-Pair Generation in Periodically Poled $MTiOXO_4$ ($M = K, Rb, Cs$; $X = P, As$), [Phys. Rev. Applied](#) **8**, 024035 (2017).
- [83] M. Barbieri, E. Roccia, L. Mancino, M. Sbroscia, I. Gianani, and F. Sciarrino, What Hong-Ou-Mandel interference says on two-photon frequency entanglement, [Scientific Reports](#) **7**, 7247 (2017).
- [84] C. Chen, C. Bo, M. Y. Niu, F. Xu, Z. Zhang, J. H. Shapiro, and F. N. C. Wong, Efficient generation and characterization of spectrally factorable biphotons, [Opt. Express](#) **25**, 7300–7312 (2017).
- [85] R. A. McCracken, F. Graffitti, and A. Fedrizzi, Numerical investigation of mid-infrared single-photon generation, [J. Opt. Soc. Am. B](#) **35**, C38–C48 (2018).
- [86] C. Rulliere *et al.*, *Femtosecond laser pulses* (Springer, New York, NY, 2005).
- [87] P. J. Mosley, J. S. Lundeen, B. J. Smith, and I. A. Walmsley, Conditional preparation of single photons using parametric downconversion: a recipe for purity, [New Journal of Physics](#) **10**, 093011 (2008).
- [88] P. J. Mosley, J. S. Lundeen, B. J. Smith, P. Wasylczyk, A. B. U'Ren, C. Silberhorn, and I. A. Walmsley, Heralded Generation of Ultrafast Single Photons in Pure Quantum States, [Phys. Rev. Lett.](#) **100**, 133601 (2008).
- [89] A. M. Brańczyk, A. Fedrizzi, T. M. Stace, T. C. Ralph, and A. G. White, Engineered optical nonlinearity for quantum light sources, [Opt. Express](#) **19**, 55–65 (2011).
- [90] P. B. Dixon, J. H. Shapiro, and F. N. C. Wong, Spectral engineering by Gaussian phase-matching for quantum photonics, [Opt. Express](#) **21**, 5879–5890 (2013).
- [91] A. Dosseva, L. Cincio, and A. M. Brańczyk, Shaping the joint spectrum of down-converted photons through optimized custom poling, [Phys. Rev. A](#) **93**, 013801 (2016).
- [92] J.-L. Tambasco, A. Boes, L. G. Helt, M. J. Steel, and A. Mitchell, Domain engineering algorithm for practical and effective photon sources, [Opt. Express](#) **24**, 19616–19626 (2016).
- [93] F. Graffitti, D. Kundys, D. T. Reid, A. M. Brańczyk, and A. Fedrizzi, Pure down-conversion photons through sub-coherence-length domain engineering, [Quantum Science and Technology](#) **2**, 035001 (2017).
- [94] A. M. Brańczyk, T. C. Ralph, W. Helwig, and C. Silberhorn, Optimized generation of heralded Fock states using parametric down-conversion, [New Journal of Physics](#) **12**, 063001 (2010).

- [95] K. Laiho, A. Christ, K. N. Cassemiro, and C. Silberhorn, Testing spectral filters as Gaussian quantum optical channels, *Opt. Lett.* **36**, 1476–1478 (2011).
- [96] A. Christ, C. Lupo, M. Reichelt, T. Meier, and C. Silberhorn, Theory of filtered type-II parametric down-conversion in the continuous-variable domain: Quantifying the impacts of filtering, *Phys. Rev. A* **90**, 023823 (2014).
- [97] N. Quesada and A. M. Brańczyk, Gaussian functions are optimal for wave-guided nonlinear-quantum-optical processes, *Phys. Rev. A* **98**, 043813 (2018).
- [98] R.-B. Jin, R. Shimizu, K. Wakui, H. Benichi, and M. Sasaki, Widely tunable single photon source with high purity at telecom wavelength, *Opt. Express* **21**, 10659–10666 (2013).
- [99] Y.-H. Kim and W. P. Grice, Measurement of the spectral properties of the two-photon state generated via type II spontaneous parametric downconversion, *Opt. Lett.* **30**, 908–910 (2005).
- [100] O. Kuzucu, F. N. C. Wong, S. Kurimura, and S. Tovstonog, Joint Temporal Density Measurements for Two-Photon State Characterization, *Phys. Rev. Lett.* **101**, 153602 (2008).
- [101] M. Avenhaus, A. Eckstein, P. J. Mosley, and C. Silberhorn, Fiber-assisted single-photon spectrograph, *Opt. Lett.* **34**, 2873–2875 (2009).
- [102] M. Liscidini and J. E. Sipe, Stimulated Emission Tomography, *Phys. Rev. Lett.* **111**, 193602 (2013).
- [103] A. Eckstein, G. Boucher, A. Lemaître, P. Filloux, I. Favero, G. Leo, J. E. Sipe, M. Liscidini, and S. Ducci, High-resolution spectral characterization of two photon states via classical measurements, *Laser & Photonics Reviews* **8**, L76–L80 (2014).
- [104] K. Zielnicki, K. Garay-Palmett, D. Cruz-Delgado, H. Cruz-Ramirez, M. F. O’Boyle, B. Fang, V. O. Lorenz, A. B. U’Ren, and P. G. Kwiat, Joint spectral characterization of photon-pair sources, *Journal of Modern Optics* **65**, 1141–1160 (2018).
- [105] I. Gianani, M. Sbroscia, and M. Barbieri, Measuring the time–frequency properties of photon pairs: A short review, *AVS Quantum Science* **2**, 011701 (2020).
- [106] I. Jizan, B. Bell, L. G. Helt, A. C. Bedoya, C. Xiong, and B. J. Eggleton, Phase-sensitive tomography of the joint spectral amplitude of photon pair sources, *Opt. Lett.* **41**, 4803–4806 (2016).
- [107] K.-K. Park, J.-H. Kim, T.-M. Zhao, Y.-W. Cho, and Y.-H. Kim, Measuring the frequency-time two-photon wavefunction of narrowband entangled photons from cold atoms via stimulated emission, *Optica* **4**, 1293–1297 (2017).

- [108] I. Gianani, Robust spectral phase reconstruction of time-frequency entangled bi-photon states, *Phys. Rev. Research* **1**, 033165 (2019).
- [109] J. A. Miszczak, Singular value decomposition and matrix reorderings in quantum information theory, *International Journal of Modern Physics C* **22**, 897–918 (2011).
- [110] K. Edamatsu, R. Shimizu, W. Ueno, R.-B. Jin, F. Kaneda, M. Yabuno, H. Suzuki, S. Nagano, A. Syouji, and K. Suizu, Photon pair sources with controlled frequency correlation, *Prog. Inform.* **8**, 19–26 (2011).
- [111] A. Fedrizzi, T. Herbst, M. Aspelmeyer, M. Barbieri, T. Jennewein, and A. Zeilinger, Anti-symmetrization reveals hidden entanglement, *New Journal of Physics* **11**, 103052 (2009).
- [112] F. Graffitti, P. Barrow, A. Pickston, A. M. Brańczyk, and A. Fedrizzi, Direct Generation of Tailored Pulse-Mode Entanglement, *Phys. Rev. Lett.* **124**, 053603 (2020).
- [113] M. M. Fejer, G. A. Magel, D. H. Jundt, and R. L. Byer, Quasi-phase-matched second harmonic generation: tuning and tolerances, *IEEE Journal of Quantum Electronics* **28**, 2631–2654 (1992).
- [114] M. A. Arbore, A. Galvanauskas, D. Harter, M. H. Chou, and M. M. Fejer, Engineerable compression of ultrashort pulses by use of second-harmonic generation in chirped-period-poled lithium niobate, *Opt. Lett.* **22**, 1341–1343 (1997).
- [115] G. Imeshev, M. A. Arbore, M. M. Fejer, A. Galvanauskas, M. Fermann, and D. Harter, Ultrashort-pulse second-harmonic generation with longitudinally nonuniform quasi-phase-matching gratings: pulse compression and shaping, *J. Opt. Soc. Am. B* **17**, 304–318 (2000).
- [116] V. Y. Shur, E. L. Rumyantsev, E. V. Ndcloaeva, E. I. Shishkin, R. G. Batchko, M. M. Fejer, and R. L. Byer, Recent achievements in domain engineering in lithium niobate and lithium tantalate, *Ferroelectrics* **257**, 191–202 (2001).
- [117] Y. Zhang and B.-Y. Gu, Optimal design of aperiodically poled lithium niobate crystals for multiple wavelengths parametric amplification, *Optics Communications* **192**, 417 – 425 (2001).
- [118] D. T. Reid, Engineered quasi-phase-matching for second-harmonic generation, *Journal of Optics A: Pure and Applied Optics* **5**, S97–S102 (2003).
- [119] Ł. Kornaszewski, M. Kohler, U. K. Sapaev, and D. T. Reid, Designer femto-second pulse shaping using grating-engineered quasi-phase-matching in lithium niobate, *Opt. Lett.* **33**, 378–380 (2008).

- [120] C. Cui, R. Arian, S. Guha, N. Peyghambarian, Q. Zhuang, and Z. Zhang, Wave-Function Engineering for Spectrally Uncorrelated Biphotons in the Telecommunication Band Based on a Machine-Learning Framework, *Phys. Rev. Applied* **12**, 034059 (2019).
- [121] S. Kirkpatrick, C. D. Gelatt, and M. P. Vecchi, Optimization by Simulated Annealing, *Science* **220**, 671–680 (1983).
- [122] S. Kirkpatrick, Optimization by simulated annealing: Quantitative studies, *Journal of Statistical Physics* **34**, 975–986 (1984).
- [123] A. Christ and C. Silberhorn, Limits on the deterministic creation of pure single-photon states using parametric down-conversion, *Phys. Rev. A* **85**, 023829 (2012).
- [124] L. G. Helt, A. M. Brańczyk, M. Liscidini, and M. J. Steel, Parasitic Photon-Pair Suppression via Photonic Stop-Band Engineering, *Phys. Rev. Lett.* **118**, 073603 (2017).
- [125] G. D. Miller, *Periodically Poled Lithium Niobate: Modeling, Fabrication, and Nonlinear-Optical Performance*, Ph.D. thesis, Stanford University, Stanford, California (1998).
- [126] S. Helmfrid and G. Arvidsson, Influence of randomly varying domain lengths and nonuniform effective index on second-harmonic generation in quasi-phase-matching waveguides, *J. Opt. Soc. Am. B* **8**, 797–804 (1991).
- [127] H. Karlsson, F. Laurell, P. Henriksson, and G. Arvidsson, Frequencydoubling in periodically poled RbTiOAs₄, *Electronics Letters* (1996).
- [128] H. Karlsson and F. Laurell, Electric field poling of flux grown KTiOPO₄, *Applied Physics Letters* **71**, 3474–3476 (1997).
- [129] J. S. Pelc, C. Langrock, Q. Zhang, and M. M. Fejer, Influence of domain disorder on parametric noise in quasi-phase-matched quantum frequency converters, *Opt. Lett.* **35**, 2804–2806 (2010).
- [130] J. S. Pelc, C. R. Phillips, D. Chang, C. Langrock, and M. M. Fejer, Efficiency pedestal in quasi-phase-matching devices with random duty-cycle errors, *Opt. Lett.* **36**, 864–866 (2011).
- [131] R. van der Meer, J. J. Renema, B. Brecht, C. Silberhorn, and P. W. H. Pinkse, Optimizing spontaneous parametric down-conversion sources for boson sampling, *Phys. Rev. A* **101**, 063821 (2020).
- [132] R. S. Bennink, Optimal collinear Gaussian beams for spontaneous parametric down-conversion, *Phys. Rev. A* **81**, 053805 (2010).
- [133] W. P. Grice, R. S. Bennink, D. S. Goodman, and A. T. Ryan, Spatial entanglement and optimal single-mode coupling, *Phys. Rev. A* **83**, 023810 (2011).

- [134] P. B. Dixon, D. Rosenberg, V. Stelmakh, M. E. Grein, R. S. Bennink, E. A. Dauler, A. J. Kerman, R. J. Molnar, and F. N. C. Wong, Heralding efficiency and correlated-mode coupling of near-IR fiber-coupled photon pairs, *Phys. Rev. A* **90**, 043804 (2014).
- [135] V. D’Auria, O. Morin, C. Fabre, and J. Laurat, Effect of the heralding detector properties on the conditional generation of single-photon states, *The European Physical Journal D* **66**, 249 (2012).
- [136] M. Erhard, M. Malik, M. Krenn, and A. Zeilinger, Experimental Greenberger-Horne-Zeilinger entanglement beyond qubits, *Nature Photonics* **12**, 759–764 (2018).
- [137] J. Wang, S. Paesani, Y. Ding, R. Santagati, P. Skrzypczyk, A. Salavrakos, J. Tura, R. Augusiak, L. Mančinska, D. Bacco, D. Bonneau, J. W. Silverstone, Q. Gong, A. Acín, K. Rottwitt, L. K. Oxenløwe, J. L. O’Brien, A. Laing, and M. G. Thompson, Multidimensional quantum entanglement with large-scale integrated optics, *Science* **360**, 285–291 (2018).
- [138] M. Kues, C. Reimer, P. Roztocki, L. R. Cortés, S. Sciara, B. Wetzels, Y. Zhang, A. Cino, S. T. Chu, B. E. Little, D. J. Moss, L. Caspani, J. Azaña, and R. Morandotti, On-chip generation of high-dimensional entangled quantum states and their coherent control, *Nature* **546**, 622–626 (2017).
- [139] N. T. Islam, C. C. W. Lim, C. Cahall, J. Kim, and D. J. Gauthier, Provably secure and high-rate quantum key distribution with time-bin qudits, *Science Advances* **3**, e1701491 (2017).
- [140] H.-H. Lu, J. M. Lukens, N. A. Peters, B. P. Williams, A. M. Weiner, and P. Lougovski, Quantum interference and correlation control of frequency-bin qubits, *Optica* **5**, 1455–1460 (2018).
- [141] P. Imany, J. A. Jaramillo-Villegas, M. S. Alshaykh, J. M. Lukens, O. D. Odele, A. J. Moore, D. E. Leaird, M. Qi, and A. M. Weiner, High-dimensional optical quantum logic in large operational spaces, *npj Quantum Information* **5**, 59 (2019).
- [142] Q. Ding, R. Chatterjee, Y. Huang, and T. Yu, High-dimensional temporal mode propagation in a turbulent environment, (2019), [arXiv:1907.02321 \[quant-ph\]](https://arxiv.org/abs/1907.02321).
- [143] A. Eckstein, B. Brecht, and C. Silberhorn, A quantum pulse gate based on spectrally engineered sum frequency generation, *Opt. Express* **19**, 13770–13778 (2011).
- [144] V. Ansari, J. M. Donohue, B. Brecht, and C. Silberhorn, Tailoring nonlinear processes for quantum optics with pulsed temporal-mode encodings, *Optica* **5**, 534–550 (2018).

- [145] B. Brecht, D. V. Reddy, C. Silberhorn, and M. G. Raymer, Photon Temporal Modes: A Complete Framework for Quantum Information Science, *Phys. Rev. X* **5**, 041017 (2015).
- [146] Y.-P. Huang and P. Kumar, Mode-resolved photon counting via cascaded quantum frequency conversion, *Opt. Lett.* **38**, 468–470 (2013).
- [147] V. Ansari, J. M. Donohue, M. Allgaier, L. Sansoni, B. Brecht, J. Roslund, N. Treps, G. Harder, and C. Silberhorn, Tomography and Purification of the Temporal-Mode Structure of Quantum Light, *Phys. Rev. Lett.* **120**, 213601 (2018).
- [148] D. V. Reddy and M. G. Raymer, High-selectivity quantum pulse gating of photonic temporal modes using all-optical Ramsey interferometry, *Optica* **5**, 423–428 (2018).
- [149] A. O. C. Davis, V. Thiel, and B. J. Smith, Measuring the quantum state of a photon pair entangled in frequency and time, (2018), [arXiv:1809.03727 \[quant-ph\]](https://arxiv.org/abs/1809.03727) .
- [150] K. Wang, Quantum theory of two-photon wavepacket interference in a beamsplitter, *Journal of Physics B: Atomic, Molecular and Optical Physics* **39**, R293 (2006).
- [151] A. Eckstein and C. Silberhorn, Broadband frequency mode entanglement in waveguided parametric downconversion, *Opt. Lett.* **33**, 1825–1827 (2008).
- [152] T. Douce, A. Eckstein, S. P. Walborn, A. Z. Khoury, S. Ducci, A. Keller, T. Coudreau, and P. Milman, Direct measurement of the biphoton Wigner function through two-photon interference, *Scientific Reports* **3**, 3530 (2013).
- [153] D. L. P. Vitullo, M. G. Raymer, B. J. Smith, M. Karpiński, L. Mejling, and K. Rottwitt, Entanglement swapping for generation of heralded time-frequency-entangled photon pairs, *Phys. Rev. A* **98**, 023836 (2018).
- [154] S. Merkouche, V. Thiel, A. O. C. Davis, and B. J. Smith, Two-color Bell states heralded via entanglement swapping, (2019), [arXiv:1910.06506 \[quant-ph\]](https://arxiv.org/abs/1910.06506) .
- [155] A. Pe’er, B. Dayan, A. A. Friesem, and Y. Silberberg, Temporal Shaping of Entangled Photons, *Phys. Rev. Lett.* **94**, 073601 (2005).
- [156] N. Matsuda, Deterministic reshaping of single-photon spectra using cross-phase modulation, *Science Advances* **2**, e1501223 (2016).
- [157] V. Averchenko, D. Sych, G. Schunk, U. Vogl, C. Marquardt, and G. Leuchs, Temporal shaping of single photons enabled by entanglement, *Phys. Rev. A* **96**, 043822 (2017).
- [158] C. J. McKinstrie, J. B. Christensen, K. Rottwitt, and M. G. Raymer, Generation of two-temporal-mode photon states by vector four-wave mixing, *Opt. Express* **25**, 20877–20893 (2017).

- [159] S. Francesconi, F. Baboux, A. Raymond, N. Fabre, G. Boucher, A. Lemaître, P. Milman, M. I. Amanti, and S. Ducci, Engineering two-photon wavefunction and exchange statistics in a semiconductor chip, *Optica* **7**, 316–322 (2020).
- [160] T. Hiemstra, T. Parker, P. Humphreys, J. Tiedau, M. Beck, M. Karpiński, B. Smith, A. Eckstein, W. Kolthammer, and I. Walmsley, Pure Single Photons From Scalable Frequency Multiplexing, *Phys. Rev. Applied* **14**, 014052 (2020).
- [161] D. Kundys, F. Graffitti, R. A. McCracken, A. Fedrizzi, and B. Kundys, Numerical Study of Reconfigurable Mid-IR Single Photon Sources Based on Functional Ferroelectrics, *Advanced Quantum Technologies* **3**, 1900092 (2020).
- [162] A. Lyons, G. C. Knee, E. Bolduc, T. Roger, J. Leach, E. M. Gauger, and D. Faccio, Attosecond-resolution Hong-Ou-Mandel interferometry, *Science Advances* **4**, eaap9416 (2018).
- [163] M. Santandrea, M. Stefszky, V. Ansari, and C. Silberhorn, Fabrication limits of waveguides in nonlinear crystals and their impact on quantum optics applications, *New Journal of Physics* **21**, 033038 (2019).
- [164] M. F. Saleh, Modelling spontaneous four-wave mixing in periodically tapered waveguides, *Opt. Express* **27**, 11979–11990 (2019).
- [165] H. Rubinsztein-Dunlop, A. Forbes, M. V. Berry, M. R. Dennis, D. L. Andrews, M. Mansuripur, C. Denz, C. Alpmann, P. Banzer, T. Bauer, E. Karimi, L. Marrucci, M. Padgett, M. Ritsch-Marte, N. M. Litchinitser, N. P. Bigelow, C. Rosales-Guzmán, A. Belmonte, J. P. Torres, T. W. Neely, M. Baker, R. Gordon, A. B. Stilgoe, J. Romero, A. G. White, R. Fickler, A. E. Willner, G. Xie, B. McMorrán, and A. M. Weiner, Roadmap on structured light, *Journal of Optics* **19**, 013001 (2016).